MODELLING THE BEHAVIOUR OF DENSE COLLOIDAL SUSPENSIONS OF CUBOIDS.

Effect of ordered crowding on dynamics and microrheology.

A thesis submitted to The University of Manchester for the degree of Doctor of Philosophy in the Faculty of Science and Engineering

2023

Luca Tonti

Department of Chemical Engineering

The University of Manchester

blank page

Contents

Word count: 36351

blank page

List of Figures

List of Tables

Abstract

The shape of colloidal particles drives their self-organisation in ordered structures, that in turn confer peculiar characteristics to the suspension. In the design of new smart materials, we first need to understand how particle diffusion and self-assembly relate to each other and to the macroscopic properties of the entire system. To this end, this thesis focused on the dynamics and microrheology of crowded suspensions with different degrees of long-range ordering. We modelled different systems using hard spheres and hard board-like particles, i.e., cuboids: the latter can self-assemble in many liquid crystalline phases depending on their geometry. All the systems have been studied by means of classic Monte Carlo and dynamic Monte Carlo simulations, which proved to be effective to model hard-core particles of any shape and to mimic Brownian motion. The first part of the thesis is dedicated to the derivation and benchmarking of our collision detection algorithm between one sphere and one cuboid. Thanks to the use of OpenMP directives, we managed to make the algorithm both time efficient and stable in different scenarios and user-friendly. Then, we investigated the diffusion of globular macromolecules in isotropic and uniaxial nematic phases of hard board-like particles. Macromolecules, modelled as hard spheres, showed anisotropic diffusion in nematic phases, with preferential displacement in the direction parallel or perpendicular to the director. Non-Gaussian distribution of particle displacements has been observed for both hard spheres and cuboids, in particular for prolate cuboids in isotropic phases. We performed cluster analysis in the isotropic phase, and we observed the formation of nematic-like cluster of hard board-like particles, which may induce local temporary non-isotropic diffusion. The third part of the thesis focuses on electrorheological fluids of nanocubes. At low dilution and specific field strength, we observed the formation of string-like clusters, with an equilibrium distribution of chain lengths and fixed response times. Performing passive microrheology simulations in the field-on and field-off states, we observed anisotropic viscoelasticity of concentrated string-like fluids, depending on the direction of the external field. We then investigated the rotational dynamics of cuboids in the induced transition from a uniaxial to a biaxial nematic phase. The response time is geometry-dependent, with remarkable slow dynamics for cuboids close to self-dual shape, despite such geometry is known to favour biaxiality. In the last part of the thesis, we applied active microrheology simulation techniques in isotropic phases of cuboids with prolate, self-dual shaped and oblate geometries. Local friction coefficient at different Péclet numbers shows typical force-thinning behaviour, both density and geometry dependent. Differences in the effective friction for systems with different particle geometry may be explained by the presence of nematic-like clusters and the ratio in size between the bath and the tracer particles.

blank page

Declaration

No portion of the work referred to in the thesis has been submitted in support of an application for another degree or qualification of this or any other university or other institute of learning.

blank page

Copyright Statement

blank page

Acknowledgments

First of all, I would like to express my warmest gratitude to my supervisors Alessandro Patti and Carlos Avendaño. I personally thank Alessandro for his guidance, support and tireless patience. Because of this opportunity and your trust, you nourished in me passion for new fields of study and I will always be grateful for it. My personal gratitude goes also to Carlos for his patience and dedicated availability in every step of my PhD, discussions with you have been deeply resourceful in this journey.

I would also like to thank my collaborators and friends, Fabián and Effran. Your knowledge and continuous support have been essential to improve the quality of the research and I will always be grateful for that. Alejandro Cuetos deserves a special recognition, for his technical suggestions and resources that have been helpful to develop the source code needed for all the work presented in this thesis.

Next, I would like to thank everyone from the Multiscale Modelling group. The academics Paola, Andrew, Claudio and especially Flor, for providing a different point of view and challenging me with new points of discussion on my work. I also want to thank all my friends and colleagues, the ones I started my PhD with, the ones I finished with and the ones who have always been there with me: it has been a pleasure to meet, work and have fun with all of you.

My deepest gratitude goes to Mara, Vincenzo, Rosa, Nicola, Alex, Eugenia, Chiara, Sonia, Daniele and Oscar: they have been a shoulder to lean on in times of need, joyful people I had the fortune to spend time and make new memories with, my second family in rainy Manchester. I also want to mention my old friends, Gaia, Sharon, Sophia, Silvia, Silvia, Antonio, Maria Chiara, Emilio, Andrea, Clara: they have always been ready to support me and to cheer me up in hard times. I will always be grateful for them to be part of my life.

Last but not least, I am indebted to all my family. You all have always believed in me: all my present achievements, and the ones that hopefully will come in the future, are the results of all your support and help. Thank you with all my heart.

blank page

Publications

Articles derived from this thesis:

Chapter 3
Luca Tonti and Alessandro Patti
Fast overlap detection between hard-core colloidal cuboids and spheres. The OCSI algorithm
Algorithms **14**, 72 (2021)

Chapter 4
Luca Tonti, Fabián A. García Daza and Alessandro Patti
Diffusion of globular macromolecules in liquid crystals of colloidal cuboids
Journal of Molecular Liquids **338**, 116640 (2021)

Chapter 5
Luca Tonti, Fabián A. García Daza and Alessandro Patti
Kinetics of isotropic to string-like phase switching in electrorheological fluids of nanocubes
Journal of Chemical Physics **157**, 224906 (2022)

Chapter 6
Effran Mirzad Rafael, Luca Tonti, Daniel Corbett, Alejandro Cuetos and Alessandro Patti
Dynamics of uniaxial-to-biaxial nematics switching in suspensions of hard cuboids
Physics of Fluids **33**, 067115 (2021)

Chapter 7
Effran Mirzad Rafael, Luca Tonti, Fabián A. García Daza and Alessandro Patti
Active Microrheology of Colloidal Suspensions of Hard Cuboids
Physical Review E **106**, 034612 (2022)

blank page

Chapter 1

Introduction

Abstract

In this chapter a basic introduction of colloidal particles is presented. Here, we describe the static and dynamical properties that characterise colloidal particles, by comparing them to atoms and molecules. We then give a brief overview of hard board-like particles and, finally, an outline of the structure of the thesis.

1.1 Colloids and ordering

By definition, a colloid is a biphasic system composed of a "dispersed" phase and a surrounding dispersion medium, where the former is organised in subdomains with least one of their three spatial dimensions between 1 nm and 1 µm [1]. Blood is composed of blood cells immersed in liquid plasma; in clay, tiny aggregates of mineral particles are separated by thin layers of water; one single cell contains a myriad of organelles and supramolecular structures immersed in liquid cytoplasm; in industry, solid particles within a range of 1-100 nm, e.g., nanoparticles, are added in paint, lubricant and detergent to confer specific physical and chemical properties to the entire solution. All the aforementioned materials are examples of colloids. Colloidal systems are classified depending on the thermodynamic state of the two phases that compose them. In this thesis, we mainly focus our attention on suspensions of solid particles dispersed in liquid medium, and we refer to the dispersed phase as "colloidal particles".

Despite the difference in size, colloidal particles and molecules have features in common. From a topological point of view, colloidal particles of many different shapes can

be found in nature or can be artificially synthesised, and shape alone can be a determinant factor in their spatial organisation. Tobacco Mosaic Virus (TMV) is an example: this single-strand molecule of RNA encapsulated in a protein supramolecular structure has a unique cylindrical shape. It has been observed that, depending on ion concentration in solution and pH, particles of TMV tend to align with each other with respect to their length [2, 3, 4]. A similar behaviour has been observed in suspensions of synthetic nanorods of different materials, at specific conditions of concentration [5, 6, 7]. The spontaneous reconfiguration of cylindrical particles in domains with a preferential orientation is a typical liquid crystal phase transition. Liquid crystals (LCs) are thermodynamic phases of matter that are characterised by their intermediate level of spatial symmetry between the one of an isotropic liquid and a perfect crystalline phase [8]. LCs have been observed both in the molecular and the colloidal scales [9]. The seminal work of Onsager proved that a system made of infinitely long rigid rod-like particles, at a specific concentration, undergoes phase transition from a state of pure disorder (e.g., an isotropic (I) phase) to having a preferential orientation in space (e.g., a nematic (N) phase). This I-to-N phase transition is entropically favoured, formally proving that particle shape is sufficient to induce self-organisation [10]. This discovery lead to the investigation of the phase behaviour of particles of any shape, from prolate [11] to oblate geometry [12], disk-like or board-like [13, 14], to particles with a certain degree of curvature [15], *via* theoretical studies and nanoparticle synthesis [16]. We dedicate here a special attention to hard board-like particles (HBPs), i.e., cuboids: despite their simple shape, they can self-assemble in many different LC phases, from nematic to smectic (Sm), columnar (Col), cubatic (Cu) and parquet (Par) phases, when changing their size from prolate to oblate geometries [13, 17, 18]. It has been shown that their biaxial geometry can also promote the formation of biaxial nematic (N_B) phases, in which HBPs have not one but two different main axes of preferential orientation. Experiments on particles of this shape managed to stabilise this elusive LC phase [19], and particle simulations suggested that polydispersed systems of HBPs tend to naturally form stable N_B phases [20, 21]. Particular attention has been dedicated also to biaxial particles with dual-shaped geometry, where one particle extent is the geometric average of the other two, since different studies show that such a specific geometry, intermediate between prolate and oblate, promote biaxiality [22, 23]. The augmented orientational order of

biaxial rather than uniaxial nematic phases, make the former appealing for the design of new optical materials [24].

Another similar characteristic in common between colloidal particles and molecules is their inter-particle interaction. Colloidal particles can attract or repel each other. Their attraction can be reversible or not, and they can bind with each other. Their interaction can also be directional, and selective of specific sites. These features give them the possibility to assemble in different kind of structures, regardless of their shape [25, 26, 27]. These characteristics make colloidal particles the perfect candidate to investigate physical phenomena that occur in the molecular scale, while being more easily accessible to be observed from an experimental point of view [28]; at the same time, their physical and chemical properties can be optimised and tuned to fabricate new materials with exceptional properties.

1.2 Dynamics of colloidal particles

Despite the similarities between molecular and colloidal systems, one major difference between the two is their dynamics. Colloidal particles are much slower than single molecules, and the motion of the former depends on both the interaction between particles of the same scale, and the interactions with the surrounding medium, which is commonly made of molecules. The presence of the medium make the dispersed phase move in a unique way, known as Brownian motion, in honour of botanist Robert Brown, who observed random fluctuating motion of grains of pollen under microscope [29]. Brownian motion is peculiar of colloidal systems, such that particles with this dynamics are also known as Brownian particles. In 1905, Albert Einstein presented a theoretical explanation of the Brownian motion of suspended particles using molecular kinetic theory: the dynamics of one single particle in suspension, in the absence of other forces, depends solely on the drag resistance of the medium and the thermal energy with molecules of the medium; the motion of a colloidal particle is hindered by the resistance of the surrounding fluid; this resistance is dissipated into thermal energy, and, consequently, as kinetic energy by the molecules that compose the medium; solvent particles randomly collide with the surface of the dispersed particles, which start moving randomly in the medium [30]. The work of Einstein and Smoluchowski prove that the probability dis-

tribution function of particle position in space is described exactly by Fick's second law of diffusion [31], and that particle motion is characterized by a diffusivity which is dependent on the viscosity of the medium and temperature [32]. Later, Paul Langevin showed that Brownian motion can be equivalently described by a stochastic differential equation, based on classical Newtonian mechanics plus a random fluctuating force [33].

According to both formulations, the mean square displacement of the particles is linear with time, i.e., $\langle \Delta r^2 \rangle \propto t$, but only in the absence of other forces. The inclusion of interactions with other particles and other external forces adds a higher degree of complexity to the theoretical treatment of Brownian motion. If we take into account solely particle concentration, it has been observed that when Brownian particles start to collide with each other, their diffusion is damped and their motion show a *subdiffusive* regime, i.e., $\langle \Delta r^2 \rangle \propto t^\beta, \beta < 1$. Eventually, the diffusive regime is restored, with a diffusivity lower than the diffusion coefficient at infinite dilution [34]. If we also consider the presence of ordered structures surrounding one or a collection of moving particles, their dynamics gets even more complex. This is commonly observed in nature, for macromolecules that move from one organelle to another, passing through the cytoplasm, which is rich of macromolecules and supramolecular structures of any kind [35, 36, 37]. Studies of macromolecular crowding are fundamental for research in cancer medicine. Innovative treatments of cancer focus on targeted therapy and they exploit nanoparticles as drug carriers; due to the structural complexity of the system that such particles have to move into, not only particle size but also their shape plays a determinant role in diffusion in living tissue [38, 39, 40]. Understanding the dynamics of Brownian particles is fundamental also in the design of new smart materials, that respond to the application of an external stimulus. Examples of materials of this kind are electorheological and magnetorheological fluids, i.e., suspensions of solid particles that reversibly transform from a fluid-like to a plastic-like states when an external electric or magnetic field is applied. The sudden change in rheological properties of the suspension is caused by the particle alignment and the formation of fibrous structures along the direction of the field. These devices have already been used as electric valves, clutches and damping devices [41, 42]. The effect of particle shape on these systems is still under investigation, but it is crucial to be taken into account[43, 44]. Going a step further, not only the dynamics of Brownian particles influences the macroscopic behaviour of the entire suspension,

but their dynamics retains itself information of the local viscoelastic properties of the suspension, because of possible collisions with their surroundings. This field of study, known as "microrheology", exploits the motion of a probe particle, with or without an external field acting on it, to recover local viscoelastic properties of the material in the vicinity of the moving probe particle [45, 46]. It is clear that a deep comprehension of the effect of shape and self-organisation of Brownian particles in their motion, and the consequent effect of their motion on macroscopic properties of the entire suspension, is undoubtedly fundamental for developments in different areas, from biology to material science, and this is what this PhD project is focused on.

Computer simulation so far have proved to be an excellent tool to study colloidal systems, to investigate their self-assembly and their dynamics, and it has become a useful instrument to predict and, at the same time, confirm experimental observation and theoretical expectations. Nowadays, Monte Carlo simulations are a standard method of investigation of particle self-assembly, due to their simple implementation and effectiveness. This technique has been widely used to study the phase behaviour of particles of hypothetically any shape, usually neglecting the effective nature of interactions that particles may have in a real systems, in favour of a selective attention on volume excluded interactions [47]. Several techniques like Brownian Dynamics [48, 49], Dissipative Particle Dynamics [50], Stokesian Dynamics [51], just to mention a few, have been developed to study the nature of the dynamics of colloidal systems, where any of them either neglects or incorporates different kind of interactions between the particles, and between particles and liquid medium. Due to the stochastic nature of Brownian motion, Monte Carlo methods have been developed to integrate particle motion [52, 53]. In this PhD research, we performed dynamic Monte Carlo simulations, following the algorithm proposed by Patti and Cuetos [54].

1.3 Outline of the thesis

The aim of this PhD project is to unravel the mechanisms in play in the dynamics of colloidal particles in crowded media with a degree of ordering. We focused our attention on how the non-trivial relations between particle shape, concentration and self organisation may induce anomalous diffusion in suspensions, and if and how their dynamical

behaviour can explain macroscopic properties of the suspension, with a focus on its mechanical and rheological ones. To do so, we modelled different problems in soft matter by simulating colloidal suspensions of hard board-like particles (HPBs) and hard spheres *via* dynamic Monte Carlo simulations. All the DMC simulations performed over the course of this PhD research project, neglected the effect of hydrodynamic interactions on the motion of the colloidal systems simulated.

In the first part of the thesis, we focused on developing the algorithm for collision detection between spheres and cuboids. We optimised the algorithm for simulation purposes, we developed a FORTRAN version of the algorithm and we compared its efficiency with other algorithms available in literature. We showed its computational efficiency in scenarios made of one sphere and one cuboid of anisotropic (oblate to prolate) shape, at a specific acceptance rate. An article of this project is published in *Algorithms*, volume 14, page 72 (2021); the content of the article is presented in Chapter 3.

In the second part of the project, we performed dynamic Monte Carlo (DMC) simulations of suspensions of small hard spheres and prolate and oblate HBPs, to model the diffusion of globular macromolecules in crowded suspensions. More specifically, we wanted to investigate how long-range ordering affects the dynamics of macromolecules in purely diffusive regime, analysing the dynamics of host spheres moving in a bath of isotropic and uniaxial nematic liquid crystal phases of cuboids. We observed anisotropic diffusion of spherical tracers in uniaxial nematic phases along the directions parallel and perpendicular to the nematic director of the host phase, with the formation of temporary cages at intermediate time scales. We observed strong deviation of the total non-Gaussian parameter (NGP) of prolate cuboids in the isotropic phase; to this end we analysed their local structural properties and we observed that some HBPs form clusters with nematic-like organisation, whose formation could explain the observed deviation from expected Gaussian distribution of particle displacements. An article of this project is published in *Journal of Molecular Liquids*, volume 338, page 116640 (2021) and its content can be found in Chapter 4.

In the third part of the project, we implemented the Ewald summation method for dipolar interactions in our software, and we performed out-of-equilibrium simulations of electrorheological fluids of colloidal cubes, switching an external electric field on and off. We analysed the kinetics of formation of clusters of cubic particles in the transient

regime: at low dilution and specific field strength, such systems tend to form string-like clusters, separated from each other, with an equilibrium distribution of string lengths and a characteristic response time. We then added one hard spherical tracer to the system of cubes and we performed passive microrheology DMC simulations at equilibrium with the field on and off. While at low dilution the viscoelastic response of the suspension is the same regardless of the presence of the external field, at higher density the suspension exhibits different viscous and elastic behaviour in the direction parallel and perpendicular to the applied field, due to the presence of string-like clusters oriented along the field. An article of this project is published in *Journal of Chemical Physics* volume 157, page 224906 (2022) and its content is presented in Chapter 4.

While working on my main research project, I contributed as co-author in two different projects.

In the first one, we investigated the rotational dynamics of HBPs, whose orientation changes under the application of a model external field, spanning from prolate to oblate particle anisotropy. At specific concentration, these systems form uniaxial and biaxial nematic phases when the external field is off and on, respectively. We computed the response times of the suspensions in the off-to-on and on-to-off transient regimes: self-dual shaped cuboids, theoretically considered as the most suitable to promote phase biaxiality, exhibit slow response times, especially if compared to prolate cuboids. It this project, I contributed by providing coding support for the computation of dynamical properties, by contributing in the investigation and the discussion of the simulation results over the course of the entire project, and by co-writing and editing the manuscript. These results are published in *Physics of Fluids*, volume 33, page 067115 (2021); Chapter 6 of this thesis is dedicated to this research.

In the second project, we performed active microrheology simulations of isotropic phases of HBPs at different particle anisotropy and volume fraction, for different Péclet (Pe) numbers. The effective friction coefficients show two plateaus at low and high Pe numbers with a force-thinning regime at intermediate Pe; this profile, typical for suspensions, is observed for all system packing and particle geometry investigated. While enhanced friction of the bath of HBPs is observed at higher densities, non-monotonic behaviour of the effective fiction coefficient is evident when passing from prolate to oblate cuboids at fixed volume fraction. In this project, I contributed by implementing active

microrheology simulations in the main software for DMC simulations, by investigating and discussing the simulations results over the course of the entire project, and by reviewing and editing the manuscript. An article on this project has been published in Physical Review E and its content can be found in Chapter 7 of this thesis.

Bibliography

[1] Everett, D. H. Manual of Symbols and Terminology for Physicochemical Quantities and Units, Appendix II: Definitions, Terminology and Symbols in Colloid and Surface Chemistry. *Pure and Applied Chemistry* **31**, 577–638 (1972).

[2] Caspar, D. L. D. Assembly and stability of the tobacco mosaic virus particle. vol. 18 of *Advances in Protein Chemistry*, 37–121 (Academic Press, 1964).

[3] Fraden, S., Maret, G., Caspar, D. L. D. & Meyer, R. B. Isotropic-nematic phase transition and angular correlations in isotropic suspensions of tobacco mosaic virus. *Phys. Rev. Lett.* **63**, 2068–2071 (1989).

[4] Meyer, R. B. Ordered phases in colloidal suspensions of tobacco mosaic virus. In *Dynamics and Patterns in Complex Fluids*, 62–73 (Springer Berlin Heidelberg, 1990).

[5] Cheng, G., Wang, Y., Liu, K. & Yu, J. Entropy-driven self-assembly of chiral nematic liquid crystalline phases of AgNR@Cu2O hyper branched coaxial nanorods and thickness-dependent handedness transition. *Nano Research* **11**, 1018–1028 (2018).

[6] Hegmann, T., Qi, H. & Marx, V. M. Nanoparticles in Liquid Crystals: Synthesis, Self-Assembly, Defect Formation and Potential Applications. *Journal of Inorganic and Organometallic Polymers and Materials* **17**, 483–508 (2007).

[7] Jana, N. R. *et al.* Liquid crystalline assemblies of ordered gold nanorods. *J. Mater. Chem.* **12**, 2909–2912 (2002).

[8] Barón, M. & Stepto, R. F. T. Definitions of basic terms relating to polymer liquid crystals (IUPAC Recommendations 2001). *Pure and Applied Chemistry* **74**, 493–509 (2002).

[9] Ingo, D. From colloids in liquid crystals to colloidal liquid crystals. *Liquid Crystals* **46**, 2057–2074 (2019).

[10] Onsager, L. The effects of shape on the interaction of colloidal particles. *Annals of the New York Academy of Sciences* **51**, 627–659 (1949).

[11] Bolhuis, P. & Frenkel, D. Tracing the phase boundaries of hard spherocylinders. *J. Chem. Phys.* **106**, 666–687 (1997).

[12] Veerman, J. A. C. & Frenkel, D. Phase behavior of disklike hard-core mesogens. *Phys. Rev. A* **45**, 5632–5648 (1992).

[13] John, B. S. & Escobedo, F. A. Phase behavior of colloidal hard tetragonal parallelepipeds (cuboids): A monte carlo simulation study. *J. Phys. Chem. B* **109**, 23008–23015 (2005).

[14] Batten, R. D., Stillinger, F. H. & Torquato, S. Phase behavior of colloidal superballs: Shape interpolation from spheres to cubes. *Phys. Rev. E* **81**, 061105 (2010).

[15] Chiappini, M., Drwenski, T., van Roij, R. & Dijkstra, M. Biaxial, twist-bend, and splay-bend nematic phases of banana-shaped particles revealed by lifting the "smectic blanket". *Phys. Rev. Lett.* **123**, 068001 (2019).

[16] Grzelczak, M., Pérez-Juste, J., Mulvaney, P. & Liz-Marzán, L. M. Shape control in gold nanoparticle synthesis. *Chem. Soc. Rev.* **37**, 1783–1791 (2008).

[17] Cuetos, A., Dennison, M., Masters, A. & Patti, A. Phase behaviour of hard boardlike particles. *Soft Matter* **13**, 4720–4732 (2017).

[18] Yang, Y. *et al.* Synthesis and assembly of colloidal cuboids with tunable shape biaxiality. *Nature Communications* **9**, 4513 (2018).

[19] van den Pol, E., Petukhov, A. V., Thies-Weesie, D. M. E., Byelov, D. V. & Vroege, G. J. Experimental realization of biaxial liquid crystal phases in colloidal dispersions of boardlike particles. *Phys. Rev. Lett.* **103**, 258301 (2009).

[20] Belli, S., Patti, A., Dijkstra, M. & van Roij, R. Polydispersity stabilizes biaxial nematic liquid crystals. *Phys. Rev. Lett.* **107**, 148303 (2011).

[21] Mirzad Rafael, E., Corbett, D., Cuetos, A. & Patti, A. Self-assembly of freely-rotating polydisperse cuboids: unveiling the boundaries of the biaxial nematic phase. *Soft Matter* **16**, 5565–5570 (2020).

[22] Mulder, B. Isotropic-symmetry-breaking bifurcations in a class of liquid-crystal models. *Phys. Rev. A* **39**, 360–370 (1989).

[23] Allen, M. P. Computer simulation of a biaxial liquid crystal. *Liquid Crystals* **8**, 499–511 (1990).

[24] Lee, J.-H., Lim, T.-K., Kim, W.-T. & Jin, J.-I. Dynamics of electro-optical switching processes in surface stabilized biaxial nematic phase found in bent-core liquid crystal. *J. Appl. Phys.* **101**, 034105 (2007).

[25] Glotzer, S. C. & Solomon, M. J. Anisotropy of building blocks and their assembly into complex structures. *Nature Materials* **6**, 557–562 (2007).

[26] Yi, G.-R., Pine, D. J. & Sacanna, S. Recent progress on patchy colloids and their self-assembly. *Journal of Physics: Condensed Matter* **25**, 193101 (2013).

[27] Sacanna, S. & Pine, D. J. Shape-anisotropic colloids: Building blocks for complex assemblies. *Current Opinion in Colloid & Interface Science* **16**, 96–105 (2011).

[28] Frenkel, D. Playing tricks with designer "atoms". *Science* **296**, 65–66 (2002).

[29] Brown, R. A brief account of microscopical observations made in the months of june, july and august 1827, on the particles contained in the pollen of plants; and on the general existence of active molecules in organic and inorganic bodies. *The Philosophical Magazine* **4**, 161–173 (1828).

[30] Einstein, A. Über die von der molekularkinetischen theorie der wärme geforderte bewegung von in ruhenden flüssigkeiten suspendierten teilchen. *Annalen der Physik* **322**, 549–560 (1905).

[31] Fick, A. V. on liquid diffusion. *The London, Edinburgh, and Dublin Philosophical Magazine and Journal of Science* **10**, 30–39 (1855).

[32] von Smoluchowski, M. Zur kinetischen theorie der brownschen molekularbewegung und der suspensionen. *Annalen der Physik* **326**, 756–780 (1906).

[33] Lemons, D. S. & Gythiel, A. Paul langevin's 1908 paper "on the theory of brownian motion" ["sur la théorie du mouvement brownien," c. r. acad. sci. (paris) 146, 530–533 (1908)]. *American Journal of Physics* **65**, 1079–1081 (1997).

[34] Dhont, J. K. Chapter 6 - diffusion. In *An Introduction to Dynamics of Colloids*, vol. 2 of *Studies in Interface Science*, 315–441 (Elsevier, 1996).

[35] Weiss, M., Elsner, M., Kartberg, F. & Nilsson, T. Anomalous subdiffusion is a measure for cytoplasmic crowding in living cells. *Biophysical Journal* **87**, 3518–3524 (2004).

[36] Szymanski, J. & Weiss, M. Elucidating the origin of anomalous diffusion in crowded fluids. *Phys. Rev. Lett.* **103**, 038102 (2009).

[37] Grima, R. & Schnell, S. A systematic investigation of the rate laws valid in intracellular environments. *Biophysical Chemistry* **124**, 1–10 (2006).

[38] Black, K. C. L. *et al.* Radioactive 198au-doped nanostructures with different shapes for in vivo analyses of their biodistribution, tumor uptake, and intratumoral distribution. *ACS Nano* **8**, 4385–4394 (2014).

[39] Yavuz, M. S. *et al.* Gold nanocages covered by smart polymers for controlled release with near-infrared light. *Nature Materials* **8**, 935–939 (2009).

[40] Truong, N. P., Whittaker, M. R., Mak, C. W. & Davis, T. P. The importance of nanoparticle shape in cancer drug delivery. *Expert Opinion on Drug Delivery* **12**, 129–142 (2015).

[41] Dong, Y. Z., Seo, Y. & Choi, H. J. Recent development of electro-responsive smart electrorheological fluids. *Soft Matter* **15**, 3473–3486 (2019).

[42] Kumar, J. S., Paul, P. S., Raghunathan, G. & Alex, D. G. A review of challenges and solutions in the preparation and use of magnetorheological fluids. *International Journal of Mechanical and Materials Engineering* **14**, 13 (2019).

[43] Noh, J., Yoon, C.-M. & Jang, J. Enhanced electrorheological activity of polyaniline coated mesoporous silica with high aspect ratio. *Journal of Colloid and Interface Science* **470**, 237–244 (2016).

[44] Han, S., Choi, J., Han, H. N., Kim, S. & Seo, Y. Effect of particle shape anisotropy on the performance and stability of magnetorheological fluids. *ACS Applied Electronic Materials* **3**, 2526–2533 (2021).

[45] Mason, T. G. & Weitz, D. A. Optical measurements of frequency-dependent linear viscoelastic moduli of complex fluids. *Phys. Rev. Lett.* **74**, 1250–1253 (1995).

[46] Squires, T. M. & Mason, T. G. Fluid mechanics of microrheology. *Annual Review of Fluid Mechanics* **42**, 413–438 (2010).

[47] Damasceno, P. F., Engel, M. & Glotzer, S. C. Predictive self-assembly of polyhedra into complex structures. *Science* **337**, 453–457 (2012).

[48] Ermak, D. L. & McCammon, J. A. Brownian dynamics with hydrodynamic interactions. *The Journal of Chemical Physics* **69**, 1352–1360 (1978).

[49] Delong, S., Balboa Usabiaga, F. & Donev, A. Brownian dynamics of confined rigid bodies. *The Journal of Chemical Physics* **143**, 144107 (2015).

[50] Santo, K. P. & Neimark, A. V. Dissipative particle dynamics simulations in colloid and interface science: a review. *Advances in Colloid and Interface Science* **298**, 102545 (2021).

[51] Brady, J. F. & Bossis, G. Stokesian dynamics. *Annual Review of Fluid Mechanics* **20**, 111–157 (1988).

[52] Sanz, E. & Marenduzzo, D. Dynamic monte carlo versus brownian dynamics: A comparison for self-diffusion and crystallization in colloidal fluids. *J. Chem. Phys.* **132**, 194102 (2010).

[53] Kikuchi, K., Yoshida, M., Maekawa, T. & Watanabe, H. Metropolis monte carlo method as a numerical technique to solve the fokker—planck equation. *Chemical Physics Letters* **185**, 335–338 (1991).

[54] Patti, A. & Cuetos, A. Brownian dynamics and dynamic monte carlo simulations of isotropic and liquid crystal phases of anisotropic colloidal particles: A comparative study. *Phys. Rev. E* **86**, 011403 (2012).

Chapter 2

Theoretical Background

Abstract

In this chapter, we describe in detail the main methods employed in our investigations. We first introduce basic concepts of statistical mechanics and how Monte Carlo algorithms are commonly used in particle simulation. We then thoroughly present dynamic Monte Carlo methods, which are the main computational simulation techniques used in the research project presented in this thesis. We conclude with a brief discussion on how to describe inter-particle interaction in simulations.

2.1 Statistical mechanics

A system made of colloidal particles, as well as molecular systems, obeys the rules of statistical mechanics [1]. In statistical mechanics, a macroscopical property of the entire system at equilibrium can be defined as follows:

$$\lim_{t\to\infty} \frac{1}{t} \int_0^t A(\mathbf{p}(t'), \mathbf{q}(t'))\, dt' = \langle A \rangle = \frac{\iint A(\mathbf{p}, \mathbf{q}) f(\mathbf{p}, \mathbf{q})\, d\mathbf{p} d\mathbf{q}}{\iint f(\mathbf{p}, \mathbf{q})\, d\mathbf{p} d\mathbf{q}}. \tag{2.1}$$

The property A is averaged over time in the LHS and in the phase space in the RHS. $f(\mathbf{p}, \mathbf{q})$ is the probability distribution of the system in the phase space at equilibrium, $\mathbf{q} = (q_{1,x}, q_{1,y}, q_{1,z}, q_{2,x}, ..., q_{N,x}, q_{N,y}, q_{N,z})$ contains the positions of all the particles, $\mathbf{p}$ the momenta. The equivalence of the two different averages is valid if the ergodic hypothesis is respected, i.e., if the particles can access the entire phase space after a certain amount of time [2]. The average of A in the phase space has specific forms depending

on the statistical ensemble we are using to define the system. All the research projects presented in this thesis focused on systems in the canonical (NVT) ensemble. In statistical mechanics, an ensemble is a set of identical copies of a system, characterised by some macroscopic variables. In the canonical ensemble, each copy of the system has constant number of particles N, temperature T and volume V. In this ensemble, the average of a property depending on $\mathbf{q}$ and $\mathbf{p}$ has the following expression:

$$\langle A \rangle = \frac{1}{N! h^{3N}} \frac{\iint A(\mathbf{p},\mathbf{q}) e^{-\beta \mathcal{H}(\mathbf{p},\mathbf{q})} d\mathbf{p} d\mathbf{q}}{Q}, \tag{2.2}$$

$$Q = \frac{1}{N! h^{3N}} \iint e^{-\beta \mathcal{H}(\mathbf{p},\mathbf{q})} d\mathbf{p} d\mathbf{q}. \tag{2.3}$$

Q is the canonical partition function, h is the Planck constant and $\mathcal{H}$ is the Hamiltonian of the system, which is defined as the sum of kinetic ($E_K(\mathbf{p})$) and potential ($U(\mathbf{q})$) energies. We can split the Hamiltonian in two terms and integrate Eq. 2.3 over the momenta, to obtain:

$$Q = \frac{1}{N!} \frac{Z_{NVT}}{\Lambda^{3N}}, \quad \Lambda = \sqrt{\frac{h^2}{2mk_BT}}, \quad Z_{NVT} = \int e^{-\beta U(\mathbf{q})} d\mathbf{q}, \tag{2.4}$$

where Λ is the thermal de Broglie wavelength. If the property A depends only on the positions, i.e., $A = A(\mathbf{q})$, then Eq. 2.1 can be simplified and, using formulas in Eq. 2.4, $\langle A \rangle$ becomes:

$$\langle A \rangle = \frac{\int A(\mathbf{q}) e^{-\beta U(\mathbf{q})} d\mathbf{q}}{Z_{NVT}}, \tag{2.5}$$

where $e^{-\beta U(\mathbf{q})}$ is the Boltzmann probability distribution of our system and Z_{NVT} its normalisation factor.

According to Eq. 2.1, we have two different ways to average properties of the entire system: *(i)* we describe the physical motion of the particles that compose our system, *(ii)* we estimate the probability density distribution of all the possible states of our system. In both cases, we reduce the physical problem to a mathematical one: in case *(i)* we need to solve the equation of motion of all the particles; in case *(ii)* we instead perform a numerical integration of Eq. 2.5, assuming that we know the probability distribution of all the states of our system, which is the Boltzmann distribution. These two different methods have their own advantages and limitations, and either of them is preferable depending on the properties we want to estimate numerically. In the research projects presented in this thesis, we used both types of algorithms to investigate our systems of study, to

recover both statistical and dynamical properties, in equilibrium and out-of-equilibrium conditions. The next sections will give a detailed description of standard Monte Carlo (MC) methods, which fall in case *(ii)*, and novel dynamic Monte Carlo (DMC) algorithms, specific for Brownian particles, which fall in case *(i)*.

2.2 Monte Carlo simulation

With the name "Monte Carlo" (MC), we describe all the procedures that make use of pseudo-random number generators to obtain numerical solutions of a variety of problems. This method was first presented as a procedure for general application in the seminal work of Nicholas Metropolis and Stanislaw Ulam [3]. In this section, we will focus on Monte Carlo integration and simulation. In order to give a general idea of the technique, we consider the following integral:

$$G = \int_{\mathcal{V}} g(x)dx = \int_{\mathcal{V}} \left(\frac{g(x)}{f(x)}\right) f(x)dx. \tag{2.6}$$

G is the value that we want to obtain, $g(x)$ is the function that we want to integrate, $\mathcal{V}$ is the space in which we want to estimate the integral and $f(x)$ in the RHS is a probability distribution. G can be computed by common quadrature methods, evaluating $g(x)$ on a grid of points in $\mathcal{V}$, or with Monte Carlo methods, where we average $(g(x^*)/f(x^*))$, estimated from a random set of x^* values sampled from $f(x)$. In our case, can not use neither of the two methods straight away to solve Eq. 2.5: we do not know Z_{NVT}, and estimating it would require solving a $3N$-dimensional integral, for N the total number of particles. If we consider all the possible configurations of particles in the system, the majority of them will have at least two particles really close to each other, if not overlapping: these configurations have high energy and, according to Boltzmann distribution, low probability to occur, and their contribution to the integral can be discarded. Thus, we can sample the possible states of our system of particles using the Boltzmann distribution, to estimate the integral only in the "most important" areas of the phase space. The first algorithm to implement this kind of method on computer machines was proposed by Nicholas Metropolis *et al.* and it is known as Metropolis algorithm [4]. The Metropolis algorithm generates random states of the system and uses a known probability distribution $\tilde{f}(x)$, which must be proportional to the target one, in our case $f(x)$

of Eq. 2.6, to select the states in the process. The sequence of accepted states generated by the algorithm is a stochastic process known as Markov chain. A Markov chain has the following properties:

- the probability of a certain state of the system depends only on the previous state of the chain, i.e., $P(\mathbf{X}^{(t+1)}|\mathbf{X}^{(t)}, \mathbf{X}^{(t-1)}, \dots, \mathbf{X}^{(0)}) = P(\mathbf{X}^{(t+1)}|\mathbf{X}^{(t)})$,
- all the possible states of the system are contained in a finite space state, $\mathbf{X}^{(t)} \in \mathcal{V} \, \forall \, t$.

Metropolis algorithm is structured as follows:

1. the initial state is a configuration of particles $\mathbf{X}^{(0)} = \mathbf{q}^{(0)}$,
2. starting from the old state $o = 0$, we estimate its probability as $p_0 = \tilde{f}\left(\mathbf{X}^{(o)}\right)$,
3. we generate a new state n, with configuration of particles $\mathbf{X}^{(n)}$, starting from the previous configuration $\mathbf{X}^{(o)}$,
4. we estimate the probability of state n as $p_n = \tilde{f}\left(\mathbf{X}^{(n)}\right)$,
5. we generate a random number $\zeta\{0, 1\}$ from a uniform distribution,
6. we decide whether we accept of reject the new state n:
   (a) $p^{(n)}/p^{(o)} > \zeta\{0, 1\} \implies$ the new state n is accepted,
   (b) $p^{(n)}/p^{(o)} \leq \zeta\{0, 1\} \implies$ the new state n is rejected and the new state remains the old one, $n \to o$,
7. the new state becomes the old one, $o \to n$,
8. the algorithm restarts from 3.

This algorithm, with an appropriate choice of transformation from configuration $\mathbf{X}^{(o)}$ to $\mathbf{X}^{(n)}$, accepts the generated states over the chain with probability $acc = \{1, p^{(n)}/p^{(o)}\}$. In stage 6 of the algorithm, the transition probability from one state to another depends on the ratio $p^{(n)}/p^{(o)}$; since $\tilde{f}(\mathbf{X}) \propto f(\mathbf{X})$, then $\tilde{f}(\mathbf{X}^{(n)})/\tilde{f}(\mathbf{X}^{(o)}) = f(\mathbf{X}^{(n)})/f(\mathbf{X}^{(o)})$. This choice in the definition of transition probability guarantees that the generated states are sampled correctly from the target probability distribution. In *NVT* Monte Carlo simulations, the target equilibrium probability distribution is $f(\mathbf{X}) = \exp(-\beta(U(\mathbf{X})))/Z_{NVT}$; in

the algorithm we instead define the probability of a state with the distribution $\tilde{f}(\mathbf{X}) = \exp(-\beta(U(\mathbf{X})))$. N number of trials are commonly referred to as a "cycle", to compare it with one standard time step in a Molecular Dynamics simulation. The Markov chain generated in this way does not have any correspondence with an arrow of time. Thus, also unphysical moves, like displacements of clusters of particles, or insertion/deletion of particles, can be performed in Monte Carlo simulations and they have been implemented in different versions of the Metropolis algorithm to accelerate its rate of convergence to the stationary distribution [5].

2.2.1 Dynamic Monte Carlo

The Langevin equation describes the motion of a Brownian particle immersed in a fluid:

$$m\dot{\mathbf{v}}(t) = -\nabla U(\mathbf{r}) - \gamma \mathbf{v}(t) + R(t), \tag{2.7}$$

where the the inertia of the particle depends on the frictional forces acting on the moving particle ($-\gamma \mathbf{v}(t)$), the random fluctuating forces caused by the continuous collisions of solvent molecules with the Brownian particle ($R(t)$), and all the other external forces acting on the particle ($-\nabla U(\mathbf{r})$). Due to the nature of the fluctuating term, Langevin equation is a stochastic differential equation [6]. In the overdamped limit, i.e., $\gamma \gg m$, Eq. 2.7 gives the true Brownian dynamics of a particle. Monte Carlo simulations can be exploited to mimic the stochastic nature of the Brownian motion, thanks to the random sampling of particle displacement in a trial move. Several application of Monte Carlo methods can be found in literature to numerically solve the Fokker-Plank equation or to mimic Brownian Dynamics (BD) simulations [7, 8, 9]. The simulations performed in all the research projects of this thesis followed the approach developed by Patti and Cuetos initially for pure systems [10], then expanded for multicomponent mixtures [11], both in equilibrium and out-of-equilibrium conditions [12], in the presence of system inhomogeneities [13] and for active microrheology simulations [14].

We consider a general case, with a multicomponent system of particles of n_c different species, in an NVT ensemble. The total number of particles is

$$N = \sum_{j=1}^{n_c} N_j. \tag{2.8}$$

Following the Metropolis algorithm, we sample a new state of the system from the old one: in this case we randomly select one particle and we randomly move it at each trial. A rigid particle has a certain number of degrees of freedom to describe its position and orientation in space. So, the position and orientation of a particle p of species j are described as a point $\boldsymbol{\xi}_j = (\xi_{1,j}, \dots, \xi_{k,j})$ in a k-dimensional space, where k is the number of degrees of freedom for j-type particles. At every new state, we attempt to move particle p of species j in a point inside a k-dimensional hyperprism Ξ_j, with volume $V_{\Xi,j} = \prod_{i=1}^{k} 2\delta\xi_{i,j}$. The probability of moving one particle p of species j for one trial is:

$$\mathscr{P}^{(p)}_{move,j}(\boldsymbol{\xi}_j) = \begin{cases} \dfrac{1}{N}\dfrac{1}{V_{\Xi,j}}\mathscr{A}_j, & if \quad \boldsymbol{\xi}_j \in \Xi_j, \\ 0 \quad if \quad \boldsymbol{\xi}_j \notin \Xi_j. \end{cases} \tag{2.9}$$

$1/N$ is the probability to choose particle p, $1/V_{\Xi,j}$ the probability to pick the point $\boldsymbol{\xi}_j$ inside Ξ_j (since it is sampled with a uniform distribution), $\mathscr{A}_j$ is the acceptance rate for j-type particles. Since every movement is sampled inside Ξ_j, the probability of moving particle p outside the hyperprism is zero. Being $\mathscr{P}^{(p)}_{move,j}$ independent among attempted moves, the total probability of moving a j-type particle after one cycle of N trials is

$$\mathscr{P}_{move,j}(\boldsymbol{\xi}_j) = N\,\mathscr{P}^{(p)}_{move,j}(\boldsymbol{\xi}_j) = \begin{cases} \dfrac{1}{V_{\Xi,j}}\mathscr{A}_j, & if \quad \boldsymbol{\xi}_j \in \Xi_j, \\ 0 \quad if \quad \boldsymbol{\xi}_j \notin \Xi_j. \end{cases} \tag{2.10}$$

So far, we did not impose any condition on the acceptance rate $\mathscr{A}_j$. The probability of a move to be accepted will depend on the forces acting on the trial particles and the local density distribution: in out-of-equilibrium conditions, the system will evolve from one stationary condition to a different one, and the acceptance rate will consequently change over the Monte Carlo cycles; in the presence of density inhomogeneities, $\mathscr{A}_j$ will be different in different areas of the box; in constant-force active microrheology simulations, where a tracer particle is attracted by an external field along a specific direction, the Metropolis algorithm determines the probability for a trial move of the tracer to be accepted moving towards or in the opposite direction of the external field. We consider the case of a homogeneous system out-of-equilibrium, where each particle of species j has its own average acceptance rate, and we assume $\mathscr{A}_j$ to be uniform over the sampling

hyperprism Ξ_j but dependent on the state of the simulation. We can use the defined probability to calculate the mean square displacement (MSD) of a degree of freedom i, for j-type particles, after one cycle:

$$\left\langle \xi_{i,j}^2 \right\rangle = \int \xi_{i,j}^2 \mathscr{P}_{move,j}(\boldsymbol{\xi}_j) d\xi_{1,j} \dots d\xi_{i,j} \dots d\xi_{k,j} = \frac{\mathscr{A}_{j,l} \left(\delta\xi_{i,j}\right)^2}{3}, \tag{2.11}$$

where now $\mathscr{A}_{j,l}$ is the acceptance rate of particle of species j at cycle l. The relative formula for the MSD after $\mathscr{C}_{MC}$ cycles is

$$\left\langle \xi_{i,j}^2 \right\rangle = \frac{\left(\delta\xi_{i,j}\right)^2}{3} \sum_{l=1}^{\mathscr{C}_{MC}} \mathscr{A}_{j,l}. \tag{2.12}$$

To link the Monte Carlo simulation with a proper timescale, we use the Einstein relation to define the maximum variation $\delta\xi_{i,j}$ and define a MC timescale δt_{MC} for j-type particles:

$$\left(\delta\xi_{i,j}\right)^2 = 2D_{i,j}\delta t_{MC,j}, \tag{2.13}$$

where $D_{i,j}$ is the diffusion coefficient at infinite dilution of the degree of freedom i of particle species j. In a Brownian Dynamics (BD) simulation, the MSD is directly dependent on time through the Einstein relation:

$$\left\langle \xi_{i,j}^2 \right\rangle = 2D_{i,j}t_{BD}, \tag{2.14}$$

where t_{BD} is the time unit of the BD simulation. Equating Eq. 2.14 and 2.12, and using the definition in Eq. 2.13, we can recover the correct timescale in a DMC simulation:

$$t_{BD} = \frac{\delta t_{MC,j}}{3} \sum_{l=1}^{\mathscr{C}_{MC}} \mathscr{A}_{j,l}. \tag{2.15}$$

Eq. 2.15 shows that, despite each particle has a distinct MC timescale, they all must be linked with the correct arrow of time of a BD simulation. Indeed, the equivalence of Eq. 2.15 for all the particles of species j poses a fundamental relation between MC timescales of different particles:

$$\mathscr{A}_{1,l}\delta t_{MC,1} = \mathscr{A}_{2,l}\delta t_{MC,2} = \dots = \mathscr{A}_{n_c,l}\delta t_{MC,n_c}. \tag{2.16}$$

To respect all the constraints in Eq. 2.16, the MC timescale of one species of particle must be kept fixed, while all the other must be adjusted during the simulation, for each MC cycle. When the system has only one species of particles, no constraint in the definition of the MC timescale is needed, and it is fixed over the entire duration of the simulation. The results on kinetics of formation of chains presented in Chapter 5 and all the results reported in Chapter 6 have been obtained by performing out-of-equilibrium DMC simulations of one-component systems. If the system is at equilibrium, the acceptance rate of each species will fluctuate around an average value, and Eq. 2.15 can be simplified:

$$t_{BD} = \frac{\delta t_{MC,j}}{3} \mathscr{C}_{MC} \mathscr{A}_j, \tag{2.17}$$

where $\mathscr{A}_j$ is the total average acceptance rate of particle species j. All the results in Chapter 4 and the passive microrheology results in Chapter 5 have been obtained by performing equilibrium bi-component DMC simulations.

DMC simulations are useful to explore a broad time scale with low computational cost, since it proved to efficiently recover BD results even with larger MC timescales. Moreover, since BD simulations perform numerical integration of overdamped Langevin equation of motion, they require the definition of forces and, as a consequence, differentiable interaction potentials between particles. DMC methods overcome this issue, since Metropolis-based MC simulations do not require the momenta of the particles, making this method a perfect candidate to explore the dynamics of Brownian rigid bodies with any shape. It is important to notice that DMC methods described so far neglect the effect of hydrodynamic interactions (HI) between different particles: while there are algorithms capable to take into account also HI [15, 16, 17], they mainly rely on spherical particles, and rigid bodies defined as clusters of spheres, or they necessarily simulate also the flow of the medium.

2.3 Microrheology

In this section we will present in more detail how active and passive rheology simulations can be performed in the DMC framework. In the case of constant-force active microrheology simulations, an external force is imposed only on one spherical tracer

particle:

$$\mathbf{F}_{ext} = F_{ext}\hat{\mathbf{x}} = \mathrm{Pe}\frac{2k_BT}{\sigma}\hat{\mathbf{x}}, \tag{2.18}$$

where σ is the diameter of the tracer, $\hat{\mathbf{x}}$ is the orientation of the external field and Pe is the Péclet number, i.e., the ratio between the external force and the thermal forces. In the presence of an external force, the acceptance rate of the tracer is space dependent. This requires a more detailed analysis of the behaviour of the Metropolis algorithm in this specific conditions. Considering that the equilibrium acceptance rate of the tracer due to the interaction with the surrounding particles is $\mathscr{A}_0$, the probability of moving the tracer particle along $\hat{\mathbf{x}}$ depends also on the potential energy $\beta U_{ext} = -\beta F_{ext}x$ as follows:

$$\mathscr{P}_{move,t}(x) = \begin{cases} \dfrac{1}{2\delta x}\mathscr{A}_0 \quad if \quad 0 < x \leq \delta x, \\ \dfrac{1}{2\delta x}\mathscr{A}_0 \exp\left(\beta F_{ext}x\right) \quad if \quad -\delta x \leq x \leq 0, \\ 0 \quad if \quad x \notin [-\delta x, \delta x], \end{cases} \tag{2.19}$$

where the trial move along the direction of the force is in the range $[-\delta x, \delta x]$. We can use the definition of $\mathscr{P}_{move,t}(x)$ to obtain the average displacement of the tracer along $\hat{\mathbf{x}}$ and the acceptance rate of the tracer:

$$\langle x_t \rangle = \int_{-\infty}^{\infty} x\mathscr{P}_{move,t}dx \simeq \frac{\beta F_{ext}\mathscr{A}_0\left(\delta x\right)^2}{6}\left(1 - \frac{3}{8}\beta F_{ext}\delta x\right) + \mathcal{O}\left(\left(\beta F_{ext}\delta x\right)^2\right), \tag{2.20}$$

$$\mathscr{A}_t = \int_{-\infty}^{\infty} \mathscr{P}_{move,t}dx \simeq \mathscr{A}_0\left(1 - \frac{1}{4}\beta F_{ext}\delta x\right) + \mathcal{O}\left(\left(\beta F_{ext}\delta x\right)^2\right), \tag{2.21}$$

where we expanded $\exp(\beta F_{ext}x)$ up to the first term, and we neglected $\mathcal{O}\left(\left(\beta F_{ext}\delta x\right)^2\right)$ terms, which is true for $\beta F_{ext}\delta x \ll 1$. In a BD simulation with an external force, the average displacement of the tracer along $\hat{\mathbf{x}}$ reads:

$$\langle x_t \rangle = D_t\beta F_{ext}t_{BD}. \tag{2.22}$$

We can substitute Eq. 2.21 into Eq. 2.20, and then compare the resulting equation with Eq. 2.22, for $\mathscr{C}_{MC}$ cycles, to recover the BD time for the tracer in an active microrheology DMC simulation:

$$t_{BD} = \frac{1}{3}\left(\frac{3}{2}\mathscr{A}_t - \frac{1}{2}\mathscr{A}_0\right)\delta t_{MC,t}. \tag{2.23}$$

Since the tracer will likely move towards the direction of the field rather than perpendicular to it, the maximum displacement of the tracer is different in different directions:

$$\delta r_{\parallel,t}^{max} = \sqrt{2D_t\delta t_{MC,t} + \left(D_t\beta F_{ext}\delta t_{MC,t}\right)^2}, \tag{2.24}$$

$$\delta r_{\perp,t}^{max} = \sqrt{2D_t\delta t_{MC,t}}. \tag{2.25}$$

To ensure that the approximations applied in Eq. 2.20 and 2.21 are correct, we must respect the inequality $\beta F_{ext}\delta x \ll 1$. In the same way as generic multicomponent DMC simulations, also in the case of active microrheology the constrains in Eq. 2.16 must be respected, between the tracer particle and the bath (b) particles:

$$\left(\frac{3}{2}\mathscr{A}_t - \frac{1}{2}\mathscr{A}_0\right)\delta t_{MC,t} = \mathscr{A}_b\delta t_{MC,b}. \tag{2.26}$$

For the case of passive microrheology simulations, Pe $= 0$ and we recover the standard equilibrium multicomponent DMC simulations presented above. Nevertheless, in the case of a single spherical tracer moving in a bath of colloidal particles, we can recover the linear viscoelastic response of the suspension following the trajectory of the tracer. In the seminal works of Mason and Weitz [18, 19, 20], the authors showed how the motion of the tracer particle in suspension can be described by a generalised Langevin equation, where the viscous damping of the fluid is time-dependent. By performing a Fourier transform of the Langevin equation, and assuming the validity of a frequency-dependent Stokes-Einstein relation for a viscoelastic fluid at all frequencies, the complex shear modulus can be recovered from the MSD of the tracer:

$$G^*(\omega) = \frac{k_BT}{\pi a i\omega\mathcal{F}_u\left\{\langle\Delta r^2(t)\rangle\right\}}, \tag{2.27}$$

where:

$$|G^*(\omega)| = \frac{k_BT}{\pi a\langle\Delta r^2(1/\omega)\rangle\,\Gamma\left[1+\alpha(\omega)\right]} \tag{2.28}$$

$$G'(\omega) = |G^*(\omega)|\cos\left(\pi\alpha(\omega)/2\right) \tag{2.29}$$

$$G''(\omega) = |G^*(\omega)|\sin\left(\pi\alpha(\omega)/2\right) \tag{2.30}$$

$$\alpha(\omega) \equiv \left.\frac{d\ln\langle\Delta r^2(t)\rangle}{d\ln t}\right|_{t=1/\omega} \tag{2.31}$$

Active and passive microrheology simulations can be implemented in DMC simulations and they proved to be a powerful tool to have an insight on the local viscoelastic properties of colloidal suspensions. In this thesis, results in Chapter 7 have been obtained through active microrheology simulations, while equilibrium passive microrheology simulations have been carried out to explore the linear viscoelastic response of the electrorheological fluid of nanocubes, whose results can be found in Chapter 5.

2.4 Collision detection

One of the main problems of particle simulations is the definition of an interaction potential between two particles. Generally, we can distinguish hard-core and soft-core potentials. The former defines the interaction between two rigid impenetrable objects, with the generic formula:

$$\phi(d_{min}) = \begin{cases} 0, \, d_{min} > 0 \\ \infty, \, d_{min} \leq 0, \end{cases} \tag{2.32}$$

where d_{min} is the minimum distance between the surfaces of the two particles. The latter describes soft particles, that can attract and/or repel each other, depending on how the potential is defined. A generic formula for two convex objects is $\phi(\mathbf{r}_i, \mathbf{r}_j, \boldsymbol{\theta}_i, \boldsymbol{\theta}_j)$, where $\mathbf{r} = (r_x, r_y, r_z)$ contains the position of the centre of mass and $\boldsymbol{\theta} = (\theta_1, \theta_2, \theta_3)$ the orientation of the particle in space. If we consider the complexity of the problem, we can realize why the first simulations ever performed to mimic real systems involved the use of disks and spheres. As a matter of fact, two spheres with diameters σ_1, σ_2 and positions of their centres of mass $\mathbf{r}_1, \mathbf{r}_2$ do overlap, or at least be in contact, if:

$$\|\mathbf{r}_2 - \mathbf{r}_1\| \leq \frac{\sigma_1 + \sigma_2}{2}, \tag{2.33}$$

which is a set of simple operations to compute in a processing unit. However, when particles have different shapes, the problem of collision detection (and, possibly, minimum distance computation) gets more complicated. Even though algorithms for the collision detection of general convex objects can be found and are commonly used in computer graphics [21], they are computationally expensive and they can compromise the efficiency of particle simulations. To overcome this problem, there are, generally,

two possible solutions:

1. describe the complex object as a composition of spheres or other shapes whose properties are easier to compute [22, 23],

2. find the easiest and most efficient way to define the overlap between the two particles with their exact shapes.

Case 1 can be applied depending on the set up of the simulations and on the relevance that the roughness of the surface of the "composed" particle has on the results of the simulations; the smaller are the unit particles used for the definition, the bigger the total number of particles is, with consequences on the computational cost of the simulation. Case 2 is more appealing, but optimized algorithms for collision detection or computation of the minimum distance are not available for all the particle shapes that we may want to simulate.

In all the research projects reported in this thesis, we simulated systems of hard cuboidal particles and hard spherical particles, with cases of external forces dependent of the position of particle centres of mass or orientation, with no inter-particle potential dependent on the minimum distance between the surfaces of two particles. The algorithm we used to detect collision between to randomly oriented cuboids is the one developed by Gottschalk *et al.* for Oriented Bounded Boxes [24]. For the collision detection between one cuboid and one sphere, we developed our Oriented Cuboid Sphere Intersection (OCSI) algorithm, whose description and performance is published as an article in *Algorithms* and it is presented in Chapter 3.

Bibliography

[1] Frenkel, D. Soft condensed matter. *Physica A: Statistical Mechanics and its Applications* **313**, 1–31 (2002).

[2] Hansen, J.-P. & McDonald, I. R. Chapter 2 - Statistical Mechanics. In Hansen, J.-P. & McDonald, I. R. (eds.) *Theory of Simple Liquids*, 13–59 (Academic Press, 2013), 4th edn.

[3] Metropolis, N. & Ulam, S. The Monte Carlo Method. *Journal of the American Statistical Association* **44**, 335–341 (1949).

[4] Metropolis, N., Rosenbluth, A. W., Rosenbluth, M. N., Teller, A. H. & Teller, E. Equation of state calculations by fast computing machines. *J. Chem. Phys.* **21**, 1087 (1953).

[5] Allen, M. & Tildesley, D. Chapter 4 - Monte Carlo Methods. In Allen, M. & Tildesley, D. (eds.) *Computer Simulation of Liquids*, 110–139 (Clarendon Press, 1989).

[6] Hansen, J.-P. & McDonald, I. R. Chapter 7 - Time-dependent Correlation and Response Functions. In Hansen, J.-P. & McDonald, I. R. (eds.) *Theory of Simple Liquids*, 265–310 (Academic Press, 2013), 4th edn.

[7] Sanz, E. & Marenduzzo, D. Dynamic Monte Carlo versus Brownian dynamics: A comparison for self-diffusion and crystallization in colloidal fluids. *J. Chem. Phys.* **132**, 194102 (2010).

[8] Heyes, D. M. & Branka, A. C. Monte Carlo as Brownian dynamics. *Molecular Physics* **94**, 447–454 (1998).

[9] Kikuchi, K., Yoshida, M., Maekawa, T. & Watanabe, H. Metropolis Monte Carlo method as a numerical technique to solve the Fokker—Planck equation. *Chemical Physics Letters* **185**, 335–338 (1991).

[10] Patti, A. & Cuetos, A. Brownian dynamics and dynamic Monte Carlo simulations of isotropic and liquid crystal phases of anisotropic colloidal particles: A comparative study. *Phys. Rev. E* **86**, 011403 (2012).

[11] Cuetos, A. & Patti, A. Equivalence of Brownian dynamics and dynamic Monte Carlo simulations in multicomponent colloidal suspensions. *Phys. Rev. E* **92**, 022302 (2015).

[12] Corbett, D., Cuetos, A., Dennison, M. & Patti, A. Dynamic Monte Carlo algorithm for out-of-equilibrium processes in colloidal dispersions. *Phys. Chem. Chem. Phys.* **20**, 15118–15127 (2018).

[13] García Daza, F. A., Cuetos, A. & Patti, A. Dynamic monte carlo simulations of inhomogeneous colloidal suspensions. *Phys. Rev. E* **102**, 013302 (2020).

[14] García Daza, F. A., Puertas, A. M., Cuetos, A. & Patti, A. Microrheology of colloidal suspensions via dynamic Monte Carlo simulations. *J. Colloid Interface Sci.* **605**, 182–192 (2022).

[15] Ermak, D. L. & McCammon, J. A. Brownian dynamics with hydrodynamic interactions. *J. Chem. Phys.* **69**, 1352–1360 (1978).

[16] Brady, J. F. & Bossis, G. Stokesian dynamics. *Annual Review of Fluid Mechanics* **20**, 111–157 (1988).

[17] Delong, S., Balboa Usabiaga, F. & Donev, A. Brownian dynamics of confined rigid bodies. *J. Chem. Phys.* **143**, 144107 (2015).

[18] Mason, T. G. & Weitz, D. A. Optical Measurements of Frequency-Dependent Linear Viscoelastic Moduli of Complex Fluids. *Phys. Rev. Lett.* **74**, 1250–1253 (1995).

[19] Mason, T. G., Ganesan, K., van Zanten, J. H., Wirtz, D. & Kuo, S. C. Particle Tracking Microrheology of Complex Fluids. *Phys. Rev. Lett.* **79**, 3282–3285 (1997).

[20] Mason, T. G. Estimating the viscoelastic moduli of complex fluids using the generalized Stokes–Einstein equation. *Rheologica Acta* **39**, 371–378 (2000).

[21] Gilbert, E. G., Johnson, D. W. & Keerthi, S. S. A fast procedure for computing the distance between complex objects in three-dimensional space. *IEEE Journal on Robotics and Automation* **4**, 193–203 (1988).

[22] John, B. S. & Escobedo, F. A. Phase behavior of colloidal hard tetragonal parallelepipeds (cuboids): A Monte Carlo simulation study. *J. Phys. Chem. B* **109**, 23008–23015 (2005).

[23] Rosenberg, M., Dekker, F., Donaldson, J. G., Philipse, A. P. & Kantorovich, S. S. Self-assembly of charged colloidal cubes. *Soft Matter* **16**, 4451–4461 (2020).

[24] Gottschalk, S., Lin, M. C. & Manocha, D. OBBTree: A Hierarchical Structure for Rapid Interference Detection. In *Proceedings of the 23rd Annual Conference on Computer Graphics and Interactive Techniques*, SIGGRAPH '96, 171–180 (Association for Computing Machinery, New York, NY, USA, 1996).

Chapter 3

Fast Overlap Detection Between Hard-Core Colloidal Cuboids and Spheres. The OCSI Algorithm

The content of this Chapter has been published as a full article in the journal *Algorithms*. My contributions are listed as follows: Luca Tonti developed the methodology and the software; Luca Tonti and Alessandro Patti performed the validation; Luca Tonti performed the formal analysis; Luca Tonti and Alessandro Patti performed the investigation; Luca Tonti was responsible for data curation; Luca Tonti wrote the original draft; Luca Tonti produced the data visualisation.

Abstract

Collision between rigid three-dimensional objects is a very common modelling problem in a wide spectrum of scientific disciplines, including Computer Science and Physics. It spans from realistic animation of polyhedral shapes for computer vision to the description of thermodynamic and dynamic properties in simple and complex fluids. For instance, colloidal particles of especially exotic shapes are commonly modelled as hard-core objects, whose collision test is key to correctly determine their phase and aggregation behaviour. In this work, we propose the Oriented Cuboid Sphere Intersection (OCSI) algorithm to detect collisions between prolate or oblate cuboids and spheres. We investigate OCSI's performance by bench-marking it against a number of algorithms commonly employed in computer graphics and colloidal science: Quick Rejection First (QRF), Quick Rejection Intertwined (QRI) and a vectorized version of the OBB-sphere collision detection algorithm that explicitly uses SIMD Streaming Extensions (SSE) intrinsics, here referred to as SSE-intr. We observed that QRI and QRF significantly depend on the specific cuboid anisotropy and sphere radius, while

SSE-intr and OCSI maintain their speed independently of the objects' geometry. While OCSI and SSE-intr, both based on SIMD parallelization, show excellent and very similar performance, the former provides a more accessible coding and user-friendly implementation as it exploits OpenMP directives for automatic vectorization.

3.1 Introduction

Employing computer programs and algorithms to generate 2D or 3D images is referred to as rendering. Rendering is a topic of striking relevance in computer graphics with practical impact on many heterogeneous disciplines, spanning engineering, simulators, video games and movie special effects. Collision detection and collision determination are key elements of rendering as they determine the distance between two objects and their possible intersection [1]. Due to their widespread use in video representation of time-evolving systems, with tens of frames displayed per second, algorithms for rendering are expected to be very efficient [2, 3]. Generally, to assess whether two complex objects collide, the distance between their respective bounding volumes is evaluated first. Common bounding volumes are cuboidal boxes, whose axes might or might not be aligned, or spheres. Due to their simple geometry, the collision between cuboids and/or spheres is computationally easier [4, 5, 6, 7], thus enhancing the speed and efficiency of the overall rendering process [2]. Collision detection algorithms are of utmost relevance in many heterogeneous applications spanning computer graphics for shape modelling and video games [8, 9, 10, 11, 12], robotics to prevent potential collisions in man–robot interactions [13, 14, 15, 16, 17], risk assessment associated to vessel collision [18] or machining of sculptured surfaces [19], and simulations of molecular or particle systems to estimate their thermodynamic properties [20, 21].

Collision algorithms have also been key to address the thermodynamics of liquid and solid phases and their phase transition by early molecular simulation studies that employed the hard-sphere model [22, 23, 24]. More recently, and following the seminal theory by Onsager on the isotropic-to-nematic transition of hard rods [25], they were fundamental to confirm the crucial role of excluded volume effects in the formation of colloidal liquid crystal phases of anisotropic particles [20]. Realising the practical impact of the particle shape on the design of nanomaterials triggered the blooming of

biosynthetic [26], chemical [27] and physical [28] experimental routes to manufacture precise building blocks with *ad hoc* properties, including lock-and-key particles [29], fused spheres [30], superballs [31] and cuboids [32, 33, 34, 35]. The appearance of these exotic shapes unveiled a realm of novel opportunities in nanomaterials science by offering an increasingly varied selection of morphologies for state-of-the-art applications spanning medicine (controlled drug delivery), smart materials (self-healing coatings) and photonics (light detection), among others. Often anticipating experimental evidence, computer simulations have significantly contributed to our comprehension of the effect of particle shape and interaction at the nanoscale on the material properties at the macroscale [36, 37, 38, 39]. Understanding the fundamentals of such a complex correlation, which develops over orders of magnitude in length and time scales, dramatically depends on the existence of reliable force fields mimicking the interactions between particles. This is not always the case for most exotic particle shapes, whose force field is assumed to be described by mere excluded volume effects and thus only incorporates a hard-core interaction potential. Consequently, efficient and robust algorithms able to detect collisions and intersections between objects become essential to extract structural, thermodynamic and dynamic properties of such systems from a molecular simulation. In colloid science, cuboids are especially intriguing building blocks that can form a rich variety of liquid crystal phases [40, 41, 42, 43, 44]. Incorporating guest spherical particles in these phases is relevant to understand phenomena of diffusion in crowded environments that display a significant degree of ordering.

In the light of these considerations, which highlight the harmonious inter-disciplinary convergence of computer graphics and colloid science, here we report on the specific case of cuboid-sphere collision detection. In particular, we propose our own Oriented Cuboid Sphere Intersection (OCSI) algorithm to detect collisions in monodispersed systems of cuboids and spheres oriented in a 3D space. OCSI is found to be especially efficient when compared to the Quick Rejection First (QRF) and the Quick Rejection Intertwined (QRI) algorithms, and more user-friendly and easier to implement than the vectorized version of the algorithm that employs SSE intrinsic functions [7]. For simplicity, we refer to the vectorized version of the collision detection algorithm developed by Larsson *et. al.* with the abbreviation "SSE-intr", since it uses Intel ® intrinsic functions specific for SSE instruction set. In particular, QRI and QRF make use of a quick

rejection test that discards overlaps if the minimum distance, d_{min}, between the surface of a cuboid and the center of a sphere is larger than the sphere radius. Because this test depends on the cuboid size and shape, the efficiency of both QRI and QRF is expected to be determined, to some extent, by the specific sphere and cuboid geometry. By contrast, SSE-intr, which runs in parallel and it is therefore significantly faster than QRI and QRF, does not need quick rejection tests and makes use of vectorization to estimate d_{min}. Our algorithm, available in C and FORTRAN 90, incorporates a few key elements (e.g., the absolute value to estimate the minimum distance and OpenMP directives to parallelize the code with no use of SIMD intrinsics) that make it faster than QRI and QRF and more versatile than SEE-intr. This paper is organised as follows. In Section 2, we detail the theoretical framework of the cuboid-sphere intersection problem and the state-of-the-art in software implementation. In Section 3, we describe the code that we have specifically developed to test each of the above-mentioned algorithms' efficiency for cuboids of different shape and spheres of different size. The comparison between the algorithms is then discussed in Section 4, while, in Section 5, we draw our conclusions.

3.2 Algorithms

In geometry, a sphere S is identified by its radius, R, and the position of its centre, $\mathbf{r}_\mathrm{S}$,with respect to a reference point. Similarly, a cuboid C can be defined by the extension of its thickness, $2c_T$, length, $2c_L$, and width, $2c_W$, the position of its centre of mass, $\mathbf{r}_\mathrm{C}$, and the unit vectors $\hat{\mathbf{e}}_\mathrm{T}$, $\hat{\mathbf{e}}_\mathrm{L}$ and $\hat{\mathbf{e}}_\mathrm{W}$ that indicate the orientation of its three orthogonal axes. As a result, all the points within the volume occupied by the cuboid can be indicated by a vector $\mathbf{C}$ that reads

$$\mathbf{C} = \mathbf{r}_\mathrm{C} + \sum_{i=T,L,W} \alpha_i c_i \hat{\mathbf{e}}_\mathbf{i}, \tag{3.1}$$

where T, L and W indicate, respectively, the cuboid thickness, length and width, whereas $\alpha = \left[-1, 1\right]$ is a scalar interval. With these essential definitions, the minimum distance, d_{min}, between the surface of a randomly oriented cuboid and the center of a sphere can be calculated as follows:

$$d_{min} = \sqrt{\sum_{i=T,L,W} \Theta\Big(\left|\mathbf{r}_{SC} \cdot \hat{\mathbf{e}}_i\right| - c_i\Big)\Big\{\left|\mathbf{r}_{SC} \cdot \hat{\mathbf{e}}_i\right| - c_i\Big\}^2}, \tag{3.2}$$

where $\mathbf{r}_{SC} = \mathbf{r}_S - \mathbf{r}_C$ and Θ is the Heaviside step function:

$$\Theta(x) = \begin{cases} 0 & x \leq 0 \\ 1 & x > 0 \end{cases} \tag{3.3}$$

The interested reader is referred to Appendix 3.A1 for a formal derivation of Eq. 3.2. To the best of our knowledge, Arvo was the first to propose an algorithm detecting the intersection between a sphere and an axis-aligned cuboid, that is a cuboid whose orientation matches that of the reference axes [5]. For this specific case, we assume that the cuboid thickness is aligned with the x axis, i.e., $\hat{\mathbf{e}}_T = \hat{\mathbf{x}}$, its length with the y axis, i.e., $\hat{\mathbf{e}}_L = \hat{\mathbf{y}}$, and its width with the z axis, i.e., $\hat{\mathbf{e}}_W = \hat{\mathbf{z}}$. Following this assumption, Eq. 3.1 can be rewritten as

$$\begin{aligned} \mathbf{C} &= \mathbf{r}_C + \alpha_T c_T \hat{\mathbf{x}} + \alpha_L c_L \hat{\mathbf{y}} + \alpha_W c_W \hat{\mathbf{z}} = \\ &= \mathbf{r}_C + \left[-c_T, c_T\right]\hat{\mathbf{x}} + \left[-c_L, c_L\right]\hat{\mathbf{y}} + \left[-c_W, c_W\right]\hat{\mathbf{z}} = \\ &= \left[r_{C,x} - c_T, r_{C,x} + c_T\right]\hat{\mathbf{x}} + \left[r_{C,y} - c_L, r_{C,y} + c_L\right]\hat{\mathbf{y}} + \\ &\quad + \left[r_{C,z} - c_W, r_{C,z} + c_W\right]\hat{\mathbf{z}} = \\ &= \sum_{i=x,y,z} B_i \hat{\mathbf{i}} \end{aligned} \tag{3.4}$$

where $\hat{\mathbf{i}} = \hat{\mathbf{x}}, \hat{\mathbf{y}}, \hat{\mathbf{z}}$ are the reference axes for T, L and W, respectively, and $B_x = \left[r_{C,x} - c_T, r_{C,x} + c_T\right]$, $B_y = \left[r_{C,y} - c_L, r_{C,y} + c_L\right]$ and $B_z = \left[r_{C,z} - c_W, r_{C,z} + c_W\right]$. Therefore, for an axis-aligned cuboid, d_{min} can be calculated as

$$d_{min} = \sqrt{\sum_{i=x,y,z} \Big\{ \min\left(r_{S,i} - B_i\right) \Big\}^2}. \tag{3.5}$$

By using the infimum and supremum of B_i, the terms in the above sum can be easily calculated:

1. if $r_{S,i} < B_{i,inf}$, then $\min\left(r_{S,i} - B_i\right) = B_{i,inf} - r_{S,i}$,
2. if $r_{S,i} > B_{i,sup}$, then $\min\left(r_{S,i} - B_i\right) = r_{S,i} - B_{i,sup}$,
3. if $r_{S,i} \in B_i$, then $\min\left(r_{S,i} - B_i\right) = 0$.

Consequently, the algorithm proposed by Arvo only requires the extreme values of B_x, B_y, B_z along with the sphere radius and position and detects cuboid-sphere collisions if $d_{min} \leq R$. An illustrative example of a pseudocode describing its main steps is reported in Algorithm 1.

Algorithm 1 - Arvo

```
1:  function ARVO(r_S, R, B_{i,inf}, B_{i,sup})
2:      d ← 0                                        ▷ initialising minimum distance
3:      for i ∈ {x, y, z} do
4:          if (r_{S,i} < B_{i,inf}) then
5:              d ← d + (B_{i,inf} − r_{S,i})^2
6:          else if (r_{S,i} > B_{i,sup}) then
7:              d ← d + (r_{S,i} − B_{i,sup})^2
8:          end if
9:      end for
10:     if (d ≤ R^2) return true                     ▷ checking overlap
11:     return false
12: end function
```

The alignment of the cuboid unit vectors with the reference axes is a particular case of a more general scenario with the cuboid randomly oriented. Eventually, Arvo's algorithm can also be applied to randomly oriented cuboids by performing a transformation of the vectors involved in the calculation of d_{min} in the reference frame of $\mathcal{C}$. Rokne and Ratschek proposed to estimate d_{min} by employing interval analysis and reported a test to determine whether a point $P \in \mathcal{C}$ is within a sphere delimited by four peripheral points [6]. The algorithms proposed by Larsson and co-workers employ quick rejection overlap tests to enhance the efficiency of collision detection between a sphere and either an aligned or a randomly oriented cuboid [7]. The pseudocode of these algorithms are reported in Algorithm 2 and Algorithm 3, respectively. Both QRI and QRF are based on the implementation of a quick rejection test that immediately excludes an overlap if at least one of the summands in Eq. 3.2 or Eq. 3.5 is larger than R^2. For the general case of a randomly oriented cuboid, this condition reads

$$\left\{ \left| \mathbf{r}_{SC} \cdot \hat{\mathbf{e}}_i \right| - c_i \right\}^2 > R^2 \;\Leftrightarrow \mathbf{r}_{SC} \cdot \hat{\mathbf{e}}_i < -c_i - R \;\cup\; \mathbf{r}_{SC} \cdot \hat{\mathbf{e}}_i > c_i + R \qquad \forall\, i = T, L, W \tag{3.6}$$

A geometrical representation of this condition is provided in Fig. 3.1, where a sphere $\mathcal{S}$ of radius R and centered at $\mathbf{r}_S$ is at the distance $\mathbf{r}_{SC} \cdot \hat{\mathbf{e}}_L$ from the center of mass of a

cuboid $\mathcal{C}$ that is centered at $\mathbf{r}_\mathrm{C}$. For this specific arrangement, the left-hand side of Eq. 3.6 measures the distance of $\mathcal{S}$ from the face of $\mathcal{C}$ delimited by T and W and schematically identified by the vertical solid line of Fig. 3.1.

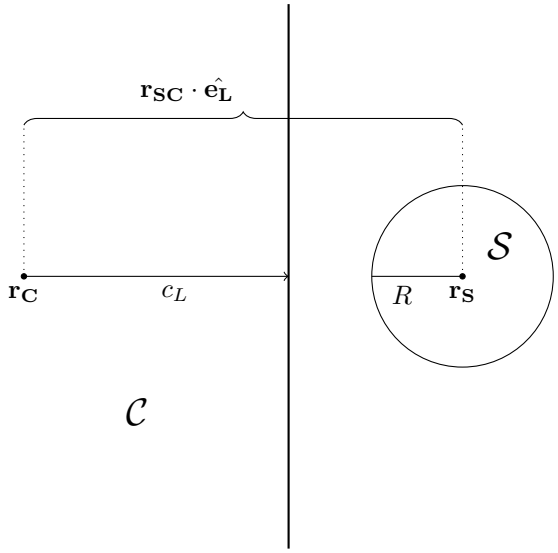

Figure 3.1: Schematic representation of a sphere $\mathcal{S}$ and a cuboid $\mathcal{C}$ at relative distance $\mathbf{r}_\mathrm{SC} \cdot \hat{\mathbf{e}}_\mathrm{L}$. Sphere and cuboid are centered, respectively, at $\mathbf{r}_\mathrm{S}$ and $\mathbf{r}_\mathrm{C}$, and c_L is half of the cuboid length. If $\mathbf{r}_\mathrm{SC} \cdot \hat{\mathbf{e}}_L > c_L + R$, then $\mathcal{S}$ and $\mathcal{C}$ do not overlap.

QRI applies this rejection criterion within the loop that evaluates the minimum distance, precisely at lines 6 and 9 of Algorithm 2. By contrast, QRF performs the three quick rejection tests, one for each summand of Eq. 3.2, before the computation of the minimum distance, between lines 3 and 6 of Algorithm 3. In this case, the scalar products $\mathbf{r}_\mathrm{SC} \cdot \hat{\mathbf{e}}_\mathbf{i}$ are stored in line 4 and eventually employed to compute $d = d^2_{min}$ in the following loop. The different location of the quick rejection tests in QRI and QRF is expected to determine a difference in the efficiency of the two algorithms, which is analysed in detail in Section 4. Additionally, QRI and QRF quick rejection tests depend on both c_i and R, so these algorithms' efficiency are expected to be influenced also by sphere and cuboid geometry. Finally, keeping in mind the potential application in computational colloid science, where crowded systems are usually simulated, the efficiency of QRI and QRF is also influenced by the system packing, which determines the probability for an attempted move to produce an overlap.

Larsson *et. al.* also proposed a parallel version of Algorithm 1, generalised for randomly oriented cuboids and using SSE intrinsic functions (SSE-intr) [7]. SSE is an instruction set available in x86 architectures; it uses 128-bit registers to process simple in-

Algorithm 2 - QRI

```
1:  function QRI(r_SC, R, ê_T, ê_L, ê_W, c_T, c_L, c_W)
2:      d ← 0                                          ▷ initialising minimum distance
3:      for i ∈ {T, L, W} do
4:          a ← r_SC · ê_i
5:          if ((l ← a + c_i) < 0) then
6:              if (l < −R) return false               ▷ quick rejection test
7:              d ← d + l²
8:          else if ((l ← a − c_i) > 0) then
9:              if (l > R) return false                ▷ quick rejection test
10:             d ← d + l²
11:         end if
12:     end for
13:     if (d ≤ R²) return true                        ▷ checking overlap
14:     return false
15: end function
```

Algorithm 3 - QRF

```
1:  function QRF(r_SC, R, ê_T, ê_L, ê_W, c_T, c_L, c_W)
2:      d ← 0                                          ▷ initialising minimum distance
3:      for i ∈ {T, L, W} do
4:          a_i ← r_SC · ê_i
5:          if (a_i < −c_i − R or
              a_i > c_i + R) return false              ▷ quick rejection test
6:      end for
7:      for i ∈ {T, L, W} do
8:          if (a_i < −c_i) then
9:              l ← a_i + c_i
10:             d ← d + l²
11:         else if (a_i > c_i) then
12:             l ← a_i − c_i
13:             d ← d + l²
14:         end if
15:     end for
16:     if (d ≤ R²) return true                        ▷ checking overlap
17:     return false
18: end function
```

structions on multiple data in parallel [45]. By substituting the "if" statements in lines 8 and 11 of Algorithm 3 to compute the minimum distance, with the "max" and "min" functions available in SSE instruction set, the computation of the minimum distance can be vectorized. This algorithm, running in parallel and thus significantly faster than QRI and QRF, does not need quick rejection tests. A pseudocode for this algorithm, here named after the SSE instruction set, is presented in Algorithm 4 for the general case of

randomly oriented cuboids.

Algorithm 4 - SSE-intr

1: **function** SSE($\mathbf{r}_{SC}, R, \hat{\mathbf{e}}_T, \hat{\mathbf{e}}_L, \hat{\mathbf{e}}_W, c_T, c_L, c_W$)
2: **for** $i \in \{T, L, W\}$ **do**
3: $a_i \leftarrow \mathbf{r}_{SC} \cdot \hat{\mathbf{e}}_i$ ▷ vectorizing the dot product
4: **end for**
5: **for** $i \in \{T, L, W\}$ **do** ▷ vectorizing the cycle
6: $l_i \leftarrow \min(a_i + c_i, 0) + \max(a_i - c_i, 0)$
7: $l_i \leftarrow l_i^2$
8: **end for**
9: **if** $(l_T + l_L + l_W \leq R^2)$ **return** *true* ▷ checking overlap
10: **return** *false*
11: **end function**

Finally, we present our own algorithm, which incorporates a number of elements providing additional efficiency when compared to Algorithms 1, 2 and 3, and versatility when compared to Algorithm 4. A new element that significantly simplifies the algorithm is the use of the absolute value to estimate the minimum distance. In addition, we employed OpenMP directives for an SIMD parallelization of the two loops, one over the computation of the dot products of the distance of the centres of mass of the two particles with the orientation of the cuboid, and the other over the computation of the minimum distance, without using SSE intrinsic instructions. OpenMP is an application programming interface specification composed of compiler directives, library routines and environment variables for parallel programming in FORTRAN and C/C++. From version 4.0 it provides mechanisms to assist SIMD parallelization of loops [46]. The advantage of avoiding explicit SIMD vectorization is the possibility to vectorize the algorithm using different instruction set architectures, such as the more modern Advanced Vector Extensions (AVX) instruction set [47], by simply changing compiler settings during compilation. Moreover, in this way vectorization of the algorithm can be assisted for different programming languages, e.g., FORTRAN, since SIMD intrinsic functions are available only in C and C++. Given the heterogeneous nature of the communities using collision-detection algorithms and their preference for likely different programming languages, an user-friendly code is a crucial advantage. Our algorithm, referred to as Oriented Cuboid Sphere Intersection (OCSI), proved to be efficient and functional for both C and FORTRAN 90 (F90). Its pseudocode is presented in Algorithm 5.

Algorithm 5 - OCSI

```
1: function OCSI(r_SC, R, ê_T, ê_L, ê_W, c_T, c_L, c_W)
2:     for i ∈ {T, L, W} do                          ▷ this cycle is vectorized
3:         a_i = r_SC · ê_i
4:     end for
5:     for i ∈ {T, L, W} do                          ▷ this cycle is vectorized
6:         l_i = max(|a_i| − c_i, 0)
7:         l_i = l_i^2
8:     end for
9:     if (l_T + l_L + l_W ≤ R^2) return true        ▷ checking overlap
10:    return false
11: end function
```

3.3 Computational details

To test the relative performance of the above algorithms, we have developed two versions of the same program in C and in F90 that detect collision between one cuboid and one sphere. For compatibility with the benchmark program by Larsson *et al.*, all the floating point variables are expressed in 32-bit single precision. The dimensions of the cuboid and sphere are given in units of the cuboid thickness T, which is our unit length, and do not change within the same detection-collision test. In particular, the colloid length and width are $L^* \equiv L/T$ and width $W^* \equiv W/T$, respectively, whereas the sphere radius is $R^* \equiv R/T$. For each of the cuboid shapes analysed, we have pondered the impact on the algorithms' efficiency of changing the sphere radius between $R^* = 0.05$ and $R^* = 5$. To control the value of the acceptance ratio, i.e., the percentage of random configurations that do not produce overlaps, the sphere $\mathcal{S}$ is generated within a spherocuboid. This spherocuboid, centred and oriented as $\mathcal{C}$, results from the Minkowski addition [48] of $\mathcal{C}$ and a sphere larger than $\mathcal{S}$ and whose diameter is optimized to obtain the desired acceptance rate. A dedicated program optimises the volume of the spherocuboid according to the target value of the acceptance ratio and the dimensions of both $\mathcal{C}$ and $\mathcal{S}$, which are specified as input parameters. To generate a configuration, $\mathcal{C}$ is initially aligned with the reference axes and its centre is set as origin, while the centre of $\mathcal{S}$ is randomly positioned within the volume of the spherocuboid. Then, the reference system is randomly rotated and the cuboid-sphere overlap checked. For consistency, the section of the code that calls the overlap function is the same as that proposed by Larsson *et al.* [7]. The time spent by each algorithm to detect collisions for a specific case of cuboid and sphere (in term of

radius of the sphere and dimensions of the cuboid) is computed for 3 independent sets of $N_c = 2 \times 10^6$ configurations and then averaged out. The efficiency of the algorithms has been assessed on a Lenovo ThinkCentre M920s Desktop PC, with 8 Gb of DDR4 RAM and Intel ® Core™ i5-8500 CPU @ 3.00GHz (Coffee Lake) CPU with 9 Mb of cache, with Ubuntu 18.04 Desktop version OS. In order to prove the versatility of our algorithm, we performed benchmarks using two different compilers. In particular, we compiled the F90 and C/C++ versions of the program using Intel ® FORTRAN and C Compilers version 19 [49] and GNU FORTRAN and C++ Compilers version 10 [50]. Both the compilers used OpenMP API 4.5 specification for vectorization [51]. In addition, for all the cases listed above, we compiled two versions of the same program, enabling the generation of SSE or AVX instructions. In this work, configurations of cuboids with $L^* = [1, 20]$, $W^* = [1, 20]$ and spheres with $R^* = \{0.05, 0.5, 5\}$ with an average acceptance ratio of 40% have been tested.

3.4 Results and discussion

Due to the large number of benchmarks performed, we intended to report here the behaviour of the run-time efficiency of the algorithms with respect to the shape of the cuboid and the sphere only for the programs compiled using Intel ® C and Intel ® FORTRAN Compiler, enabling the use of AVX instruction set for SIMD parallelization. The dependence of the algorithms run-time with respect to the shape of the cuboid and the sphere is generally similar for all the compilers and the instruction sets specified during compilation. All the results obtained for the other cases are reported in the Supplementary Information. The relative performance of each algorithm is assessed in Fig. 3.2 and Fig. 3.3 for codes written in C and F90, respectively.

Fig. 3.2 offers a benchmark between QRI, QRF, SSE-intr and OCSI, while Fig. 3.3 only for QRI, QRF and OCSI , since SSE-intr uses specific Intel ® intrinsic functions: these sets of functions enable to use SIMD instructions (like SSE and AVX) without the need of an assembly code for vectorization, but they are available only for C programming language. Both figures report the run-times for detecting collisions between one cuboid of $1 \leq L^* \leq 20$ and $1 \leq W^* \leq 20$ and one sphere of radius $R^* = 0.05$ (frames (a)), 0.5 (frames (b)) and 5 (frames (c)). The N_c random configurations tested per run have been

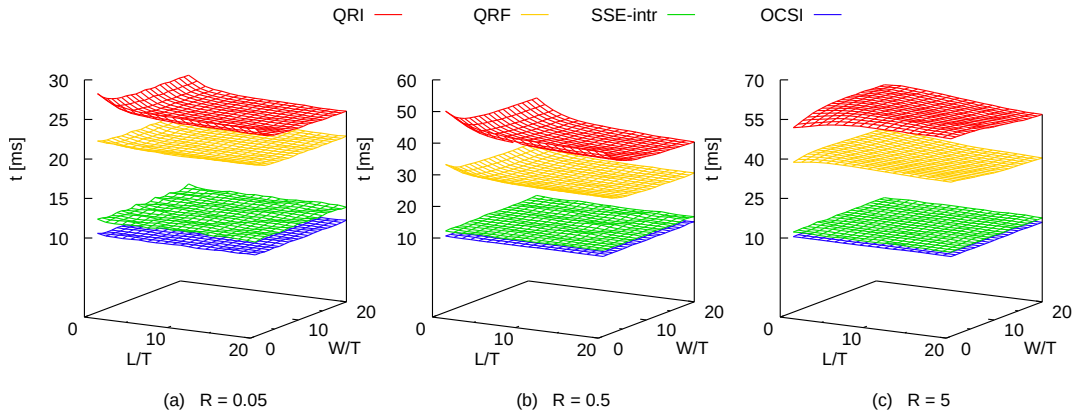

Figure 3.2: Run-times of algorithms written in C/C++ that detect collision between one cuboid of length L^* and width W^* and one sphere of radius $R^* = 0.05$ (a), 0.5 (b) and 5 (c). The program was compiled using Intel ® C Compiler and enabling the generation of AVX instructions. Each test generates 2×10^6 random configurations at constant acceptance ratio of 40%.

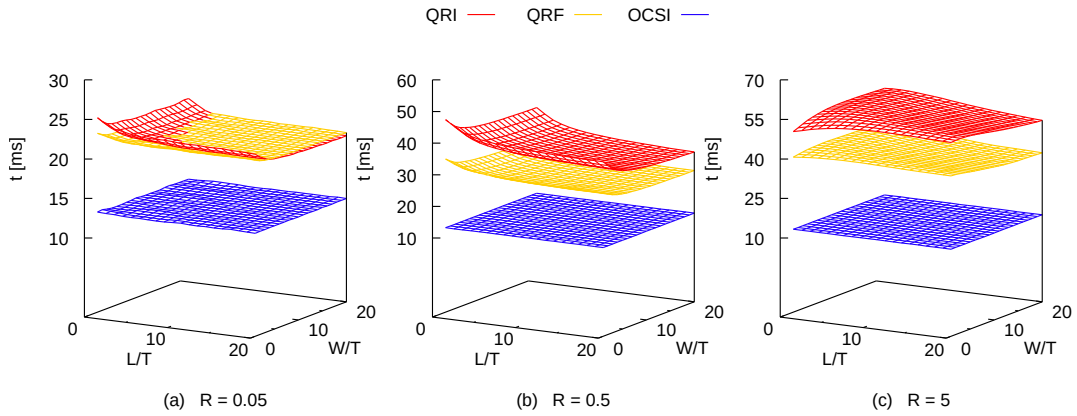

Figure 3.3: Run-times of algorithms written in F90 that detect collision between one cuboid of length L^* and width W^* and one sphere of radius $R^* = 0.05$ (a), 0.5 (b) and 5 (c). The program was compiled using Intel ® FORTRAN Compiler and enabling the generation of AVX instructions. Each test generates 2×10^6 random configurations at constant acceptance ratio of 40%.

produced at the constant acceptance ratio of 40%, which is within the usual range of values employed in Metropolis Monte Carlo simulations of hard-core particles [52]. It is evident that SSE-intr and OCSI perform significantly better than QRI and QRF under the conditions specified here, although we have also tested cuboids of larger length and width (up to $100T$) with the same acceptance ratio and observed very similar tendencies. The difference in performance is especially evident at $R^* = 5$ as SSE-intr and OCSI run-times are up to 5 and 6 times faster than QRF and QRI, respectively. In general, C codes show a better performance than F90 codes, although this difference is not substantial.

Interestingly enough, SSE-intr and OCSI do not present any relevant dependence on the cuboid and sphere geometry, being the run-times basically constant across the whole range of dimensions. This is probably due to the SIMD parallelism implemented, different from QRI and QRF, which have to run in serial for their use of quick rejection tests (see lines 6 and 9 in QRI and line 5 in QRF). Basically, if the quick rejection test is true for the first dot product, the algorithms exit the loop with negative result (C and S do not overlap) with no need to compute the remaining two.

The geometry of both cuboid and sphere exhibits a very intriguing effect on the performance of QRI and QRF as the shape of the run-time surfaces in the L^*W^* plane suggests. More specifically, for spheres with $R^* = 0.5$ (frames b in Figs. 3.2 and 3.3) the time required for the collision detection decreases upon increasing the cuboid dimensions, with the shortest time detected at $L^* = W^* = 20$ (disk-like cuboid). Larger spheres, with $R^* = 5$ (frames (c) in Figs. 3.2 and 3.3), induce a different performance resulting in an opposite concavity of the run-time surface as compared to that observed for smaller spheres. In this case, for the results obtained using Intel ® Compilers and specifying AVX instruction set during compilation, the slowest detection is measured at $(L^*, W^*) = (7, 8)$ and $(3, 5)$ for QRI and QRF in C/C++ program, respectively, and $(6, 7)$ and $(3, 5)$ for QRI and QRF in F90 program, respectively. For the parameters set in these benchmarks, in terms of acceptance ratio and shapes of cuboids and spheres, QRF is generally faster than QRI. The only exceptions to this tendency are observed for the C/C++ program compiled either with Intel ® C Compilers with AVX instructions (panel (a) of Fig. 3.2) or with GNU C++ Compiler with SSE instructions (see Supplementary Information), in both cases when the spheres are especially small ($R^* = 0.05$). The difference in performance between QRI and QRF might also be due to how data are stored and read by C/C++ and F90 compilers. As a matter of fact, Larsson and coworkers had already noticed that the run-times of QRI and QRF were very similar for acceptance ratios of approximately 50%, although their collision-detection method tests run-times for sets of configurations with cuboids and sphere of random dimensions [7]. Despite the main differences between C /C++ and FORTRAN programming languages, the average run-time performance of QRI and QRF with respect to the radius of the sphere available in C is similar to the ones we translated and provide also in FORTRAN in our benchmark source code.

To more easily compare the efficiency of the algorithms tested, the run-times computed for each possible combination of cuboid and sphere size studied here have been averaged out for each value of R^*. The resulting averaged run-times for all these cases, which are 400 considering all the possible combinations of $1 \leq L^* \leq 20$ and $1 \leq W^* \leq 20$ of the cuboids, are reported in Tables 3.1 and 3.2. For every averaged run-time reported in both tables, we evaluated also its standard deviation, which resulted to be less than 0.5 ms for all the cases. For comparison with benchmarks performed by Larsson *et al.*, the run-times are reported with a precision of 1 ms [7]. We stress that these average run-times should be taken as indicative values for QRI and QRF as their speed strongly depends on the cuboid geometry. We observe that QRI and QRF average run-times tend to be longer for larger spheres, with no significant difference between C/C++ and F90. By contrast, both SSE-intr and OCSI are completely insensible to the sphere radius as no relevant change in their average run-time is detected between $R^* = 0.05$ and 0.5.

Intel ® C Compiler								
R^*	*SSE*				*AVX*			
	QRI	QRF	OCSI	SSE-intr	QRI	QRF	OCSI	SSE-intr
0.05	24	22	11	12	25	21	10	12
0.50	38	28	11	12	39	27	10	12
5.00	54	39	11	12	55	38	10	12
GNU C++ Compiler								
R^*	*SSE*				*AVX*			
	QRI	QRF	OCSI	SSE-intr	QRI	QRF	OCSI	SSE-intr
0.05	23	24	13	11	23	22	12	11
0.50	37	30	13	11	37	28	12	11
5.00	53	41	13	11	53	38	12	11

Table 3.1: Average run-times of the C/C++ version of algorithms for collision detection between one cuboid of $1 \leq L^* \leq 20$ and $1 \leq W^* \leq 20$ and one sphere of radius R^* over 2×10^6 configurations with 40% of acceptance ratio. Results, reported in ms, are obtained compiling the benchmark program using Intel ® C Compiler and GNU C++ Compiler, enabling the generation of SSE and AVX instructions. The standard deviations of all the run-times are < 0.5 ms.

Regarding the performance of OCSI, we notice that its C version is faster than the F90 version for both the compilers. Moreover, checking the optimization report of the two compilers, we observed that GNU compilers were not capable of vectorizing the first loop of OCSI over the dot products. This seems to be the reason why Intel ® Compilers

Intel ® FORTRAN Compiler						
R^*	*SSE*			*AVX*		
	QRI	QRF	OCSI	QRI	QRF	OCSI
0.05	22	21	13	22	22	13
0.50	36	27	13	36	28	13
5.00	53	38	13	53	40	13
GNU FORTRAN Compiler						
R^*	*SSE*			*AVX*		
	QRI	QRF	OCSI	QRI	QRF	OCSI
0.05	23	21	17	22	21	18
0.50	38	27	17	36	27	18
5.00	56	37	17	53	36	18

Table 3.2: Average run-times of the F90 version of algorithms for collision detection between one cuboid of $1 \leq L^* \leq 20$ and $1 \leq W^* \leq 20$ and one sphere of radius R^* over 2×10^6 configurations with 40% of acceptance ratio. Results, reported in ms, are obtained compiling the benchmark program using Intel FORTRAN ® Compiler and GNU FORTRAN Compiler, enabling the generation of SSE and AVX instructions. The standard deviations of all the run-times are < 0.5 ms.

performed better in terms of run-time efficiency. Anyway, except the F90 version compiled with GNU FORTRAN Compiler, for all the other cases the average OCSI run-time to analyze 2×10^6 cuboid-sphere configurations oscillates between 10 and 12 ms. Even for the worst-case scenario, OCSI is still faster than QRI and QRF.

Looking at the relative performance of the C/C++ version of OCSI with respect to SSE-intr, OCSI is between 8.3 and 16.7% faster than SSE-intr when using Intel ® C Compiler, and between 9.1 and 18.2% slower if the GNU C++ Compiler is employed. At the same time, SSE-intr is 1 ms faster when compiled with the GNU C++ Compiler instead of the Intel ® C Compiler. The difference in performance between OCSI and SSE-intr, *per se*, would not be especially significant if the overlap checks were limited to 2×10^6 configurations. However, the typical number of configurations generated in Monte Carlo simulations of colloids is usually a few millions per particle, which are rarely less than a few thousands. Moreover, because colloids can be especially dense systems, one random configuration might generate more than a single collision. Consequently, it is reasonable to assume that, within a single Monte Carlo simulation, a collision-detection algorithm might be called between 10^3 and 10^5 times the configurations explored here. This would produce a difference of seconds between OCSI and SSE-intr, which anyway is still not

especially relevant.

The main advantage of using OCSI is that it is based on automatic vectorization and employs OpenMP libraries to be parallelized, making it a very user-friendly algorithm. Since SSE-intr uses intrinsic functions that are specific for SSE, this version of the algorithm for cuboid-sphere collision detection is limited only to that instruction set. Moreover, Intel ® intrinsic functions are available only in C and cannot be used in FORTRAN, unless we compile a mixed C/FORTRAN program. By contrast, OCSI is based on automatic vectorization by the compiler, guided using OpenMP pragmas and directives. In this way, the algorithm can be extended to different instruction sets without changing the source code, simply specifying the instruction set during compilation. It can also implement vectorization in FORTRAN and extend its use to 64-bit floating point arithmetic, which is commonly used in molecular modelling. OCSI proved to be efficient for the most two common compilers, for two different programming languages and for two different instruction sets, SSE and AVX, highlighting its versatility with respect to SSE-intr.

3.5 Conclusions

In summary, we have benchmarked four different collision-detection algorithms that check the occurrence of overlaps between one cuboid and one sphere. Our analysis focused on a specific acceptance ratio, which is within the usual range applied to efficiently sample the configuration space of hard-core systems in Monte Carlo simulations [52]. We notice that SSE-intr has been previously tested for different acceptance ratios and did not show relevant changes in performance [7]. A similar tendency is also expected for OCSI, but should be confirmed by further tests. While QRI and QRF are observed to be geometry-dependent, SSE-intr and OCSI are basically insensible to the cuboid anisotropy and sphere radius and, thanks to automatic vectorization, they are also significantly faster. According to these results, we expect OCSI and SSE-intr run-times to be constant also for bigger spheres, while QRI and QRF run-times can show a different behaviour than the ones observed so far. To ascertain these tendencies, further tests should be performed. In particular, the OCSI algorithm proved to be especially valuable in terms of performance and simplicity of implementation in both C and F90.

Intel ®compilers and GNU Compilers were not able to automatically vectorize QRI and QRF. Anyway, there are ways to perform conditional statements like the ones used in the quick rejection test implementing SIMD parallelism [53]. Whether or not vectorized versions of QRF and QRI are possible and, if so, how efficient they would be as compared to the current versions requires further study.

It should be stressed that the method applied to generate the sphere around the cuboid is crucial to provide a robust comparison between different algorithms. The choice of the spherocuboid as a sampling volume allows to precisely set the desired acceptance ratio and guarantees that the algorithms are tested for all the possible positions of the sphere around or inside the cuboid. This is especially relevant to fairly assess the performance of QRI and QRF, due to their use of quick rejection tests. In Monte Carlo simulations, where the generation of configurations follows a different procedure, the performance of collision-detection algorithms, most likely affected by the degree of system order and packing, should be tested. Finally, it is important to mention that the OCSI algorithm allows for the calculation of the cuboid-sphere minimum distance, hence suggesting future study to determine a suitable interaction potential beyond mere hard-core interactions. The formal proof reported here can also be useful to test the intersection of cuboids with particles of different shape. As a final note, we stress that our algorithm has been only tested for a specific pairs of geometries (cuboids and spheres), while it might be relevant, in computational colloid science as well as in computer graphics, to assess its performance with other geometries. We are currently working on extending our algorithm to detect collisions between cuboids and oblate or prolate spherocylinders. It would also be especially interesting to investigate to what extent our methodology could be applied to more complex geometries, whose collision is generally detected by more sophisticated decomposition techniques, such as e.g., Voronoi diagrams [54] or convex polygon triangulations [55, 56]. We hope that our contribution might stimulate further research in this direction.

Acknowledgments

The authors acknowledge the use of Computational Shared Facility at the University of Manchester and Dr Benedetto Di Paola (University of Palermo) for a critical reading of

the manuscript.

Appendices

3.A1 On the minimum distance between a sphere and a randomly oriented cuboid

Let $\mathbf{V}$ be a n-dimensional vector space in an orthonormal basis $\mathcal{B} = \left\{ \hat{\mathbf{x}}_1, \hat{\mathbf{x}}_2, ..., \hat{\mathbf{x}}_n \,\middle|\, \hat{\mathbf{x}}_i \cdot \hat{\mathbf{x}}_j = \delta_{ij} \right\}$, with δ_{ij} the Kronecker delta. The set of points of a cuboid $\mathcal{C}$ in $\mathbf{V}$ is

$$\mathbf{C} = \mathbf{r}_C + \sum_{i=1}^{n} \alpha_i c_i \hat{\mathbf{e}}_i \tag{3.7}$$

where $\mathbf{r}_C$ is the position of the centre of the cuboid, $c_i > 0$ is a scalar equal to half of the cuboid length, width or thickness, α_i is also a scalar with values in $[-1, 1]$, and $\hat{\mathbf{e}}_i$ is a unit vector that defines the orientation of $\mathcal{C}$. Specifically $\hat{\mathbf{e}}_i \cdot \hat{\mathbf{e}}_j = \delta_{ij}$, so also $\mathcal{B}' = \{\hat{\mathbf{e}}_1, \hat{\mathbf{e}}_2, ..., \hat{\mathbf{e}}_n\}$ is an orthonormal basis for $\mathbf{V}$. The minimum distance between $\mathbf{C}$ and a random point $\mathbf{r}_S$ reads

$$\min\left(\left\| \mathbf{r}_S - \mathbf{C} \right\| \right) = \min\left(\left\| \mathbf{r}_S - \mathbf{r}_C - \sum_{i=1}^{n} \alpha_i c_i \hat{\mathbf{e}}_i \right\| \right). \tag{3.8}$$

Since $\mathcal{B}'$ is an orthonormal basis for $\mathbf{V}$, the vector $\mathbf{r}_{SC} = \mathbf{r}_S - \mathbf{r}_C$ can be written as

$$\mathbf{r}_{SC} = \sum_{i=1}^{n} \left(\mathbf{r}_{SC} \cdot \hat{\mathbf{e}}_i \right) \hat{\mathbf{e}}_i \tag{3.9}$$

and substituting Eq. 3.9 in Eq. 3.8

$$\begin{aligned} &\min\left(\left\| \sum_{i=1}^{n} \left\{ \left(\mathbf{r}_{SC} \cdot \hat{\mathbf{e}}_i \right) - \alpha_i c_i \right\} \hat{\mathbf{e}}_i \right\| \right) = \\ &= \sqrt{\min\left(\sum_{i=1}^{n} \sum_{j=1}^{n} \left\{ \left(\mathbf{r}_{SC} \cdot \hat{\mathbf{e}}_i \right) - \alpha_i c_i \right\} \left\{ \left(\mathbf{r}_{SC} \cdot \hat{\mathbf{e}}_j \right) - \alpha_j c_j \right\} \hat{\mathbf{e}}_i \cdot \hat{\mathbf{e}}_j \right)} = \\ &= \sqrt{\sum_{i=1}^{n} \min\left(\left\{ \left(\mathbf{r}_{SC} \cdot \hat{\mathbf{e}}_i \right) - \alpha_i c_i \right\}^2 \right)} \end{aligned} \tag{3.10}$$

The last term in Eq. 3.10 has been obtained considering that $\hat{\mathbf{e}}_i \cdot \hat{\mathbf{e}}_j = \delta_{ij}$ and that every member of the sum depends on just one value α_i, hence they are all independent. It is

sufficient to calculate only one term of this sum as all dimensions are equivalent. In particular, this term equals zero if the following conditions are met:

$$\alpha_i c_i - \left(\mathbf{r}_{SC} \cdot \hat{\mathbf{e}}_i\right) = 0 \;\Leftrightarrow\; \alpha_i = \frac{\mathbf{r}_{SC} \cdot \hat{\mathbf{e}}_i}{c_i} \tag{3.11}$$

Because $\alpha_i = [-1, 1]$, this implies that

$$-1 \leq \frac{\mathbf{r}_{SC} \cdot \hat{\mathbf{e}}_i}{c_i} \leq 1 \;\Leftrightarrow\; \left|\frac{\mathbf{r}_{SC} \cdot \hat{\mathbf{e}}_i}{c_i}\right| \leq 1 \;\Leftrightarrow\; \left|\mathbf{r}_{SC} \cdot \hat{\mathbf{e}}_i\right| \leq c_i \tag{3.12}$$

If $|\mathbf{r}_{SC} \cdot \hat{\mathbf{e}}_i| > c_i$, then $(\mathbf{r}_{SC} \cdot \hat{\mathbf{e}}_i) > c_i$ or $(\mathbf{r}_{SC} \cdot \hat{\mathbf{e}}_i) < -c_i$. The former inequality implies that

$$\min\left(\left\{\alpha_i c_i - \left(\mathbf{r}_{SC} \cdot \hat{\mathbf{e}}_i\right)\right\}^2\right) = \left\{c_i - \left(\mathbf{r}_{SC} \cdot \hat{\mathbf{e}}_i\right)\right\}^2 = \left\{c_i - \left|\mathbf{r}_{SC} \cdot \hat{\mathbf{e}}_i\right|\right\}^2 \tag{3.13}$$

while, the latter inequality implies

$$\min\left(\left\{\alpha_i c_i - \left(\mathbf{r}_{SC} \cdot \hat{\mathbf{e}}_i\right)\right\}^2\right) = \left\{-c_i - \left(\mathbf{r}_{SC} \cdot \hat{\mathbf{e}}_i\right)\right\}^2 = \left\{-c_i + \left|\mathbf{r}_{SC} \cdot \hat{\mathbf{e}}_i\right|\right\}^2 = \left\{c_i - \left|\mathbf{r}_{SC} \cdot \hat{\mathbf{e}}_i\right|\right\}^2 \tag{3.14}$$

Because the solution of Eqs. 3.13 is the same as that of 3.14, if $|\mathbf{r}_{SC} \cdot \hat{\mathbf{e}}_i| > c_i$, then one can write

$$\min\left(\left\{\alpha_i c_i - \left(\mathbf{r}_{SC} \cdot \hat{\mathbf{e}}_i\right)\right\}^2\right) = \left\{c_i - \left|\mathbf{r}_{SC} \cdot \hat{\mathbf{e}}_i\right|\right\}^2 = \left\{\left|\mathbf{r}_{SC} \cdot \hat{\mathbf{e}}_i\right| - c_i\right\}^2 \tag{3.15}$$

The solutions of Eqs. 3.11 and 3.15 can be incorporated in a single equation by using a step function defined as

$$\Theta(x) = \begin{cases} 0 & x \leq 0 \\ 1 & x > 0 \end{cases} \tag{3.16}$$

Therefore, the minimum distance of a point $\mathbf{r}_S$ from the surface of a cuboid C reads

$$\min\left(\left\|\mathbf{r}_S - \mathbf{C}\right\|\right) = \sqrt{\sum_{i=1}^{n} \Theta\left(\left|\mathbf{r}_{SC} \cdot \hat{\mathbf{e}}_i\right| - c_i\right)\left\{\left|\mathbf{r}_{SC} \cdot \hat{\mathbf{e}}_i\right| - c_i\right\}^2} \tag{3.17}$$

Finally, a cuboid C overlaps with a sphere of radius R and centre in $\mathbf{r}_S$, if the following inequality is satisfied:

$$\sqrt{\sum_{i=1}^{n} \Theta\Big(\big|\mathbf{r}_{\mathrm{SC}} \cdot \hat{\mathbf{e}}_i\big| - c_i\Big)\Big\{\big|\mathbf{r}_{\mathrm{SC}} \cdot \hat{\mathbf{e}}_i\big| - c_i\Big\}^2} \leq R \tag{3.18}$$

Supporting information

The source code of the program for the optimisation of the spherocuboid volume, the C/C++ and F90 benchmark programs and the raw data required to reproduce our findings can be downloaded at http://dx.doi.org/10.17632/w7g3ynkc6n.2.

Bibliography

[1] Ericson, C. *Real-Time Collision Detection* (CRC Press, Inc., 2004).

[2] Akenine-Möller, T., Haines, E., Hoffman, N. & Pesce, A. *Real-Time Rendering, Fourth Edition* (Chapman and Hall/CRC, 2018).

[3] Chang, J.-W., Wang, W. & Kim, M.-S. Efficient collision detection using a dual obb-sphere bounding volume hierarchy. *Computer-Aided Design* **42**, 50–57 (2010).

[4] Gottschalk, S., Lin, M. C. & Manocha, D. OBBTree: A Hierarchical Structure for Rapid Interference Detection. In *Proceedings of the 23rd Annual Conference on Computer Graphics and Interactive Techniques*, SIGGRAPH '96, 171–180 (Association for Computing Machinery, New York, NY, USA, 1996).

[5] Arvo, J. A simple method for box-sphere intersection testing. In Glassner, A. S. (ed.) *Graphic Gems*, 335–339 (Academic Press, 1990).

[6] Ratschek, H. & Rokne, J. Box-sphere intersection tests. *Computer-Aided Design* **26**, 579–584 (1994).

[7] Larsson, T., Akenine-Möller, T. & Lengyel, E. On faster sphere-box overlap testing. *Journal of Graphics Tools* **12**, 3–8 (2007).

[8] Moore, M. & Wilhelms, J. Collision detection and response for computer animation. In Beach, R. J. (ed.) *Proceedings of the 15th Annual Conference on Computer Graphics and Interactive Techniques*, 289–298 (Association for Computing Machinery, 1988).

[9] Pungotra, H., Knopf, G. K. & Canas, R. Efficient algorithm to detect collision between deformable b-spline surfaces for virtual sculpting. *Computer-Aided Design* **40**, 1055–1066 (2008).

[10] Pan, J. & Manocha, D. Gpu-based parallel collision detection for fast motion planning. *Int. J. Robot. Res.* **31**, 187–200 (2012).

[11] Govender, N., Wilke, D. N. & Kok, S. Collision detection of convex polyhedra on the nvidia gpu architecture for the discrete element method. *Appl. Math. Comput.* **267**, 810–829 (2015).

[12] Zhang, R., Liu, X. & Wei, J. Collision detection based on obb simplified modeling. *J. Phys.: Conf. Ser.* **1213**, 042079 (2019).

[13] Yang, C., Wang, X. & Cheng, L. Neural-learning-based telerobot control with guaranteed performance. *IEEE T Cybernetics* **47**, 3148–3159 (2017).

[14] Zou, Y., Liu, P. X., Li, C. & Cheng, Q. Collision detection for virtual environment using particle swarm optimization with adaptive cauchy mutation. *Cluster. Comput.* **20**, 1765–1774 (2017).

[15] Tomić, T., Ott, C. & Haddadin, S. External wrench estimation, collision detection, and reflex reaction for flying robots. *IEEE Transactions on Robotics* **33**, 1467–1482 (2017).

[16] Xiao, J., Zhang, Q., andG. Wang, Y. H. & Zeng, F. Collision detection algorithm for collaborative robots considering joint friction. *IJARS* **15**, 1–13 (2018).

[17] Ren, T., Dong, Y., Wu, D. & Chen, K. Collision detection and identification for robot manipulators based on extended state observer. *Control Eng. Pract.* **79**, 144–153 (2018).

[18] Nguyen, M., Zhang, S. & Wang, X. A. A novel method for risk assessment and simulation of collision avoidance for vessels based on ais. *Algorithms* **11**, 204–217 (2018).

[19] Tang, T. D. Algorithms for collision detection and avoidance for five-axis nc machining: A state of the art review. *Computer-Aided Design* **51**, 1–17 (2014).

[20] Frenkel, D., Lekkerkerker, H. N. W. & Stroobants, A. Thermodynamic stability of a smectic phase in a system of hard rods. *Nature* **332**, 822–823 (1988).

[21] Anderson, J. A., Glaser, J. & Glotzer, S. C. Hoomd-blue: A python package for high-performance molecular dynamics and hard particle monte carlo simulations. *Computational Materials Science* **173**, 109363 (2020).

[22] Rosenbluth, M. N. & Rosenbluth, A. W. Further results on Monte Carlo equations of state. *J. Chem. Phys.* **22**, 881–884 (1954).

[23] Wood, W. W. & Jacobson, J. D. Preliminary results from a recalculation of the Monte Carlo equation of state of hard spheres. *J. Chem. Phys.* **27**, 1207–1208 (1957).

[24] Alder, B. J. & Wainwright, T. E. Phase transition for a hard sphere system. *J. Chem. Phys.* **27**, 1208–1209 (1957).

[25] Onsager, L. The effects of shape on the interaction of colloidal particles. *Annals of the New York Academy of Sciences* **51**, 627–659 (1949).

[26] Shankar, S. S. *et al.* Biological synthesis of triangular gold nanoprisms. *Nat. Mat.* **3**, 482–488 (2004).

[27] Sun, Y. & Xia, Y. Shape-controlled synthesis of gold and silver nanoparticles. *Science* **298**, 2176–2179 (2002).

[28] Manoharan, V. N., Elsesser, M. T. & Pine, D. J. Dense packing and symmetry in small clusters of microspheres. *Science* **301**, 483–487 (2003).

[29] Sacanna, S., Irvine, W. T. M., Chaikin, P. M. & Pine, D. J. Lock and key colloids. *Nature* **464**, 575–578 (2010).

[30] Sacanna, S. *et al.* Shaping colloids for self-assembly. *Nat. Comm.* **4**, 1688 (2013).

[31] Rossi, L. *et al.* Shape-sensitive crystallization in colloidal superball fluids. *PNAS* **112**, 5286–5290 (2015).

[32] Xiang, Y. *et al.* Formation of rectangularly shaped Pd/Au bimetallic nanorods: Evidence for competing growth of the Pd shell between the 110 and 100 side facets of Au nanorods. *Nano Letters* **6**, 2290–2294 (2006).

[33] Okuno, Y. *et al.* Uniform and controllable preparation of Au–Ag core–shell nanorods using anisotropic silver shell formation on gold nanorods. *Nanoscale* **2**, 1489–1493 (2010).

[34] Cortie, M. B., Liu, F., Arnold, M. D. & Niidome, Y. Multimode resonances in silver nanocuboids. *Langmuir* **28**, 9103–9112 (2012).

[35] Khlebtsov, B. N., Liuc, Z., Yec, J. & Khlebtsov, N. G. Au@Ag core/shell cuboids and dumbbells: Optical properties and sers response. *J. Quant. Spectrosc. Radiat. Transf.* **167**, 64–75 (2015).

[36] Glotzer, S. C. & Solomon, M. J. Anisotropy of building blocks and their assembly into complex structures. *Nat. Mat.* **6**, 557–562 (2007).

[37] Damasceno, P. F., Engel, M. & Glotzer, S. C. Crystalline assemblies and densest packings of a family of truncated tetrahedra and the role of directional entropic forces. *ACS Nano* **6**, 609–614 (2012).

[38] van Anders, G., Ahmed, N. K., Smith, R., Engel, M. & Glotzer, S. C. Entropically patchy particles: Engineering valence through shape entropy. *ACS Nano* **8**, 931–940 (2014).

[39] de Nijs, B. *et al.* Entropy-driven formation of large icosahedral colloidal clusters by spherical confinement. *Nat. Mat.* **14**, 56–60 (2015).

[40] Cuetos, A., Dennison, M., Masters, A. & Patti, A. Phase behaviour of hard board-like particles. *Soft Matter* **13**, 4720–4732 (2017).

[41] Cuetos, A. & Patti, A. Monte Carlo simulation of binary mixtures of hard colloidal cuboids. *Mol. Sim.* **44**, 516–522 (2018).

[42] Cuetos, A., Mirzad Rafael, E., Corbett, D. & Patti, A. Biaxial nematics of hard cuboids in an external field. *Soft Matter* **15**, 1922–1926 (2019).

[43] Cuetos, A. & Patti, A. Dynamics of hard colloidal cuboids in nematic liquid crystals. *Phys. Rev. E* **101**, 052702 (2020).

[44] Mirzad Rafael, E., Corbett, D., Cuetos, A. & Patti, A. Self-assembly of freely-rotating polydisperse cuboids: Unveiling the boundaries of the biaxial nematic phase. *Soft Matter* **16**, 5565–5570 (2020).

[45] Thakkar, S. & Huff, T. Internet streaming simd extensions. *Computer* **32**, 26–34 (1999).

[46] Van der Pas, R., Stotzer, E. & Terboven, C. *Using OpenMP - The Next Step: Affinity, Accelerators, Tasking, and SIMD* (MIT Press, 2017).

[47] *Intel Advanced Vector Extensions Programming Reference, Ref # 319433-011, www.intel.com* (2011).

[48] Schneider, R. *Minkowski addition*, chap. 3, 139–207 (Cambridge University Press, 1993).

[49] Intel ® Corporation. *Intel ® C++ Compiler Classic Developer Guide and Reference* (2020).

[50] Stallman, R. M. & the GCC Developer Community. *Using the GNU Compiler Collection, for gcc version 10.2.0* (2020).

[51] OpenMP Architecture Review Board. *OpenMP Application Programming Interface Version 4.5* (2015).

[52] Frenkel, D. & Smit, B. *Monte Carlo Simulations*, chap. 3, 45–46 (Academic Press, Inc., 1996).

[53] Sun, H., Gorlatch, S. & Zhao, R. Vectorizing programs with if-statements for processors with simd extensions. *The Journal of Supercomputing* **76**, 4731–4746 (2020).

[54] Aurenhammer, F. Voronoi diagrams - a survey of a fundamental geometric data structure. *ACM Comput. Surv.* **23**, 345–405 (1991).

[55] Saračević, M. & Selimi, A. A. convex polygon triangulation based on planted trivalent binary tree and ballot problem. *Turk. J. Elec. Eng. & Comp. Sci.* **27**, 346–361 (2019).

[56] Stanimirović, P. S., Krtolica, P. V., Saračević, M. H. & Mašović, S. H. Decomposition of catalan numbers and convex polygon triangulations. *Int. J. Comput. Math.* **91**, 1315–1328 (2014).

blank page

Chapter 4

Diffusion of Globular Macromolecules in Liquid Crystals of Colloidal Cuboids

The content of this Chapter has been published as a full article in the *Journal of Molecular Liquids*. My contributions are listed as follows: Luca Tonti was responsible for data curation; Luca Tonti developed the methodology and the software; Luca Tonti, Fabián A. García Daza and Alessandro Patti performed the investigation; Luca Tonti and Fabián A. García Daza wrote the original draft.

Abstract

Macromolecular diffusion in dense colloidal suspensions is an intriguing topic of interdisciplinary relevance in Science and Engineering. While significant efforts have been undertaken to establish the impact of crowding on the dynamics of macromolecules, less clear is the role played by long-range ordering. In this work, we perform Dynamic Monte Carlo simulations to assess the importance of ordered crowding on the diffusion of globular macromolecules, here modelled as spherical tracers, in suspensions of colloidal cuboids. We first investigate the diffusion of such guest tracers in very weakly ordered host phases of cuboids and, by increasing density above the isotropic-to-nematic phase boundary, study the influence of long-range orientational ordering imposed by the occurrence of liquid-crystalline phases. To this end, we analyse a spectrum of dynamical properties that clarify the existence of slow and fast tracers and the extent of deviations from Gaussian behaviour. Our results unveil the existence of randomly oriented clusters of cuboids that display a relatively large size in dense isotropic phases, but are basically absent in the nematic phase. We believe that these clusters are responsible for a pronounced non-Gaussian dynamics that is much weaker in the nematic phase, where orientational ordering smooths out such structural heterogeneities.

4.1 Introduction

Understanding the diffusion of tracers in crowded colloidal suspensions is a problem with a multifaceted interdisciplinary impact. In Biology, it is especially related to the ability of macromolecules, such as proteins, of penetrating the cell membrane, diffusing through the cytosol and organelles and thus contributing to regulate the cell function [1]. In Nanomedicine, the release rate of a drug from a nanovehicle, such as a micelle, depends on its ability to diffuse through its hydrophobic core and hydrophilic corona [2]. In Food Science, moisture migration in dried food products determines how long these can be preserved from spoilage [3]. In Materials Science, the self-healing ability of a smart coating, which is activated by an external stimulus, such as a pH or temperature gradient, relies on the diffusion of a corrosion inhibitor through a polymeric matrix into the defect [4]. Additionally, investigating the dynamics of tracers in colloids has also opened a path to the study of rheology of the host phase, a technique commonly referred to as microrheology, which allows to extract the viscoelastic response of a soft material from a tracer's mean square displacement (MSD) [5, 6].

Although specific attributes and properties make them unique and different from each other, all the above-mentioned soft-matter systems exhibit interesting common features. One is that macromolecular diffusion shows an *anomalous* behaviour, where the MSD, rather than growing linearly with time, as predicted by Fick's diffusion theory [7], follows a power-law of the type $r^2(t) \propto t^\beta$, with $0 < \beta < 1$ the anomalous diffusion exponent [8, 9, 10, 11]. Such a subdiffusion usually develops at intermediate time scales, but it is not persistent and, at sufficiently long times, the MSD recovers a Brownian-like behaviour, generally referred to as Fickian diffusion [12, 13, 14]. Crowded soft-matter systems can also exhibit a degree of ordering that might influence the diffusion of macromolecules or nanoparticles, for instance by creating preferential paths [15], and thus should not *a priori* be disregarded. Nevertheless, when assessing macromolecular diffusion in crowded media, most research works have especially focused on the host-guest affinity [16, 17], relative characteristic lengths [18, 19] and volume fractions [20, 21] as well as on the effect of structural heterogeneities [22], but much less on whether or not it could be enhanced, inhibited or made more complex by the occurrence of long-range ordering and spatial anisotropy.

Due to their rich phase behaviour, colloidal liquid crystals (LCs), namely colloidal

suspensions of orientationally and/or positionally ordered anisotropic particles, are particularly appropriate to gain insight into the effect of ordered crowding on macromolecular diffusion. This is especially evident in systems of biaxial particles, whose phase behaviour is decorated by a plethora of intriguing morphologies that cannot be observed with uniaxial particles [23]. Over the last few years, our group has specifically explored the self-assembly of oblate and prolate cuboidal particles, unveiling the existence of uniaxial and biaxial nematic and positionally-ordered smectic and columnar phases [24, 25, 26, 27]. More recently, we have also determined the main features of their equilibrium dynamics in uniaxial nematics, detecting Fickian and Gaussian dynamics at both short-time and long-time scales [28]. In this work, we investigate the diffusion of globular macromolecules, here modelled as spherical tracers, in uniaxial nematics of oblate and prolate colloidal cuboids, modelled as hard board-like particles (HBPs). Our main goal is understanding how long-range ordering affects tracers' diffusion as compared to diffusion in weakly ordered (isotropic) phases. To this end, we employ a stochastic simulation technique, referred to as Dynamic Monte Carlo (DMC), that is especially efficient to mimic the Brownian motion of particles interacting by mere excluded volume effects [29, 30, 31, 32, 33].

4.2 Model and simulation methodology

The systems studied in this work comprise $N_c = 2000$ HBPs of thickness T, which is the system unit length, reduced length $L^* \equiv L/T$ and width $W^* \equiv W/T$, and $N_s = 200$ hard spheres (HSs) with diameter $d_s{}^* \equiv d_s/T$. The size of the spherical tracers with respect to that of cuboids has been set to mimic the diffusion of macromolecules, such as globular proteins like enzymes, whose diameter is generally in the order of 1 to 10 nm [34]. Given that these model macromolecular tracers are incorporated in a host phase of significantly larger colloidal particles, their diameter has been set to $d_S = T/10$. In particular, we investigated the dynamics of spherical tracers in systems of HBPs with reduced dimensions $(L^*, W^*) = \{(12, 1), (12, 8)\}$ at packing fractions $\eta = 0.15$ and $\eta = 0.34$, where HBPs self-assemble, respectively, into isotropic (I) and uniaxial nematic (N_U) phases [24]. The packing fraction is defined as $\eta^{pure} \equiv LWTN_c/V$, with V the volume of the simulation box. Initial configurations have been prepared by incorporating the tracers into pure

systems of cuboids at the desired packing fraction η^{pure}. The actual packing fraction of the mixture should also include the volume occupied by the spherical tracers as follows

$$\eta = \eta^{pure}\left[1 + \delta\eta\right], \tag{4.1}$$

$$\delta\eta = \frac{\pi N_s d_s^3}{6N_c LWT}, \tag{4.2}$$

where $\delta\eta$ provides the difference in packing fraction between the pure system of HBPs and the mixture of HBPs and HSs. Within the range of cuboid dimensions explored here, $\delta\eta < 10^{-5}$ and it is therefore reasonable to assume that $\eta \sim \eta^{pure}$.

To equilibrate I and N_U phases, we performed standard Monte Carlo (MC) simulations in the canonical ensemble at the above-mentioned packing fractions and considered the systems at equilibrium when order parameters achieved a steady state value within reasonable statistical fluctuations. Given that all particles interact via hard-core potentials, MC moves are always accepted if they do not overlap. Overlap tests between two cuboids are based on the separating axes algorithm [35] adapted to investigate the phase behaviour of colloidal HBPs with square cross section [36]. Overlap tests between spheres and cuboids are based on our recent Oriented Cuboid Sphere Intersection (OCSI) algorithm [37].

Uniaxial order parameters have been obtained from the diagonalization of the following tensor:

$$\mathbb{Q}^{kk} = \frac{1}{2N_c}\sum_{i=1}^{N_c}\left[3\left(\hat{\mathbf{e}}_{k,i}\otimes\hat{\mathbf{e}}_{k,i}\right) - \mathbb{I}\right], \tag{4.3}$$

where the unit vector $\hat{\mathbf{e}}_{k,i}$ indicates the orientation of $k = T, L, W$ for each cuboid i and $\mathbb{I}$ is the unit tensor. The largest eigenvalue of $\mathbb{Q}^{kk}$, is the uniaxial order parameter relative to size k, here referred to as U_k, while the corresponding eigenvector, $\mathbf{d}_k$, indicates its preferential orientation. In an I phase, $U_T \approx U_W \approx U_L \approx 0$ and the vectors $\mathbf{d}_k$ are meaningless. By contrast, in an N_U phase, one eigenvalue is significantly larger than 0 and the associated eigenvector $\hat{\mathbf{n}}$ defines the direction of the nematic director. The tensor $\mathbb{Q}^{kk}$ also allows for the computation of the biaxial order parameters, which are anyway all close to zero for the systems studied here. To characterise the positional order of HBPs and spheres, we computed the radial distribution function, $g(r)$, in the I phases and pair correlation functions parallel, $g_\parallel(r)$, and perpendicular, $g_\perp(r)$, to the nematic director in the N_U phases. All of them have been obtained for cuboid-cuboid, sphere-sphere and

sphere-cuboid distributions. The interested reader is referred to Refs. [27, 38] for additional details on the calculation of parallel and perpendicular pair correlation functions.

W^*	$D_T^{tra}{D_0}^{-1}$	$D_W^{tra}{D_0}^{-1}$	$D_L^{tra}{D_0}^{-1}$	$D_T^{rot}\tau$	$D_W^{rot}\tau$	$D_L^{rot}\tau$
1	2.2×10^{-2}	2.2×10^{-2}	3.1×10^{-2}	1.1×10^{-3}	1.1×10^{-3}	$2.3 \cdot 10^{-2}$
8	9.4×10^{-3}	1.4×10^{-2}	1.5×10^{-2}	3.5×10^{-4}	3.6×10^{-4}	6.3×10^{-4}

Table 4.1: Translational and rotational diffusion coefficient at infinite dilution of the HBPs studied in this work.

As far as the dynamics is concerned, we generated time trajectories by employing the Dynamic Monte Carlo (DMC) simulation method [29, 30, 31, 32]. In DMC simulations, the Brownian motion of colloidal particles in a fluid is modelled through stochastic displacements and rotations, whose timescale is set by the Einstein relation [39]. In particular, a random particle is selected and a trial translation is attempted if the particle is a sphere, $\mathbf{r}_{s,new} = \mathbf{r}_{s,old} + \delta\mathbf{r}_s$, or a rototranslation if it is a cuboid, namely $\mathbf{r}_{c,new} = \mathbf{r}_{c,old} + \delta\mathbf{r}_c$ for translation and $\hat{\mathbf{e}}_{k,new} = \mathbb{R}_{TLW}\ \hat{\mathbf{e}}_{k,old}$ for rotations. The rotation matrix $\mathbb{R}_{TLW}$ is employed to rotate the cuboids around their axes of orientation $\hat{\mathbf{e}}_T, \hat{\mathbf{e}}_L, \hat{\mathbf{e}}_W$. The elementary displacements $\delta r_{k,s}$ of spheres along the reference axes $k = \hat{\mathbf{x}}, \hat{\mathbf{y}}, \hat{\mathbf{z}}$ are uniformly sampled in the interval $[-\delta r_{k,max,s}; \delta r_{k,max,s}]$. Similarly, the elementary displacements of cuboids, $\delta r_{k,c}$, are sampled in the interval $[-\delta r_{k,max,c}; \delta r_{k,max,c}]$, while their elementary rotations, $\delta\theta_{k,c}$, in $[-\delta\theta_{k,max,c}; \delta\theta_{k,max,c}]$, for $k = T, L, W$. The maximum displacements and rotations are defined using the Einstein relation given below:

$$\delta r_{k,max,s} = \sqrt{2D_s\delta t_{MC,s}} \quad k = \hat{\mathbf{x}}, \hat{\mathbf{y}}, \hat{\mathbf{z}}, \tag{4.4}$$

$$\delta r_{k,max,c} = \sqrt{2D_{k,c}^{tra}\delta t_{MC,c}} \quad k = T, L, W, \tag{4.5}$$

$$\delta\theta_{k,max,c} = \sqrt{2D_{k,c}^{rot}\delta t_{MC,c}} \quad k = T, L, W, \tag{4.6}$$

where δt_{MC} is the MC timescale of the simulation, D_s is the sphere diffusion coefficient at infinite dilution, whereas $D_{k,c}^{tra}$ and $D_{k,c}^{rot}$ are, respectively, the translational and rotational cuboid diffusion coefficients also at infinite dilution. In a DMC simulation of a binary mixture, the MC timescales of the two components are different, but the Brownian timescale is unique. These timescales are therefore related as follows:

$$\mathscr{A}_c\delta t_{MC,c} = \mathscr{A}_s\delta t_{MC,s}, \tag{4.7}$$

where $\mathscr{A}_c$ and $\mathscr{A}_s$ are the acceptance rates of the attempted moves of cuboids and spheres, respectively. In practice, the MC timescale of either HBPs or HSs is kept constant to a given input value, while the other converges according to Eq. 4.7 by updating the acceptance rates. The Brownian timescale of the DMC simulation is linked to the acceptance rate of the components of the system and their MC timescales, according to Eq. 4.8:

$$t_{BD} = \frac{\mathscr{A}_c}{3}\mathscr{C}_{MC}\delta t_{MC,c} = \frac{\mathscr{A}_s}{3}\mathscr{C}_{MC}\delta t_{MC,s}, \tag{4.8}$$

where $\mathscr{C}_{MC}$ is the number of MC cycles performed, with 1 MC cycle corresponding to N_s+N_c attempted moves. A detailed theoretical discussion of the DMC method for mono- and multi-component systems is reported in Refs. [29, 30].

To apply Eqs. 4.4-4.6, one needs to estimate the diffusion coefficient of spheres and cuboids at infinite dilution. The former is obtained from the Stokes-Einstein equation:

$$D_s = \frac{D_0}{3\pi d_s^*} \sim 1.061 D_0, \tag{4.9}$$

where $D_0 \equiv T^2\tau^{-1}$ is a diffusion constant, with τ the time unit. The diffusion tensor of HBPs at infinite dilution was estimated numerically using HYDRO++, an open-source software that calculates the solution properties of macromolecules and colloidal particles by approximating their shape and volume with an array of spherical beads of arbitrary size [40, 41]. The diffusion tensor of biaxial particles is in principle non-diagonal, implying the existence of a rototranslational coupling that is taken into account by a generalised version of the DMC method [33]. Nevertheless, the diffusion tensor that we obtained showed that its off-diagonal terms were at least 4 orders of magnitude smaller than the remaining terms and thus safely negligible. The translational and rotational diffusion coefficients at infinite dilution of prolate and oblate HBPs are listed in Table 4.1. As in typical Brownian Dynamics and Langevin Dynamics simulations, Hydrodynamic Interactions (HI) are neglected also in DMC simulations. The effect of HI in BD simulations of crowded suspensions has been evaluated for binary mixtures of Lennard-Jones spheres of different sizes and results show that HI interactions slow down the dynamics of the spheres without modifying the qualitative features of the diffusion [42].

In all DMC simulations, we set the MC time step of spheres in the range $\delta t_{MC,s} = \{5 \times 10^{-5}; 10^{-2}\}\tau$. The smallest time step determined a maximum displacement approximately

equal to $d_s^*/10$, whereas the largest time step has been set in order to reproduce the same conditions as those recently studied in pure systems of HBPs [28]. We first performed a preliminary simulation of 10^4 MC cycles to find the time step of cuboids according to Eq. 4.7, that is $\delta t_{MC,c} = \mathscr{A}_s^{(10)} \delta t_{MC,s} / \mathscr{A}_c^{(10)}$, averaging every 10 MC cycles. A summary of the systems investigated with the corresponding time steps are listed in Table 4.2.

Systems	N_s	N_c	$d_s{}^*$	W^*	L^*	η^{pure}	Phase	$\delta t_{MC,s}$	$\delta t_{MC,c}$	$\mathscr{A}_s$	$\mathscr{A}_c$
S_1	200	2000	0.1	1	12	0.15	I	5.000×10^{-5}	5.015×10^{-5}	0.998	0.995
S_1	200	2000	0.1	1	12	0.15	I	1.000×10^{-2}	1.043×10^{-2}	0.972	0.932
S_2	200	2000	0.1	1	12	0.34	N_U^+	5.000×10^{-5}	5.034×10^{-5}	0.994	0.987
S_2	200	2000	0.1	1	12	0.34	N_U^+	1.000×10^{-2}	1.109×10^{-2}	0.912	0.822
S_3	200	2000	0.1	8	12	0.15	I	5.000×10^{-5}	5.000×10^{-5}	0.999	0.999
S_3	200	2000	0.1	8	12	0.15	I	1.000×10^{-2}	1.006×10^{-2}	0.984	0.979
S_4	200	2000	0.1	8	12	0.34	N_U^-	5.000×10^{-5}	5.013×10^{-5}	0.997	0.995
S_4	200	2000	0.1	8	12	0.34	N_U^-	1.000×10^{-2}	1.031×10^{-2}	0.952	0.924

Table 4.2: Systems investigated in this work and associated simulation parameters. N_s and N_c refer to the number of HSs and HBPs, respectively; d_s^* is the diameter of spherical tracers; L^* and W^* are the reduced cuboid length and width, respectively; $\eta^{pure} \approx \eta$ is the system packing fraction; $\delta t_{MC,s}$ and $\delta t_{MC,c}$ are the MC time steps of HSs and HBPs, respectively; and $\mathscr{A}_s$ and $\mathscr{A}_c$ are the MC acceptance rates of HSs and HBPs, respectively. The symbols N_U^+ and N_U^- refer to uniaxial prolate and oblate nematic phases, respectively. The systems are indexed according to the shape of the HBPs and the packing fraction. Systems that have the same settings, but different input MC time step, are given the same index.

We characterised the dynamics of the systems investigated by computing the mean square displacement (MSD), the non-Gaussian parameter (NGP), the apparent exponent of the generalized Einstein relation and the self-part of the Van-Hove distribution functions (s-VHF), averaging out over 90 different uncorrelated trajectories. All these properties were computed for both the HBPs and the HSs and for different components: the 3D position of the particles, i.e., $\mathbf{r}_{tot}$ with dimensionality $d = 3$, the components in the direction parallel and perpendicular to the nematic director in the N_U phases, i.e., $\mathbf{r}_\parallel$ with dimensionality $d = 1$ and $\mathbf{r}_\perp$ with $d = 2$, respectively, and along the three box axes in the I phases, $\mathbf{r}_x, \mathbf{r}_y, \mathbf{r}_z$, with $d = 1$. In the following, we use the symbol $\lambda = \{tot, \parallel, \perp, x, y, z\}$ to indicate that the dynamical properties of a given observable have been estimated in 1, 2 and 3 dimensions. The MSD is defined as the ensemble average of the particle dis-

placement from their original position at time 0:

$$\left\langle \Delta r_\lambda^2(t) \right\rangle = \frac{1}{N} \left\langle \sum_{i=1}^{N} \left\| \mathbf{r}_{\lambda,i}(t) - \mathbf{r}_{\lambda,i}(0) \right\|^2 \right\rangle. \tag{4.10}$$

The diffusion coefficients at long timescales are obtained from the MSD as follows:

$$D_{\lambda,long} = \frac{1}{2dt} \lim_{t\to\infty} \langle \Delta r_\lambda^2(t) \rangle. \tag{4.11}$$

Considering the generalised Einstein relation, where the MSD can have a nonlinear dependence on time, i.e., $\langle \Delta r_\lambda^2 \rangle = 2dD_\lambda t^{\beta_\lambda}$, we can define the apparent exponent β_λ as follows [43]:

$$\ln \langle \Delta r_\lambda^2 \rangle = \ln (2dD_\lambda) + \beta_\lambda \ln t, \tag{4.12}$$

$$\beta_\lambda = \frac{d \ln \langle \Delta r_\lambda^2 \rangle}{d \ln t}, \tag{4.13}$$

where β_λ describes deviations from a linear dependence of the MSD on time.

The probability distribution of particle displacements at time t, given their position at time 0 can be defined as

$$v_d G_{s,\lambda}(r,t) = \frac{1}{N} \left\langle \sum_{i=1}^{N} \delta \left(r - \left\| \mathbf{r}_{\lambda,i}(t) - \mathbf{r}_{\lambda,i}(0) \right\| \right) \right\rangle, \tag{4.14}$$

where $v_d G_{s,\lambda}(r,t)$ represents the probability that a particle i has displaced a distance r, in 1, 2 or 3 dimensions, from its initial position at time t. In particular, $G_{s,\lambda}$ are the s-VHFs, and v_d a normalization factor: $\int_0^\infty G_{s,\lambda}(r_\lambda,t) v_d dr_\lambda = 1$, where $v_1 = 1$ for the distributions parallel to the nematic director in the N_U phases or along $\hat{\mathbf{x}}, \hat{\mathbf{y}}, \hat{\mathbf{z}}$ in the I phases, $v_2 = 2\pi r$, and $v_3 = 4\pi r^2$. If $G_{s,\lambda}$ are Gaussian-distributed, the s-VHFs can be approximated as:

$$G_{s,\lambda}(r,t) = \frac{1}{\sqrt{\left(4\pi D_{\lambda,t} t\right)^d}} \exp\left(- \frac{r^2}{4D_{\lambda,t} t} \right), \tag{4.15}$$

where $D_{\lambda,t} = \langle \Delta r_\lambda^2(t) \rangle / 2dt$ is the instantaneous diffusion coefficient along the direction λ. It has been recently showed that, if the diffusion of the particle is anisotropic, Eq. (4.15) does not correctly estimate (deviations from) the Gaussianity of particle displacements in all the 3D space, i.e., when $\lambda = tot$, and a Gaussian distribution with an ellipsoidal

symmetry has been proposed [14].

Finally, the non-Gaussian parameter (NGP) expresses deviations from the expected Gaussian distribution of the displacements. A general formula for the NGP is:

$$\alpha_{2,d} = \frac{\langle \Delta r_\lambda^4(t) \rangle}{c_{2,d} \langle \Delta r_\lambda^2(t) \rangle^2} - 1. \tag{4.16}$$

The constant $c_{2,d}$ depends on the equivalence between the fourth moment, $\langle \Delta r_\lambda^4(t) \rangle$, and second moment, $\langle \Delta r_\lambda^2(t) \rangle$, of the Gaussian distribution of the displacements. For a perfect isotropic system, where there is no preferential direction for diffusion, the Gaussian distribution is spherical and the constant $c_{2,d} = (1 + 2/d)$, with $d = 1, 2, 3$. Eq. 4.16, first defined by Rahman [44], was initially employed in the analysis of experimental and simulation results to evaluate if the s-VHF and the self intermediate scattering function follow a normal distribution, as expected for fluids in the diffusive limit at long times. Positive values of $\alpha_{2,3}$ at intermediate times have been observed in simulation of liquid argon modelled with Lennard-Jones and Buckingham interaction potentials, caused by collision between particles and cage effects [45, 46]. The same parameter has been employed also to study the dynamical behaviour of colloidal suspensions of spherical [47, 48] and anisotropic shapes [49, 50], and it showed similar patterns previously observed in studies of atomic liquids. For systems with orientational anisotropy, with particles that tend to diffusive preferentially in a specific direction, a modification of the constant in Eq. 4.16 has been proposed, for a 3D particle displacement. The modified parameter $c'_{2,3}$ reads [14]

$$c'_{2,3} = \frac{3D_{\parallel,t}^2 + 8D_{\perp,t}^2 + 4D_{\parallel,t}D_{\perp,t}}{D_{\parallel,t}^2 + 4D_{\perp,t}^2 + 4D_{\parallel,t}D_{\perp,t}}. \tag{4.17}$$

4.3 Results and discussion

In this section, we study the dynamical properties of globular macromolecules immersed in colloidal suspensions of cuboids. The former are modelled as hard spherical tracers, while the latter as hard boards. Following standard MC simulations in the canonical ensemble, the complete set of uniaxial order parameters of the equilibrated systems were calculated and their values are summarised in Table 4.3.

We also computed the biaxial order parameters and no significant long-ranged biaxiality

Systems	Phase	U_T	U_W	U_L
S_1	I	0.020	0.020	0.025
S_2	N_U^+	0.255	0.256	0.962
S_3	I	0.031	0.021	0.023
S_4	N_U^-	0.943	0.250	0.252

Table 4.3: Average uniaxial order parameters relative to T, L, W of oblate and prolate HBPs in I ($\eta = 0.15$) and N_U ($\eta = 0.34$) phases. The results reported are obtained from standard MC simulations in the canonical ensemble, after equilibration of the systems and before running DMC simulations. Absolute errors are lower than 5×10^{-3}.

was detected, in agreement with previous works on monodispersed HBPs [24]. Additionally, inspection of the pair correlation functions and the snapshots of the equilibrated systems, respectively reported in Figs. 4.11, 4.12 and 4.13 of the Supporting information, does not reveal long-ranged positional ordering of HBPs, thus suggesting that smectic phases are not formed. We also note that the presence of spherical tracers does not affect the morphology of the phases observed in pure systems of HBPs at the same packing fractions. In order to ensure that the positional distribution of the spherical tracers is homogeneous in the entire volume of the systems simulated, we computed the HS - HS radial distribution functions (Fig. 4.1) and the density profile of the HS along the $\hat{\mathbf{x}}, \hat{\mathbf{y}}, \hat{\mathbf{z}}$ directions of the reference axes (Fig. 4.2). The density profile was computed as the average number of HS found in a slab, i.e., $\rho_r = \langle N_s \rangle_{\text{slab}} / V_{\text{slab}}$, with $V_{\text{slab}} = V^{2/3} \Delta r$ for Δr oriented in the three directions of the box frame, normalised by the density of the tracers all over the box, i.e., N_s/V. All the one-particle distributions along the reference axes are flat and equal to the numeral density of the tracers, clearly proving that the tracers are homogeneously distributed. In addition, all the HS - HS radial distribution functions decay to unity at short distances, proving that the position of the tracers is completely uncorrelated in all the systems.

4.3.1 Dynamical properties

Fig. 4.3 depicts the MSD, NGP and apparent exponent of prolate ($W^* = 1$) and oblate ($W^* = 8$) HBPs in N_U phases in the directions parallel and perpendicular to the nematic director. The dynamics of HBPs is anisotropic as the distinct dependence of $\langle \Delta r_\parallel^2 \rangle$ and $\langle \Delta r_\perp^2 \rangle$ on time reveals. However, an analogous sequence of dynamical regimes is observed for all the cases studied. At short times, HBPs diffuse within the cage formed

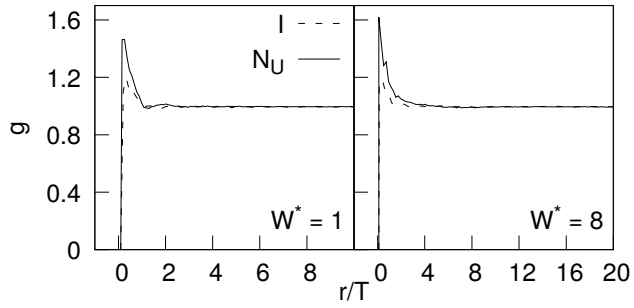

Figure 4.1: HS - HS Radial distribution functions in I (dashed lines) and N_U (straight lines) phases of prolate (left panel) and oblate (right panel) HBPs. The flat profile of the radial distribution functions from short radius proves the uncorrelation of the relative position of the spherical tracers for all the systems investigated.

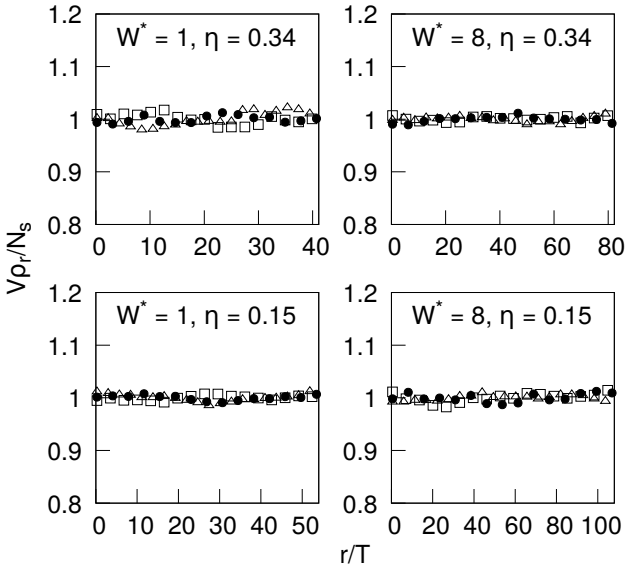

Figure 4.2: Profile of the average numeral density of HS in slabs, i.e., ρ_r, normalized by the numeral density of the HS in the entire box, i.e., N_s/V, for all the systems investigated. The slabs have volume $V^{2/3}\Delta r$, where Δr is oriented along $\hat{\mathbf{x}}$ (△), along $\hat{\mathbf{y}}$ (•) and along $\hat{\mathbf{z}}$ (□). Flat profiles prove that the spherical tracers are homogeneously distributed.

by nearby particles, rattling around their initial location and not yet interacting with their neighbours. At this stage, the MSD is linear with time. At slightly larger times, the effect of this cage fully develops as diffusion is slowed down due to the collisions with the surrounding particles, resulting in a nonlinear MSD with time. Finally, the expected Brownian motion sparks at sufficiently long time scales, when the MSD recovers its linear dependence on time.

According to Fig. 4.3, the MSD perpendicular to $\hat{\mathbf{n}}$ is larger than its parallel counterpart at short times. This is caused by the higher dimensionality in the displacements perpendicular to $\hat{\mathbf{n}}$ ($d = 2$) compared to those parallel to it ($d = 1$). At intermediate times, a

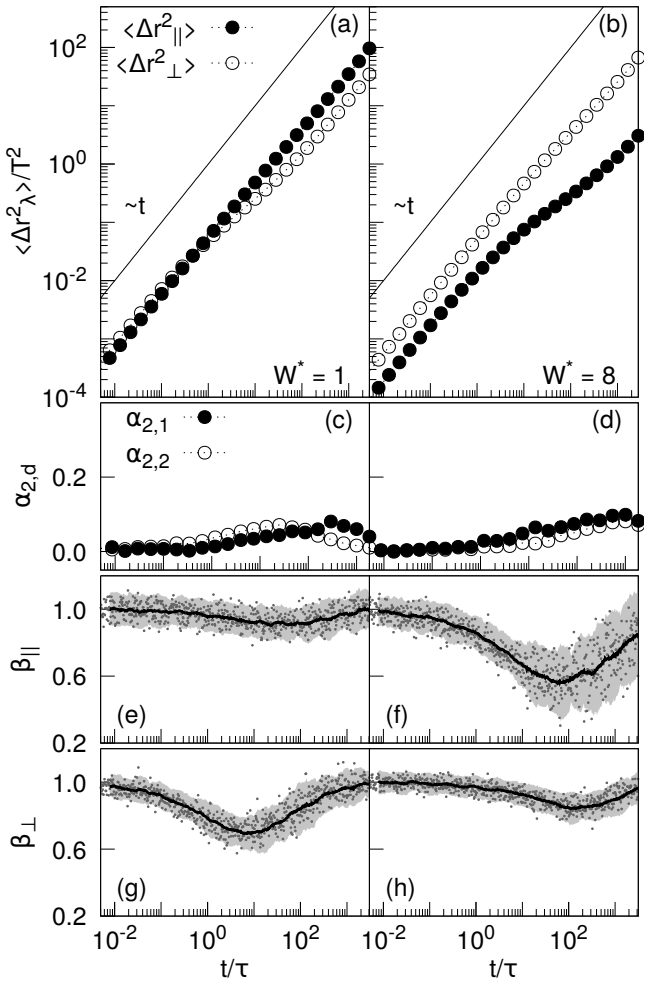

Figure 4.3: MSDs (a,b) and NGPs (c,d) of HBPs in the direction parallel (•) and perpendicular (◦) to $\hat{\mathbf{n}}$ in prolate (left) and oblate (right) nematic phases, at packing fraction $\eta = 0.340$. Frames (e) to (h) report the instantaneous values (dots), average (thick line) and twice its standard deviation (gray-shaded area) of the apparent exponents $\beta_\parallel$ and $\beta_\perp$. Solid lines in panels (a) and (b) show the linear regime where $\langle \Delta r_\lambda^2 \rangle / T^2 = t/\tau$, as a guide to the eye.

sub-diffusive behaviour is observed for both prolate and oblate HBPs, which depends on the preferential orientation of the nematic phases and particle anisotropy. While HBPs in the N_U^+ phase ($W^* = 1$) are predominantly oriented along the axis parallel to their length L and move preferentially along $\hat{\mathbf{n}}$ (solid circles in Fig. 4.3(a)), particles in the N_U^- phase ($W^* = 8$) are mostly oriented along their thickness T and their motion along $\hat{\mathbf{n}}$ is hampered (solid circles in Fig. 4.3(b)). Prolate HBPs also experience a similar slow down in planes perpendicular to $\hat{\mathbf{n}}$, but this effect is significantly less pronounced. Finally, at long times, the particles enter a new diffusive regime in which $\langle \Delta r_\lambda^2 \rangle$ recovers its linearity with time. All these observations can be further appreciated by the evolution of the apparent exponents $\beta_\parallel$ and $\beta_\perp$ in Figs. 4.3(e) and 4.3(g) for prolate HBPs and Figs. 4.3(f)

and 4.3(h) for oblate HBPs, respectively. In the direction along which the particle motion is especially hampered, β_λ shows larger deviations from 1 (the Fickian-like value), corresponding to a sub-diffusive behaviour and the formation of temporary cages. The most relevant sub-diffusive regime is observed in systems of oblate HBPs in the direction parallel to $\hat{\mathbf{n}}$, where $\beta_\parallel \sim 0.6$ at $t/\tau \sim 100$. The NGP of prolate and oblate HBPs are shown in panels (c) and (d) of Fig. 4.3, respectively, along $\hat{\mathbf{n}}$ and perpendicularly to it. Although a subtle growth of the NGP is observed in all systems, its maximum value is relatively low as it does not exceed 0.1. For comparison, the NGP of hard spherocylinders in smectic phases was reported to be between 3 at $\eta = 0.508$ and 7 at $\eta = 0.557$ in the direction of $\hat{\mathbf{n}}$ [51]. This suggests that the dynamics in nematic LC phases of HBPs is basically Gaussian-like as also reported in a recent work [28]. To better understand the effect of particle geometry on the mobility of HBPs in nematic LCs, we have calculated the long-time translational diffusion coefficients, which are listed in Table 4.4. One can observe that, as the particle width increases, the diffusion coefficient parallel to $\hat{\mathbf{n}}$ decreases significantly. Upon increasing W^*, the probability of HBPs to collide with their neighbours increases as well, which in turn slows down the overall mobility. The opposite effect occurs for diffusion coefficients perpendicular to $\hat{\mathbf{n}}$ where a small increment is observed when the width of the HBPs increases. Our MSDs and diffusion coefficients are in excellent quantitative agreement with those reported by Cuetos and Patti in systems of pure HBPs [28]. This agreement suggests that the presence of spherical tracers does not affect the dynamics of HBPs in N_U^+ or N_U^- phases.

Systems	$D_{\parallel,long}{D_0}^{-1}$	$D_{\perp,long}{D_0}^{-1}$
S_2	1.7×10^{-2}	3.1×10^{-3}
S_4	4.8×10^{-4}	5.9×10^{-3}

Table 4.4: Long-time translational diffusion coefficients of HBPs parallel and perpendicular to $\hat{\mathbf{n}}$ in N_U phases of HBPs, at packing fraction $\eta = 0.34$ for both systems. The absolute errors are lower than half of the last significant digit.

In the light of these considerations on the dynamics of HBPs, we now examine the dynamics of the dispersed HSs. In Fig. 4.4, we show their MSDs, NGPs and apparent exponents in N_U phases of prolate (left panels) and oblate (right panels) HBPs. Due to their relatively small size, spherical tracers are expected to explore the available space more effectively than HBPs. This is indeed confirmed by their MSDs, which are larger

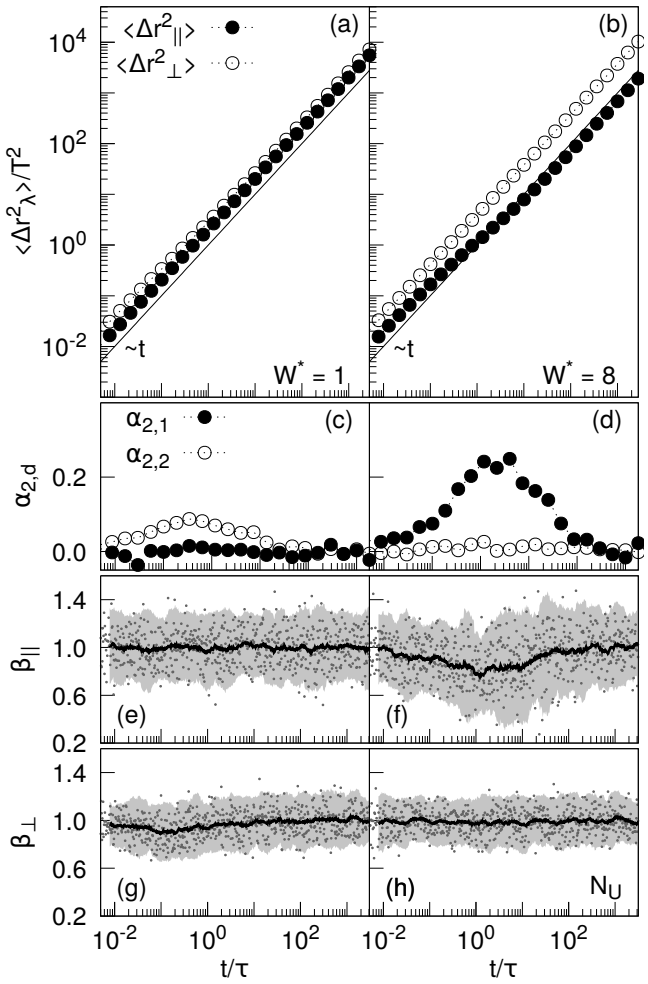

Figure 4.4: MSDs (a,b) and NGPs (c,d) of HSs in the direction parallel (•) and perpendicular (◦) to $\hat{\mathbf{n}}$ in prolate (left) and oblate (right) nematic phases of HBPs, at packing fraction $\eta = 0.340$. Frames (e) to (h) report the instantaneous values (dots), average (thick line) and twice its standard deviation (gray-shaded area) of the apparent exponents $\beta_\parallel$ and $\beta_\perp$. Solid lines in panels (a) and (b) show the linear regime where $\langle \Delta r_\lambda^2 \rangle / T^2 = t/\tau$, as a guide to the eye.

than those of HBPs at all time scales. These results are also in agreement with Brownian dynamics simulations of mixtures of spheres of different sizes [42, 52]. The MSDs of the spherical tracers have a behaviour similar to that observed for HBPs: a linear behaviour at short and long times, and a very soft, almost negligible sub-diffusive behaviour at intermediate times. As the geometry of HBPs changes from prolate (Fig. 4.4(a)) to oblate (Fig. 4.4(b)), the sub-diffusive regime of $\langle \Delta r_\parallel^2 \rangle$ becomes more evident, while no changes are practically detected in $\langle \Delta r_\perp^2 \rangle$. These tendencies can be better appreciated by analysing the NGPs in Figs. 4.4(c) and 4.4(d). While the peak of $\alpha_{2,2}$ vanishes from $\mathrm{N_U^+}$ to $\mathrm{N_U^-}$, the peak of $\alpha_{2,1}$ increases, indicating more pronounced deviations from Gaussianity in nematic LCs of oblate HBPs. Interestingly, while the peak of $\alpha_{2,2}$ in the $\mathrm{N_U^+}$ phase occurs

at $t/\tau \sim 0.4$ and is lower than 0.1, confirming the substantially Gaussian dynamics of tracers in prolate nematics, the peak of $\alpha_{2,1}$ in the N_U^- phase, observed at $t/\tau \sim 3.3$, is significantly larger and approximately equal to 0.3. This result indicates that long-range ordering can have a relevant influence on macromolecular diffusion as not only does it establish preferential paths of mobility, but it can also affect the nature of these paths by inducing deviations from Gaussianity, at least at intermediate times. At long time scales, the NGPs decay to zero and, correspondingly, the MSDs end up displaying Fickian behaviour. The cage effect exerted by the neighboring HBPs determine the transient sub-diffusive regimes. This cage provides a barrier against diffusion of both HBPs and guest molecules. Due to their smaller size and increased mobility as compared to HBPs, the spherical tracers perceive the effect of the surrounding cage at shorter times and over a shorter time interval than HBPs, as the position and broadness of the peak of the NGPs in panels (c) and (d) of Fig. 4.3 with respect to those in Fig. 4.4 reveal. The analysis of the HSs' apparent exponents in Fig. 4.4(e-h) suggests that the tracers maintain a Fickian-like diffusion at all times. The only exception is detected in the N_U^- phase for diffusion along $\hat{\mathbf{n}}$, where $\beta_\parallel < 1$ for $t < 10^2\tau$. Such a temporary non-Fickian and non-Gaussian dynamics is also observed in the host phase (see Fig. 4.3(f)). The main difference between the dynamics of host and guest particles, in this case, is in the peak of $\alpha_{2,1}$, which is larger for HSs than for HBPs. This is not surprising if one considers that HSs are mostly surrounded by oblate HBPs whose dynamics, relatively slow in the direction of $\hat{\mathbf{n}}$, slows down the diffusion of HSs, rather abruptly, after the initial diffusive regime. Parallel and perpendicular long-time diffusion coefficients of HSs, obtained with Eq. 4.11, are listed in Table 4.5.

Systems	$D_{\parallel,long}D_0{}^{-1}$	$D_{\perp,long}D_0{}^{-1}$
S_2	9.9×10^{-1}	6.4×10^{-1}
S_4	3.5×10^{-1}	9.0×10^{-1}

Table 4.5: Long-time translational diffusion coefficients of HSs parallel and perpendicular to $\hat{\mathbf{n}}$ in N_U phases of HBPs, at $\eta = 0.34$. Absolute errors are smaller than half of the last significant digit.

While, in prolate nematics, spherical tracers diffuse faster in the direction of $\hat{\mathbf{n}}$ than perpendicularly to it, with $D_{\parallel,long} \approx 1.55 D_{\perp,long}$, in oblate nematics this tendency changes dramatically as the parallel diffusion becomes significantly slower than the perpendic-

ular diffusion, with $D_{\parallel,long} \approx 0.39 D_{\perp,long}$. Such a dependence of the dynamics of HSs on the geometry of the host HBPs and, ultimately, on the symmetry of the nematic phase, reveals a close analogy with the diffusion of HBPs, which is faster along $\hat{\mathbf{n}}$ in the N_U^+ phase and perpendicularly to it in the N_U^- phase (see Table 4.4). This result suggests that the anisotropic mobility of guest HSs is closely controlled by the dynamics of host HBPs. We notice that the decoupling of the dynamics of our spherical tracers as a result of the space anisotropy determined by the host cuboids, exhibits common characteristics with the dynamics of apoferritin, a globular protein generally found in the intestinal membrane, in I and N suspensions of *fd* viruses at different concentrations [53, 54]. The time evolution of the self-Van Hove functions of HSs in prolate and oblate nematic phases is presented, respectively, in the left and right frames of Fig. 4.5.

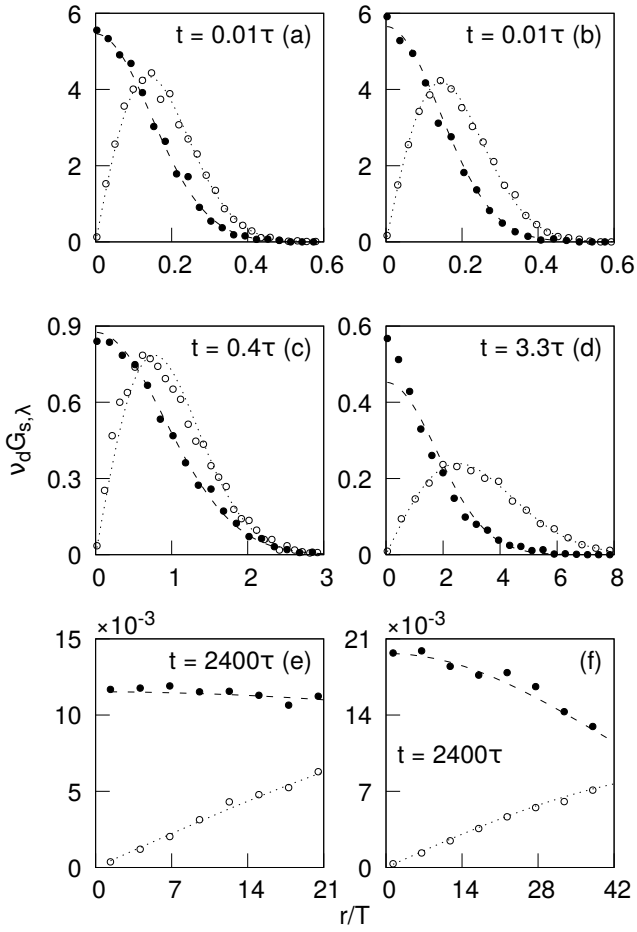

Figure 4.5: Self-Van Hove distributions of HSs in nematic phases of HBPs with $W^* = 1$ (panels (a), (c) and (e)) and $W^* = 8$ (panels (b), (d) and (f)), at $\eta = 0.340$, at different times. Histograms obtained from simulations are plotted as points for the components parallel (•) and perpendicular (◦) to $\hat{\mathbf{n}}$. Dashed and dotted lines refer to the theoretical Gaussian distributions obtained from Eq. 4.15 for the directions parallel and perpendicular to $\hat{\mathbf{n}}$, respectively.

For each phase, we show the s-VHFs at three different times: (*i*) $t/\tau = 0.01$ (frames (a) and (b)), being a representative time for short-time diffusion in both phases; (*ii*) $t/\tau = 0.4$ (frame (c)) and $t/\tau = 3.3$ (frame (d)), which pinpoint the crossover from short- to long-time diffusion in prolate and oblate nematics, respectively; and (*iii*) $t/\tau = 2400$ (frames (e) and (f)), which is a representative time of the long-time diffusive regime. Parallel and perpendicular s-VHFs were also estimated with the Gaussian approximation of Eq. 4.15 with $d = 1$ and 2, respectively. These Gaussian distributions are also plotted in Fig. 4.5 as dotted and dashed lines. As a general tendency, the distribution of displacements as obtained from simulations is practically Gaussian at short and long times, while small deviations are detected at intermediate times, especially in the N_U^- phase (frame (d) in Fig. 4.5). In this case, the Gaussian approximation significantly sub-estimates the probability of HSs to remain in their original position or very close to it at $t/\tau = 3.3$. This implies that there are more *slow* tracers than those a Gaussian distribution would predict. By contrast, the probability of observing *fast* tracers, given by the tail of the s-VHFs at large distances, is approximated very well by a Gaussian distribution across the six time decades simulated here and in both N_U^+ and N_U^- phases. We also notice that, at long times, the Fickian-like dynamics of our model globular macromolecules is also Gaussian, again discarding the ubiquity of Fickian yet non-Gaussian diffusion in soft-matter systems [14, 28].

To better understand how the long-range orientational ordering of nematics influences macromolecular diffusion, we have also investigated the dynamics of our tracers in I phases of HBPs. We firstly notice that the MSDs and NGPs of both host and guest species along the three space directions (shown in Figs. 4.14 and 4.15 of the Supporting information) reveal the same quantitative behaviour and confirm the absence of any preferential direction of motion. Consequently, it makes sense to limit our analysis only to the total MSD ($\langle \Delta r_{tot}^2 \rangle$) and NGP ($\alpha_{2,3}$). Both properties are reported, along with the total apparent exponent (β_{tot}), in Figs. 4.6 and 4.7 for HBPs and HSs, respectively. More specifically, Fig. 4.6 displays these three dynamical properties in I and N_U phases of prolate (left frames) and oblate (right frames) HBPs. At short times, the dynamics of HBPs results to be unaffected by the degree of local ordering, if any, as the total MSDs in the I and N_U phases, shown in Figs. 4.6(a) and 4.6(b), are practically identical. This is not surprising as, at these short time scales, HBPs are still rattling around their original po-

sition and do not yet perceive the presence and degree of ordering of their neighbours. At longer time scales, the MSD slightly deviates from its linear behaviour with time and

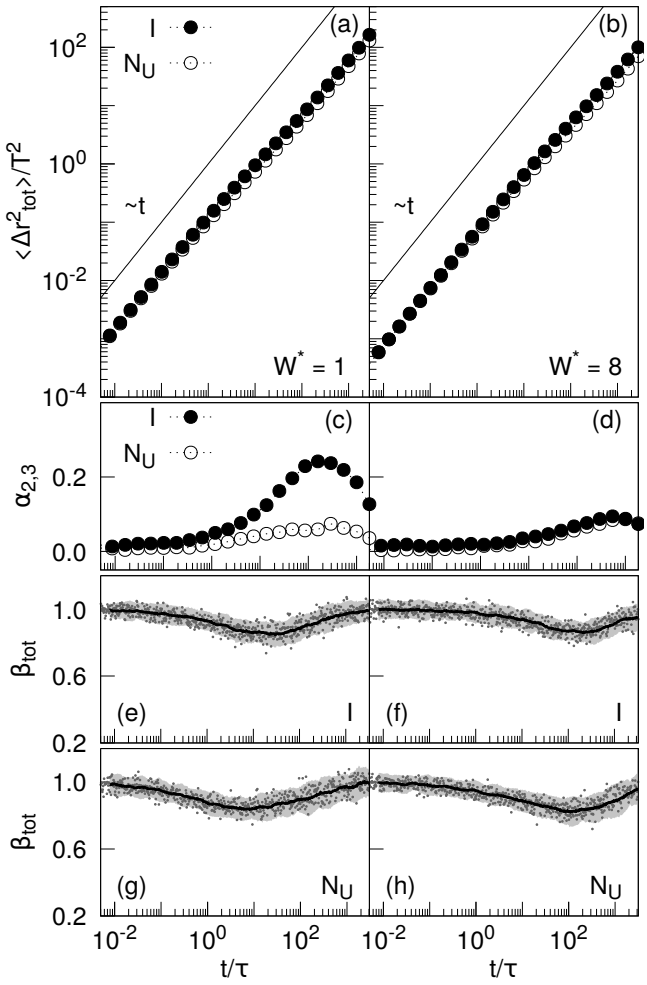

Figure 4.6: Total MSDs (a-b), NGPs (c-d) and apparent exponents (e-h) of prolate (left) and oblate (right) HBPs in I (•), at $\eta = 0.150$, and N_U phases (◦), at $\eta = 0.340$. Solid lines in panels (a) and (b) show the linear regime where $\langle \Delta r_\lambda^2 \rangle / T^2 = t/\tau$, as a guide to the eye. NGPs in (c) and (d) are computed using Eq. 4.16 for HBPs in I phases (•), with $c_{2,3} = 5/3$, and for HBPs in N_U phases (◦), with $c'_{2,3}$ from Eq. 4.17. Frames (e-h) report the instantaneous values (dots), average (thick line) and twice its standard deviation (gray-shaded area) of the apparent exponent.

enters a sub-diffusive regime. At this stage, HBPs start to collide with each other and their dynamics slow down. Such a temporary cage effect is more effectively appreciated by analysing $\alpha_{2,3}$ (Fig. 4.6(c-d)) and β_{tot} (Fig. 4.6(e-h)). The apparent exponent presents very similar trends at $W^* = 1$ and 8, with deviations from unity that do not depend on the background ordering. Because β_{tot} is a measure of the instantaneous Fickianity of the diffusion, these features and the analogies between the dynamics in I and N_U phases, are also observed in the MSDs at intermediate and long time scales. Especially intriguing

is the analysis of the NGPs, reported in Fig. 4.6(c) and 4.6(d). Oblate HBPs show almost indistinguishable NGPs in both I and N_U^- phases and across the three time regimes, with a very small peak at $t/\tau \approx 500$. A very similar trend is also observed for prolate HBPs, but only in the N_U^+ phase (empty circles in frame (c)). The NGP of prolate HBPs in the I phase exhibits a peak that is located at slightly earlier times ($t/\tau \approx 200$) and is surprisingly larger than any other. Because deviations from Gaussianity usually increase with system packing [55, 56, 57, 58], it is quite remarkable to find a family of particles that inverts this tendency when compressed from the I to the N_U^+ phase. We remind the reader that $\alpha_{2,3}$ of a N_U phase is estimated using the modified parameter $c'_{2,3}$ defined in Eq. 4.17, which assumes an anisotropic particle displacement with respect to the nematic director, while $c_{2,3} = 5/3$ is used for I phases, as expected for particles moving in systems with spherical symmetry. We have analysed the origin of this atypical behaviour and found that it is most probably determined by the occurrence of randomly-oriented nematic-like clusters in the I phase. A detailed discussion is provided in Section 4.3.2.

In Fig. 4.7, we report the total MSDs, NGPs and apparent exponents of the spherical tracers in I and N_U phases of prolate (left frames) and oblate (right frames) HBPs. The three sets of observables suggest a Fickian and Gaussian dynamics across the whole time scales and in both phases. These results might appear in contradiction with those reported in Fig. 4.4, showing sub-diffusive, non-Gaussian dynamics at intermediate time scales in the direction parallel to $\hat{\mathbf{n}}$ in the N_U^- phase. Nevertheless, spherical tracers move preferentially in planes perpendicular to $\hat{\mathbf{n}}$ as the difference between the MSDs measured in Fig. 4.4(b) indicates. Consequently, although the dynamics along $\hat{\mathbf{n}}$ deviates from Brownian diffusion over a relevant period of time, these deviations are averaged out when one computes $\langle \Delta r^2_{tot} \rangle$, $\alpha_{2,3}$ and β_{tot}. It is only by decoupling the HSs' dynamics according to the background anisotropy imposed by the host phase that we are able to detect the full picture and appreciate elements that otherwise would go underground. The total long-time diffusion coefficients, $D_{tot,long}$, of HBPs and HSs in the I and N_U phases are calculated by using Eq. 4.11 with $d = 3$ and summarised in Table 4.6. Increasing the system packing has a negative effect on the mobility of HSs and HBPs by substantially decreasing the free space available for diffusion. Consequently, the long-time diffusion coefficient of HBPs in N_U phases is $\sim 20-30\%$ smaller than that measured in the I phases (systems S_1 *vs* S_2 and S_3 *vs* S_4).

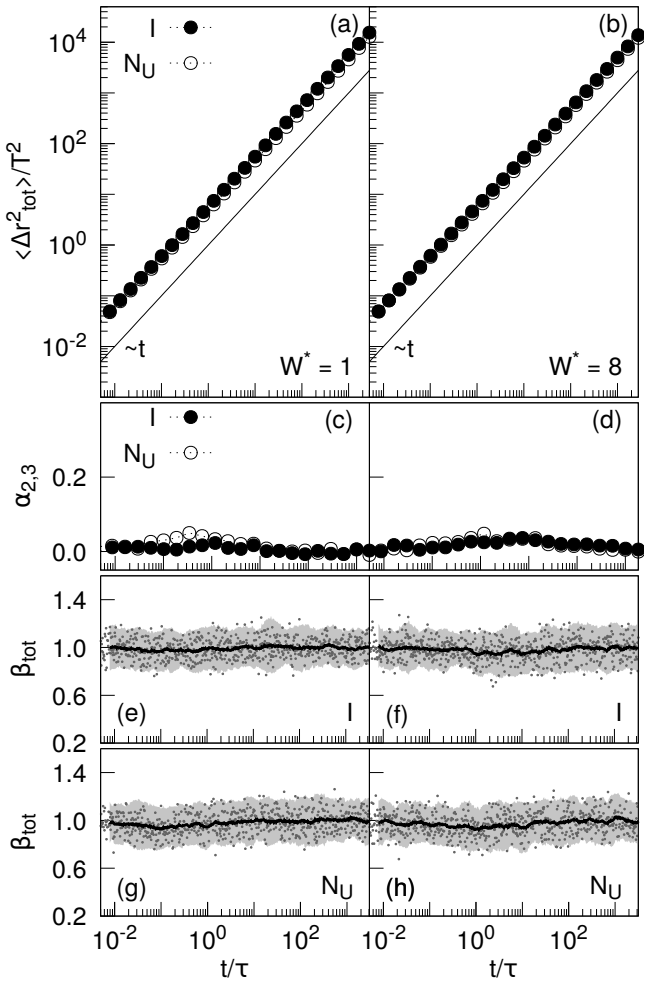

Figure 4.7: Total MSDs (a-b), NGPs (c-d) and apparent exponents (e-h) of HSs in I (•) and N_U phases (◦) of prolate (left frames) and oblate (right frames) HBPs. Both I phases have a packing fraction of $\eta = 0.150$, while both N_U phases have a packing fraction of $\eta = 0.340$. Solid lines in panels (a) and (b) show the linear regime where $\langle \Delta r_\lambda^2 \rangle / T^2 = t/\tau$, as a guide to the eye. NGPs in (c) and (d) are computed using Eq. 4.16 for HSs in I phases (•), with $c_{2,3} = 5/3$, and for HSs in N_U phases (◦), with $c'_{2,3}$ from Eq. 4.17. Frames (e-h) report the instantaneous values (dots), average (thick line) and twice its standard deviation (gray-shaded area) of the apparent exponent.

Systems	$D_{tot,long}{D_0}^{-1}$, HBPs	$D_{tot,long}{D_0}^{-1}$, HSs
S_1	9.7×10^{-3}	9.3×10^{-1}
S_2	7.7×10^{-3}	7.6×10^{-1}
S_3	5.7×10^{-3}	8.1×10^{-1}
S_4	4.1×10^{-3}	7.2×10^{-1}

Table 4.6: Total long-time translational diffusion coefficients of HBPs and HSs, in I ($\eta = 0.15$ for systems S_1 and S_3) and N_U ($\eta = 0.34$ for systems S_2 and S_4) phases of HBPs. Absolute errors are smaller than half of the last significant digit.

A slightly less strong effect is observed in the case of the HSs, whose long-time diffusivities in the N_U phases are $\sim 10-20\%$ smaller than those in the I phase.

4.3.2 Cluster formation in isotropic phases of HBPs

To throw light on the origin of the intriguing non-Gaussian dynamics of prolate HBPs observed in the I phase at intermediate time scales, we first compare the results obtained in isotropic mixtures at $\eta = 0.15$ with those of pure systems of HBPs at $\eta = \{0.07, 0.15, 0.20\}$. At each of these packing fractions, we kept the total number of cuboids equal to $N = 2000$ and particle thickness and length constant to T and $12T$, respectively, and varied particle width. In particular, we confirmed $W^* = 1$ and 8 to mimic prolate and oblate HBPs, respectively, and added $W^* = \sqrt{L^*} \approx 3.46$ for self-dual shaped HBPs, a geometry exactly in between the oblate and prolate shape. The so-defined nine systems were all in the I phase. In the I mixtures of Fig. 4.6, deviations from Gaussian dynamics, where $\alpha_{2,3} > 0$, become significant at $t/\tau > 1$ for $W^* = 1$ and $t/\tau > 10$ for $W^* = 8$. To explore the same time scales in pure systems of HBPs, we set the MC time step to $\delta t_{MC,c} = 1.0 \times 10^{-2}$. The resulting MSDs and NGPs are shown, respectively, in the top and bottom frames of Fig. 4.8. As expected, the MSDs corresponding to the same particle geometry collapse on a single curve at short times, when the effect of packing is still negligible. As time increases, a moderate deviation from the linear regime is observed at all concentrations, with the long-time MSD decreasing with increasing system packing. This decrease in MSD with packing correlates very well with the increase in the peak of the NGP. While prolate HBPs exhibit a relatively pronounced non-Gaussianity at $\eta = 0.15$ and 0.20 (see frame (d) in Fig. 4.8), the NGP of self-dual and oblate HBPs is less significant at all packing fractions, suggesting a quasi-Gaussian dynamics.

Typically, large values of the NGP at intermediate time scales stem from the occurrence of transient cages. If the morphology of these cages followed a common pattern, independent from their location in the system, deviations from a Gaussian behaviour would be very limited, even at large system densities. In N_U phases, HBPs are almost perfectly aligned as the large values of their order parameters confirms [24]. This suggests that cages are very similar to each other, being the random orientation of the particle minor axes possibly the only discerning feature. By contrast, in I phases, particles are randomly oriented and, if the resulting NGP is large, such a structural randomness must

be somehow transferred to their dynamics. In I phases of 4-n-hexyl-4'-cyanobiphenyl, a prolate molecule able to form LCs, the occurrence of anomalous diffusion was ascribed to the presence of cages comprising molecules that tend to align in the direction of their longitudinal axis [59]. If this picture holds at the colloidal scale, one might expect the occurrence of clusters of similarly oriented HBPs with broad enough size and shape distributions to spark non-Gaussian dynamics. To test these intuitions, we have verified whether clusters actually exist in the I phase. To this end, following past works on the nucleation of crystals and nematic LCs in systems of colloidal rods [60, 61], we defined a criterion able to identify nematic-like clusters in I phases. According to this criterion, two HBPs i and j belong to the same cluster if their relevant axes ($\hat{\mathbf{e}}_L$ for prolate and $\hat{\mathbf{e}}_T$ for oblate HBPs) are sufficiently aligned. For prolate HBPs, $|\hat{\mathbf{e}}_{L,i} \cdot \hat{\mathbf{e}}_{L,j}| > K_1$. Additionally, the resulting order parameter of this cluster should be larger than a threshold value, i.e., $U_{L,local} > K_2$. Finally, i and j should be close enough along the cluster's nematic director, $\hat{\mathbf{n}}_{local}$, and perpendicularly to it, i.e., $\|\mathbf{r}_{i,j}^{\parallel}\| < K_{\parallel,3}$ and $\|\mathbf{r}_{i,j}^{\perp}\| < K_{\perp,3}$. The threshold values, K_1, K_2, $K_{\parallel,3}$ and $K_{\perp,3}$, were first optimised to identify a cluster containing at least 95% of HBPs in an N_U phase. The parameters optimised with this procedure are listed in Table 4.7, for both oblate and prolate HBPs.

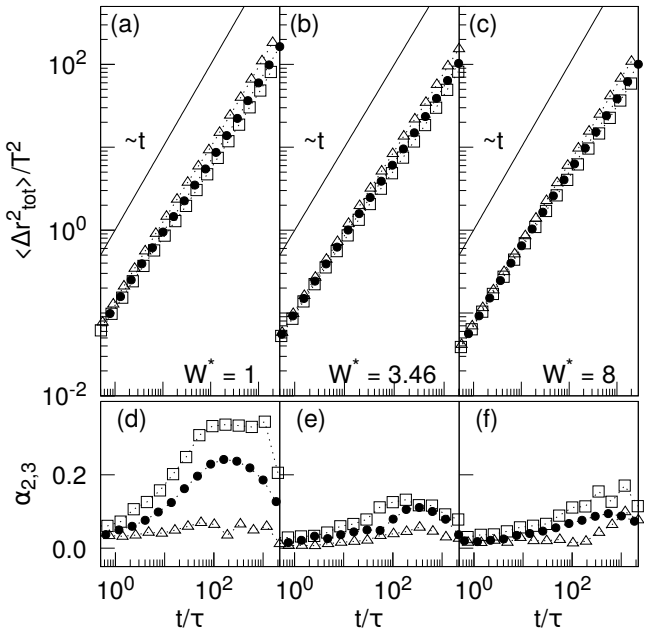

Figure 4.8: Total MSDs (top frames) and corresponding NGPs (bottom frames) in I phases of pure HBPs of different shape anisotropy. Empty triangles (△), solid circles (•) and empty squares (□) refer to packing fractions $\eta = 0.07$, 0.15 and 0.20, respectively. Solid lines in frames (a-c) show the linear regime where $\langle \Delta r_\lambda^2 \rangle / T^2 = t/\tau$, as a guide to the eye.

Parameters	$W^* = 1$	$W^* = 8$
K_1	0.85	0.85
K_2	0.90	0.90
$K_{\parallel,3}$	12.25	1.32
$K_{\perp,3}$	1.55	13.00

Table 4.7: Optimised parameters for nematic-like cluster identification in I phases. The parameterisation procedure has been performed in N_U phases of prolate and oblate HBPs at $\eta = 0.34$ (see text for details).

We then applied this criterion in I phases of prolate and oblate HBPs to ponder the existence of nematic-like clusters and estimate their size distribution. Results are shown in Fig. 4.9 for both prolate and oblate HBPs at the three packing fractions studied. Most clusters contain no more than $n = 5$ particles at the largest system density and this number reduces to $n = 2$ in very dilute I phases. While at low particle concentrations the average cluster size, $\langle N_n \rangle$, decays rapidly with n, the cluster size distribution becomes broader as the particle concentration increases. Consequently, as system packing increases, more and larger clusters are observed. Cluster distributions of prolate and oblate systems are very similar and, excluding the more dilute suspension at $\eta = 0.07$, prolate HBPs are slightly more prone to form clusters as the density increases. Differences in cluster formation can be better appreciated from the average total number of clusters, i.e., $\langle N_{tot} \rangle$, which reveals a larger number of clusters formed in systems of prolate HBPs at sufficiently large packing. To assess whether the orientation of the clusters is isotropic, we estimated the orientational distributions of the local nematic director along the Cartesian coordinates $\hat{\mathbf{x}}, \hat{\mathbf{y}}, \hat{\mathbf{z}}$. Our results revealed that clusters are randomly oriented, with a uniform distribution of their directors (see Fig. 4.16 in Supporting information). Illustrative examples of nematic-like clusters forming in I phases are reported in Fig. 4.10 for prolate HBPs at $\eta = 0.20$ and in Fig. 4.17 for oblate HBPs at $\eta = 0.20$. The structure of the clusters in the snapshots suggest that the shape and size of the HBPs affect also the morphology of the clusters: prolate particles form prolate-like clusters, while oblate particles seem to arrange in oblate-structured clusters. Additionally, we observe that the presence of spherical tracers does not seem to play a significant role in the formation of clusters. This is evinced from the monotonic behaviour of many of the properties analysed with respect to density, together with uniform distributions of HSs observed in Fig. 4.1. However, we stress that we have only investigated this effect

at $\eta = 0.150$, while at the remaining packing fractions the formation of clusters was analysed in pure systems of HBPs. A more thorough investigation of the dynamics of the clusters in the presence of spheres is necessary to address their stability over time in I phases.

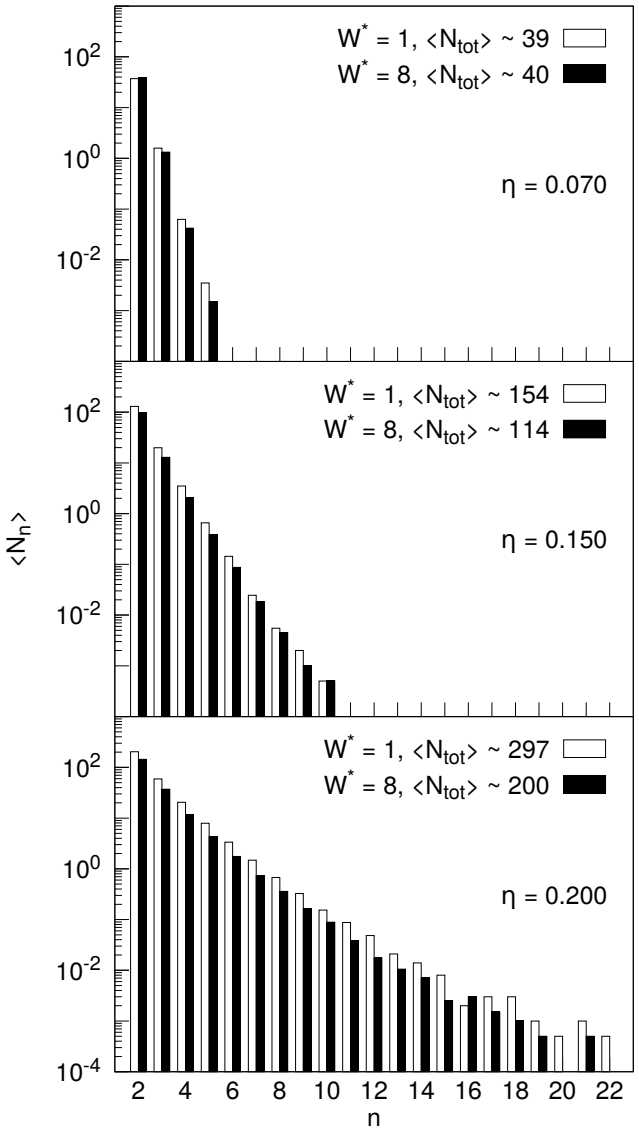

Figure 4.9: Average number of clusters $\langle N_n \rangle$ containing n HBPs with $W^* = 1$ (empty bars) and $W^* = 8$ (solid bars). All particle systems are made of $N = 2000$ HBPs forming I phases at packing fractions $\eta = 0.07$ (top frame), 0.15 (middle frame), and 0.20 (bottom frame). In the panel legend is reported the average number of clusters found in a sample configuration, i.e., $\langle N_{tot} \rangle$.

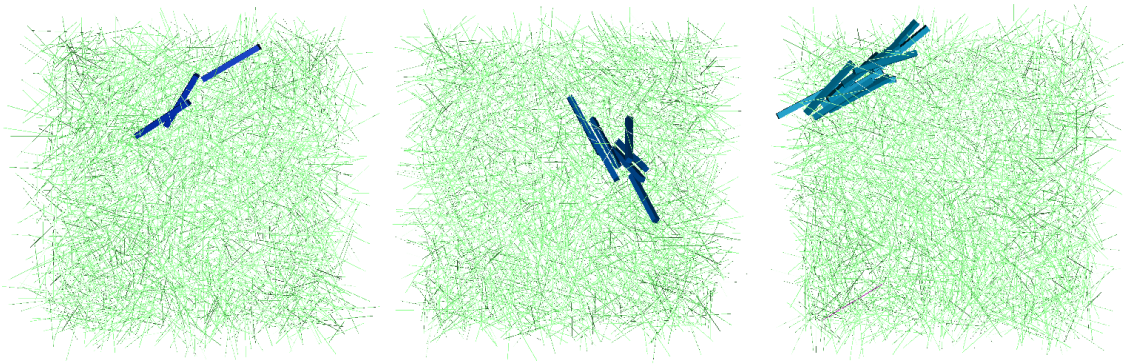

(a) (b) (c)

Figure 4.10: Snapshots of HBPs with $W^* = 1$ in I phase with packing fraction $\eta = 0.20$. While clusters of sizes 3 (a), 7 (b) and 11 (c) are highlighted in blue, the remaining particles are represented as green lines.

4.4 Conclusions

In summary, we have analysed the dynamics of globular macromolecules, modeled as hard spherical tracers, in isotropic and nematic suspensions of colloidal HBPs. To this end, we have implemented DMC simulations, which allow one to replicate the Brownian motion of particles and cover a broad range of timescales. The small size of HSs compared to HBPs does not affect the structural and dynamical properties of the host phase, at least at the concentrations considered in this work. The MSD of HBPs and the corresponding apparent exponents, which measure the deviations from Fickian diffusion, show three distinct regimes: a linear behaviour of the MSD with time at short and long timescales, and a nonlinear trend at intermediate times representing sub-diffusive dynamics. This sub-diffusive behaviour develops simultaneously to the onset of deviations from Gaussian dynamics. The MSD parallel to the nematic director exhibits a more pronounced sub-diffusive region in systems of oblate HBPs. An opposite tendency is detected in systems of prolate HBPs. Consequently, prolate HBPs diffuse faster along $\hat{\mathbf{n}}$, whereas oblate HBPs diffuse faster in the direction perpendicular to $\hat{\mathbf{n}}$. This overall behaviour dominates the diffusion of guest HSs. On the one hand, while the NGPs of HSs perpendicular to $\hat{\mathbf{n}}$ vanish with increasing particle width, parallel NGPs increase. On the other hand, the tracers qualitatively replicate the changes in diffusion coefficients with the geometry of the host HBPs. As W^* increases, the diffusivities of HSs parallel and perpendicular to the $\hat{\mathbf{n}}$ decrease and increase, respectively. This indicates that the diffusion of tracers depends on the structural organization of the systems in which they displace,

and anisotropic suspensions of surrounding particles make the diffusion of the tracers anisotropic, with the formation of temporary cages only along specific directions.

The packing fraction, the size and the shape of the HBPs guide the suspension to the formation of preferential orientations and structures, which enable preferential pathways for the tracers' diffusion. The s-VHFs of the tracers deviate slightly from the theoretical Gaussian distribution only at the same time where the correspondent NGPs > 0 and reach local maxima. The comparison of the total diffusion of HSs between I and N_U phases showed that larger system densities hamper the tracers's diffusion at long timescales, similar to experimental results on the dynamics in crowded suspensions of spherical particles [62]. The occurrence of cage effects in crowded suspensions is related to the percolation of the systems [63], which depends not only on the system density, but also on the shape of the colloidal particles and, as a consequence, on their structural organisation. In systems of prolate HBPs, we observed larger deviations of the total NGP in I phases rather than in N_U phases, even though I suspensions are less packed. By further investigating the possible origin of this interesting behaviour, we noticed that, in dense I phases, HBPs form nematic-like randomly-oriented clusters, whose size and morphology depends on particle anisotropy. We believe that the presence of these clusters determine significant deviations from Gaussian dynamics.

Acknowledgments

The authors acknowledge the Leverhulme Trust Research Project Grant RPG-2018-415 and the use of Computational Shared Facility at the University of Manchester.

Supporting information

4.S1 Pair correlation functions

In this section are reported the relevant HBP - HBP and HBP - HS pair correlation functions for all the systems investigated. As expected, all the distributions do not show any preferential ordering of both the HBPs and the HSs, as all the functions fluctuate close to unity and decay at short distances.

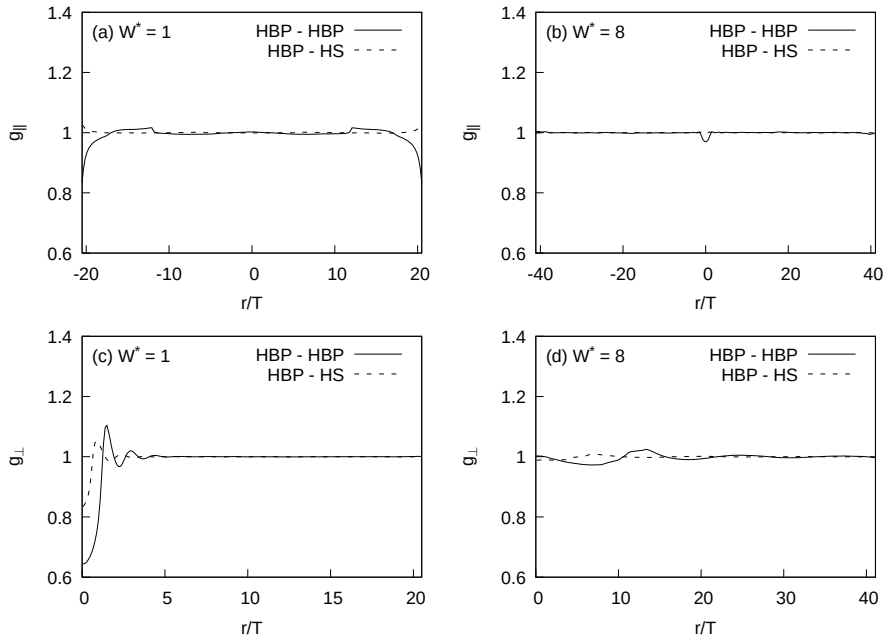

Figure 4.11: HBP - HBP (straight line) and HBP - HS (dashed line) pair correlation functions, obtained from N_U phases of HBPs with $W^* = 1$ (frames (a) and (c)) and $W^* = 8$ (frames (b) and (d)), both at packing fraction $\eta = 0.340$. Frames (a) and (b) show the pair correlation functions in the direction parallel to $\hat{\mathbf{n}}$ of the correspondent phases. The perpendicular pair correlation functions are shown in frames (c) and (d).

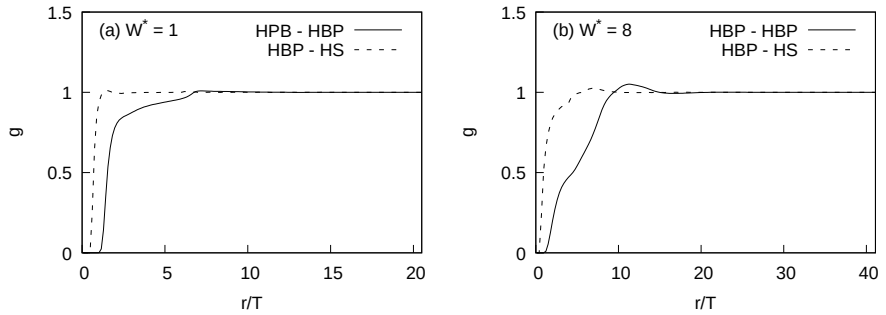

Figure 4.12: HBP - HBP (straight line) and HBP - HS (dashed line) radial distribution functions, obtained from I phases of HBPs with $W^* = 1$ (frame (a)) and $W^* = 8$ (frame (b)), both at packing fraction $\eta = 0.150$.

4.S2 Snapshot of equilibrated LC phases

This section contains snapshots of equilibrated systems of HBPs and HSs, for both prolate and oblate HBPs organised in I and N_U phases. Magnification of the configurations in insets show spherical tracers diffusing in the bath HBPs.

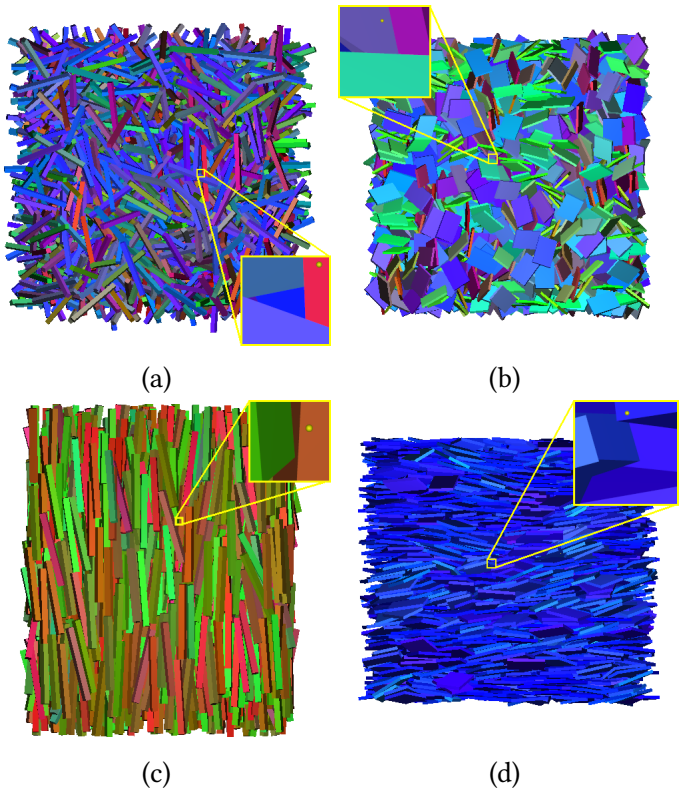

Figure 4.13: Snapshots of equilibrated systems of HSs and HBPs with $W^* = 1$ in I phase (a), and N_U^+ phase (c) and HBPs with $W^* = 8$ in I phase (b) and N_U^- phase (d). Magnification insets show spherical tracers dispersed in the host phase of HBPs. Both I systems have packing fraction $\eta = 0.15$, while both N_U systems have $\eta = 0.34$.

4.S3 MSDs and NGPs of HBPs and HSs along the Cartesian axes

Figs. 4.14 and 4.15 display MSDs and NGPs of HBPs and HSs in isotropic phases of oblate and prolate HBPs. In all the cases, both the MSD and the NGP along the three box axes follow the same trend, proving the isotropy of the displacement of all the particles.

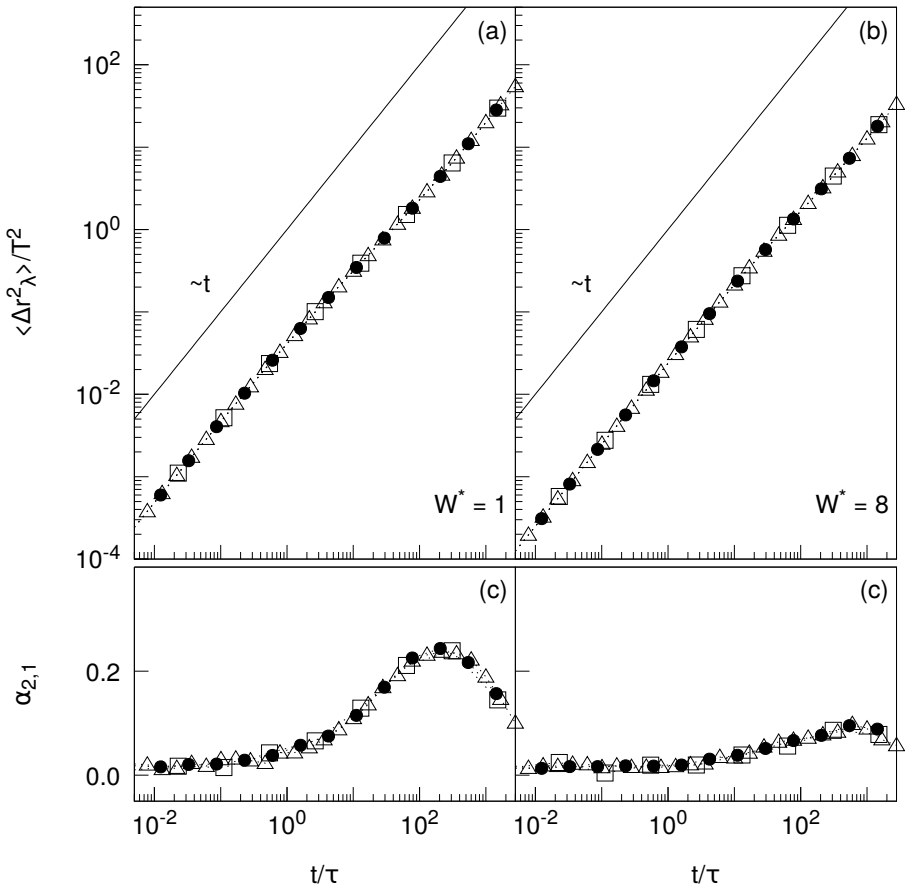

Figure 4.14: MSDs (top frames) and corresponding NGPs (bottom frames) of HBPs in I phases of HBPs with $W^* = 1$ and $W^* = 8$, both at packing fraction $\eta = 0.150$. Both MSDs and NGPs are computed and shown for different directions: empty triangles (△) for displacements along $\hat{\mathbf{x}}$, solid circles (•) along $\hat{\mathbf{y}}$ and empty squares (□) along $\hat{\mathbf{z}}$ reference axis. Solid lines in panels (a-b) indicate the expected dependence of MSD on time in Fickian diffusion.

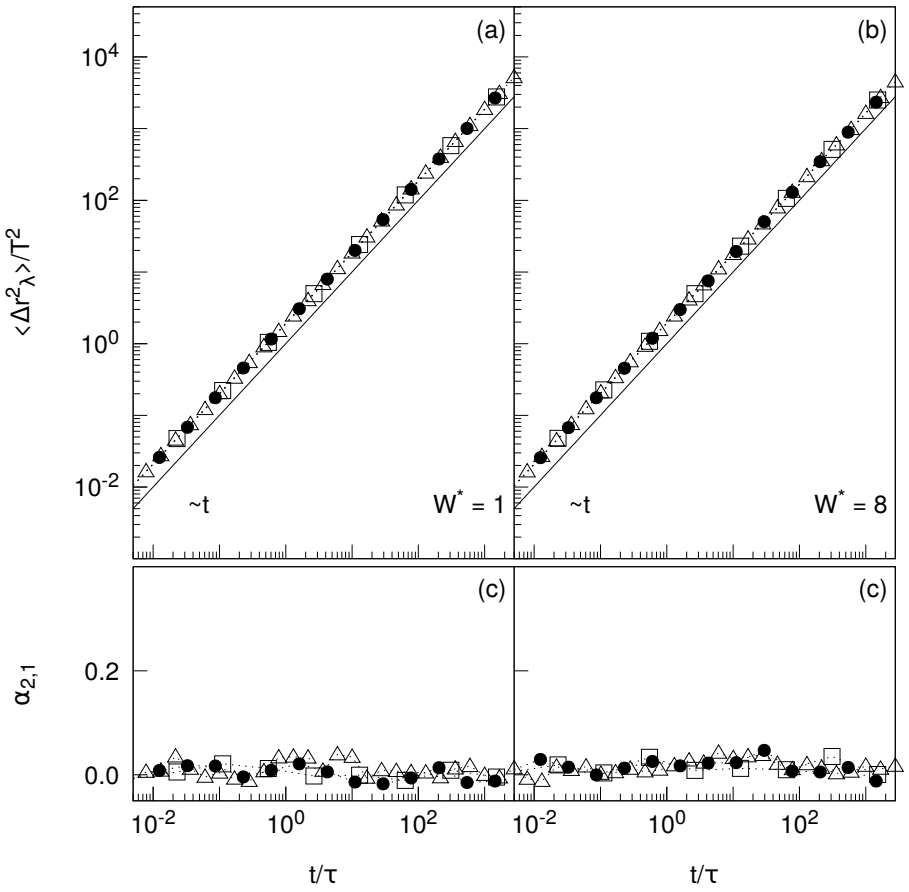

Figure 4.15: MSDs (top frames) and corresponding NGPs (bottom frames) of HSs in I phases of HBPs with $W^* = 1$ and $W^* = 8$, both at packing fraction $\eta = 0.150$. Both MSDs and NGPs are computed and shown for different directions: empty triangles (△) for displacements along $\hat{\mathbf{x}}$, solid circles (•) along $\hat{\mathbf{y}}$ and empty squares (□) along $\hat{\mathbf{z}}$ reference axis. Solid lines in panels (a-b) indicate the expected dependence of MSD on time in Fickian diffusion.

4.S4 Nematic-like clusters in I phases of HBPs

Fig. 4.16 shows the probability distribution of the orientation of the nematic-like clusters with respect to the box reference axes, in I phases of HBPs with $W^* = 1$ and $W^* = 8$ at different packing fractions. The distribution are reported as function of $|cos\theta|$ because of the symmetry of the cuboid with respect to its three axes of orientation. All the distributions are close to unity, proving that the cluster do not have a preferential orientation for all cases. Frames (a-c) in Fig. 4.17 display clusters of oblate HBPs found in an I phase at $\eta = 0.20$.

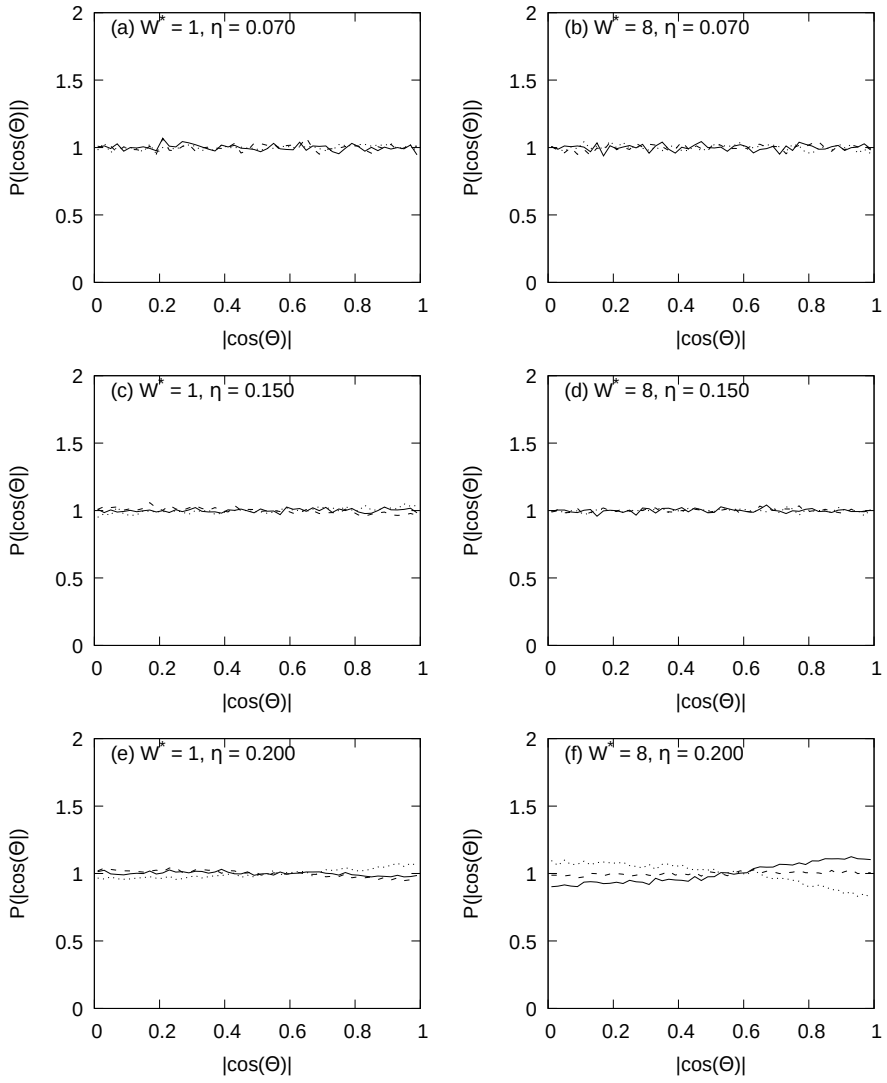

Figure 4.16: Probability density distribution of the orientation of the nematic-like clusters with respect to the box axes $\hat{\mathbf{x}}$ (straight line), $\hat{\mathbf{y}}$ (dashed lines) and $\hat{\mathbf{z}}$ (dotted lines), in I phases of HBPs with $W^* = 1$ and $W^* = 8$, at packing fractions $\eta = 0.07, 0.15, 0.20$.

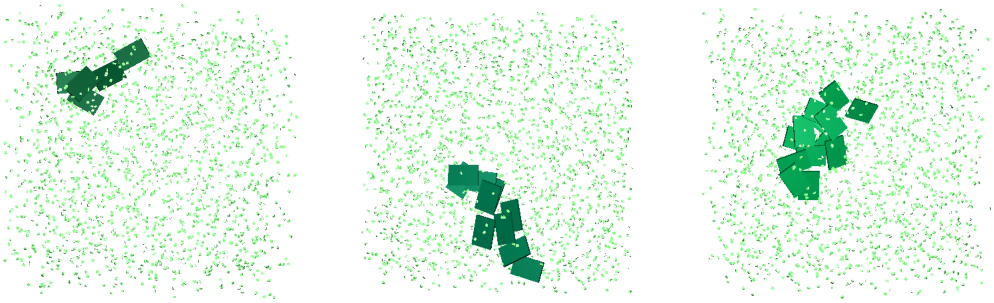

(a) (b) (c)

Figure 4.17: Snapshots of HBPs with $W^* = 8$ in I phase with packing fraction $\eta = 0.20$. While clusters of 5 (a), 10 (b) and 14 (c) HBPs are highlighted in dark green, the remaining particles are represented as small light green cubes.

Bibliography

[1] Dix, J. A. & Verkman, A. Crowding effects on diffusion in solutions and cells. *Annual Review of Biophysics* **37**, 247–263 (2008).

[2] Kamaly, N., Yameen, B., Wu, J. & Farokhzad, O. C. Degradable controlled-release polymers and polymeric nanoparticles: Mechanisms of controlling drug release. *Chemical Reviews* **116**, 2602–2663 (2016).

[3] Biji, K., Ravishankar, C., Mohan, C. & Srinivasa Gopal, T. K. Smart packaging systems for food applications: a review. *J. Food. Sci. Technol.* **52**, 6125–6135 (2015).

[4] Wei, H. *et al.* Advanced micro/nanocapsules for self-healing smart anticorrosion coatings. *J. Mater. Chem. A* **3**, 469–480 (2015).

[5] Puertas, A. M. & Voigtmann, T. Microrheology of colloidal systems. *Journal of Physics: Condensed Matter* **26**, 243101 (2014).

[6] Habibi, A., Blanc, C., Mbarek, N. B. & Soltani, T. Passive and active microrheology of a lyotropic chromonic nematic liquid crystal disodium cromoglycate. *J. Mol. Liq.* **288**, 111027 (2019).

[7] Fick, A. On liquid diffusion. *Journal of Membrane Science* **100**, 33–38 (1995).

[8] Bouchaud, J.-P. & Georges, A. Anomalous diffusion in disordered media: Statistical mechanisms, models and physical applications. *Physics Reports* **195**, 127–293 (1990).

[9] Metzler, R. & Klafter, J. The random walk's guide to anomalous diffusion: a fractional dynamics approach. *Physics Reports* **339**, 1–77 (2000).

[10] Metzler, R., Jeon, J.-H., Cherstvy, A. G. & Barkai, E. Anomalous diffusion models and their properties: non-stationarity, non-ergodicity, and ageing at the centenary of single particle tracking. *Phys. Chem. Chem. Phys.* **16**, 24128–24164 (2014).

[11] Hanneken, J. W., Narahari Achar, B. N., Vaught, D. M. & Harrington, K. L. A random walk simulation of fractional diffusion. *J. Mol. Liq.* **114**, 153–157 (2004).

[12] Sokolov, I. M. Models of anomalous diffusion in crowded environments. *Soft Matter* **8**, 9043–9052 (2012).

[13] Ghosh, S. K., Cherstvy, A. G. & Metzler, R. Non-universal tracer diffusion in crowded media of non-inert obstacles. *Phys. Chem. Chem. Phys.* **17**, 1847–1858 (2015).

[14] Cuetos, A., Morillo, N. & Patti, A. Fickian yet non-gaussian diffusion is not ubiquitous in soft matter. *Phys. Rev. E* **98**, 042129 (2018).

[15] Burgos-Mármol, J. J., Álvarez Machancoses, O. & Patti, A. Modeling the effect of polymer chain stiffness on the behavior of polymer nanocomposites. *The Journal of Physical Chemistry B* **121**, 6245–6256 (2017).

[16] Groen, J. *et al.* Associative interactions in crowded solutions of biopolymers counteract depletion effects. *Journal of the American Chemical Society* **137**, 13041–13048 (2015).

[17] Nogueira, T. P. O., Frota, H. O., Piazza, F. & Bordin, J. R. Tracer diffusion in crowded solutions of sticky polymers. *Phys. Rev. E* **102**, 032618 (2020).

[18] Gam, S. *et al.* Macromolecular diffusion in a crowded polymer nanocomposite. *Macromolecules* **44**, 3494–3501 (2011).

[19] Dey, P. & Bhattacherjee, A. Disparity in anomalous diffusion of proteins searching for their target dna sites in a crowded medium is controlled by the size, shape and mobility of macromolecular crowders. *Soft Matter* **15**, 1960–1969 (2019).

[20] Roosen-Runge, F. *et al.* Protein self-diffusion in crowded solutions. *Proceedings of the National Academy of Sciences* **108**, 11815–11820 (2011).

[21] Chakrabarti, R., Kesselheim, S., Kosovan, P. & Holm, C. Tracer diffusion in a crowded cylindrical channel. *Phys. Rev. E* **87**, 062709 (2013).

[22] Smith, S., Cianci, C. & Grima, R. Macromolecular crowding directs the motion of small molecules inside cells. *Journal of The Royal Society Interface* **14**, 20170047 (2017).

[23] Glotzer, S. C. & Solomon, M. J. Anisotropy of building blocks and their assembly into complex structures. *Nature Materials* **6**, 557–562 (2007).

[24] Cuetos, A., Dennison, M., Masters, A. & Patti, A. Phase behaviour of hard board-like particles. *Soft Matter* **13**, 4720–4732 (2017).

[25] Patti, A. & Cuetos, A. Monte carlo simulation of binary mixtures of hard colloidal cuboids. *Molecular Simulation* **44**, 516–522 (2018).

[26] Cuetos, A., Mirzad Rafael, E., Corbett, D. & Patti, A. Biaxial nematics of hard cuboids in an external field. *Soft Matter* **15**, 1922–1926 (2019).

[27] Mirzad Rafael, E., Corbett, D., Cuetos, A. & Patti, A. Self-assembly of freely-rotating polydisperse cuboids: unveiling the boundaries of the biaxial nematic phase. *Soft Matter* **16**, 5565–5570 (2020).

[28] Cuetos, A. & Patti, A. Dynamics of hard colloidal cuboids in nematic liquid crystals. *Phys. Rev. E* **101**, 052702 (2020).

[29] Patti, A. & Cuetos, A. Brownian dynamics and dynamic monte carlo simulations of isotropic and liquid crystal phases of anisotropic colloidal particles: A comparative study. *Physical Review E* **86**, 011403 (2012).

[30] Cuetos, A. & Patti, A. Equivalence of brownian dynamics and dynamic monte carlo simulations in multicomponent colloidal suspensions. *Physical Review E* **92**, 022302 (2015).

[31] Corbett, D., Cuetos, A., Dennison, M. & Patti, A. Dynamic monte carlo algorithm for out-of-equilibrium processes in colloidal dispersions. *Physical Chemistry Chemical Physics* **20**, 15118–15127 (2018).

[32] García Daza, F. A., Cuetos, A. & Patti, A. Dynamic monte carlo simulations of inhomogeneous colloidal suspensions. *Phys. Rev. E* **102**, 013302 (2020).

[33] Chiappini, M., Patti, A. & Dijkstra, M. Helicoidal dynamics of biaxial curved rods in twist-bend nematic phases unveiled by unsupervised machine learning techniques. *Phys. Rev. E* **102**, 040601 (2020).

[34] Erickson, H. P. Size and shape of protein molecules at the nanometer level determined by sedimentation, gel filtration, and electron microscopy. *Biological Procedures Online* **11**, 32–51 (2009).

[35] Gottschalk, S., Lin, M. & Manocha, D. Obbtree: A hierarchical structure for rapid interference detection. In *23rd Annual Conference on Computer Graphics and Interactive Techniques*, 171–180 (New Orleans, LA, USA, 1996).

[36] John, B. S. & Escobedo, F. A. Phase behavior of colloidal hard tetragonal parallelepipeds (cuboids): A monte carlo simulation study. *The Journal of Physical Chemistry B* **109**, 23008–23015 (2005).

[37] Tonti, L. & Patti, A. Fast overlap detection between hard-core colloidal cuboids and spheres. the ocsi algorithm. *Algorithms* **14** (2021).

[38] Cuetos, A. *Caracterización de las propiedades termodinámicas y estructurales de fases de cristales líquidos mediante modelos moleculares rígidos.* Ph.D. thesis, Área de Química-Física, Departamento de Ciencias Ambientales Universidad Pablo Olavide (2004).

[39] Topping, J. Investigations on the theory of the brownian movement. *Physics Bulletin* **7**, 281–281 (1956).

[40] Carrasco, B. & García de la Torre, J. Hydrodynamic properties of rigid particles: Comparison of different modeling and computational procedures. *Biophysical Journal* **76**, 3044–3057 (1999).

[41] García de la Torre, J., del Rio Echenique, G. & Ortega, A. Improved calculation of rotational diffusion and intrinsic viscosity of bead models for macromolecules and nanoparticles. *J. Chem. Phys. B* **111**, 955—-961 (2007).

[42] Kwon, G., Sung, B. J. & Yethiraj, A. Dynamics in crowded environments: Is non-gaussian brownian diffusion normal? *J. Phys. Chem. B* **118**, 8128–8134 (2014).

[43] Cieśla, M., Gudowska-Nowak, E., Sagués, F. & Sokolov, I. M. Tracer diffusion inside fibrinogen layers. *The Journal of Chemical Physics* **140**, 044706 (2014).

[44] ùRahman, A. Correlations in the motion of atoms in liquid argon. *Phys. Rev.* **136**, A405–A411 (1964).

[45] Levesque, D. & Verlet, L. Computer "experiments" on classical fluids. iii. time-dependent self-correlation functions. *Phys. Rev. A* **2**, 2514–2528 (1970).

[46] Nijboer, B. & Rahman, A. Time expansion of correlation functions and the theory of slow neutron scattering. *Physica* **32**, 415–432 (1966).

[47] van Megen, W. & Underwood, S. M. Tracer diffusion in concentrated colloidal dispersions. ii. non-gaussian effects. *The Journal of Chemical Physics* **88**, 7841–7846 (1988).

[48] van Megen, W. & Snook, I. Dynamic computer simulation of concentrated dispersions. *The Journal of Chemical Physics* **88**, 1185–1191 (1988).

[49] Patti, A., El Masri, D., van Roij, R. & Dijkstra, M. Collective diffusion of colloidal hard rods in smectic liquid crystals: Effect of particle anisotropy. *The Journal of Chemical Physics* **132**, 224907 (2010).

[50] Patti, A., Belli, S., van Roij, R. & Dijkstra, M. Relaxation dynamics in the columnar liquid crystal phase of hard platelets. *Soft Matter* **7**, 3533–3545 (2011).

[51] Patti, A., El Masri, D., van Roij, R. & Dijkstra, M. Stringlike clusters and cooperative interlayer permeation in smectic liquid crystals formed by colloidal rods. *Phys. Rev. Lett.* **103**, 248304 (2009).

[52] Hwang, J., Kim, J. & Sung, B. J. Dynamics of highly polydisperse colloidal suspensions as a model system for bacterial cytoplasm. *Phys. Rev. E* **94**, 022614 (2016).

[53] Kang, K., Wilk, A., Buitenhuis, J., Patkowski, A. & Dhont, J. K. G. Diffusion of spheres in isotropic and nematic suspensions of rods. *J. Chem. Phys.* **124**, 044907 (2006).

[54] Kang, K., Wilk, A., Patkowski, A. & Dhont, J. K. G. Diffusion of spheres in isotropic and nematic networks of rods: Electrostatic interactions and hydrodynamic screening. *J. Chem. Phys.* **126**, 214501 (2007).

[55] Vorselaars, B., Lyulin, A. V., Karatasos, K. & Michels, M. A. J. Non-gaussian nature of glassy dynamics by cage to cage motion. *Phys. Rev. E* **75**, 011504 (2007).

[56] Belli, S., Patti, A., van Roij, R. & Dijkstra, M. Heterogeneous dynamics in columnar liquid crystals of parallel hard rods. *Journal of Chemical Physics* **133**, 154514 (2010).

[57] Matena, R., Dijkstra, M. & Patti, A. Non-gaussian dynamics in smectic liquid crystals of parallel hard rods. *Phys. Rev. E* **81**, 021704 (2010).

[58] Patti, A., Belli, S., van Roij, R. & Dijkstra, M. Relaxation dynamics in the columnar liquid crystal phase of hard platelets. *Soft Matter* **7**, 3533–3545 (2011).

[59] De Gaetani, L., Prampolini, G. & Tani, A. Anomalous diffusion and cage effects in the isotropic phase of a liquid crystal. *Journal of Physical Chemistry B* **111**, 7473–7477 (2007).

[60] Cuetos, A. & Dijkstra, M. Kinetic pathways for the isotropic-nematic phase transition in a system of colloidal hard rods: A simulation study. *Phys. Rev. Lett.* **98**, 095701 (2007).

[61] Cuetos, A., van Roij, R. & Dijkstra, M. Isotropic-to-nematic nucleation in suspensions of colloidal rods. *Soft Matter* **4**, 757–767 (2008).

[62] Sentjabrskaja, T. *et al.* Anomalous dynamics of intruders in a crowded environment of mobile obstacles. *Nature Communications* **7**, 11133 (2016).

[63] Polanowski, P. & Sikorski, A. Motion in a crowded environment: the influence of obstacles' size and shape and model of transport. *J Mol Model* **25**, 84 (2019).

Chapter 5

Kinetics of Isotropic to String-Like Phase Switching in Electrorheological Fluids of Nanocubes

The content of this Chapter has been published as a full article in the *Journal of Molecular Liquids*. My contributions are listed as follows: Luca Tonti was responsible for data curation; Luca Tonti and Fabián A. García Daza developed the methodology; Luca Tonti developed the software; Luca Tonti and Fabián A. García Daza performed the validation; Luca Tonti performed the formal analysis and validation; Luca Tonti, Fabián A. García Daza and Alessandro Patti performed the investigation; Luca Tonti, Fabián A. García Daza and Alessandro wrote the original draft and reviewed and edited the draft.

Abstract

Applying an electric field to polarisable colloidal particles, whose permittivity differs from that of the dispersing medium, generates induced dipoles that promote the formation of string-like clusters and ultimately alter the fluid mechanical and rheological properties. Complex systems of this kind, whose electric-field-induced rheology can be manipulated between that of viscous and elastic materials, are referred to as electrorheological fluids. By dynamic Monte Carlo simulations, we investigate the dynamics of self-assembly of dielectric nanocubes upon application of an electric field. Switching the field on induces in-particle dipoles and, at sufficiently large field intensity, leads to string-like clusters of variable length across a spectrum of volume fractions. The kinetics of switching from the isotropic to the string-like state suggests the existence of two mechanisms, the first related to the nucleation of chains and the second to the competition between further merging and separation. We characterise the transient unsteady state by following the chain length distribution and

analysing the probability of transition of nanocubes from one chain to another over time. Additionally, we employ passive microrheology to gain an insight on the viscoelastic behaviour of the suspension in the isotropic state, in the field-off scenario.

5.1 Introduction

In his 1949 seminal paper, Winslow demonstrated that the application of an electric field to high-dielectric-constant particles dispersed in low-viscosity oils induces their self-assembly in fibrous filaments, with dramatic changes in the rheological properties (e.g., shear modulus, viscosity, yield stress) of the suspension [1]. These systems, generally referred to as electrorheological (ER) fluids, are a class of smart soft materials that can adapt their viscoelasticity in response to an electric field of a given intensity. Due to their relatively simple manufacturing, significant responsiveness to external stimuli and reversible recovery, ER fluids are especially suitable for industry-relevant applications, such as damping systems, microfluidics, tactile displays, where an abrupt change in material rheology is required [2, 3, 4].

As originally predicted by Clausius [5] and Mossotti [6], the application of an external electric field generates an induced dipole in non-conducting suspended particles when their dielectric constant differs from that of the dispersing medium. Under these circumstances, particles polarise and tend to align with each other and with the direction of the electric field [7]. The effect of external fields on suspensions of spherical particles has been extensively investigated by experiments [8, 9, 10, 11, 12] and simulations [13, 14, 15, 16, 17, 18]. Thanks to recent advances in chemical [19], physical [20] and biosynthetic [21] techniques for the synthesis of anisotropic particles [22, 23, 24, 25, 26, 27, 28], which were key to discover new phases either driven by simple excluded-volume effects [29, 30, 31, 32, 33, 34, 35, 36, 37, 38, 39] or induced by external stimuli [40, 41, 42, 43, 44], electrorheology has been extended to more exotic colloidal suspensions [45, 46, 47]. Polarisation has then been employed to explore the fabrication of an intriguing family of novel materials, termed colloidal polymers, where a field-induced alignment of particles in polymer-like chains of tunable flexibility is subsequently made permanent even when the field is switched off [48, 49]. Most of the work on colloidal polymers and, more generally, on ER fluids has so far explored

suspensions of spherical particles, with very few exceptions. One of these exceptions is the very recent experimental work by Cai and co-workers who prepared colloidal polymers of micron-sized α-Fe_2O_3 cubes combining dipolar-directed assembly and in situ hydrolysis-condensation of tetraethylorthosilicate [50]. Despite the widespread interest in ER fluids of colloidal spheres, particle shape definitely plays a crucial role in the kinetics of clustering as well as in the resulting rheology of the suspension, thus opening the path to novel materials with tunable properties.

We have recently developed a stochastic method to mimic the dynamics of Brownian particles via standard Markov Chain Monte Carlo (MC) simulations with specific settings on the particle elementary moves. This method, referred to as dynamic Monte Carlo (DMC), allows one to implement discontinuous interaction potentials and generate time trajectories in equilibrium or over transitory unsteady states [51, 52, 53, 54, 55, 56, 57]. In this work, we apply a novel DMC technique to assess the response of a suspension of perfect hard dielectric nanocubes under the application of an electric field. At sufficiently low volume fraction and moderate field strength, colloidal hard nanocubes are expected to assemble into string-like clusters, as predicted by equilibrium MC simulations and observed experimentally [58]. While the phase behaviour of these ER fluids has been well documented, very little attention has been given to the kinetics of such an isotropic to string-like phase switching and to its impact on the viscoelastic properties of the material. To bridge this gap, here we investigate the responsiveness of nanocubes to the application of an electric field and compute the time scales associated to the formation of these chains and their length distribution. Additionally, we apply passive microrheology (MR) to infer, from the computation of the mean square displacement of a free-diffusing tracer, the elastic and viscous moduli of the suspension of nanocubes in the field-off scenario. While at low dilution, the motion of the tracer is unaffected by the presence of the surrounding particles, at higher concentration of nanocubes $\eta = 0.2$, the analysis showed a typical predominantly viscous behaviour of the suspension at all frequencies.

5.2 Computational methodology

5.2.1 Model

We set the length of a cube edge σ, the reciprocal of the thermal energy $\beta \equiv 1/k_B T$, with k_B the Boltzmann constant and T the absolute temperature, and the solvent viscosity μ as system units. It follows that time has units $\tau \equiv \beta\mu\sigma^3$. Polarised cubes are modeled via hard core interactions, and the induced dipole-dipole interaction between their centers of mass is considered only in the presence of an electric field. We apply an algorithm based on the separating axis theorem to detect overlaps between two nanocubes [59]. Hard core models neglect more complex phenomena of anisotropic interactions, observed in simulations and experiments of dielectric nanocubes with electric double layers, where the type of the solvent and the salt concentration proved to have a role in the preferential relative orientation as they get closer to each other [60].

We modelled the induced polarisation of the cubic particles using a point-dipole approximation, i.e., $\mathbf{p}_i = \alpha E_0 \hat{\mathbf{E}} = p\hat{\mathbf{E}}$, where p is the magnitude of the dipole moment, α the particle polarizability and $E_0\hat{\mathbf{E}}$ the external field. The point dipole approximation has been proven to successfully mimic the phase behaviour of polarised cubes at different densities and strengths of the external electric fields. The Clausius-Mossotti relationship is used to express the particle polarizability:

$$\alpha = 3V_p\epsilon_o\epsilon_s\left(\frac{\epsilon_p - \epsilon_s}{\epsilon_p + 2\epsilon_s}\right) = \frac{3V_p\epsilon_s}{4\pi k}\left(\frac{a-1}{a+2}\right) \tag{5.1}$$

where $k \equiv 1/(4\pi\epsilon_0)$ is the Coulomb constant, set as unit in our simulations, $V_p = \sigma^3$ is the volume of one cubic particle, ϵ_0 is the vacuum permittivity and $a = \epsilon_p/\epsilon_s$ the ratio between permittivities of the particles and the solvent [5, 6, 61]. The dipolar interaction between two dipoles is:

$$u_{ij,dip} = -\frac{k}{\epsilon_s}\frac{3(\mathbf{p}_i \cdot \hat{\mathbf{r}}_{ij})(\mathbf{p}_j \cdot \hat{\mathbf{r}}_{ij}) - \mathbf{p}_i \cdot \mathbf{p}_j}{r_{ij}^3}, \tag{5.2}$$

where $r_{ij}\hat{\mathbf{r}}_{ij}$ is the distance vector between particles i and j. One can simplify Eq. 5.2 considering that $\mathbf{p}_i \cdot \mathbf{p}_j = p^2$ and $\mathbf{p}_i \cdot \hat{\mathbf{r}}_{ij} = \mathbf{p}_j \cdot \hat{\mathbf{r}}_{ij} = p\cos(\theta_{ij})$, where $\cos(\theta_{ij}) = \hat{\mathbf{E}} \cdot \hat{\mathbf{r}}_{ij}$. We can finally express Eq. 5.2 as a function of a dimensionless interaction parameter γ, as

already defined in the work by Vutukuri *et al.* [58]:

$$\beta u_{ij,dip}(r_{ij}, \theta_{ij}) = \frac{\gamma}{2}\left(\frac{\sigma}{r_{ij}}\right)^3 \left[1 - 3\cos^2(\theta_{ij})\right], \tag{5.3}$$

where

$$\gamma = \frac{2k\beta p^2}{\epsilon_s \sigma^3}. \tag{5.4}$$

Fig. 5.1 shows a schematic representation of the model dipolar interaction described by Eq. 5.3, while Table 5.1 lists the units of the physical quantities used in this work.

Quantity	Units
Length of cube edge	σ
Solvent viscosity	μ
Thermodynamic beta	$\beta \equiv 1/(k_B T)$
Time	$\tau \equiv \beta\mu\sigma^3$
Frequency	$1/\tau$
Translational diffusivity	σ^2/τ
Rotational diffusivity	rad^2/τ
Pressure	$1/(\beta\sigma^3)$
Coulomb constant	$k \equiv 1/(4\pi\epsilon_0)$
Magnitude of dipole moment	$\sqrt{\sigma^3/(\beta k)}$
Polarizability	σ^3/k
Intensity of external field	$\sqrt{k/(\beta\sigma^3)}$

Table 5.1: List of units used in this work.

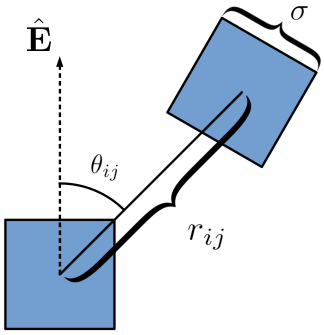

Figure 5.1: Model of dipolar interactions between nanocubes. The interaction potential $u_{ij,dip}(r_{ij}, \theta_{ij})$ depends on the module of the vector $\mathbf{r}_{ij}$ between the centers of mass of particle i and j, and θ_{ij}, i.e., the angle between $\mathbf{r}_{ij}$ and the external field with orientation $\hat{\mathbf{E}}$.

Since simulations are performed in boxes with periodic boundaries, we employ the Ewald summation method for dipolar interactions to compute the long range contribu-

tions to the system's energy [62]. In all simulations with field on, γ is set equal to 13. At this field intensity, one can observe the formation of isolated strings that do not percolate through the simulation box and do not cluster. For this value of the dipole-dipole interaction strength, Vutukuri *et al.* [58] determined that no phase transition has been observed within the packing fractions we investigated.

For simulations of passive microrheology, where a spherical probe is added to the suspension of nanocubes, the external field is kept off and only hard-core interactions between the tracer and the cubic particles are considered. For each trial move of the tracer, collisions between the sphere and the cubes are checked by using the OCSI algorithm [63].

5.2.2 Dynamic Monte Carlo simulations

We perform simulations in the *NVT* ensemble using the dynamic Monte Carlo (DMC) technique to investigate the Brownian motion of nanocubes. Each trial consists of one translation of the center of mass and one body-centered rotation of a randomly selected particle. Random moves are sampled uniformly within $[-\delta\xi_k, \delta\xi_k]$, where $\delta\xi_k$ are defined by the Einstein relation

$$\delta\xi_k^2 = 2D_{kk}\delta t_{\mathrm{MC}}, \tag{5.5}$$

being D_{kk} the diagonal element of the diffusion tensor of the particle, and δt_{MC} the MC timescale of the particle. One time step in our simulations corresponds to 1 MC cycle (N attempts to displace particles). In out-of-equilibrium DMC simulations, the physical time is recovered using Eq. 5.6

$$t_{\mathrm{BD}} = \delta t_{\mathrm{MC}} \sum_{c=0}^{\mathscr{C}_{\mathrm{MC}}} \frac{\mathscr{A}_c}{3}, \tag{5.6}$$

where $\mathscr{A}_c$ indicates the average acceptance of trial moves in one MC cycle, and $\mathscr{C}_{\mathrm{MC}}$ the total number of MC cycles simulated [53]. We note that if the system is at equilibrium, the acceptance rate is constant over the the entire simulation and Eq. 5.6 can be further simplified to

$$t_{\mathrm{BD}} = \frac{\mathscr{A}}{3}\delta t_{\mathrm{MC}}\mathscr{C}_{\mathrm{MC}}. \tag{5.7}$$

Particles with different sizes and shapes exhibit different diffusivities and acceptance rates. Accordingly, since every particle holds its own MC timescale, they all have to be balanced with their respective acceptance rates to recover a unique timescale. In our microrheology simulations, $\delta_{\mathrm{MC},sphere}$ and $\delta_{\mathrm{MC},cube}$ are balanced using Eq. 5.8

$$\mathscr{A}_{sphere}\delta t_{\mathrm{MC},sphere} = \mathscr{A}_{cube}\delta t_{\mathrm{MC},cube}. \tag{5.8}$$

As in this case the systems are in equilibrium, $\mathscr{A}_{sphere}$ and $\mathscr{A}_{cube}$ will be constant over time. The validity of Eq. 5.8 is ensured before running the DMC simulations by fixing one timescale and recalculating the other one using the estimated acceptance rate in a preliminary trial-and-error simulation [52, 64].

The dynamics and kinetics of string formation are investigated by performing simulations of a system of $N_{cube} = 1500$ nanocubes in cubic simulation boxes with periodic boundary conditions, at packing a fraction $\eta = 0.02$. We perform 30 independent simulations, setting $\delta t_{\mathrm{MC},cube} = 10^{-3}\,\tau$. The diffusion tensor of the cube is estimated using the software Hydro++ [65], from which we obtain translational and rotational diffusivities, $D_{t,cube} = 8.35\times10^{-2}\,\sigma^2\tau^{-1}$, and $D_{r,cube} = 1.48\times10^{-1}\,\mathrm{rad}^2\tau^{-1}$. We simulate 3 consecutive sequences over which the external electric field is turned on and off. In a single sequence, starting from a perfect isotropic phase (field off), the external field is switched on for $2{\times}10^6$ time steps and then turned off for 3×10^5 time steps.

The study of microrheology is performed in suspensions of $N_{cube} = 1500$ cubes of side σ and 1 spherical tracer with diameter $d_{sphere} = 3\,\sigma$ at a packing fraction $\eta = 0.2$, at equilibrium states when the external field is off. The diffusivity of the tracer at infinite dilution is $D_{t,sphere} = (1/9\pi)\,\sigma^2\tau^{-1}$, and attempted moves to displace it are sampled through trial translations in all the tree spatial directions. We set the nanocubes time step to $\delta t_{\mathrm{MC},cube} = 5.0\times10^{-3}\,\tau$ and perform preliminary equilibration runs to recover $\delta t_{\mathrm{MC},sphere,OFF} = 5.307\times10^{-3}\,\tau$ according to Eq. 5.8. We compute the rheological properties of the host phase from 1000 independent trajectories of the system.

5.2.3 Structural properties

The positional pair correlation functions are employed to investigate the structural properties of the suspension. Due to the system's anisotropy, we decompose the analysis

in the direction parallel and perpendicular to the external field. We define $r_{ij} = \|\mathbf{r}_{ij}\|$, $r_{ij,\parallel} = |\mathbf{r}_{ij} \cdot \hat{\mathbf{E}}|$ and $r_{ij,\perp} = \|\mathbf{r}_{ij} - (\mathbf{r}_{ij} \cdot \hat{\mathbf{E}})\hat{\mathbf{E}}\|$ as the moduli of the relative distance between particles i and j for the total, parallel and perpendicular directions to the field, respectively. The generic definition of positional pair correlation function is

$$g_\zeta(r) = \frac{\left\langle \sum_{i=1}^{N} \sum_{j \neq i} \mathbf{1}_\zeta \left(\mathbf{r}_{ij}\right) \right\rangle}{N v_\zeta \rho}, \tag{5.9}$$

where ζ is a portion of the simulation box and $\mathbf{1}_\zeta$ is an indicator function defined as follows

$$\mathbf{1}_\zeta = \begin{cases} 1 & \mathbf{r}_{ij} \in \zeta\,, \\ 0 & \mathbf{r}_{ij} \notin \zeta\,, \end{cases} \tag{5.10}$$

the double sum in the angle brackets of Eq. 5.9 counts the number of particles j contained in ζ with respect to a reference particle i, for all the particles i in the system. The angle brackets define an average over the configurations analyzed, while v_ζ is the volume of ζ. N is the total number of particles in the system and ρ the average numeral density, i.e., $\rho = N/V$. The following Table lists the definitions of ζ and v_ζ for all the positional pair correlation functions computed:

Function symbol	ζ	v_ζ
$g(r)$	$r \leq r_{ij} < r + \Delta r$	$4\pi[(r+\Delta r)^3 - r^3]/3$
$g_\parallel(r)$	$r \leq r_{ij,\parallel} < r + \Delta r \bigcap \leq r_{ij,\perp} < R_\parallel$	$\pi R_\parallel^2 \Delta r$
$g_\perp(r)$	$r \leq r_{ij,\perp} < r + \Delta r \bigcap \leq r_{ij,\parallel} < h_\perp$	$\pi[(r+\Delta r)^2 - r^2]h_\perp$

Table 5.2: Definition of positional pair correlation functions used in this work.

We analysed the structure of the suspension with field off using the classical radial distribution function $g(r)$, whose corresponding v_ζ is the volume of a hollow sphere of radii r and $r + \Delta r$ [66]. To assess the formation of chains when the field is applied, we computed $g_\parallel(r)$ and $g_\perp(r)$. $g_\parallel(r)$ is the parallel pair correlation function, and its corresponding v_ζ is the volume of a cylinder with radius $R_\parallel$ and height Δr. $g_\perp(r)$ is the perpendicular pair correlation function, and its corresponding v_ζ is the volume of a cylindrical annulus of height $h_\perp$ and thickness Δr [67, 68].

We assess the degree of orientational order with respect to the field by computing a specific uniaxial order parameter for each particle i, that takes into account the cubic

symmetry of the particles

$$S_i = \frac{\pi\left(3\max\left((\hat{\mathbf{E}}\cdot\hat{\mathbf{e}}_{k,i})^2\right)-1\right)-2\sqrt{3}}{2\pi-2\sqrt{3}}, \tag{5.11}$$

where $\hat{\mathbf{e}}_{k,i}$ are the three axes of orientation of particle i, for $k = 1, 2, 3$. A detailed proof for the normalisation of the order parameter is reported in Section 5.S2 of the Supporting information. Since, by definition, each S_i does not depend on the orientation of particles $j \neq i$, we could compute different order parameters depending on the set of particles considered for the average: the total order parameter is obtained by averaging over all the cubes in the system, i.e., $S^{(tot)} = \langle S_i\rangle_{\forall i}$; the average order parameter of cubes that belong to chains is $S^{(c)} = \langle S_i\rangle_{\forall i\in c}$, for c the set of cubes in clusters.

To investigate the formation of string-like structures we perform a cluster analysis on the simulated trajectories. Given that βu_{max} is our choice of the threshold energy for the cluster definition, two polarised cubes i and j are considered to form a cluster if $u_{ij,dip} \leq u_{max}$. The cluster analysis of the trajectories is performed following the algorithm described by Sevick and co-workers [69]. To properly optimize the threshold parameter βu_{max}, we apply a density-based clustering algorithm to independent configurations of cubes in the string-like state. A detailed description of the method is reported in Section 5.S1 of the Supporting information. From the cluster analysis, we estimate the number of clusters of size l at time t, $N(l,t)$. The molar fraction of strings of size l (free cubes are labeled as $l = 1$) reads

$$X(l,t) = \frac{N(l,t)}{N_{cube}}. \tag{5.12}$$

From the above expression we can recover the molar fraction of cubes that belong to strings as $X_c = \sum_{l=2}^{\infty} lX(l,t)$. Numerical and weighted average chain lengths read

$$\langle l\rangle_n(t) = \frac{\sum_{l=2}^{\infty} lN(l,t)}{\sum_{l=2}^{\infty} N(l,t)} \tag{5.13}$$

$$\langle l\rangle_w(t) = \frac{\sum_{l=2}^{\infty} l^2N(l,t)}{\sum_{l=2}^{\infty} lN(l,t)}. \tag{5.14}$$

5.2.4 Microrheological properties

In passive microrheology, the viscoelastic properties of complex systems can be computed from the MSD of a tracer particle embedded in the host phase [70, 71, 72, 73, 74]. More specifically, according to Mason [72], the complex shear modulus $G^*(\omega) = G'(\omega) + iG''(\omega)$, where $G'(\omega)$ and $G''(\omega)$ are the elastic and viscous moduli, respectively, can be written as

$$|G^*(\omega)| = \frac{2\sigma^3}{\pi d_{sphere}\langle \Delta r_t^2\,(1/\omega)\rangle \Gamma[1+\chi(\omega)]}\frac{1}{\beta\sigma^3}, \tag{5.15}$$

where $\chi(\omega) = d\ln(\Delta r_t^2(t))/d\ln(t)|_{t=\omega^{-1}}$ indicates the local exponent of tracer's MSD , Γ is the gamma function and the modulus is in units of pressure, expressed as $1/(\beta\sigma^3)$. Consequently, the elastic and viscous moduli are computed as follows

$$G'(\omega) = |G^*(\omega)|\cos\left(\frac{\pi\chi(\omega)}{2}\right) \tag{5.16}$$

$$G''(\omega) = |G^*(\omega)|\sin\left(\frac{\pi\chi(\omega)}{2}\right). \tag{5.17}$$

While in a viscous system the motion of the particles is mainly diffusive ($\chi(\omega) \approx 1$) and $G''(\omega)$ is larger than $G'(\omega)$, in a elastic system the tracer motion is hindered by the local distribution of surrounding bath particles ($\chi(\omega) \ll 1$) and $G'(\omega)$ dominates over $G''(\omega)$. It should be pointed out that in addition to the Fourier approximation, other methods have been proposed to calculate the viscoelastic response of the bath from the tracer dynamics, including Laplace transform [70] and compliance-based [73, 74] methods among others. In Fig. 5.12 of the Supporting information, we compare the viscoelastic moduli calculated from the Fourier-based method (Eqs. 5.15-5.17) and the compliance approach proposed by Evans *et al.* [73] and show that they are in excellent quantitative agreement.

5.3 Results and discussion

In the following, we first discuss the effect of applying an electric field to a suspension of polarisable nanocubes and what structural changes it determines. Then, we analyse the nanocubes' dynamics in the transitory unsteady state to gain an insight into the mechanisms underpinning the process of formation of chains. Finally, we employ pas-

sive MR to infer the local viscoelastic behaviour of our model ER fluid in the case where no external stimuli are applied. As a reference system, we consider a suspension of hard nanocubes, whose packing fraction *vs* field intensity phase diagram has been calculated by MC simulations by Dijkstra and co-workers [58].

5.3.1 Effect of external field on system conformation

Fig. 5.2 shows the time evolution of the molar fraction X_c of nanocubes in string-like clusters, and the uniaxial order parameter $S^{(tot)}$ averaged over all nanocubes, for three on/off field-switching cycles, at $\eta = 0.02$ and $\gamma = 13$. This order parameter is specifically proposed for particles with cubic symmetry (see Eq. 5.11). To identify the nanocubes

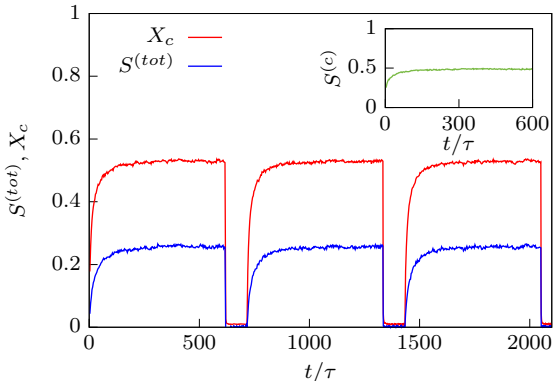

Figure 5.2: Average molar fraction of nanocubes in chains (X_c) and uniaxial order parameter ($S^{(tot)}$) over three on/off switching cycles. The inset depicts the average uniaxial order parameter that only considers the nanocubes in chains ($S^{(c)}$), for the first on/off cycle (from $t = 0$ to $600\,\tau$). The packing fraction and field strength are $\eta = 0.02$ and $\gamma = 13$, respectively.

belonging to the same cluster, we define an energy-based cluster criterion whose optimal parameterization was achieved via a density-based cluster analysis (see Methods and Section 5.S1 of Supporting information). When the external field is switched on, X_c increases up to $\sim$ 0.50, indicating that nearly half of the nanocubes are assembled in strings. The clustering is completed at a response time $t_r \approx 150\,\tau$. We notice that, when the field is off, nanocubes displace an average distance approximately equal to $9\,\sigma$ over the same period of time. This suggests that, in terms of the nanocubes' ability to diffuse in an isotropic phase, the response time t_r is relatively long.

Fig. 5.3 shows a typical snapshot of the system in the string-like state, with the strings of nanocubes oriented along $\hat{\mathbf{E}}$. Most string-like clusters comprise between 2 and 4 nanocubes, while longer chains are less likely to be observed. Our simulation results

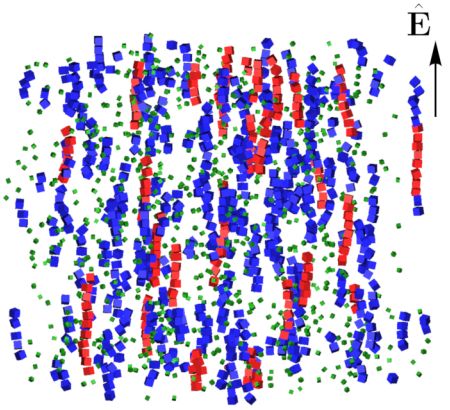

Figure 5.3: Suspensions of $N_{cube} = 1500$ nanocubes upon the application of an external electric field. The orientation of the field $\hat{\mathbf{E}}$ is shown with a black arrow on the top right of the Figure. Blue chains contain less than 6 nanocubes, while red chains contain at least 6 of them. Isolated nanocubes are shown in green and reduced in size for clarity. Packing fraction and field strength are $\eta = 0.02$ and $\gamma = 13$, respectively.

also reveal the presence of isolated nanocubes (reduced in size for clarity in Fig. 5.3) that are free to assume random orientations with respect to the field direction, in agreement with former experiments and simulations [58]. In Fig. 5.2, we compare the total uniaxial order parameter $S^{(tot)}$ with the same parameter averaged exclusively over particles that belong to strings $S^{(c)}$ (see inset). In particular, $S^{(c)} = \langle S_i \rangle_{i \in c}$ is defined as the average contribution of particles in chains to $S^{(tot)}$, while $S^{(free)} = \langle S_i \rangle_{i \in free}$ is the contribution of free nanocubes. According to Fig. 5.2, during the switching on, the nanocubes in chains ($X_c \sim 50\%$) lead to $S^{(c)} \sim 0.50$ whereas $S^{(tot)} \sim 0.25$. Thereby, the contribution of free particles ($S^{(free)}$) to $S^{(tot)}$ is negligible since $S^{(tot)} \approx (S^{(c)} + S^{(free)})/2 \approx S^{(c)}/2$. One should notice that the dipolar interaction only depends on the distance between nanocubes and not on their space orientation. However, this interaction becomes very attractive when the nanocubes are face-to-face piled, minimizing their mutual distance and thus forming strings aligned with $\mathbf{E}$ as shown in Fig. 5.3.

When the field is switched off the system relaxes nearly instantaneously from the string-like state. At equilibrium, the isotropic configurations where both $X_c \approx 0$ and $S_c \approx 0$ are fully recovered. Their sudden decay is due to the approximations in our model, where the particle polarisation is assumed to be exclusively triggered by the external field. It is worth noting that a more general definition of particle polarisation should involve the contributions of both the external field and the particle-particle polarisation i.e., $\mathbf{p}_i = \alpha(\mathbf{E} + \sum_{i \neq j} \mathbf{E}_j)$. Nevertheless, the approximation $\mathbf{p} = \alpha \mathbf{E}$ is often found in

simulations of ER fluids [14, 15, 75, 12]. Incorporating both local and external fields into the particles' dynamics would require either the inversion of a $3N \times 3N$ matrix or the use of iterative procedures [76, 77, 78], resulting in very demanding calculations. However, we notice that, for moderate electric fields, simulations of dilute ER fluids of spheres reveal that the particle-particle polarisation may contribute up to 5% of the total dipole moment, and no tangible effects on dynamics are reported [18].

One may suggest that point-dipole approximations play a role in determining the dynamics of cubes when an electric field is applied. Vutukuri *et al.* estimated the energy differences for pairs of aligned and misaligned cubes at face-to-face contact, being discretized in smaller cubes each containing one point dipole [58]. These authors found that energy differences level off to a limiting value of $0.01\gamma k_{\mathrm{B}}T$ and, when comparing simulation results on single point-dipole cubes to those on multiple point-dipole cubes, they did not observe any notable difference in cubes alignment for field intensities below $\gamma = 30$. Moreover, Kwaadgras *et al.* applied the Couple Dipole Method to estimate the exact self-consistent dipolar interaction between two axis-aligned cubes polarised by an external field, as a function of their relative position in space, and compared it to the two aforementioned models [79]. Both single and multiple point-dipole approximations showed similar discrepancies with respect to the exact model of interaction, underestimating attraction and overestimating repulsion. In conclusion, according to the findings reported in these works, the point-dipole approximation used here is not expected to be determinant in the formation of chains, at least for the field strength investigated in this work. Nonetheless, a more detailed description of the potential may highlight intriguing anisotropic phenomena occurring in the dynamics of cubes, especially at short distances, that cannot be observed when modelling the polarisation as a point-dipole.

5.3.2 Structural properties at equilibrium

The structural organisation of nanocubes in suspension is inferred from the pair correlation functions parallel ($g_{\parallel}(r)$) and perpendicular ($g_{\perp}(r)$) to the electric field. In Fig. 5.4, we present $g_{\parallel}(r)$ and $g_{\perp}(r)$. For comparison, we also include the radial distribution function, $g(r)$, of the nanocubes in the isotropic phase, that is when the electric field is off. The peaks observed in $g_{\parallel}(r)$ indicate a strong ordering of particles at short distances, arising from the piling of nanocubes on top of each other and the subsequent formation of

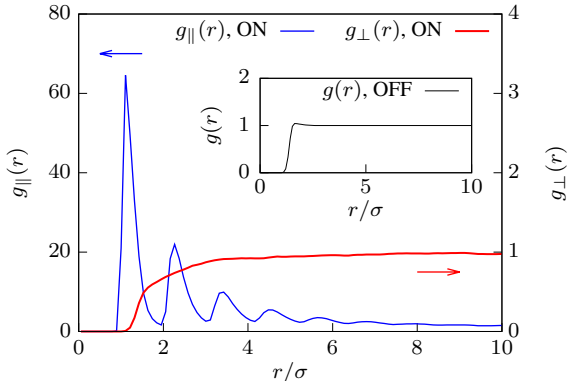

Figure 5.4: Pair correlation functions of nanocubes in the presence of an external field, in the direction parallel (blue line) and perpendicular (red line) to the field. For comparison, the radial distribution function when the field is off is also shown in the inset.

string-like structures oriented along $\hat{\mathbf{E}}$. This order vanishes for $r > 6\,\sigma$, suggesting that the occurrence of strings comprising more than 6 nanocubes is very unlikely. Moreover, we confirm that the string-like clusters do not percolate through the box boundaries, as $g_\parallel(r)$ decays at distances $r < l_{box}/2$, with $l_{box} \sim 42.2\,\sigma$ the box length. By contrast, no structural order is observed in the perpendicular direction. Since $g_\perp(r) < 1$ at short distances, the chains are usually separated from each other and from isolated nanocubes by a long distance. Consequently, at $\eta = 0.02$ and $\gamma = 13$ the suspension is characterised by strong density heterogeneities that are not found in the isotropic phase, as illustrated by $g(r)$ in the inset of Fig. 5.4.

5.3.3 Dynamics of chain formation in transitory state

In this section, we study the kinetics of string formation. To this end, we estimate the 2-particle connectivity with the aid of an energy threshold parameter, $\beta u_{max} = -3.2$. More specifically, two nanocubes i and j are considered to be connected if $\beta u_{ij,dip} < \beta u_{max}$. The cluster parameter βu_{max} has been calculated by applying a density-based cluster analysis (DBSCAN) [80, 81] on equilibrated configurations of strings of nanocubes. Details of these calculations are given in Section 5.S1 of Supporting information.

Fig. 5.5 reports the results obtained from the cluster analysis in suspensions of nanocubes at $\eta = 0.02$ starting from an isotropic phase (field off) and ending into a phase of string-like clusters (field on). Numerical (Eq. 5.13) and weighted (Eq. 5.14) averaged chain lengths are reported in Fig. 5.5(a). Similarly, Fig. 5.5(b) presents the time dependence of the molar fraction of chains whose length ranges between $l = 2$ and $l = 7$. At short

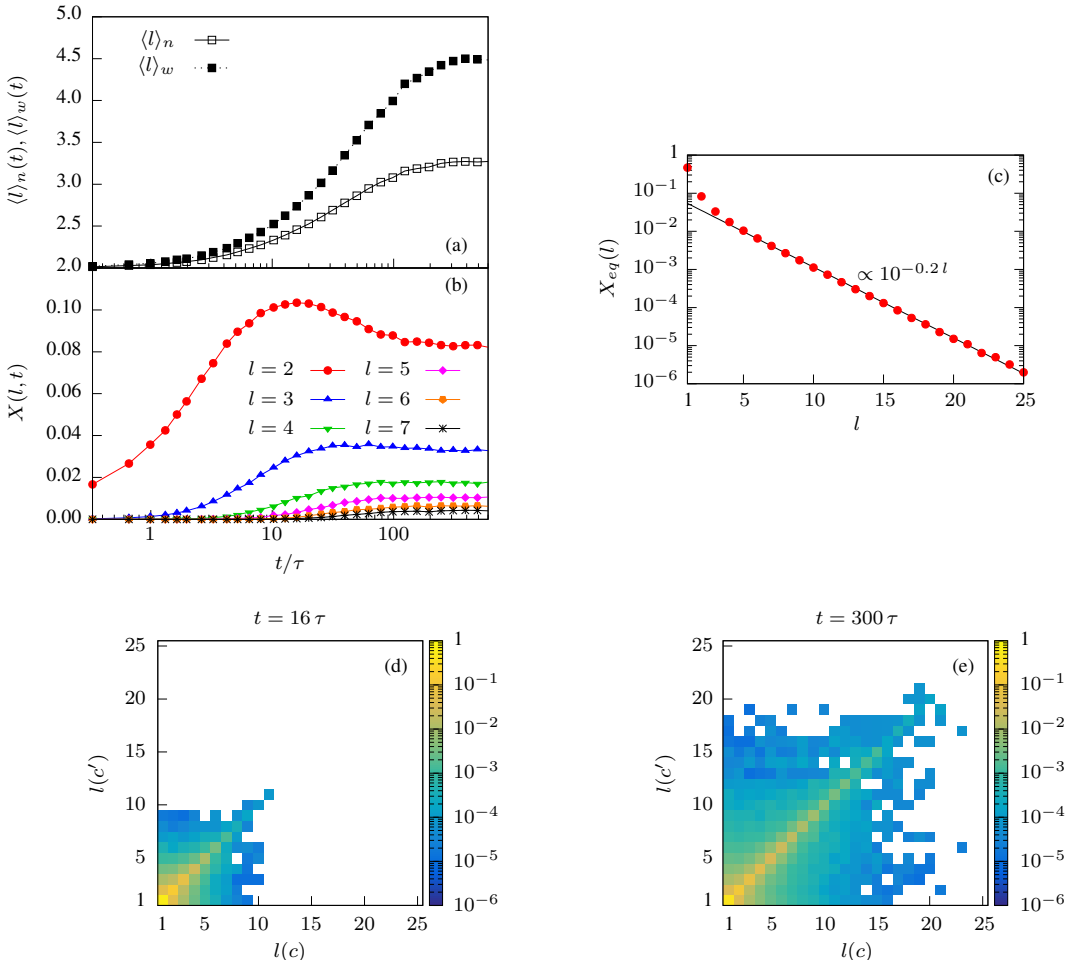

Figure 5.5: (a) Profiles of numerical ($\langle l\rangle_n(t)$) and weighted ($\langle l\rangle_w(t)$) average chain lengths over time, for the isotropic (field off) to string-like (field on) phase. (b) Time dependent profiles of molar fractions of chains of length $2 \leq l \leq 7$, starting from the isotropic phase and switching the field on. (c) Equilibrium distribution of molar fraction of chain lengths in the string-like state from simulations (red points), together with the exponential decay obtained by nonlinear regression of data (black solid line). (d, e) Probability transition matrix of a nanocube moving from an initial cluster c of size $l(c)$ to a cluster c' of size $l(c')$ after $0.3\,\tau$, (d) at time $16\,\tau$, corresponding to the maximum of $X(2,t)$ and (e) at $300\,\tau$, when the system reaches the string-like state. Transition probabilities lower than 10^{-6} are in white.

times ($t/\tau < 1$), strings of sizes 2 and 3 are more likely to form. While the concentration of these short strings displays a local maximum at intermediate times ($10 < t/\tau < 50$), that of longer strings, with $l \geq 4$, is smoothly increasing until a plateau at times $t > t_r$ is achieved. Interestingly, although the molar fraction, X_c, of cubes in chains reaches a steady value at $t_r \sim 150\,\tau$, numerical ($\langle l\rangle_n$) and weighted ($\langle l\rangle_w$) lengths are still relaxing at this time. This suggests that strings of different sizes are continuously breaking and merging while reaching the equilibrium distribution regardless the fact that the percentage of nanocubes in chains remains basically constant for $t > t_r$ (see Fig. 5.2).

Fig. 5.5(c) contains the resulting equilibrium distribution of fraction of strings of length l, $X_{eq}(l)$, for the different sizes of the string-like clusters. Our simulation results (red circles) are compared to a fitting model (black line) that assumes an exponential decay of $X_{eq}(l)$. According to the first-order Wertheim's perturbation theory of associating fluids, if the probability of two particles to be connected is constant and equal to p_b, a probability distribution of clusters at equilibrium can be defined as follows [82, 83, 84, 43]

$$X_{eq}(l) = (1 - p_b)^2 p_b^{l-1}. \tag{5.18}$$

From Eq. 5.18, the linear dependence $\ln(X_{eq}) \propto l$ can be recovered. In our case, however, concentrations of free nanocubes and chains of 2 and 3 particles are significantly larger than those predicted by Wertheim's theory. We hypothesise that this discrepancy may arise from the crucial assumption underlying Wertheim's theory that considers particle connectivity to be independent from the cluster size. This approximation is not directly applicable to our system as dipolar interactions are long-ranged. Indeed, the mechanisms involved in the formation of string-like clusters of polarised particles are more complex than those in simple associating fluids. More specifically, the kinetics of formation of chains consisting of polarised nanoparticles is governed by the dipole moment of each particle, excluded-volume interactions and thermal fluctuations.

To gain better insights into the kinetics of formation of string-like clusters of nanocubes, we compute the transition probability matrix of a cubic particle to belong to chain c of size $l(c)$ at time t_1 and be in chain c' of size $l(c')$ at time $t_2 = t_1 + \delta t$, where δt is set to $0.3\,\tau$ [85]. Fig. 5.5(d) and (e) present the transition matrices computed at times $t = 16\,\tau$ and $t = 300\,\tau$, corresponding, respectively, to the maximum and stationary values of $X(2,t)$ in Fig. 5.5(b). Since the largest probabilities have a tendency to lie on the diagonal ($l(c) = l(c')$), at long and short times most nanocubes prefer to remain in chain c rather than diffusing to chain c'. At short times, strings contain no more than 10 nanocubes, while they grow up to $l \sim 20$ at longer times. Nonetheless, at the stationary state ($t = 300\,\tau$), clusters with more than 25 nanocubes have been occasionally seen, with $X_{eq}(l \geq 25) < 10^{-6}$ (Fig. 5.5(c)). It is interesting to note that, at both short and long time scales, a smooth decay of the transition probabilities is observed from short to long strings along the diagonal elements of the matrix, i.e., where $l(c) = l(c')$, and also where $|l(c) - l(c')|$ gradually becomes larger. It has to be pointed out, however, that the transi-

tion matrices are not weighted by the size of the chains since their individual elements are computed tracking the single nanocubes rather than the cluster themselves. Nevertheless, a wide variety of transitions between chains of different lengths is still observed. We would expect that the kinetic rates characterising these transitions were string-size dependent and, what we actually observe is that aggregation and disaggregation mechanisms involving individual cubes or small clusters are more likely to occur rather than those involving larger strings. Equally interesting is the change of the mechanical properties of ER fluids upon switching the electric field on/off. The change in the viscoelastic behaviour of nanocubes in the presence of the external field is analysed in the following section by applying passive microrheology.

5.3.4 DMC microrheology of ER fluids

In passive MR, one can obtain the viscoelastic response of a soft material from the mean square displacement (MSD) of a tracer particle embedded in it. By estimating the complex shear modulus G^*, where ω is the frequency of interest, it is possible to identify the viscous (G'') and elastic (G') moduli of the system from $G^*(\omega) = G'(\omega) + iG''(\omega)$. A number of methods have been proposed to determine G^* from the dynamics of a tracer particle [70, 71, 72, 73, 74]. In this work, we apply the method developed by Mason [72] where the Fourier transform of tracer's MSD serves to estimate the viscoelastic properties of the bath.

A preliminary MR analysis of a bath of nanocubes at a packing fraction $\eta = 0.02$ revealed that the very low concentration of bath particles does not affect the mobility of the tracer when the field is off, as the MSD reported in the Supporting information appears to be linear with time in the entire timescale investigated. Consequently, we have increased the system packing by one order of magnitude. In Fig. 5.6, we report the viscous and elastic moduli for a system of nanocubes containing a spherical tracer of size $3\,\sigma$ at packing fraction $\eta = 0.20$. The Figure reports G' and G'' calculated from the tracer's total MSD when the field is off. In these conditions, the system exhibits a dominant viscous response as expected from a typical colloidal suspension of purely repulsive particles.

These preliminary results show how passive microrheology techniques can be employed to shed light on the viscoelastic behaviour of ER fluid by means of dynamic Monte

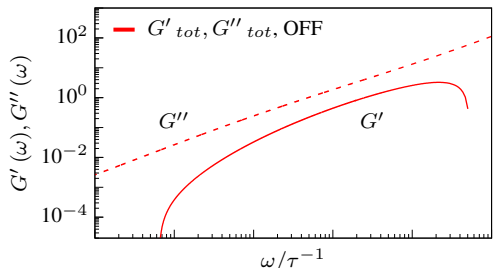

Figure 5.6: Viscous G'' (dashed line) and elastic G' (solid line) moduli of a suspension of hard cubes at a packing fraction $\eta = 0.2$ containing a spherical tracer of diameter $3\,\sigma$ when the external field is off.

Carlo simulations. The application of MR on the suspension with the field on will require a mindful and appropriate choice of the tracer, taking into considerations not only interactions of the tracer with the bath, but also between the tracer and the external field.

5.4 Conclusions

In summary, we employed DMC simulation to model the behaviour of colloidal suspensions of dielectric nanocubes upon application of an electric field. We also applied machine learning techniques to define a robust cluster criterion for the study of strings aggregation and breaking over time. Our results show that, at a volume fraction $\eta = 0.02$ and field strength $\gamma = 13$, the suspension reaches a steady state where $\sim 50\%$ of particles are organized in aligned string-like clusters, with steady lengths and dispersity, or in individual cubes with no preferential orientation. Over the isotropic-to-string-like transition, one first observes the formation of relatively short strings, comprising 2 or 3 nanocubes. Subsequently, while clusters are still breaking and merging, the fraction of particles in chains converges to a steady-state value, which is fully achieved at $t_r \sim 150\,\tau$. By contrast, the concentration of chains with more than 3 nanocubes increases monotonically until equilibrium is reached.

The kinetics of formation of clusters has been further investigated by analysing the transition probability of a nanocube to move from one cluster to another. Most nanocubes remain attached to a string over times shorter than the elementary time step and only a few of them move to clusters of different sizes. In fact, the larger the difference in size between the cluster a nanocube leaves and the cluster it joins, the lower the

transition probability. This suggests that any aggregation and fragmentation mechanism can potentially occur, with larger probabilities for mechanisms that involve string-like clusters of similar sizes.

Finally, we incorporated a spherical tracer into the system to recover the viscoelastic response of the suspension in the field-off scenario, by means of passive microrheology techniques. While in the very dilute system at $\eta = 0.02$, the motion of the selected tracer is completely unaffected by the presence of nanocubes, at higher concentration, specifically at $\eta = 0.2$, MR analysis showed a predominant viscous behaviour of the bath at all frequencies. These analysis can be used as a reference for further investigation of the microrheological behaviour of the same suspension when the field is applied.

All the simulation results reported in this work have been obtained neglecting the fluid-mediated hydrodynamic interactions (HI) between the nanocubes in suspension. Different works investigating the dynamics of colloids have shown quantitative discrepancies between simulations with and without HI, while retaining similar qualitative features [86, 87, 88]. The same characteristics have been observed in the analysis of rheological properties of electrorheological [89] and magnetorheological [75] fluids of spherical particles. HI have also been found to play a non-negligible role in active microrheology [90, 91] and their inclusion in simulation generally results into a better agreement with experiments [92]. Currently, a study on how HI can be incorporated into DMC simulation is in progress. Models of ER fluids can be further improved also by (i) incorporating mutual polarisation of bath particles and (ii) studying their behaviour under confinement to better reproduce an experimental setup.

Acknowledgments

The authors acknowledge the Leverhulme Trust Research Project Grant RPG-2018-415 and the use of Computational Shared Facility at the University of Manchester. A.P. is supported by a “Maria Zambrano Senior” distinguished researcher fellowship, financed by the European Union within the NextGenerationEU program and the Spanish Ministry of Universities.

Supporting information

5.S1 Cluster criterion optimisation via density-based cluster analysis

Defining a criterion to recognize when cubes belong to chains is fundamental for the analysis of all the properties of chain-like structures. Due to the cylindrical symmetry of the chains and considering that their formation is driven only by dipolar interactions between the centers of mass of the particles, we characterized the connectivity between two particles i and j using their relative dipolar interaction energy: i and j are connected if $\beta u_{ij,dip} < \beta u_{max}$, where βu_{max} is the cluster parameter. Since $\beta u_{ij,dip}$ depends only on the relative distance between particles and the alignment of $\mathbf{r}_{ij}$ with the external field, we optimized βu_{max} from the analysis of the distribution of the first two smallest values of $\|\mathbf{r}_{ij}\|$ for each particle, named $\mathbf{r}_{ij,1}$ and $\mathbf{r}_{ij,2}$, extrapolated from an equilibrated string-like configuration of cubes, where $\mathbf{r}_{ij,1}$ and $\mathbf{r}_{ij,2}$ are decomposed in the direction parallel ($r_{ij,\parallel}$) and perpendicular ($r_{ij,\perp}$) to the orientation of the field. Most of the points of the data set are found in the proximity of the minimum of the interaction potential between two cubes, as expected for particles disposed one on top of the other and aligned with the external field (see Fig. 5.7(a) for a plot of one sample data set).

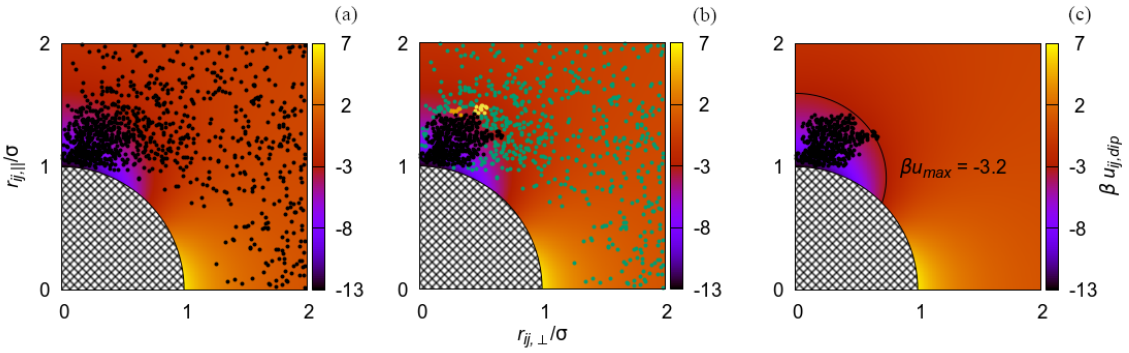

Figure 5.7: (a) Plot of the first and second closest particles j with respect to reference particle i, decomposed in the direction parallel and perpendicular to the external field, taken from a configuration of an equilibrated string-like phase of nanocubes. (b) Resulting clusters obtained from the application of DBSCAN algorithm to the points plotted in panel (a); points of the same color belong to a cluster according to DBSCAN. (c) Plot of the points of the cluster closest to the minimum of energy (black points), together with the contour line in which $\beta u_{ij,dip} = \beta u_{max}$. The background of each plot shows the value of the dipolar interaction energy $\beta u_{ij,dip}$ in color gradient, as a function of $r_{ij,\perp}$ and $r_{ij,\parallel}$. The patterned areas in black and white contain all the points for which $\|\mathbf{r}_{ij}\| < \sigma$, which are inaccessible due to hard core interactions between nanocubes.

In order to obtain an optimal value of βu_{max} for the analysis of the connectivity, we applied the DBSCAN clustering algorithm to the data set of the distances $\mathbf{r}_{ij}$. The DBSCAN algorithm analyses the local density of the data set, and assigns elements of the data set to a cluster if their density is higher than a threshold value [93]. It requires the definition of two parameters: Eps, which is the radius of the n-ball centered at element p; $MinPts$, which is the minimum number of elements q contained in the n-ball with radius Eps and center p. By definition, the set of points q found in the n-ball centered at p with radius Eps is called "Eps-neighbourhood" of p, and the number of elements of this set is N_{Eps}:

$$N_{Eps}(p) = \#\{q \in D \,|\, dist(p,q) \leq Eps\} \tag{5.19}$$

where D is the data set. The algorithm starts from a random element p_0 and computes all the neighbouring elements q. If $N_{Eps} \geq MinPts$, a new cluster is found and is made of p_0 plus all the neighbouring elements q. At this point, DBSCAN reiterates the computation of the "Eps-neighbourhood" for each element q, as long as new neighbor elements are found. The set of all the "Eps-neighbourhoods" found starting from p_0 is a cluster. When the iteration stops, the algorithm restarts the analysis from a random element left of the data set, until the entire data set is covered. A schematic representation of one step of the algorithm is shown in Fig. 5.8.

We performed density-based cluster analysis using the library DBSCAN available in R [80]. The algorithm was applied to 44 independent data sets, where each data set is extracted from uncorrelated configurations of an equilibrated chain-like phase of nanocubes. From each configuration, we computed the first ($\mathbf{r}_{ij,1}$) and second ($\mathbf{r}_{ij,2}$) closest distances between the centres of mass of two particles, with periodic boundary conditions, for all the particles of the configuration. Doubles of the distances $\mathbf{r}_{ij}$ were discarded. All the distances computed were saved as a 2D vector with components $(r_{ij,\parallel}, r_{ij,\perp})$. Since we were interested only in a portion of space were the energy reaches a minimum, we limited the data sets only to the points within the range $0 \leq r_{ij,\parallel}, r_{ij,\perp} \leq 2$. An example of resulting data set extrapolated from a configuration is shown in Fig. 5.7(a). We then applied DBSCAN to each data set independently, from which recovered only the points belonging to the cluster closest to the minimum of the energy. An example of application of the clustering algorithm to a data set is shown in Fig. 5.7(b), where the cluster of

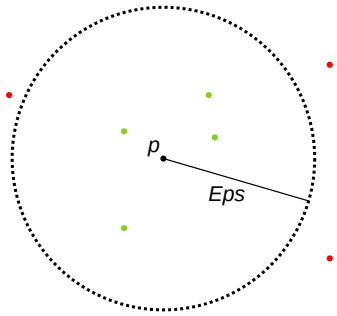

Figure 5.8: Representation of "Eps-neighbourhood" of p. All the points are elements of the data set. p is the initial element, Eps is the radius of the area in which we analyse the neighbourhood of p. Green points are elements that belong to the "Eps-neighbourhood" of p, while red points are outsiders. In one iteration, if the number of green points is $\geq MinPts$, then the green points plus p form a cluster, and the green points are chosen as new starting points p from which the cluster can be extended.

interest is highlighted in black. We finally computed the maximum value of the energy $\beta u_{ij,dip}$ for the points of each recovered cluster: all the points of each cluster belong to a portion of the $(r_{ij,\perp},r_{ij,\parallel})$ plot delimited by a contour line in which the energy is constant. We finally set the average of all contour energies of each data set as our threshold energy parameter $\beta u_{max} = \langle \beta u_{max} \rangle_{set} = -3.20$. Fig. 5.7(c) shows the the elements of the desired cluster extrapolated with DBSCAN, contained in the area delimited by the contour line in which $\beta u_{ij,dip} = \beta u_{max}$.

5.S2 Renormalisation of the uniaxial order parameter for particles with cubic symmetry

The most favoured configuration of two polarised nanocubes is for their two centers of mass to be relatively aligned with the external field and to be as close as possible, thus having one of their faces in contact with each other, and with these faces orthogonal to the orientation of the field $\hat{\mathbf{E}}$. For this reason, the orientational order of the cubic particles with respect to the external field, which can be evaluated with the uniaxial order parameter $U = \langle P_2(\hat{\mathbf{E}} \cdot \hat{\mathbf{e}}_i)\rangle$ (P_2 is the second Legendre polynomial), can indirectly give information on the formation of chain-like structures. However, due to the geometry of cubes, each of the three axes of orientation $\hat{\mathbf{e}}_1$, $\hat{\mathbf{e}}_2$, $\hat{\mathbf{e}}_3$ of every particle can be equivalently aligned with $\hat{\mathbf{E}}$ when they organise in chains. To overcome this issue, Batten *et al.* [31], in their work on the investigation of the phase behaviour of colloidal superballs, suggested to "relabel" particles axes of orientation according to their best alignment with the reference axes, hence for a reference axis $\hat{\mathbf{n}}$ they computed $\langle P_2(\max((|\hat{\mathbf{n}} \cdot e_k|), k = 1, 2, 3)\rangle$. Since in our case the director along which particles should be aligned is known and it is the orientation of the external field $\hat{\mathbf{E}}$, we computed the average of the alignment between $\hat{\mathbf{n}}$ and the most aligned axis $\hat{\mathbf{e}}_k$ of each cube, for $\hat{\mathbf{n}} = \hat{\mathbf{E}}$

$$\left\langle \max\left((\hat{\mathbf{n}} \cdot \hat{\mathbf{e}}_k)^2\right), i = \{1, 2, 3\} \right\rangle \tag{5.20}$$

Here we report the formal proof developed to normalize the order parameter in Eq. 5.20.

Fig. 5.9 shows one cube, with its axes of orientation, here taken as reference axes, and the director $\hat{\mathbf{n}}$ with one possible orientation with respect to $\hat{\mathbf{e}}_1$, $\hat{\mathbf{e}}_2$, and $\hat{\mathbf{e}}_3$. The prolongation of $\hat{\mathbf{n}}$ intersects always the surface of the cube. Due to the symmetry of the cube, for each possible direction of $\hat{\mathbf{n}}$, the most aligned axis of orientation $\hat{\mathbf{e}}_k$ with $\hat{\mathbf{n}}$ will always be the one orthogonal to the face whom the prolongation of $\hat{\mathbf{n}}$ intersects. This means that Eq. 5.20 can be normalised integrating only over the possible orientations of $\hat{\mathbf{n}}$ with respect to one of the faces of the cube: this normalisation corresponds to integrate $(\hat{\mathbf{n}} \cdot \hat{\mathbf{e}}_k)^2$ over one sixth of the surface of a unit sphere, which is schematically represented in Fig. 5.9 with blue lines, and all the angles between $\hat{\mathbf{n}}$ and one $\hat{\mathbf{e}}_k$, for which the extension of $\hat{\mathbf{n}}$ intersects the edges of one face of the cube, are boundaries of the integral. We can define $\hat{\mathbf{n}}$ in spherical coordinates as a function of two angles θ and ϕ with respect

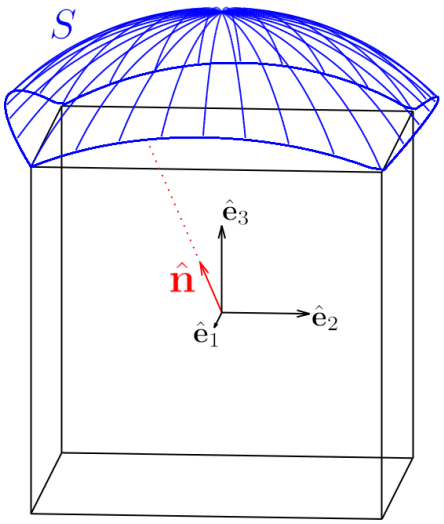

Figure 5.9: Cubic particle (black lines) topped with a portion of a sphere with surface S (in blue). $\hat{\mathbf{e}}_1$, $\hat{\mathbf{e}}_2$, $\hat{\mathbf{e}}_3$ are the three axes of orientation of the cube, originated from the center of mass. Red arrow shows one possible direction of the director $\hat{\mathbf{n}}$ and the red dot line is its extension up to surface S. S is the area in which integrate $(\hat{\mathbf{n}} \cdot \hat{\mathbf{e}}_3)^2$ for normalisation of the order parameter, where $\hat{\mathbf{e}}_3$ is here the most aligned axis with $\hat{\mathbf{n}}$.

to the axes of orientation of the cube and recover the following definitions, according to the geometric representation in Fig. 5.10 and assuming that the cube has unit length

$$\widehat{AO'H} = \phi$$

$$\widehat{HOO'} = \theta$$

$$\widehat{AO'B} = \frac{\pi}{4}$$

$$\widehat{HBO} = \widehat{BO'O} = \widehat{ABO'} = \frac{\pi}{2}$$

$$\overline{OH} = x$$

$$\overline{HB} = y$$

$$\overline{AO'} = \overline{OB} = \frac{1}{\sqrt{2}}$$

$$\overline{O'B} = \overline{OO'} = \frac{1}{2}$$

Thanks to geometry, we can recover the link between θ and ϕ for the case when $\hat{\mathbf{n}}$ intersect the edges of one of the faces of the cube. If $0 \leq \phi < \pi/4$, the following

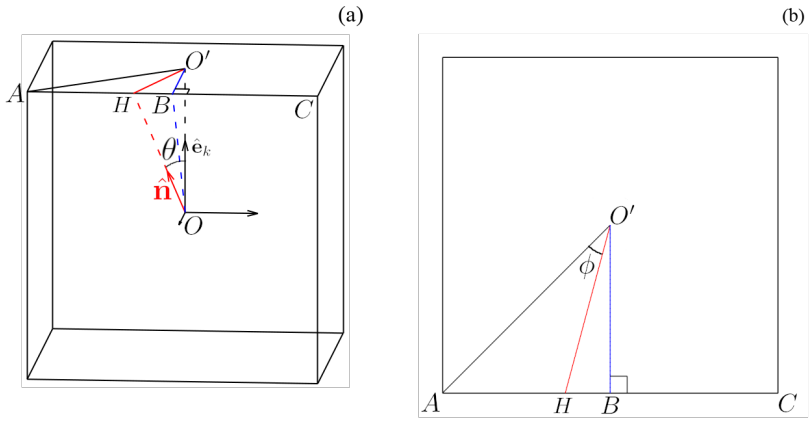

Figure 5.10: Geometric representation of the cube with the director $\hat{\mathbf{n}}$. Panel (a, left) shows the cube and all the projections in 3D; panel (b, right) shows the view from the top face of the cube. O is the center of mass of the cube. O' is the projection of O on the top face of the cube. A and C are two of the vertices of the cube. $\overline{AC}$ is one edge of the top face of the cube. B is the midpoint of $\overline{AC}$. Dashed blue line connects the origin O with the midpoint B, and straight blue line is the projection of $\overline{OB}$ on the top face of the cube. Both $\overline{OB}$ and $\overline{AO'}$ are half of the diagonal of one face of the cube. Both $\overline{O'B}$ and $\overline{OO'}$ are half of the length of one edge of the cube. Red arrow and dashed red line are, respectively, the unit vector $\hat{\mathbf{n}}$ and its extension $\overline{OH}$ to the edge $\overline{AC}$; the extension of $\hat{\mathbf{n}}$ intersect $\overline{AC}$ at H. Straight red line is the projection of $\overline{OH}$ on the top face of the cube. θ is the angle between $\hat{\mathbf{n}}$ and $\hat{\mathbf{e}}_k$. ϕ is the angle between the projection $\overline{AO'}$ and the projection $\overline{O'H}$.

equations hold

$$\cos(\theta) = \frac{\overline{OO'}}{\overline{OH}} = \frac{1}{2x}$$

$$x = \overline{OH} = \sqrt{\overline{OB}^2 + \overline{HB}^2} = \sqrt{\left(\frac{1}{\sqrt{2}}\right)^2 + y^2}$$

$$y = \overline{HB} = \overline{O'B}\tan\left(\widehat{HO'B}\right) = \frac{\tan\left(\frac{\pi}{4} - \phi\right)}{2}$$

$$\cos(\theta) = \frac{1}{\sqrt{2 + \tan^2\left(\frac{\pi}{4} - \phi\right)}} = f^{(+)}(\phi) \tag{5.21}$$

For $\pi/4 \leq \phi < \pi/2$, Eq. 5.21 holds since $\tan^2(x)$ is an even function. For $\pi/2 \leq \phi < 3\pi/4$, we obtain

$$y = \frac{\tan\left(\phi - \frac{\pi}{4} - \frac{\pi}{2}\right)}{2} = \frac{-\cot\left(\phi - \frac{\pi}{4}\right)}{2}$$

$$\cos(\theta) = \frac{1}{\sqrt{2 + \cot^2\left(\frac{\pi}{4} - \phi\right)}} = f^{(-)}(\phi) \tag{5.22}$$

The validity of Eq. 5.22 is extended to $3\pi/4 \leq \phi < \pi$ for the same reason as Eq. 5.21. Since both Eqs. 5.21 and 5.22 are periodic to π, we can define the link between θ and ϕ along the border of one face of the cube as follows

$$\cos(\theta) = \begin{cases} f^{(+)}(\phi) & if \quad 0 \leq \phi < \dfrac{\pi}{2} \cup \pi \leq \phi < \dfrac{3\pi}{2} \\ f^{(-)}(\phi) & if \quad \dfrac{\pi}{2} \leq \phi < \pi \cup \dfrac{3\pi}{2} \leq \phi < 2\pi \end{cases} \tag{5.23}$$

The average value of the order parameter for a uniform distribution of $\hat{\mathbf{n}}$ can be estimated according to the following integral

$$\left\langle \max\left((\hat{\mathbf{n}} \cdot \hat{\mathbf{e}}_k)^2\right)\right\rangle = \frac{\int\int_S \cos^2(\theta)\sin(\theta)d\theta d\phi}{\int\int_S \sin(\theta)d\theta d\phi} \tag{5.24}$$

where the limits of S depend on Eq. 5.23. We first compute the integral in the denominator of Eq. 5.24

$$\begin{aligned}\int\int_S \sin(\theta)d\theta d\phi = &\int_0^{\arccos(f^{(+)}(\phi))}\int_0^{\pi/2}\sin(\theta)d\theta d\phi + \int_0^{\arccos(f^{(-)}(\phi))}\int_{\pi/2}^{\pi}\sin(\theta)d\theta d\phi + \\ &+ \int_0^{\arccos(f^{(+)}(\phi))}\int_{\pi}^{3\pi/2}\sin(\theta)d\theta d\phi + \int_0^{\arccos(f^{(-)}(\phi))}\int_{3\pi/2}^{2\pi}\sin(\theta)d\theta d\phi\end{aligned}$$

We substitute $\int \sin(\theta)d\theta = -\cos(\theta)$, $\cos(0) = 1$ and $\cos(\arccos(f(\phi))) = f(\phi)$ in the integral

$$\begin{aligned}\int\int_S \sin(\theta)d\theta d\phi = &\int_0^{\pi/2}\left[1 - f^{(+)}(\phi)\right]d\phi + \int_{\pi/2}^{\pi}\left[1 - f^{(-)}(\phi)\right]d\phi + \\ &+ \int_{\pi}^{3\pi/2}\left[1 - f^{(+)}(\phi)\right]d\phi + \int_{3\pi/2}^{2\pi}\left[1 - f^{(-)}(\phi)\right]d\phi\end{aligned} \tag{5.25}$$

Since both $f^{(+)}$ and $f^{(-)}$ are periodic with period π and $\tan^2(x) = \cot^2(x - \pi/2)$, the following equalities hold

$$\int_0^{\pi/2} f^{(+)}(\phi)d\phi = \int_{\pi/2}^{\pi} f^{(-)}(\phi)d\phi = \int_{\pi}^{3\pi/2} f^{(+)}(\phi)d\phi = \int_{3\pi/2}^{2\pi} f^{(-)}(\phi)d\phi \tag{5.26}$$

Hence, integral in Eq. 5.25 simplifies

$$\int \int_S \sin(\theta) d\theta d\phi = 2\pi - 4 \int_0^{\pi/2} f^{(+)} d\phi$$

It can be proved that

$$\int_0^{\pi/2} f^{(+)} d\phi = \int_{-\pi/4}^{\pi/4} \frac{\cos(\phi)}{\sqrt{2 - \sin^2(\phi)}} d\phi = \frac{\pi}{3}$$

The solution of the integral is

$$\int \int_S \sin(\theta) d\theta d\phi = 2\pi - 4\frac{\pi}{3} = \frac{2\pi}{3} \tag{5.27}$$

This is what we should expect for this geometry: the surface we integrated over is exactly one sixth of the surface of a unit sphere (since we have integrated the surface of a unit sphere only for those angles of θ and ϕ for which the intersection of the prolongation of $\hat{\mathbf{n}}$ with the surface of the cube is contained in one face of the cube).

In order to solve the integral in the numerator of Eq. 5.24, we use the equality $\int \cos^2(\theta) \sin(\theta) dx = -\cos^3(\theta)/3$ and we obtain an equation similar to Eq. 5.25, with $[f^{(+)}]^3$ instead of $f^{(+)}$, and $[f^{(-)}]^3$ instead of $f^{(-)}$. Since the equalities in Eq. 5.26 hold also in this case, the desired integral can be simplified as follows

$$\int \int_S \cos^2(\theta) \sin(\theta) d\theta d\phi = \frac{2\pi}{3} - \frac{4}{3} \int_0^{\pi/2} \left[f^{(+)}(\phi) \right]^3 d\phi$$

It can be proved that

$$\int_0^{\pi/2} \left[f^{(+)}(\phi) \right]^3 d\phi = \int_{-\pi/4}^{\pi/4} \frac{1 - \sin^2(\phi)}{\left[2 - \sin^2(\phi) \right]^{3/2}} \cos(\phi) d\phi = \frac{\pi}{3} - \frac{1}{\sqrt{3}} \tag{5.28}$$

In conclusion, the integral in the numerator of Eq. 5.24 is

$$\int \int_S \cos^2(\theta) \sin(\theta) d\theta d\phi = \frac{2\pi}{3} - \frac{4}{3} \left(\frac{\pi}{3} - \frac{1}{\sqrt{3}} \right) = \frac{2\pi + 4\sqrt{3}}{9} \tag{5.29}$$

Finally, we substitute Eq. 5.27 and Eq. 5.29 into Eq.5.24 to recover the expected value of

$\max((\hat{\mathbf{n}} \cdot \hat{\mathbf{e}}_k)^2)$ for a uniform distribution of orientations of $\hat{\mathbf{n}}$

$$\left\langle \max\left((\hat{\mathbf{n}} \cdot \hat{\mathbf{e}}_k)^2\right)\right\rangle = \frac{\frac{2\pi + 4\sqrt{3}}{9}}{\frac{2\pi}{3}} = \frac{\pi + 2\sqrt{3}}{3\pi} \tag{5.30}$$

As a proof that this value is indeed correct, we remark that Batten *et al.* noticed that, for an isotropic phase of superballs, $\langle P_2(\max(\hat{\mathbf{n}} \cdot \hat{\mathbf{e}}_k))\rangle \approx 0.55$, which is exactly what we obtain:

$$\left\langle P_2\left(\max\left(|\hat{\mathbf{n}} \cdot \hat{\mathbf{e}}_k|\right)\right)\right\rangle = \frac{1}{2}\left\langle 3\max\left((\hat{\mathbf{n}} \cdot \hat{\mathbf{e}}_k)^2\right) - 1\right\rangle = \frac{1}{2}\left(3\frac{\pi + 2\sqrt{3}}{3\pi} - 1\right) = \frac{\sqrt{3}}{\pi} \approx 0.55$$

Normalising $\max((\hat{\mathbf{n}} \cdot \hat{\mathbf{e}}_k)^2)$ with the result in Eq. 5.30 and imposing that the parameter goes to 1 when $\max((\hat{\mathbf{n}} \cdot \hat{\mathbf{e}}_k)^2) = 1$, i.e., when the cube is perfectly aligned with $\hat{\mathbf{n}}$, we can finally obtain a renormalised uniaxial order parameter for particles with cubic symmetry

$$S = \frac{1}{N}\sum_{i=1}^{N} S_i = \frac{1}{N}\sum_{i=1}^{N} \frac{\pi\left(3\max\left((\hat{\mathbf{n}} \cdot \hat{\mathbf{e}}_{k,i})^2, k = 1,2,3\right) - 1\right) - 2\sqrt{3}}{2\pi - 2\sqrt{3}} \tag{5.31}$$

5.S3 Mean square displacement of a spherical tracer immersed in a bath of nanocubes

Fig. 5.11 depicts the mean square displacement (MSD) of a spherical tracer immersed in a bath of nanocubes with side σ at packing fractions $\eta = 0.02$ and $\eta = 0.2$, respectively. The MSD is estimated when the external field is off. The MSD of the tracer particle can be defined from the tracer's position $\mathbf{r}_d(t)$ at time t as follows

$$\langle \Delta \mathbf{r}_d^2(t) \rangle = \langle (\mathbf{r}_d^2(t) - \mathbf{r}_d^2(0))^2 \rangle \tag{5.32}$$

where the brackets refer to the averages over independent trajectories, and d is the dimensionality of the displacements of the tracer, in this case $d = 3$. To calculate the MSDs we have run 1000 uncorrelated trajectories to simulate the motion of the tracer and bath particles.

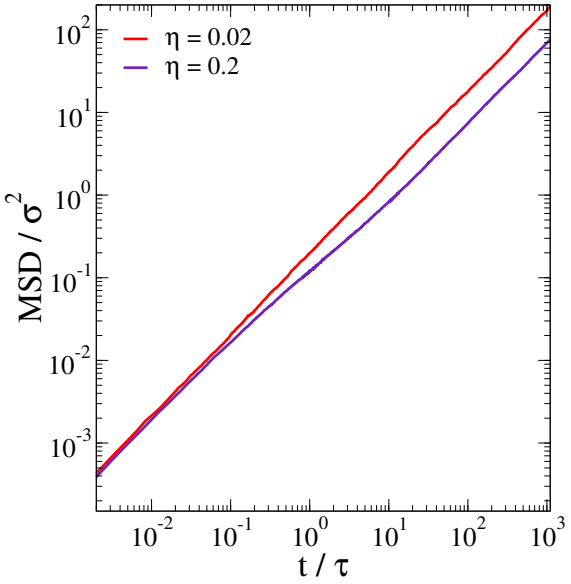

Figure 5.11: Total mean square displacement of a spherical tracer of size 3σ diffusing across a bath of nanocubes of side σ at a packing fraction $\eta = 0.02$ (red line) and $\eta = 0.2$ (purple line), in the field-off scenario.

5.S4 Benchmarking between the Fourier and compliance-based methods to calculate the elastic and viscous moduli of a bath of nanocubes

The compliance methods [73, 74] intend to transform the time dependent compliance ($J(t)$) of the material to estimate its corresponding complex modulus ($G^*(\omega)$) in the frequency domain. The compliance can be expressed as

$$J(t) = \left(\frac{\pi a_{sph}}{k_B T} \right) \langle \Delta r^2(t) \rangle, \tag{5.33}$$

where a_{sph} indicates the radius of the tracer, k_B the Boltzmann's constant, T the temperature, and $\langle \Delta r^2(t) \rangle$ the tracer's mean square displacement (MSD). According to Evans *et al.* [73], $J(t)$ can be related to $G^*(\omega)$ by

$$\frac{i\omega}{G^*(\omega)} = \left(1 - e^{-1\omega t_1}\right) \frac{J(t_1)}{t_1} + 6De^{-i\omega t_{N_t}} + \sum_{k=2}^{N_t} \frac{J_k - J_{k-1}}{t_k - t_{k-1}} \left(e^{-i\omega t_{k-1}} - e^{-i\omega t_k}\right), \tag{5.34}$$

where N_t denotes the number of points within the time window where the MSD was computed, D is linked to the inverse of the system's viscosity, and J_k refers to $J(t)$ at time t_k. The solution of Eq. 5.34 results in the viscous ($G''(\omega)$) and elastic ($G'(\omega)$) moduli since $G^*(\omega) = G'(\omega) + iG''(\omega)$.

The comparison between $G''(\omega)$ and $G'(\omega)$ calculated by the Fourier approach by Mason [72] and the compliance method proposed by Evans *et al.* [73] is presented in Fig. 5.12. In both cases, the MSD of a spherical tracer with size 3σ diffusing in a bath of nanocubes is calculated when the external field is off.

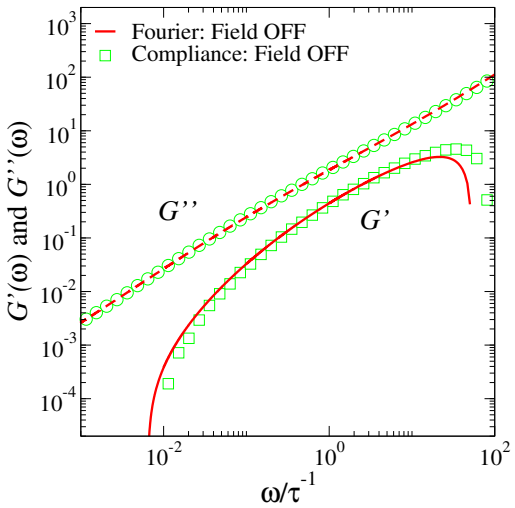

Figure 5.12: Viscous $G''(\omega)$ (empty circles, dashed lines) and elastic $G'(\omega)$ (empty squares, solid lines) moduli obtained by the Fourier approach [72] (lines) and the compliance-based method [73] (symbols) for a bath of nanocubes containing a spherical tracer of size 3σ, in the field-off scenario.

Bibliography

[1] Winslow, W. M. Induced Fibration of Suspensions. *J. Appl. Phys.* **20**, 1137–1140 (1949).

[2] Hao, T. Electrorheological fluids. *Advanced Materials* **13**, 1847–1857 (2001).

[3] Zhang, K., Liu, Y. D. & Choi, H. J. Carbon nanotube coated snowman-like particles and their electro-responsive characteristics. *Chem. Commun.* **48**, 136–138 (2012).

[4] Dong, Y. Z., Seo, Y. & Choi, H. J. Recent development of electro-responsive smart electrorheological fluids. *Soft Matter* **15**, 3473–3486 (2019).

[5] Clausius, R. *Behandlung dielectrischer Medien*, 62–97 (Vieweg+Teubner Verlag, Wiesbaden, 1879).

[6] Mossotti, O. F. *Discussione analitica sull'influenza che l'azione di un mezzo dielettrico ha sulla distribuzione dell'elettricità alla superficie di più corpi elettrici disseminati in esso*, 49–74 (Società Italiana delle Scienze, Modena, 1850).

[7] Toor, W. R. Structure Formation in Electrorheological Fluids. *J. Coll. Inter. Sci.* **156**, 335–349 (1993).

[8] Martin, J. E., Odinek, J. & Halsey, T. C. Evolution of structure in a quiescent electrorheological fluid. *Phys. Rev. Lett.* **69**, 1524–1527 (1992).

[9] Martin, J. E., Odinek, J., Halsey, T. C. & Kamien, R. Structure and dynamics of electrorheological fluids. *Phys. Rev. E* **57**, 756–775 (1998).

[10] Cao, J. G., Huang, J. P. & Zhou, L. W. Structure of Electrorheological Fluids under an Electric Field and a Shear Flow: Experiment and Computer Simulation. *J. Phys. Chem. B* **110**, 11635–11639 (2006).

[11] Horváth, B. & Szalai, I. Structure of electrorheological fluids: A dielectric study of chain formation. *Phys. Rev. E* **86**, 061403 (2012).

[12] Belijar, G. *et al.* Dynamics of particle chain formation in a liquid polymer under ac electric field: modeling and experiments. *J. Phys. D: Appl. Phys.* **50**, 025303 (2016).

[13] Baxter-Drayton, Y. & Brady, J. F. Brownian electrorheological fluids as a model for flocculated dispersions. *J. Rheo.* **40**, 1027–1056 (1996).

[14] Klingenberg, D. J., van Swol, F. & Zukoski, C. F. Dynamic simulation of electrorheological suspensions. *J. Chem. Phys.* **91**, 7888–7895 (1989).

[15] Whittle, M. Computer simulation of an electrorheological fluid. *J. Non-Newtonian Fluid Mech.* **37**, 233–263 (1990).

[16] Hass, K. C. Computer simulations of nonequilibrium structure formation in electrorheological fluids. *Phys. Rev. E* **47**, 3362–3373 (1993).

[17] Fertig, D., Boda, D. & Szalai, I. Induced permittivity increment of electrorheological fluids in an applied electric field in association with chain formation: A Brownian dynamics simulation study. *Phys. Rev. E* **103**, 062608 (2021).

[18] Fertig, D., Boda, D. & Szalai, I. A systematic study of the dynamics of chain formation in electrorheological fluids. *AIP Advances* **11**, 25243 (2021).

[19] Sun, Y. & Xia, Y. Shape-Controlled Synthesis of Gold and Silver Nanoparticles. *Science* **298**, 2176–2179 (2002).

[20] Manoharan, V. N., Elsesser, M. T. & Pine, D. J. Dense Packing and Symmetry in Small Clusters of Microspheres. *Science* **301**, 483–487 (2003).

[21] Shankar, S. S. *et al.* Biological synthesis of triangular gold nanoprisms. *Nature Materials* **3**, 482–488 (2004).

[22] Xiang, Y. *et al.* Formation of Rectangularly Shaped Pd/Au Bimetallic Nanorods: Evidence for Competing Growth of the Pd Shell between the 110 and 100 Side Facets of Au Nanorods. *Nano Letters* **6**, 2290–2294 (2006).

[23] Sacanna, S., Irvine, W. T. M., Chaikin, P. M. & Pine, D. J. Lock and key colloids. *Nature* **464**, 575–578 (2010).

[24] Okuno, Y. *et al.* Uniform and controllable preparation of Au–Ag core–shell nanorods using anisotropic silver shell formation on gold nanorods. *Nanoscale* **2**, 1489–1493 (2010).

[25] Cortie, M. B., Liu, F., Arnold, M. D. & Niidome, Y. Multimode Resonances in Silver Nanocuboids. *Langmuir* **28**, 9103–9112 (2012).

[26] Sacanna, S. *et al.* Shaping colloids for self-assembly. *Nature Communications* **4**, 1688 (2013).

[27] Khlebtsov, B. N., Liu, Z., Ye, J. & Khlebtsov, N. G. Au@Ag core/shell cuboids and dumbbells: Optical properties and SERS response. *Journal of Quantitative Spectroscopy and Radiative Transfer* **167**, 64–75 (2015).

[28] Rossi, L. *et al.* Shape-sensitive crystallization in colloidal superball fluids. *Proceedings of the National Academy of Sciences* **112**, 5286–5290 (2015).

[29] Glotzer, S. C. & Solomon, M. J. Anisotropy of building blocks and their assembly into complex structures. *Nat. Mater.* **6**, 557–562 (2007).

[30] Zhang, X., Zhang, Z. & Glotzer, S. C. Simulation Study of Dipole-Induced Self-Assembly of Nanocubes. *J. Phys. Chem. C* **111**, 4132–4137 (2007).

[31] Batten, R. D., Stillinger, F. H. & Torquato, S. Phase behavior of colloidal superballs: Shape interpolation from spheres to cubes. *Phys. Rev. E* **81**, 061105 (2010).

[32] Damasceno, P. F., Engel, M. & Glotzer, S. C. Predictive Self-Assembly of Polyhedra into Complex Structures. *Science* **337**, 453–457 (2012).

[33] Donaldson, J. G., Linse, P. & Kantorovich, S. S. How cube-like must magnetic nanoparticles be to modify their self-assembly? *Nanoscale* **9**, 6448–6462 (2017).

[34] Cuetos, A., Dennison, M., Masters, A. & Patti, A. Phase behaviour of hard board-like particles. *Soft Matter* **13**, 4720–4732 (2017).

[35] Donaldson, J. G., Pyanzina, E. S. & Kantorovich, S. S. Nanoparticle Shape Influences the Magnetic Response of Ferro-Colloids. *ACS Nano* **11**, 8153–8166 (2017).

[36] Patti, A. & Cuetos, A. Monte Carlo simulation of binary mixtures of hard colloidal cuboids. *Molecular Simulation* **44**, 516–522 (2018).

[37] Chiappini, M., Drwenski, T., van Roij, R. & Dijkstra, M. Biaxial, Twist-bend, and Splay-bend Nematic Phases of Banana-shaped Particles Revealed by Lifting the "Smectic Blanket". *Phys. Rev. Lett.* **123**, 068001 (2019).

[38] Cuetos, A., Mirzad Rafael, E., Corbett, D. & Patti, A. Biaxial nematics of hard cuboids in an external field. *Soft Matter* **15**, 1922–1926 (2019).

[39] Casquilho, J. P. & Figueirinhas, J. L. Lattice Monte Carlo study of orientational order in a confined system of biaxial particles: Effect of an external electric field. *Phys. Rev. E* **103**, 032701 (2021).

[40] Yan, J., Chaudhary, K., Chul Bae, S., Lewis, J. A. & Granick, S. Colloidal ribbons and rings from Janus magnetic rods. *Nat. Commun.* **4**, 1516 (2013).

[41] Okada, K. & Satoh, A. 3D Monte Carlo simulations on the aggregate structures of a suspension composed of cubic hematite particles. *Molecular Physics* **116**, 2300–2309 (2018).

[42] Kuijk, A. *et al.* Effect of external electric fields on the phase behavior of colloidal silica rods. *Soft Matter* **10**, 6249–6255 (2014).

[43] Smallenburg, F., Vutukuri, H. R., Imhof, A., van Blaaderen, A. & Dijkstra, M. Self-assembly of colloidal particles into strings in a homogeneous external electric or magnetic field. *Journal of Physics: Condensed Matter* **24**, 464113 (2012).

[44] Hynninen, A.-P. & Dijkstra, M. Phase Diagram of Dipolar Hard and Soft Spheres: Manipulation of Colloidal Crystal Structures by an External Field. *Phys. Rev. Lett.* **94**, 138303 (2005).

[45] Kanu, R. C. & Shaw, M. T. Enhanced electrorheological fluids using anisotropic particles. *J. Rheo.* **42**, 657–670 (1998).

[46] Qi, Y. & Wen, W. Influences of geometry of particles on electrorheological fluids. *J. Phys. D: Appl. Phys.* **35**, 2231–2235 (2002).

[47] He, K. *et al.* Synthesis of anatase TiO2 with exposed (100) facets and enhanced electrorheological activity. *Soft Matter* **13**, 7879–7889 (2017).

[48] Vutukuri, H. R. *et al.* Colloidal Analogues of Charged and Uncharged Polymer Chains with Tunable Stiffness. *Angewandte Chemie International Edition* **51**, 11249–11253 (2012).

[49] Vutukuri, H. R., Bet, B., van Roij, R., Dijkstra, M. & Huck, W. T. S. Rational design and dynamics of self-propelled colloidal bead chains: from rotators to flagella. *Sci. Rep.* **7**, 16758 (2017).

[50] Huang, S. *et al.* Colloidal Polymers of Iron Oxide Cubes Prepared by Dipolar-Driven Assembly and In Situ Welding with Silica. *Giant* **9**, 100083 (2022).

[51] Patti, A. & Cuetos, A. Brownian dynamics and dynamic Monte Carlo simulations of isotropic and liquid crystal phases of anisotropic colloidal particles: A comparative study. *Phys. Rev. E* **86**, 011403 (2012).

[52] Cuetos, A. & Patti, A. Equivalence of Brownian dynamics and dynamic Monte Carlo simulations in multicomponent colloidal suspensions. *Phys. Rev. E* **92**, 022302 (2015).

[53] Corbett, D., Cuetos, A., Dennison, M. & Patti, A. Dynamic Monte Carlo algorithm for out-of-equilibrium processes in colloidal dispersions. *Phys. Chem. Chem. Phys.* **20**, 15118–15127 (2018).

[54] García Daza, F. A., Cuetos, A. & Patti, A. Dynamic Monte Carlo simulations of inhomogeneous colloidal suspensions. *Phys. Rev. E* **102**, 013302 (2020).

[55] Chiappini, M., Patti, A. & Dijkstra, M. Helicoidal dynamics of biaxial curved rods in twist-bend nematic phases unveiled by unsupervised machine learning techniques. *Phys. Rev. E* **102**, 040601 (2020).

[56] Patti, A. & Cuetos, A. Dynamics of colloidal cubes and cuboids in cylindrical nanopores. *Physics of Fluids* **33**, 097103 (2021).

[57] García Daza, F. A., Puertas, A. M., Cuetos, A. & Patti, A. Microrheology of colloidal suspensions via dynamic Monte Carlo simulations. *J. Col. Inter. Sci.* **605**, 182–192 (2022).

[58] Vutukuri, H. R. *et al.* An experimental and simulation study on the self-assembly of colloidal cubes in external electric fields. *Soft Matter* **10**, 9110–9119 (2014).

[59] Gottschalk, S., Lin, M. C. & Manocha, D. OBBTree: A Hierarchical Structure for Rapid Interference Detection. In *Proceedings of the 23rd Annual Conference on Com-*

puter Graphics and Interactive Techniques, SIGGRAPH '96, 171–180 (Association for Computing Machinery, New York, NY, USA, 1996).

[60] Rosenberg, M., Dekker, F., Donaldson, J. G., Philipse, A. P. & Kantorovich, S. S. Self-assembly of charged colloidal cubes. *Soft Matter* **16**, 4451–4461 (2020).

[61] Parthasarathy, M. & Klingenberg, D. J. Electrorheology: Mechanisms and models. *Materials Science and Engineering: R: Reports* **17**, 57–103 (1996).

[62] Allen, M. P. & Tildesley, D. J. Chapter 6 - Long-range forces. In Allen, M. P. & Tildesley, D. J. (eds.) *Computer simulation of liquids*, 216–257 (Oxford University Press, Oxford, 2017), second edition edn.

[63] Tonti, L. & Patti, A. Fast Overlap Detection between Hard-Core Colloidal Cuboids and Spheres. The OCSI Algorithm. *Algorithms* **14**, 72 (2021).

[64] Tonti, L., García Daza, F. A. & Patti, A. Diffusion of globular macromolecules in liquid crystals of colloidal cuboids. *Journal of Molecular Liquids* **338**, 116640 (2021).

[65] García de la Torre, J., del Rio Echenique, G. & Ortega, A. Improved Calculation of Rotational Diffusion and Intrinsic Viscosity of Bead Models for Macromolecules and Nanoparticles. *J. Phys. Chem. B* **111**, 955–961 (2007).

[66] Hansen, J.-P. & McDonald, I. R. Chapter 2 - Statistical Mechanics. In Hansen, J.-P. & McDonald, I. R. (eds.) *Theory of Simple Liquids (Fourth Edition)*, 13–59 (Academic Press, Oxford, 2013), fourth edition edn.

[67] Busselez, R. *et al.* Discotic columnar liquid crystal studied in the bulk and nanoconfined states by molecular dynamics simulation. *J. Chem. Phys.* **141**, 134902 (2014).

[68] Morillo, N. *Anisotropy & self-assembly. A walk through intricate free-energy landscapes.* Ph.D. thesis, Department of Physical, Chemical and Natural System of the Pablo de Olavide University, Seville, Spain (2019).

[69] Sevick, E. M., Monson, P. A. & Ottino, J. M. Monte Carlo calculations of cluster statistics in continuum models of composite morphology. *J. Chem. Phys.* **88**, 1198–1206 (1988).

[70] Mason, T. G. & Weitz, D. A. Optical Measurements of Frequency-Dependent Linear Viscoelastic Moduli of Complex Fluids. *Phys. Rev. Lett.* **74**, 1250–1253 (1995).

[71] Mason, T. G., Ganesan, K., van Zanten, J. H., Wirtz, D. & Kuo, S. C. Particle Tracking Microrheology of Complex Fluids. *Phys. Rev. Lett.* **79**, 3282–3285 (1997).

[72] Mason, T. G. Estimating the viscoelastic moduli of complex fluids using the generalized Stokes–Einstein equation. *Rheol. Acta* **39**, 371–378 (2000).

[73] Evans, R. M. L., Tassieri, M., Auhl, D. & Waigh, T. A. Direct conversion of rheological compliance measurements into storage and loss moduli. *Phys. Rev. E* **80**, 012501 (2009).

[74] Nishi, K., Kilfoil, M. L., Schmidt, C. F. & MacKintosh, F. C. A symmetrical method to obtain shear moduli from microrheology. *Soft Matter* **14**, 3716–3723 (2018).

[75] Segovia-Gutiérrez, J. P., de Vicente, J., Hidalgo-Álvarez, R. & Puertas, A. M. Brownian dynamics simulations in magnetorheology and comparison with experiments. *Soft Matter* **9**, 6970–6977 (2013).

[76] Xie, W., Pu, J. & Gao, J. A Coupled Polarization-Matrix Inversion and Iteration Approach for Accelerating the Dipole Convergence in a Polarizable Potential Function. *J. Phys. Chem. A* **113**, 2109 (2009).

[77] Bernardo, D. N., Ding, Y., Krogh-Jespersen, K. & Levy, R. M. An Anisotropic Polarizable Water Model: Incorporation of All-Atom Polarizabilities into Molecular Mechanics Force Fields. *J. Phys. Chem.* **98**, 4180 (1994).

[78] Vesely, F. J. N-particle dynamics of polarizable Stockmayer-type molecules. *J. Comp. Phys.* **24**, 361 (1977).

[79] Kwaadgras, B. W., Van Roij, R. & Dijkstra, M. Self-consistent electric field-induced dipole interaction of colloidal spheres, cubes, rods, and dumbbells. *J. Chem. Phys.* **140**, 154901 (2014).

[80] Hahsler, M., Piekenbrock, M. & Doran, D. dbscan: Fast Density-Based Clustering with R. *Journal of Statistical Software* **91**, 1–30 (2019).

[81] Schubert, E., Sander, J., Ester, M., Kriegel, H. P. & Xu, X. DBSCAN Revisited, Revisited: Why and How You Should (Still) Use DBSCAN. *ACM Trans. Database Syst.* **42**, 19 (2017).

[82] Wertheim, M. S. Fluids with highly directional attractive forces. I. Statistical thermodynamics. *J. Stat. Phys.* **35**, 19–34 (1984)).

[83] Wertheim, M. S. Fluids with highly directional attractive forces. II. Thermodynamic perturbation theory and integral equations. *J. Stat. Phys.* **35**, 35–47 (1984).

[84] Wertheim, M. S. Fluids with highly directional attractive forces. III. Multiple attraction sites. *J. Stat. Phys.* **42**, 459–476 (1986).

[85] Chiricotto, M., Melchionna, S., Derreumaux, P. & Sterpone, F. Multiscale Aggregation of the Amyloid Aβ16–22 Peptide: From Disordered Coagulation and Lateral Branching to Amorphous Prefibrils. *J. Phys. Chem. Lett.* **10**, 1594–1599 (2019).

[86] Lettinga, M. P., Dhont, J. K. G., Zhang, Z., Messlinger, S. & Gompper, G. Hydrodynamic interactions in rod suspensions with orientational ordering. *Soft Matter* **6**, 4556–4562 (2010).

[87] Kwon, G., Sung, B. J. & Yethiraj, A. Dynamics in Crowded Environments: Is Non-Gaussian Brownian Diffusion Normal? *The Journal of Physical Chemistry B* **118**, 8128–8134 (2014).

[88] Pryamitsyn, V. & Ganesan, V. Screening of hydrodynamic interactions in Brownian rod suspensions. *The Journal of Chemical Physics* **128**, 134901 (2008).

[89] Parthasarathy, M. & Klingenberg, D. J. Large amplitude oscillatory shear of ER suspensions. *Journal of Non-Newtonian Fluid Mechanics* **81**, 83–104 (1999).

[90] Weeber, R. & Harting, J. Hydrodynamic interactions in active colloidal crystal microrheology. *Phys. Rev. E* **86**, 057302 (2012).

[91] Khair, A. S. & Brady, J. F. Single particle motion in colloidal dispersions: a simple model for active and nonlinear microrheology. *Journal of Fluid Mechanics* **557**, 73–117 (2006).

[92] García de la Torre, J. *et al.* SIMUFLEX: Algorithms and Tools for Simulation of the Conformation and Dynamics of Flexible Molecules and Nanoparticles in Dilute Solution. *Journal of Chemical Theory and Computation* **5**, 2606–2618 (2009).

[93] Ester, M., Kriegel, H. P., Sander, J. & Xu, X. A Density-Based Algorithm for Discovering Clusters in Large Spatial Databases with Noise. In *Proceedings of the Second International Conference on Knowledge Discovery and Data Mining*, 226 (1996).

Chapter 6

Dynamics of Uniaxial-to-Biaxial Nematics Switching in Suspensions of Hard Cuboids

The content of this Chapter has been published as an article in *Physics of Fluids*. My contributions are listed as follows: Luca Tonti provided coding support for dynamical property calculations; Effran Mirzad Rafael, Luca Tonti, Daniel Corbett, Alejandro Cuetos and Alessandro Patti performed the investigation; Effran Mirzad Rafael, Luca Tonti, Daniel Corbett, Alejandro Cuetos and Alessandro Patti reviewed and edited the draft.

Abstract

Field-induced reorientation of colloidal particles is especially relevant to manipulate the optical properties of a nanomaterial for target applications. We have recently shown that surprisingly feeble external stimuli are able to transform uniaxial nematic liquid crystals (LCs) of cuboidal particles into biaxial nematic LCs. In the light of these results, here we apply an external field that forces the reorientation of colloidal cuboids in nematic LCs and sparks a uniaxial-to-biaxial texture switching. By Dynamic Monte Carlo simulation, we investigate the unsteady-state reorientation dynamics at the particle scale when the field is applied (uniaxial-to-biaxial switching) and then removed (biaxial-to-uniaxial switching). We detect a strong correlation between the response time, being the time taken for the system to reorient, and particle anisotropy, which spans from rod-like to plate-like geometries. Interestingly, self-dual shaped cuboids, theoretically considered as the most suitable to promote phase biaxiality for being exactly in between prolate and oblate particles, exhibit surprisingly slow response times, especially if compared to prolate cuboids.

6.1 Introduction

Colloids are biphasic systems comprising particles homogeneously dispersed in a medium. In colloidal suspensions, the dispersed phase consists of solid particles, while the continuous phase is a liquid. In particular, the dispersed particles should have at least in one direction a dimension roughly between 1 nm and 1 μm, so that gravitational and thermal forces compensate each other [1]. This balance allows the dispersed particles to remain suspended and to diffuse randomly *via* Brownian motion, named after the Scottish botanist Robert Brown who, in 1827, described the persistent and casual jumpy moves of organelles suspended in water [2]. If the suspended particles are anisotropic, under certain conditions, they can self-assemble into liquid-crystalline phases. Liquid crystals (LCs) are mesophases that flow like liquids but, exhibit a significant degree of internal ordering like crystals. A common LC morphology is the uniaxial nematic (N_U) phase where particles have one axis pointing collectively in the same direction, but their centres of mass are randomly distributed. This merely orientational ordering allows nematic LCs to exhibit optical birefringence while maintaining mechanical fluidity. In the engineering of commercial displays, uniaxial and chiral nematic LCs are widely employed [3, 4]. Very recently, there has been reignited interest in the biaxial nematic phase (N_B) and its potential to be incorporated into display technology. In contrast to the N_U phase, the N_B phase possesses two optical axes due to the alignment of the three directors, making it very appealing for the design of nanomaterials with novel optical properties [5]. Equally important, the N_B phase is also foreseen to realise faster switching through its minor axis switching mode, an aspect that could potentially improve refresh rates in displays [6, 7, 8]. Despite these promising features, the existence of stable molecular N_B phases is still an ongoing debate within the LC community. While a biaxial geometry is indeed necessary to observe N_B phases, it has been shown that this requirement might not be sufficient as the N_B phase tends to be metastable with respect to other phases, including N_U and smectic (Sm) LCs [9]. This is for instance the case of colloidal cuboids, which can only form N_B phases at sufficiently large size dispersity [10, 11], extreme anisotropy [12], in the presence of depletants [13] or upon application of an external field [14, 15]. Unless at least one of these conditions are met, systems of monodispersed or bidispersed cuboids cannot form N_B phases [16, 17]. Research efforts have also been made to ascertain, by theory, simulation and experiments, the existence

of N_B phases in systems of other biaxial particles [18, 19, 20, 21, 22, 23, 24, 25, 26, 27] or mixtures of uniaxial particles [28].

Despite such a widespread interest in mapping the phase behaviour of colloidal suspensions of biaxial particles, including cuboids, the study of their dynamics is still at an embryonic stage, especially for the difficulty of finding suitable interaction potentials that could describe exotic geometries and still be framed within a simulation technique. Exotic shapes are commonly described by hard-core potentials, but these cannot be directly employed in Brownian dynamics (BD) or Molecular Dynamics (MD) simulations. Nevertheless, it is only by assessing the dynamics that one will be able to draw relevant conclusions on the potential use of nematic or other LC phases in specific applications. With this in mind, over the last years, our group has developed a stochastic method that can qualitatively and quantitatively mimic the Brownian motion of colloids as obtained by BD simulations [29, 30, 31, 32]. This method, referred to as Dynamic Monte Carlo (DMC), has become an established simulation technique not only for the study of the dynamics of biaxial particles, such as cuboids and curved rods [33, 34], but also for the dynamics of uniaxial particles, like rods, for which soft potentials are indeed available [35, 36].

With regards to the equilibrium dynamics of cuboids, we found that the system long-time relaxation dramatically depends on particle anisotropy, being slower at the self-dual shape, the geometry that would preferentially stabilise biaxial nematics [34]. Our simulations also confirmed the occurrence of a Fickian and Gaussian dynamics at both short and long times, thus providing an alternative picture to the claimed universality of Fickian yet non-Gaussian dynamics in soft-matter systems [37]. For its potential impact in nanotechnology, equally intriguing is the out-of-equilibrium dynamics of cuboids, especially because it can spark phase switching and new material properties. In general, the reorientation dynamics of biaxial particles induced by an external stimulus has received very limited attention. At the molecular scale, Lee and co-workers studied the reorientation dynamics of N_B phases of bent-core mesogens and measured primary and secondary axis switching, finding the latter either 3 or 100 times faster than the former depending on the mesogen [6]. Although this study was met with some scepticism [38], Zannoni and co-workers later on performed MD simulations on N_B phases of biaxial Gay-Berne ellipsoids and confirmed that the rotation of minor axes is indeed faster, although only

up to one order of magnitude, than the rotation of the main axis, both in the bulk [7] and under confinement [8]. Following our recent findings on the field-induced stability of the N_B phase [15], here we explore the field-induced dynamics of switching from uniaxial to biaxial nematics of colloidal cuboids, with special interest in the particle reorientation dynamics and associated response time. More specifically, we are interested to study the kinetics of reorientation of LCs transitioning between two different nematic textures, namely an $N_U \rightarrow N_B$ transition under an external field, and an $N_B \rightarrow N_U$ relaxation when the field is switched off, and estimate the associated response times. To gain an insight into the impact of particle anisotropy on the dynamics of phase switching, we consider monodispersed systems of prolate, oblate and self-dual shaped cuboids. Their ability of reorienting under the effect of an external field is assessed by employing a DMC algorithm specifically designed to track the dynamics of out-of-equilibrium colloidal systems [31].

This paper is organised as follows. We first introduce the methodology to simulate our systems and characterise the dynamics. We then discuss the results of our simulations by analysing the effect of particle anisotropy on the out-of-equilibrium dynamics in $N_U \rightarrow N_B$ and $N_B \rightarrow N_U$ switching before finally drawing our conclusions.

6.2 Model and simulation methodology

We modelled monodispersed colloidal cuboids as hard board-like particles (HBPs) constrained in a cubic box with periodic boundaries. The behaviour of hard-core systems is basically determined by the packing fraction, which is given by:

$$\eta \equiv \frac{N v_o}{V} \tag{6.1}$$

where N is the number of particles, v_o the volume of an individual HBP and V the volume of the simulation box. The particle thickness, T, is set as the system unit length. Consequently, particle length and width are given in units of T, and read $L^* \equiv L/T$ and $W^* \equiv W/T$, respectively. In particular, $L^* = 12$ for all systems studied, while W^* assumed values between 1 (rod-like HBPs) and 12 (plate-like HBPs) and included $W^* = \sqrt{L^*}$ at the self-dual shape. Similar to our previous work [15], we apply an external field that promotes alignment of the particle intermediate axis, defined by:

$$U_{\text{ext}} = -\frac{\varepsilon_f}{2}\left[3 \cdot (\hat{\mathbf{x}}_i \cdot \hat{\mathbf{e}})^2 - 1\right] \tag{6.2}$$

where ε_f is the field strength, $\hat{\mathbf{x}}$ is the unit vector associated with the width of particle i, while $\hat{\mathbf{e}}$ is the field direction. We have set the reduced field strength, $\varepsilon_f^* \equiv \varepsilon_f \beta = 3$, with β the inverse temperature. The unit vectors $\hat{\mathbf{y}}$ and $\hat{\mathbf{z}}$ are associated with thickness and length, respectively. The orientation of the particle unit vectors before and after application of the field is schematically displayed in Fig. 6.1.

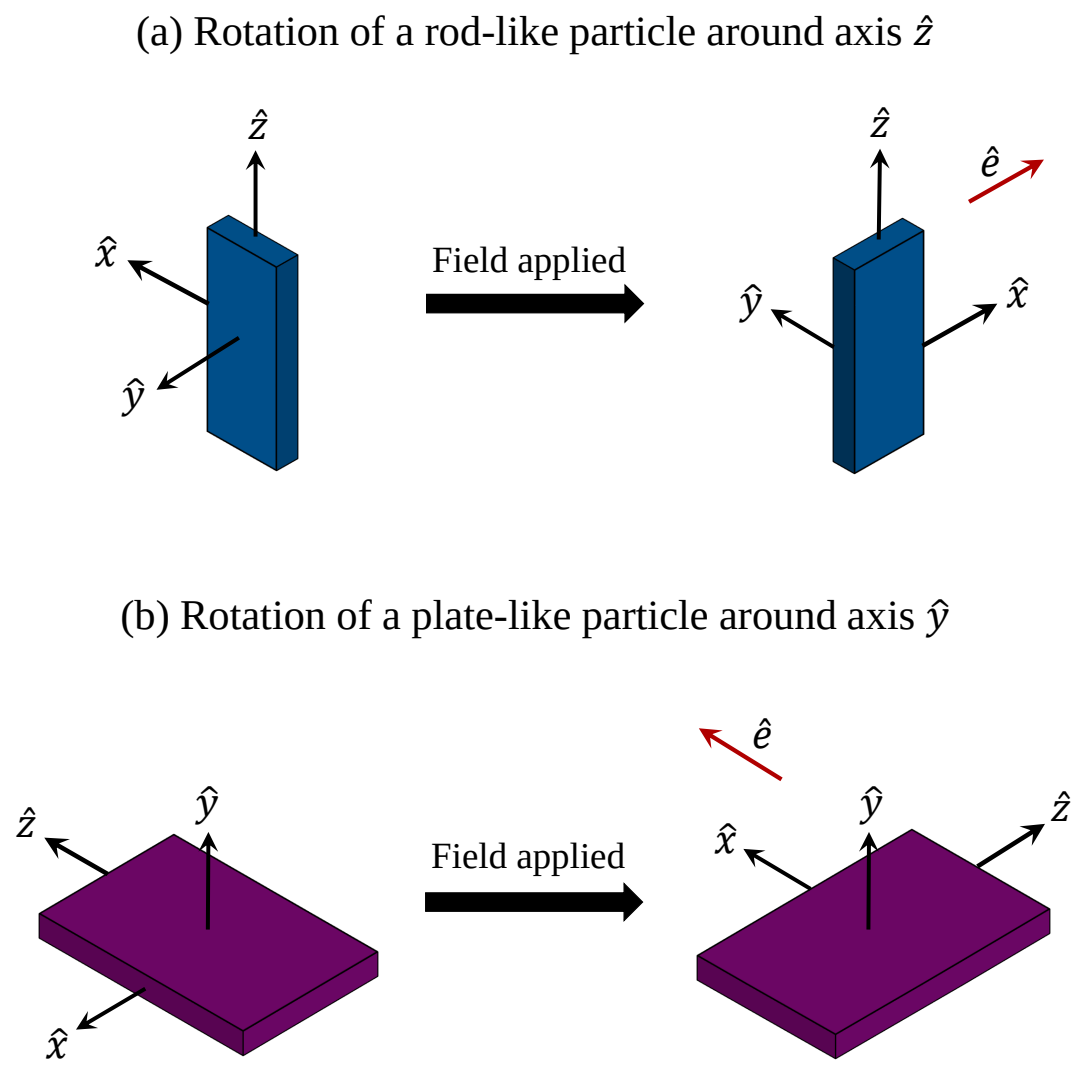

Figure 6.1: Reorientation of a prolate (a) and oblate (b) HBP due to external field $\hat{\mathbf{e}}$ coupled to the particle intermediate axis $\hat{\mathbf{x}}$.

The focus of this work is on the reorientation dynamics of HBPs in an external field.

We first performed standard Monte Carlo (MC) simulations in the canonical ensemble in a cubic box containing $N = 2000$ HBPs to equilibrate N_U^+ and N_U^- phases at $\eta = 0.34$, where N_U^+ and N_U^- refer, respectively to prolate and oblate nematic LCs. At this packing fraction, the N_U phases (either prolate or oblate) are stable across all anisotropies [16]. Each MC cycle consists of N attempts to displace and/or rotate HBPs, which are accepted if no overlaps are detected. To determine the occurrence of overlaps between pairs of HBPs, we implemented the separating axes theorem by Gottschalk *et al.* [39], adapted by John and Escobedo to study tetragonal parallelepipeds [40, 41]. To quantify the system long-range orientational order, we calculated the nematic order parameter and director associated to each particle axis. To this end, we performed the diagonalisation of a second-rank symmetric tensor of the form:

$$\mathbf{Q}^{\lambda\lambda} = \frac{1}{2N}\left\langle \sum_{i=1}^{N} \left(3\hat{\lambda}_i \cdot \hat{\lambda}_i - \mathbf{I}\right) \right\rangle \tag{6.3}$$

where $\hat{\lambda}_i = \hat{\mathbf{x}}, \hat{\mathbf{y}}, \hat{\mathbf{z}}$ are unit vectors aligned with W, T and L respectively, while $\mathbf{I}$ is the identity tensor. The diagonalisation of $\mathbf{Q}^{\lambda\lambda}$ results in three eigenvalues ($S_{2,W}$, $S_{2,T}$, $S_{2,L}$) and their corresponding eigenvectors ($\hat{\mathbf{m}}, \hat{\mathbf{l}}, \hat{\mathbf{n}}$). The nematic director of an N_U phase is the eigenvector with the largest eigenvalue. For instance, if the largest positive eigenvalue is $S_{2,L}$, then the nematic director is $\hat{\mathbf{n}}$, indicating high degree of orientational order along the $\hat{\mathbf{z}}$ axis of the particles. The biaxial order parameters can also be evaluated using the same symmetric tensor. For example, the biaxial order parameter that quantifies the fluctuations of particles' axes $\hat{\mathbf{x}}$ and $\hat{\mathbf{y}}$ respectively along the directors $\hat{\mathbf{m}}$ and $\hat{\mathbf{l}}$ reads [16]

$$B_{2,L} = \frac{1}{3}\left(\hat{\mathbf{m}} \cdot \mathbf{Q}^{xx} \cdot \hat{\mathbf{m}} + \hat{\mathbf{l}} \cdot \mathbf{Q}^{yy} \cdot \hat{\mathbf{l}} - \hat{\mathbf{m}} \cdot \mathbf{Q}^{yy} \cdot \hat{\mathbf{m}} - \hat{\mathbf{l}} \cdot \mathbf{Q}^{xx} \cdot \hat{\mathbf{l}}\right) \tag{6.4}$$

The values of $B_{2,W}$ and $B_{2,T}$ can be calculated using similar expressions. Following the definition introduced in our former work, a phase is considered to be biaxial if $B_2 \geq 0.35$, although weak biaxial phases can already be observed for $B_2 \geq 0.20$ [15, 11]. We monitor the evolution of uniaxial and biaxial order parameters until they have plateaued and fluctuate in a bounded range. The equilibrated configurations are then used for external field application in DMC simulations.

To study the dynamics, we performed DMC simulations in the canonical ensemble. Because our goal is producing realistic time trajectories, unphysical moves, such

as cluster moves, swaps, jumps and changes in box dimension (which would result in centres of mass rescaling) are not implemented. The position of the particle centre of mass is updated by decoupling the displacement $\delta \mathbf{r}_i$ into three contributions, with $\delta \mathbf{r}_i = X_W \hat{\mathbf{x}} + X_T \hat{\mathbf{y}} + X_L \hat{\mathbf{z}}$. Rotational moves are performed by three consecutive reorientations around $\hat{z}$, $\hat{x}$ and $\hat{y}$, with maximum rotations of Y_L, Y_W and Y_T, respectively. The extent of particle displacement and rotation are picked from uniform distributions that depend on the particle translational, $D^{tra}_{\alpha,i}$, and rotational, $D^{rot}_{\alpha,i}$, diffusion coefficients at infinite dilution, with $\alpha = L, W, T$. Maximum displacements and rotations are given by:

$$|X_\alpha| \leq \sqrt{2 D^{tra}_{\alpha,i} \delta t_{MC}} \tag{6.5}$$

$$|Y_\alpha| \leq \sqrt{2 D^{rot}_{\alpha,i} \delta t_{MC}} \tag{6.6}$$

where δt_{MC} is the DMC timescale for one cycle, and is set to $\delta t_{MC} = 10^{-2}\tau$ for all simulations, with τ the time unit. The coefficients $D^{tra}_{\alpha,i}$ and $D^{rot}_{\alpha,i}$ have been estimated by using the open-source software HYDRO++ [42, 43]. The interested reader is referred to our previous work [34] for the specific values of these translational and rotational diffusivities in units of $D_o \equiv T^2\tau^{-1}$ and $D_r \equiv \mathrm{rad}^2\tau^{-1}$ respectively. For a monodispersed out-of-equilibrium system, the Brownian dynamics timescale, δt_{BD}, can be obtained by rescaling the MC time scale as follows

$$\delta t_{BD} = \frac{\mathcal{A}_c}{3} \delta t_{MC} \tag{6.7}$$

where $\mathcal{A}_c$ is the time-dependent acceptance rate calculated at the cth MC cycle over the transitory unsteady state [31]. We determine $\mathcal{A}_c$ by performing an MC cycle at a fixed δt_{MC} and integrating the above equation numerically:

$$t_{\mathrm{BD}}(\mathcal{C}_{\mathrm{MC}}) = \delta t_{\mathrm{MC}} \sum_{c=0}^{\mathcal{C}_{\mathrm{MC}}} \frac{\mathcal{A}_c}{3} \tag{6.8}$$

where $t_{\mathrm{BD}}(\mathcal{C}_{MC})$ is the Brownian time after $\mathcal{C}_{\mathrm{MC}}$ MC cycles.

To characterise the dynamics, we estimated (*i*) the response times, (*ii*) the mean square angular displacement (MSAD), and (*iii*) the angular self-part of the van-Hove function (s-VHF). We refer to the field-on (t_{ON}) and field-off (t_{OFF}) response times as the

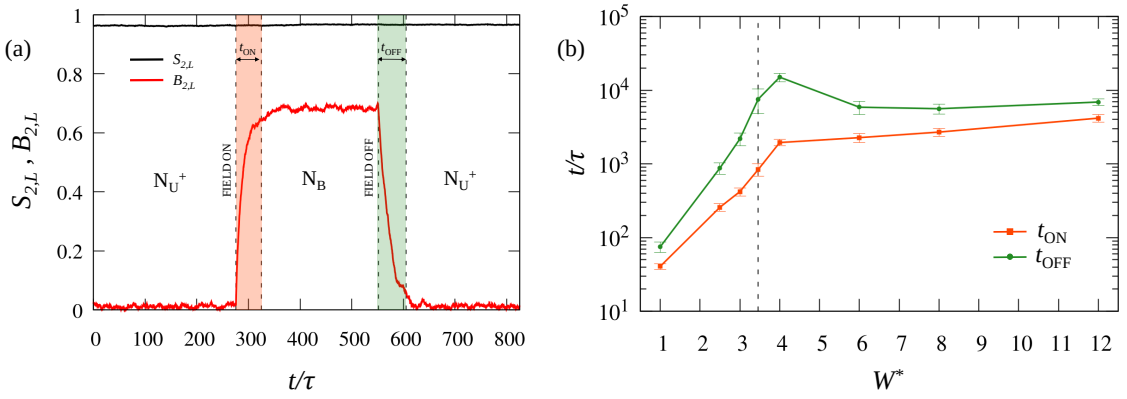

Figure 6.2: (a) Uniaxial and biaxial order parameters of a system with HBPs of $W^* = 1$ undergoing equilibration with an external field with $\varepsilon_f^* = 3$. The field is switched on at $t/\tau \approx 280$ and switched off at $t/\tau \approx 550$. The shaded orange area corresponds to t_{ON} while the green shaded area corresponds to t_{OFF}. (b) Response times (t_{ON} and t_{OFF}) as a function of W^* with $\varepsilon_f^* = 3$. The dashed vertical line in (b) represents the self-dual shape that separates the prolate and oblate geometries.

time taken for the biaxial order parameter to reach, respectively, 95% (field-on) and 105% (field-off) of its equilibrium value. In particular, when a field is applied to an $\mathrm{N_U^+}$ phase, t_{ON} is the time taken for $B_{2,L}$ to reach 95% of its equilibrium value in the field-on steady state. A schematic illustration of how we performed this evaluation is reported in Fig. 6.2(a). Both sets of response times have been calculated from an average over 50 independent trajectories per system. Approximately 2% of these trajectories have given response times that were very different from those generally observed. Since these anomalies tend to distort averages and give misleadingly large error bars, we have considered them as outliers and excluded them from the average. To this end, we employed the Modified Z-score method, a multiple outlier rejection technique to identify statistical anomalies [44]. In particular, the Modified Z-score, M_j, is given by the expression:

$$M_j = \frac{0.6745 \times \left(t_j - \tilde{t}\right)}{MAD} \tag{6.9}$$

where t_j is the response time of trajectory j, $\tilde{t}$ is the median response time of the 50 trajectories and MAD stands for median absolute deviation. An observable is considered an outlier only if $M_j > 3.5$ [44].

The MSAD provides the ensemble average of the particle angular displacements over time. To compute the MSAD, we employ a definition of an unbounded MSAD akin to the translational mean square displacement. To this end, we first introduce the definition of

a rotational displacement vector which takes the form [45, 46]:

$$\vec{\varphi}(t) = \int_0^t \delta\vec{\varphi}(t')dt' \tag{6.10}$$

where $\delta\vec{\varphi}(t')$ is a vector with direction $\hat{\lambda}_i(t') \times \hat{\lambda}_i(t' + dt')$ and magnitude $|\delta\vec{\varphi}(t')| = \cos^{-1}[\hat{\lambda}_i(t') \cdot \hat{\lambda}_i(t' + dt')]$. From this, we can define the MSAD, which is mathematically expressed as:

$$\langle \varphi^2(t) \rangle = \frac{1}{N} \left\langle \sum_{i=1}^{N} |\vec{\varphi}_i(t) - \vec{\varphi}_i(0)|^2 \right\rangle \tag{6.11}$$

where $\vec{\varphi}_i$ is the rotational displacement vector of particle i defined in Eq. 6.10. Angular brackets denote average over different trajectories. Finally, the so-defined rotational displacements are employed to compute the angular s-VHF [45, 46]:

$$G(\varphi, t) = \frac{1}{N} \left\langle \sum_{i=1}^{N} \delta(\varphi - |\vec{\varphi}_i(t + t_0) - \vec{\varphi}_i(t_0)|) \right\rangle \tag{6.12}$$

where the symbol δ is the Dirac delta function. Basically, $G(\varphi, t)$ provides the probability distribution of angular displacements of particles within a time $t + t_0$ given their position at time t_0.

6.3 Results

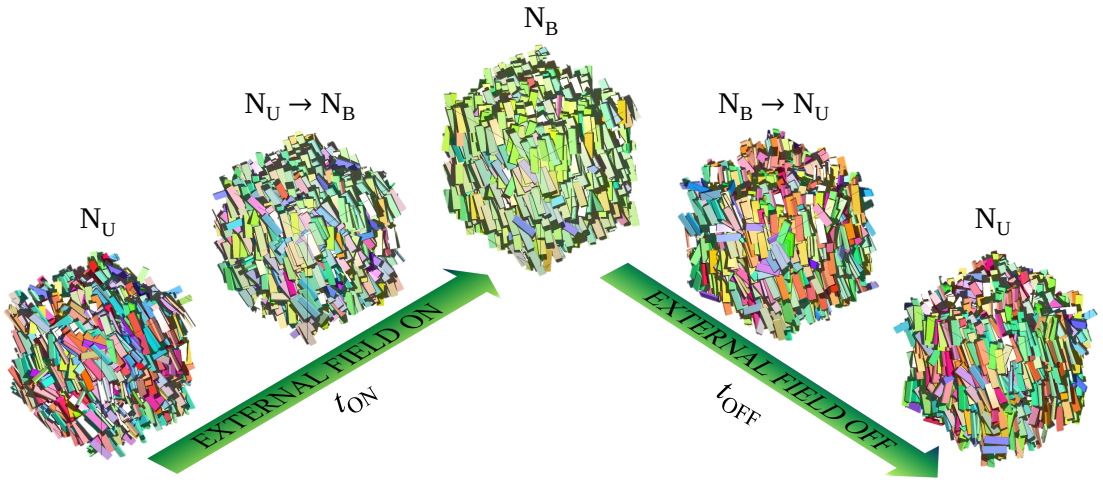

Figure 6.3: Schematic illustration of a field-induced $N_U \rightarrow N_B$ and a free $N_B \rightarrow N_U$ switching.

Upon application of a sufficiently strong external field, an N_U phase can be trans-

formed into an N_B phase [15]. This transformation is not permanent, and, when the field is removed, uniaxiality is restored. The time taken by the particles to reorient along the field director measures the system's ability of switching to a more ordered configuration. Vice-versa, when the field is removed, the particles are left free to rotate and the system recovers its original uniaxial state. A schematic illustration of both transitory states is given in Fig. 6.3. We have measured the response time associated to both $N_U \rightarrow N_B$ and $N_B \rightarrow N_U$ transitions upon application of the field U_{ext} with $\varepsilon_f^* = 3$. The effect of changing field intensity between $\varepsilon_f^* = 1.5$ and 3 on the $N_U \rightarrow N_B$ response time has also been assessed and is available, for the interested reader, in Appendix A. The resulting response times, t_{ON} and t_{OFF}, are reported in Fig. 6.2(b). Since the formation of a field-induced N_B phase is dependent on the alignment of the particle intermediate axis $\hat{x}$ with the external field, the discussion that follows is relative to this axis, unless otherwise stated. To start with, we notice that $t_{ON} < t_{OFF}$ across the complete set of anisotropies (see Fig. 6.2(b)). In other words, at a given particle width, the $N_U \rightarrow N_B$ switching is faster than the $N_B \rightarrow N_U$ switching. To understand the origin of this behaviour, we calculated the MSADs of our systems and compared the field-on and field-off profiles for each anisotropy.

The MSAD of systems with $W^* = 2.5$ and 6 are shown, respectively, in the top and bottom frames of Fig. 6.4. At very short times, the field-on and field-off MSADs are very similar to each other, with the former becoming larger immediately after and up to relatively long time scales. Over this period of time, field-induced rotation is faster than free rotation. However, on time scales comparable to t_{ON}, a crossover between the two MSADs is observed. On these time scales and beyond, free rotation grows significantly much faster with time than field-induced rotation. We therefore conclude that the presence of the external field accelerates the system orientational dynamics by forcing the reorientation of the particle $\hat{x}$ axis along the field director. As more and more HBPs are oriented, the field-on MSAD grows less and less with time and would eventually saturate to a plateau if the field strength was sufficiently large to offset and overcome thermal forces. By contrast, the field-off MSAD practically shows the same behaviour with time over the full time scale, as expected in free rotational diffusion. As for the effect of anisotropy on the response time, we first discuss the case of the field-induced uniaxial-to-biaxial transitory state.

In Fig. 6.2(b), t_{ON} increases with W^*, implying that the reorientation is slower for

oblate than for prolate particles. More specifically, for rod-like HBPs ($W^* = 1$), we observe a rapid switching with $t_{ON}/\tau \approx 41$, whereas for plate-like HBPs ($W^* = 12$), it is significantly slower, with $t_{ON}/\tau \approx 4200$. Consequently, making HBPs more oblate leads to a slower field-induced $N_U \rightarrow N_B$ transition. To confirm these preliminary tendencies, we compare the MSADs of the field-on regimes of each anisotropy along the three axes. The top frames of Fig. 6.5 display the field-on MSADs of systems containing HBPs with $W^* = 1$, 3.46 and 12. We notice that the MSAD of the particle axis oriented as the nematic director of the original N_U phase is the smallest across all the geometries. More specifically, the MSAD of rod-like particles in Fig. 6.5(a) exhibits a strong rotational coupling between $\hat{x}$ and $\hat{y}$ particle axes, while $\hat{z}$ is practically unaffected by the application of the field. Such a strong angular correlation between $\hat{x}$ and $\hat{y}$, with $\langle\varphi_W^2\rangle = \langle\varphi_T^2\rangle$ over time, is due to the square cross-sectional area of this specific set of HBPs, where $W = T$. For similar reasons, plate-like HBPs with $W = L$ exhibit strong rotational correlations between their axes $\hat{x}$ and $\hat{z}$, with $\langle\varphi_W^2\rangle = \langle\varphi_L^2\rangle$ (see Fig. 6.5(c)), while $\langle\varphi_T^2\rangle$, slightly increasing over time for mere thermal fluctuations, remains very small, practically insensible to the external field. In systems of self-dual shaped HBPs ($W^* = 3.46$), we observe that the MSADs of W and T are initially coupled, but then diverge over time. This behaviour is observed for all anisotropies that are not perfectly rod-like or plate-like and agrees very well with the tendencies reported in our recent work on the equilibrium dynamics of HBPs [34].

When analysing the field-on MSADs of the particle axes perpendicular to the original nematic director, we also notice an initially linear, rather steep dependence on time, followed by an intermediate non-linear behaviour and subsequently by a second linear regime at times comparable to t_{ON}. Such a long-time linear regime suggests that HBPs' angular displacements are gradually reducing, due to the system approaching a new equilibrium state. Under these conditions, further rotations of the particle intermediate axis $\hat{x}$, which is already aligned with the field, are suppressed, and only small angular fluctuations are detected. At much larger field strengths, with thermal fluctuations completely inhibited, we expect this second linear regime to plateau at long times. In agreement with Fig. 6.2(b), we also observe that systems with rod-like HBPs ($W^* = 1$) only take $t/\tau \approx 17$ to reach $\langle\varphi_W^2\rangle = 0.6$ rad^2, whereas systems with self-dual shaped ($W^* = 3.46$) or plate-like ($W^* = 12$) HBPs take, respectively, $t/\tau \approx 250$ and $t/\tau \approx 1600$ to

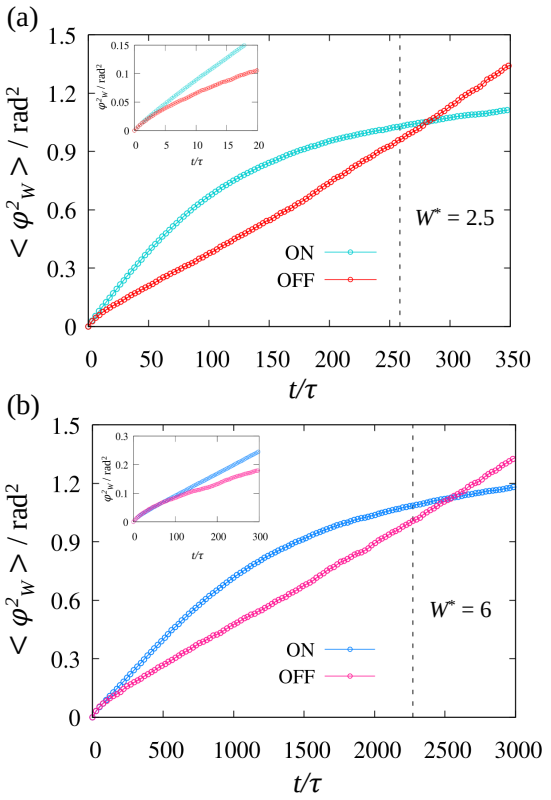

Figure 6.4: MSAD in field-on and field-off scenarios of a system of HBPs with reduced width (a) $W^* = 2.5$ and (b) $W^* = 6$. The field-on simulations apply an external field of strength $\varepsilon_f^* = 3$. The dashed vertical lines indicate t_{ON} of each systems (t_{OFF} is out of scale and not shown). The insets in (a) and (b) show the MSAD at shorter timescales.

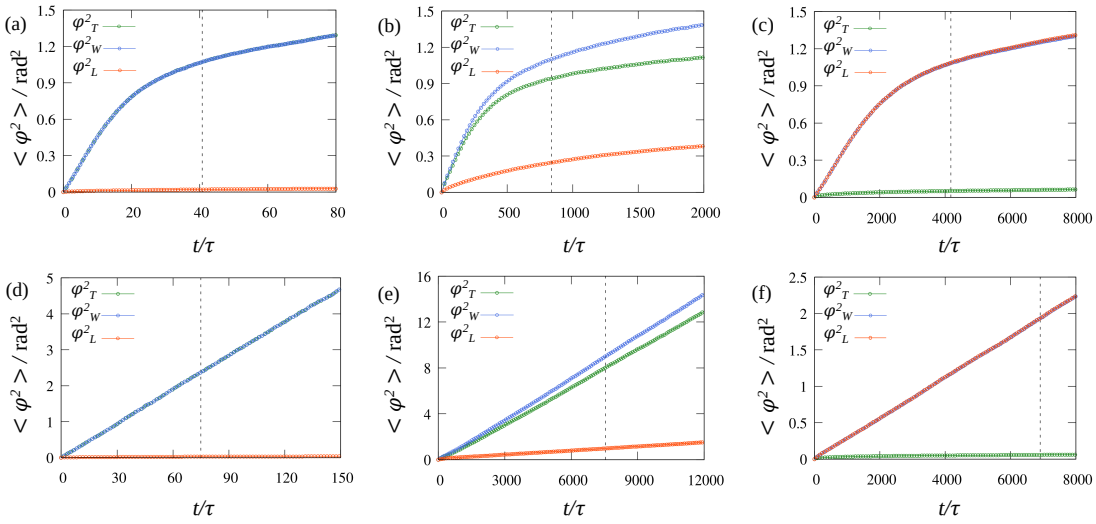

Figure 6.5: MSAD of the $\hat{x}$, $\hat{y}$ and $\hat{z}$ axes of HBPs for systems undergoing $\mathrm{N_U} \rightarrow \mathrm{N_B}$ transition with $\varepsilon_f^* = 3$ for (a) prolate; (b) self-dual and (c) oblate HBPs, and $\mathrm{N_B} \rightarrow \mathrm{N_U}$ transition when the field is switched off for a (d) prolate; (e) self-dual and (f) oblate HBPs. The dashed vertical lines in each Figure represent the t_{ON} for (a)-(c) and t_{OFF} for (d)-(f).

achieve the same MSAD value. This suggests that prolate HBPs tend to reorient significantly faster when an external field is applied, leading to a relatively rapid equilibration.

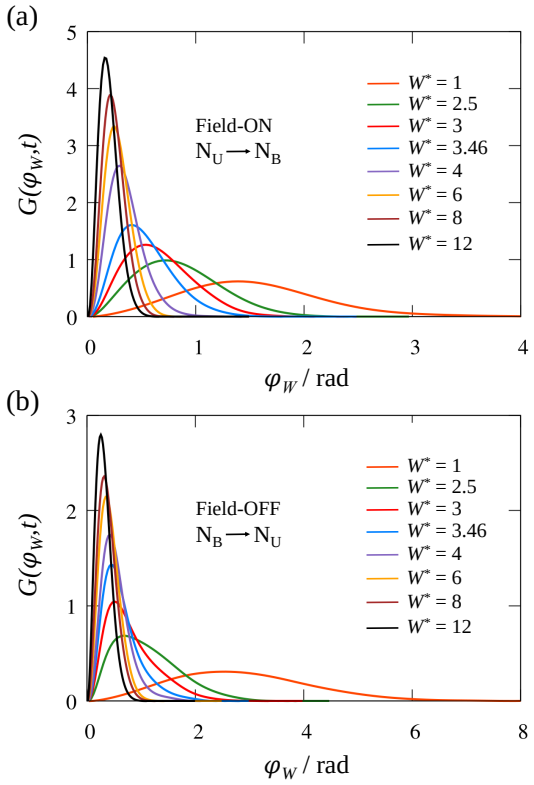

Figure 6.6: (a) Angular s-VHFs of (a) field-on reorientation at time $t/\tau = 35$ and (b) field-off reorientation at time $t/\tau = 100$.

To gain a better insight into the dynamics of reorientation during this first transitory unsteady state, we calculated the s-VHFs of all anisotropies at $t/\tau = 35$, corresponding to a time when all field-on cases are still undergoing equilibration. As the MSAD for field-off scenarios are linear, we arbitrarily picked $t/\tau = 100$ to show the field-off s-VHFs. The s-VHFs shown in Fig. 6.6 refer to the intermediate axis and have been normalised such that $\int_0^\infty 4\pi\varphi^2 G(\varphi,t)d\varphi = 1$. The first evident conclusion, confirming the results discussed so far, is that prolate HBPs rotate faster than oblate HBPs. This can be appreciated in Fig. 6.6(a) by pinpointing the location of the peak of $G(\varphi_W,t)$, which indicates the most probable rotation achieved by particles of a given geometry at $t/\tau = 35$. In particular, the peak of $G(\varphi_{W=T},t)$ and $G(\varphi_{W=L},t)$ suggests that rod-like and plate-like particles have rotated, respectively, by $\varphi_W \approx 1.4$ rad and $\varphi_W \approx 0.2$ rad. By increasing particle width from $W^* = 1$ to 12, the peak of the angular s-VHFs gradually displaces towards lower rotations. Not only does the particle anisotropy determine the location of the peak of

these distributions at a given time, but also their broadness. In other words, the angular s-VHFs provide relevant information on the most probable rotation performed by HBPs and on the existence of HBPs that rotate faster or slower than the average. In particular, the presence of fast- and slow-responsive HBPs is evinced by the tails of the distributions in Fig. 6.6(a), especially broad at $W^* = 1$ and then narrower and narrower up to $W^* = 12$. Therefore, rod-like HBPs rotate relatively fast, but heterogeneously (broad $G(\varphi_W, t)$ peaked at large distances), whereas plate-like HBPs are significantly slower, but rotate much more homogeneously (narrow $G(\varphi_W, t)$ peaked at short distances).

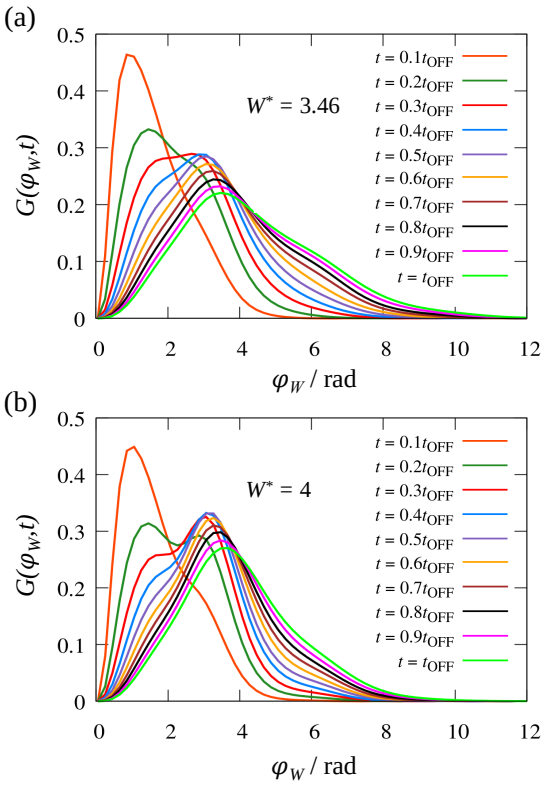

Figure 6.7: (a) Angular s-VHFs at various times, expressed as percentage of t_{OFF}, in systems of HBPs with (a) $W^* = 3.46$ and (b) $W^* = 4$.

When the field is switched off, the system recovers its original uniaxial symmetry with the particles free to reorient under the mere effect of thermal fluctuations. The time t_{OFF} taken by this field-off reorientation to re-establish the N_U phase is again much shorter in nematics of prolate HBPs (see Fig. 6.2(b)). In particular, t_{OFF} shows a tendency to increase with particle width up to $W^* = 4$, where $t_{OFF}/\tau \approx 15 \cdot 10^3$. When HBPs acquire a modest oblate geometry, such as from $W^* = 6$ to $W^* = 8$, t_{OFF} drastically decreases to around $t_{OFF}/\tau \approx 6 \cdot 10^3$, before increasing again at $W^* = 12$. We also notice that the free

reorientation at $W^* = 3.46$ and 4 is particularly slower than that of other anisotropies and deserves an explanation. The MSADs in the field-off scenarios, shown in Fig. 6.5(d)-(f), exhibit a linear profile throughout the simulation due to the absence of an external field and decrease upon increasing W^*. This tendency is also detected in the field-off s-VHFs of Fig. 6.6(b), where, similarly to the field-on case, the angular displacement decreases at increasing particle width. These elements would suggest a scenario where t_{OFF} increases and free rotation becomes slower upon increasing W^*. Because t_{OFF} is peaked for approximately self-dual shaped particles and then decreases (see Fig. 6.2(b)), there must be an additional element contributing to the field-free reorientation from the N_B to the N_U phase. We believe that this element is related to the ability of self-dual shaped HBPs of retaining phase biaxiality when the field is switched off. In our recent work on the field-induced phase behaviour of HBPs, we found that the self-dual shape requires a surprisingly weak external field, compared to prolate and oblate geometries, to spark an $N_U \rightarrow N_B$ transition [15]. In particular, the minimum field strength to stabilise N_B LCs was found to be $\varepsilon_f^* = 0.1$ and 0.25 at $W^* = 3.46$ and 4, respectively, and then increasing to $\varepsilon_f^* = 0.5$ at $W^* = 3$ and to $\varepsilon_f^* = 1$ at $W^* = 6$. Therefore, we believe that the field-free $N_B \rightarrow N_U$ transition at or very close to the self-dual shape is affected by such a modest energy barrier between the two nematic phases that the system tends to retain biaxiality over a longer time window as compared to nematics of oblate or prolate HBPs. In Fig. 6.7, we show the evolution of the s-VHFs of $W^* = 3.46$ and $W^* = 4$ at different times up to t_{OFF}. At short to intermediate time scales, after having switched the field off, these s-VHFs exhibit a double peak that suggests the presence of two populations of HBPs. Because these two populations rotate at sufficiently different rates, we can label them as *slow* and *fast*. The first peak survives over a relatively long period of time, between $0.2t_{OFF}$ and $0.7t_{OFF}$, turning gradually into a shoulder that disappears at longer times. These peaks and subsequent shoulders are especially pronounced in the case of $W^* = 4$ (Fig. 6.7(b)), explaining why t_{OFF} at $W^* = 4$ is significantly slower than t_{OFF} at $W^* = 3.46$. Double peaks and shoulders are not observed at other anisotropies or in field-on transitions (not shown here), indicating that these tendencies are especially relevant only in the field-off relaxation of self-dual shaped particles. In addition to their propensity towards biaxiality retention, HBPs with $W^* = 4$ rotate more slowly than perfectly self-dual shaped particles, as shown in Fig. 6.6(b) and in agreement with the

tendencies observed in N_U phase in the absence of external fields [34]. The resulting large value of t_{OFF} is therefore determined by the interplay between the particle's ability to rotate and the system's tendency of retaining phase biaxiality. This interplay explains the non-monotonic trend of t_{OFF} with particle shape in Fig. 6.2(b)) and provides, along with t_{ON}, a useful guideline to select the most suitable particle anisotropy for the design of field-responsive nanomaterials.

6.4 Conclusions

In summary, by Dynamic Monte Carlo simulation, we studied the field-induced dynamics in uniaxial nematic LCs of colloidal HBPs. By forcing the particles to reorient around the nematic director, the external field induces an $N_U \rightarrow N_B$ phase transition that takes the system to a new steady state. When the field is switched off, the biaxiality is gradually lost and the N_U phase is restored. The time taken for the system to reorient, also referred to as response time, strongly depends on the particle anisotropy. The response times in $N_U \rightarrow N_B$ and $N_B \rightarrow N_U$ switching were calculated and compared across all anisotropies studied. Despite being the optimal shape to promote phase biaxiality, the switching dynamics of self-dual shape HBPs is less satisfactory compared to prolate HBPs. In particular, rod-like HBPs with $W^* = 1$ exhibit the fastest reorientation times in both the field-on and field-off cases. The analysis of MSADs and s-VHFs show that the response time is a result of a trade-off between particle rotational diffusion and phase biaxiality retention, being both determined by shape anisotropy. Prolate HBPs were found to rotate faster than self-dual shaped or oblate HBPs, allowing rapid phase switching between the two nematic phases. Systems of HBPs with geometry equal or very close to the self-dual shape exhibit a particularly slow field-free reorientation, most likely due to relatively low field strength required to transform N_U into N_B phases and favouring the former in absence of an external field [15]. The ability of retaining biaxiality over a longer period of time is corroborated by the existence of a double peak in the angular s-VHFs of $N_B \rightarrow N_U$ transition at short-to-intermediate time scales. This double peak suggests the existence of two populations of (quasi) self-dual shaped HBPs whose reorientation is not uniform and delays the system relaxation. While prolate HBPs are especially field-responsive and exhibit a rapid field-free reorientation, when one analyse the distribution

of their angular displacements over time, this appears to be very broad, with particles exhibiting a very heterogeneous ability of rotating. By contrast, oblate HBPs, while significantly less responsive, are characterised by a very narrow distribution of angular displacements. All these elements offer a fundamental understanding of the impact of shape anisotropy on the dynamics of uniaxial-to-biaxial switching and a guidance to formulate nanomaterials with specific switching dynamics for target applications.

Acknowledgments

EMR would like to thank the Malaysian Government Agency Majlis Amanah Rakyat for funding his PhD at the University of Manchester. AP and LT acknowledges the financial support from the Leverhulme Trust Research Project Grant RPG-2018-415. EMR, LT, DC and AP acknowledge the assistance given by IT Services and the use of Computational Shared Facility at the University of Manchester. Finally, we thank Gerardo Campos-Villalobos (Utrecht University) for his assistance in generating the snapshots in Fig. 6.3.

Appendices

6.A1 Effect of field strength

In this appendix, we briefly discuss the effect of altering field intensity on the field-on response times, t_{ON} of HBPs. Here, we report the response times for the field-on case for all anisotropies studied at field strengths from $\varepsilon_f^* = 1.5$ to $\varepsilon_f^* = 3$. These field intensities result in the formation of strong $\mathrm{N_B}$ phases with $B_2 \geq 0.35$ [15]. The results are shown in Fig. 6.8.

At constant ε_f^*, we observe that t_{ON} generally increases with W^* and this increment is significant. For instance, at $\varepsilon_f^* = 2$, the response time increases by two orders of magnitude from $t_{\mathrm{ON}} \approx 57$ at $W^* = 1$ to $t_{\mathrm{ON}} \approx 5700$ at $W^* = 12$. We conclude that prolate particles tend to rotate faster than oblate particles, regardless the field strength. Upon increasing field strength, the reorientation becomes faster as suggested by the gradual decrease of t_{ON} with ε_f^*. In addition, we note that the statistical errors in t_{ON} decrease with ε_f^*, most likely due to a stronger suppression of rotational fluctuations. This tendency is consistent with the works by Zannoni and co-workers [7]. For rod-

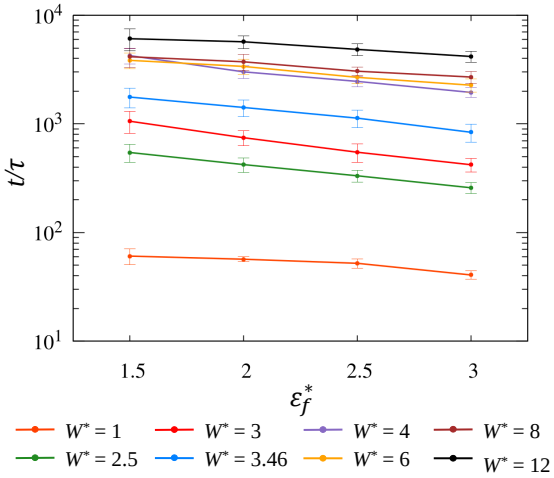

Figure 6.8: Changes in field-on response time, t_{ON} as a function of ε_f^* across different anisotropies.

like HBPs ($W^* = 1$), increasing ε_f does not significantly affect t_{ON}, probably because the reorientation capability of these HBPs is very close to its saturation value.

6.A2 Response times

In Table I, we report t_{ON} for $\varepsilon_f^* = 1.5$, 2, 2.5 and 3, and t_{OFF} for $\varepsilon_f^* = 3$.

W^*	t_{ON}				t_{OFF}
	$\varepsilon_f^* = 1.5$	$\varepsilon_f^* = 2$	$\varepsilon_f^* = 2.5$	$\varepsilon_f^* = 3$	$\varepsilon_f^* = 3$
1	60.7 ± 10.0	56.8 ± 2.9	52.1 ± 5.2	40.7 ± 3.6	75.0 ± 12.4
2.5	545.2 ± 100.9	422.0 ± 64.4	332.9 ± 40.7	258.3 ± 29.4	878.6 ± 160.1
3	1057.5 ± 243.0	746.4 ± 118.2	548.4 ± 106.8	420.9 ± 59.2	2181.0 ± 434.8
3.46	1764.9 ± 365.6	1416.6 ± 247.5	1130.0 ± 205.6	837.6 ± 160.0	7552.2 ± 2758.4
4	4247.8 ± 683.3	3012.6 ± 403.6	2461.8 ± 273.4	1948.8 ± 200.5	15004.6 ± 2011.0
6	3844.7 ± 641.8	3380.6 ± 546.0	2681.7 ± 345.7	2272.2 ± 310.4	5975.5 ± 1200.2
8	4151.4 ± 846.8	3728.3 ± 636.6	3055.4 ± 272.5	2700.0 ± 340.2	5602.0 ± 877.4
12	6084.4 ± 1376.9	5700.9 ± 777.0	4849.0 ± 598.6	4175.5 ± 487.5	6906.0 ± 733.8

Table 6.1: Table of response times for t_{ON} ($\varepsilon_f^* = 1.5$ to 3) and t_{OFF} ($\varepsilon_f^* = 3$) with associated statistical errors.

Bibliography

[1] Mormann, W., Hellwich, K.-H., Chen, J. & Wilks, E. S. Preferred names of constitutional units for use in structure-based names of polymers (iupac recommendations 2016). *Pure Appl. Chem.* **89**, 1695–1736 (2017).

[2] Brown, R. *The Miscellaneous Botanical Works of Robert Brown*, vol. 1 of *Cambridge Library Collection - Botany and Horticulture* (Cambridge University Press, 2015).

[3] Schadt, M. & Helfrich, W. Voltage-dependent optical activity of a twisted nematic liquid crystal. *Appl. Phys. Lett.* **18**, 127–128 (1971).

[4] Oh-e, M. & Kondo, K. Electro-optical characteristics and switching behavior of the in-plane switching mode. *Appl. Phys. Lett.* **67**, 3895–3897 (1995).

[5] Luckhurst, G. R. & Sluckin, T. J. *Biaxial nematic liquid crystals: theory, simulation and experiment* (Wiley, 2015).

[6] Lee, J.-H., Lim, T.-K., Kim, W.-T. & Jin, J.-I. Dynamics of electro-optical switching processes in surface stabilized biaxial nematic phase found in bent-core liquid crystal. *J. Appl. Phys.* **101**, 034105 (2007).

[7] Berardi, R. & Zannoni, C. Do thermotropic biaxial nematics exist? a monte carlo study of biaxial gay-berne particles. *J. Chem. Phys.* **113**, 5971–5979 (2008).

[8] Ricci, M., Berardi, R. & Zannoni, C. On the field-induced switching of molecular organization in a biaxial nematic cell and its relaxation. *J. Chem. Phys.* **143**, 084705 (2015).

[9] Taylor, M. P. & Herzfeld, J. Nematic and smectic order in a fluid of biaxial hard particles. *Phys. Rev. A.* **44**, 3742 (1991).

[10] Belli, S., Patti, A., Dijkstra, M. & van Roij, R. Polydispersity stabilizes biaxial nematic liquid crystals. *Phys. Rev. Lett.* **107**, 148303 (2011).

[11] Rafael, E. M., Cuetos, A., Corbett, D. & Patti, A. Self-assembly of freely rotating polydisperse cuboids: unveiling the boundaries of the biaxial nematic phase. *Soft Matter* **16**, 5565–5570 (2020).

[12] Dussi, S., Tasios, N., Drwenski, T., van Roij, R. & Dijkstra, M. Hard competition: stabilizing the elusive biaxial nematic phase in suspensions of colloidal particles with extreme lengths. *Phys. Rev. Lett.* **120**, 177801 (2018).

[13] Belli, S., Dijkstra, M. & van Roij, R. Depletion-induced biaxial nematic states of boardlike particles. *J. Phys.: Condens. Matter* **24**, 284128 (2012).

[14] Leferink op Reinink, A. B. G. M. *et al.* Tuning biaxiality of nematic phases of board-like colloids by an external magnetic field. *Soft Matter* **10**, 446–456 (2014).

[15] Cuetos, A., Rafael, E. M., Corbett, D. & Patti, A. Biaxial nematics of hard cuboids in an external field. *Soft Matter* **15**, 1922–1926 (2019).

[16] Cuetos, A., Dennison, M., Masters, A. & Patti, A. Phase behaviour of hard board-like particles. *Soft Matter* **13**, 4720–4732 (2017).

[17] Patti, A. & Cuetos, A. Monte carlo simulation of binary mixtures of hard colloidal cuboids. *Mol. Simul.* **44**, 516–522 (2018).

[18] Chiappini, M., Drwenski, T., Van Roij, R. & Dijkstra, M. Biaxial, twist-bend, and splay-bend nematic phases of banana-shaped particles revealed by lifting the "smectic blanket". *Phys. Rev. Lett.* **123**, 068001 (2019).

[19] Tasios, N. & Dijkstra, M. A simulation study on the phase behavior of hard rhombic platelets. *J. Chem. Phys.* **146**, 144901 (2017).

[20] van den Pol, E., Petukhov, A., Thies-Weesie, D., Byelov, D. & Vroege, G. Experimental realization of biaxial liquid crystal phases in colloidal dispersions of boardlike particles. *Phys. Rev. Lett.* **103**, 258301 (2009).

[21] Peroukidis, S. D., Vanakaras, A. G. & Photinos, D. J. Supramolecular nature of the nematic-nematic phase transitions of hard boardlike molecules. *Phys. Rev. E* **88**, 062508 (2013).

[22] Peroukidis, S. D. & Vanakaras, A. G. Phase diagram of hard board-like colloids from computer simulations. *Soft Matter* **9**, 7419–7423 (2013).

[23] Peroukidis, S. D. Biaxial mesophase behavior of amphiphilic anisometric colloids: a simulation study. *Soft Matter* **10**, 4199–4207 (2014).

[24] Skutnik, R. A., Geier, I. S. & Schoen, M. A biaxial nematic liquid crystal composed of matchbox-symmetric molecules. *Mol. Phys.* 1–21 (2020).

[25] Van den Pol, E., Lupascu, A., Davidson, P. & Vroege, G. The isotropic-nematic interface of colloidal goethite in an external magnetic field. *J. Chem. Phys.* **133**, 164504 (2010).

[26] Van den Pol, E. *et al.* Onsager revisited: Magnetic field induced nematic- nematic phase separation in dispersions of goethite nanorods. *Chem. Phys. Lett.* **1**, 2174–2178 (2010).

[27] Peroukidis, S. D., Klapp, S. H. & Vanakaras, A. G. Field-induced anti-nematic and biaxial ordering in binary mixtures of discotic mesogens and spherical magnetic nanoparticles. *Soft Matter* **16**, 10667–10675 (2020).

[28] Cuetos, A., Galindo, A. & Jackson, G. Thermotropic biaxial liquid crystalline phases in a mixture of attractive uniaxial rod and disk particles. *Phys. Rev. Lett.* **101**, 237802 (2008).

[29] Patti, A. & Cuetos, A. Brownian dynamics and dynamic monte carlo simulations of isotropic and liquid crystal phases of anisotropic colloidal particles: A comparative study. *Phys. Rev. E* **86**, 011403 (2012).

[30] Cuetos, A. & Patti, A. Equivalence of brownian dynamics and dynamic monte carlo simulations in multicomponent colloidal suspensions. *Phys. Rev. E* **92**, 022302 (2015).

[31] Corbett, D., Cuetos, A., Dennison, M. & Patti, A. Dynamic monte carlo algorithm for out-of-equilibrium processes in colloidal dispersions. *Phys. Chem. Chem. Phys.* **20**, 15118–15127 (2018).

[32] Daza, F. A. G., Cuetos, A. & Patti, A. Dynamic monte carlo simulations of inhomogeneous colloidal suspensions. *Phys. Rev. E* **102**, 013302 (2020).

[33] Chiappini, M., Patti, A. & Dijkstra, M. Helicoidal dynamics of biaxial curved rods in twist-bend nematic phases unveiled by unsupervised machine learning techniques. *Phys. Rev. E* **102**, 040601 (2020).

[34] Cuetos, A. & Patti, A. Dynamics of hard colloidal cuboids in nematic liquid crystals. *Phys. Rev. E* **101**, 052702 (2020).

[35] Lebovka, N. I., Vygornitskii, N. V. & Tarasevich, Y. Y. Relaxation in two-dimensional suspensions of rods as driven by brownian diffusion. *Phys. Rev. E* **100**, 042139 (2019).

[36] Chiappini, M., Grelet, E. & Dijkstra, M. Speeding up dynamics by tuning the non-commensurate size of rodlike particles in a smectic phase. *Phys. Rev. Lett.* **124**, 087801 (2020).

[37] Cuetos, A., Morillo, N. & Patti, A. Fickian yet non-gaussian diffusion is not ubiquitous in soft matter. *Phys. Rev. E* **98**, 042129 (2018).

[38] Stannarius, R. Comment on "dynamics of electro-optical switching processes in surface stabilized biaxial nematic phase found in bent-core liquid crystal". *J. Appl. Phys.* **104**, 034105 (2008).

[39] Gottschalk, S., Lin, M. C. & Manocha, D. Obbtree: A hierarchical structure for rapid interference detection. *Comp. Graph.* **30**, 171–180 (1996).

[40] John, B. S. & Escobedo, F. A. Phase behavior of colloidal hard tetragonal parallelepipeds (cuboids): A monte carlo simulation study. *J. Phys. Chem. B* **109**, 23008–23015 (2005).

[41] John, B. S., Juhlin, C. & Escobedo, F. A. Phase behavior of colloidal hard perfect tetragonal parallelepipeds. *J. Chem. Phys.* **128**, 044909 (2008).

[42] Carrasco, B. & de la Torre, J. G. Hydrodynamic properties of rigid particles: comparison of different modeling and computational procedures. *Biophys. J.* **76**, 3044–3057 (1999).

[43] García de la Torre, J., del Rio Echenique, G. & Ortega, A. Improved calculation of rotational diffusion and intrinsic viscosity of bead models for macromolecules and nanoparticles. *J. Phys. Chem. B* **111**, 955–961 (2007).

[44] Iglewicz, B. & Hoaglin, D. C. *How to detect and handle outliers*, vol. 16 (Asq Press, 1993).

[45] Mazza, M. G., Giovambattista, N., Starr, F. W. & Stanley, H. E. Relation between rotational and translational dynamic heterogeneities in water. *Phys. Rev. Lett.* **96**, 057803 (2006).

[46] Mazza, M. G., Giovambattista, N., Stanley, H. E. & Starr, F. W. Connection of translational and rotational dynamical heterogeneities with the breakdown of the stokes-einstein and stokes-einstein-debye relations in water. *Phys. Rev. E* **76**, 031203 (2007).

Chapter 7

Active Microrheology of Colloidal Suspensions of Hard Cuboids

The content of this Chapter has been published as an article in *Physical Review E*. My contributions are listed as follows: Luca Tonti and Fabián Garcia-Daza developed the software; Effran Mirzad Rafael, Luca Tonti, Fabián A. García Daza, and Alessandro Patti performed the investigation; Effran Mirzad Rafael, Luca Tonti, Fabián A. García Daza, and Alessandro Patti reviewed and edited the draft.

Abstract

By performing dynamic Monte Carlo simulations, we investigate the microrheology of isotropic suspensions of hard-core colloidal cuboids. In particular, we infer the local viscoelastic behaviour of these fluids by studying the dynamics of a probe spherical particle that is incorporated in the host phase and is dragged by an external force. This technique, known as active microrheology, allows one to characterise the microscopic response of soft materials upon application of a constant force, whose intensity spans here three orders of magnitude. By tuning the geometry of cuboids from oblate to prolate as well as the system density, we observe different responses that are quantified by measuring the effective friction perceived by the probe particle. The resulting friction coefficient exhibits a linear regime at forces that are much weaker and larger than the thermal forces, whereas a non-linear, force-thinning regime is observed at intermediate force intensities.

7.1 Introduction

Complex fluids are present in a wide variety of day-to-day consumables, including cosmetics, pharmaceuticals, paints and foods. A common thread shared by these families of products is the correlation between the interactions established at the sub-micron scale and their macroscopic response as well as the ability of their microscopic domains to rearrange upon the application of external stimuli [1]. When flow is imposed, complex fluids tend to display behaviours characteristic of non-Newtonian fluids, such as viscoelasticity [2]. Traditionally, the rheology of fluids has been studied with mechanical rheometers, providing information mainly on their bulk flow behaviour. However, advances in rheological techniques have enabled the assessment of the viscoelastic behaviour of soft materials through a technique referred to as microrheology (MR) [1]. MR operates under the mechanism of embedding a colloidal tracer in a host fluid, whose flow properties can be inferred by analysing the tracer's dynamics. This technique has been applied to study a wide spectrum of systems including chromonic liquid crystals [3], DNA [4, 5], actin networks [6], biofluids [7, 8], hard [9] and soft [10] spheres. More specifically, passive MR involves monitoring the response of the tracer merely due to the thermal fluctuations of the host fluid (or bath) - this will probe the linear response of the complex fluid. By contrast, active MR unveils the fluid's nonlinear response by applying an external force to the tracer - active MR can be performed at fixed force or fixed velocity. In fixed-forced active MR, the tracer is pulled with a constant force through the bath and, by applying the Stoke's drag law, the effective friction coefficient (or microviscosity) of the bath can then be obtained [11].

Among complex fluids, colloidal suspensions of anisotropic particles are especially attractive for their rich phase behaviour and ability to self-assemble in a wide spectrum of mesophases, such as nematic and smectic liquid crystals (LCs). In particular, biaxial particles, such as boards, ellipsoids, rhombuses and bent-core particles, are able to form exotic LC phases [12, 13, 14, 15, 16], including the biaxial nematic (N_B) phase, whose existence at molecular scale is still object of discussions [17]. As far as nanoboards are concerned, the first experimental evidence of the existence of stable N_B phases was reported about a decade ago in dispersions of mineral goethite particles [18]. This discovery has inspired further works on the phase behaviour of board-like particles, which has been extensively studied by experiments, theory and simulations

[19, 20, 21, 22, 23, 24, 25, 26, 27, 28, 29, 30, 31, 32, 33, 34]. Nevertheless, less attention has been given to the study of their dynamics, so far mostly limited to the long-time structural relaxation of uniaxial nematic LCs [35], field-driven uniaxial-to-biaxial nematic switching [36] and in cylindrical confinement [37]. Generally speaking, it was found that the dynamics of board-like particles strongly depends on their geometry, which spans prolate (rod-like) to oblate (disk-like) shapes, and interesting behaviours are observed at the self-dual shape, where oblate and prolate geometries fuse into one. In particular, the self-dual nanoboards were found to exhibit the lowest overall translational diffusivity in equilibrium uniaxial nematic phases; and show the slowest overall response time in field-induced uniaxial-biaxial nematic switching due to biaxial retention tendencies, when compared to other geometries. These findings highlight the importance of shape anisotropy to control the dynamics of board-like particles. Currently, state-of-the-art commercial displays are engineered with molecular LCs, and colloidal LCs serve mainly as model systems to understand the behaviour of their molecular counterparts. However, colloidal LCs are regarded as potential candidates for next-generation displays, as these systems are athermal, relatively cheap and highly susceptible to external fields [38, 39, 40, 41]. As such, understanding the dynamics and rheology of these systems is as relevant as mapping their phase behaviour.

To this end, in this work, we employ the dynamic Monte Carlo (DMC) simulation technique to investigate the viscoelastic response of suspensions of hard cuboids by active MR. The DMC method has been recently shown to reproduce MR results of Langevin Dynamics in systems of spherical and rod-like particles to an excellent degree of qualitative and quantitative agreement [42]. In particular, we are interested in the nonlinear response of board-like particles, as application and manufacturing processes require complex fluids to flow and be driven out-of-equilibrium. More specifically, we investigate the effective friction of a bath of board-like particles in the isotropic phase through fixed-force active MR. The investigation will be framed within the effects of altering the packing fraction of the bath and the particle geometry (board-like particles are morphed from prolate to oblate). The present paper is arranged as follows: we first discuss the details of our model systems and simulation methods, referring the reader to our recent work for details on how DMC has been adapted to study active MR [42], then we analyse the results at different Péclet numbers when varying either the system packing or the

geometry of the bath particles, and, in the final section, we draw our conclusions.

7.2 Model and simulation methodology

Our systems consist of $N_c = 1000$ hard board-like particles (HBP) and $N_s = 1$ hard spherical tracer, constrained in an elongated box with volume $V_{box} = L_x \times L_y \times L_z$, where $L_x = L_y$ and $L_z = 3L_x$. HBPs are cuboids of thickness T, length L and width W, with T the system unit length. In this work, all HBPs have a reduced length given by $L^* \equiv L/T = 12$, while the reduced width, $W^* \equiv W/T$, is a simulation parameter that takes the values $W^* = \{1, \sqrt{L^*} \approx 3.46, 8\}$, providing respectively prolate, self-dual shaped and oblate geometries. The spherical tracer has a diameter $\sigma = T$. A schematic representation of these particles is given in Fig. 7.1. Given the hard-core nature of the particles, the phase behaviour of the systems is fully characterised by the particle geometry and system packing fraction, which can be approximated to

$$\phi \approx \frac{N_c v_0}{V} \tag{7.1}$$

where $v_0 = TWL$ is the volume of one HBP and the contribution of the spherical tracer has been disregarded [43]. In the first part of this work, we will assess the impact of ϕ on the effective friction of the bath. In this part, we employ isotropic (I) phases consisting of HBPs at a fixed width, $W^* = 3.46$, and comparisons are made across three packing fractions, namely ϕ = 0.20, 0.25 and 0.30. The reason why we selected the self-dual shape to ponder the effect of density is due to the relatively large stability range of the I phase at this specific particle geometry [29]. In the second part, we are interested in altering the HBP's geometry from prolate to oblate at a fixed packing fraction. In this case, we will keep the packing fraction constant at $\phi = 0.20$ and increase the particle width from $W^* = 1$ to 8.

To equilibrate the systems we employed standard MC simulations in the canonical ensemble, reproducing the I phases from our previous work [29]. Because the interactions between particles are modelled by a hard-core potential, moves are always accepted unless an overlap is produced. Overlaps between cuboids are checked with the separating axes theorem proposed by Gottschalk and coworkers [44] and later adapted by John and Escobedo to study the phase behaviour of HBPs with square cross section [45]. To

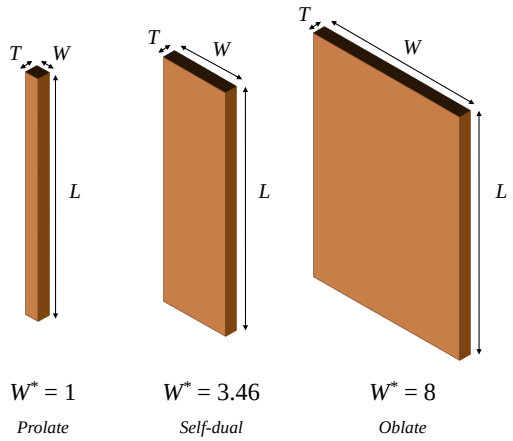

Figure 7.1: Model HBPs studied in this work. Length, width and thickness are respectively labelled as $L = 12T$, W and T, with T the system unit length. The reduced width, $W^* \equiv W/T$, assumes three different values to reproduce prolate, self-dual and oblate geometries.

check the occurrence of overlaps between the spherical tracer and cubes, we employed the OCSI algorithm [46]. Equilibration was considered achieved when the uniaxial order parameters showed a steady value within moderate statistical fluctuations. Because we are only investigating MR in I phases, equilibration was relatively fast, usually taking no more than $1{\times}10^6$ MC cycles, with each cycle consisting of $N = N_c{+}N_s$ attempts of displacing or rotating a randomly selected particle. In particular, the uniaxial order parameters have been obtained from the diagonalisation of the following symmetric tensor:

$$\mathbf{Q}^{\lambda\lambda} = \frac{1}{2N}\left\langle \sum_{i=1}^{N} \left(3\hat{\lambda}_i \cdot \hat{\lambda}_i - \mathbf{I}\right) \right\rangle \tag{7.2}$$

where $\hat{\lambda}_i = \hat{\mathbf{x}}, \hat{\mathbf{y}}, \hat{\mathbf{z}}$ are unit vectors respectively aligned with W, T and L, while $\mathbf{I}$ is the identity tensor. The diagonalisation of $\mathbf{Q}^{\lambda\lambda}$ results in three eigenvalues $(S_{2,W}, S_{2,T}, S_{2,L})$ and their corresponding eigenvectors $(\hat{\mathbf{m}}, \hat{\mathbf{l}}, \hat{\mathbf{n}})$. A phase is considered nematic if at least one of the eigenvalues is larger than 0.40. In our equilibrated phases, all the uniaxial order parameters are below the threshold required to be classified as nematics. The resulting I phases are then used as initial configurations in the DMC production runs.

The DMC method produces Brownian Dynamics (BD) trajectories by rescaling an arbitrarily set MC time step, $\delta t_{\mathrm{MC,m}}$, with the acceptance rate, $\mathcal{A}_m$, where $m = c, s$ refers to the cuboidal bath particles and spherical tracer, respectively. The interested reader is referred to our past works for further details on the DMC technique [47, 48, 49, 50, 51, 42].

Here, we only review the most relevant aspects that are instrumental to the present work. Essentially, we set $\delta t_{\mathrm{MC,s}}$ within values between $10^{-2}\tau$ and $10^{-7}\tau$, where $\tau = \eta T^3/(k_B T_b)$ is the time unit, while T_b and η are, respectively, the bath temperature and viscosity. As a result, the MC time step of the tracer is obtained through the corresponding acceptance rates (see Supporting information for details). More specifically, when the tracer is subjected to a one-dimensional external force in the positive direction of $\hat{\mathbf{z}}$, taking the form $\mathbf{F}_{\mathrm{ext}} = F_{\mathrm{ext}}\hat{\mathbf{z}}$, the time step $\delta \mathrm{t}_{\mathrm{MC,s}}$ is obtained from the following relationship [50]:

$$\left(\frac{3}{2}\mathcal{A}_s - \frac{1}{2}\right)\delta t_{\mathrm{MC,s}} = \mathcal{A}_c \delta t_{\mathrm{MC,c}} \tag{7.3}$$

where $\mathcal{A}_s$ and $\mathcal{A}_c$ are the acceptance rates of spherical tracer and cubes, respectively. It should be noted that the external force is considered in the above equation by means of $\mathcal{A}_s$. According to our previous work, $\mathcal{A}_s \sim 1 - \beta F_{ext}\delta x_z/4$ [50]. In active MR-DMC simulations, we stress that in order to produce the most reliable approximations, the following condition should be satisfied:

$$\beta F_{\mathrm{ext}}\delta x_z \ll 1 \tag{7.4}$$

where $\beta = 1/k_B T_b$, with k_B the Boltzmann's constant and δx_z the maximum displacement of the tracer in the direction of the force. The so-equilibrated $\delta t_{\mathrm{MC,s}}$, along with $\delta t_{\mathrm{MC,c}}$, are then used to produce the time trajectories by DMC simulations. We applied periodic boundary conditions to our elongated simulation boxes and do not perform unphysical moves such as jumps, swaps and cluster moves in order to produce the correct dynamics. The tracer is pulled by an external force $\mathbf{F}_{\mathrm{ext}}$ parallel to the z-axis that takes the form:

$$\beta \mathbf{F}_{\mathrm{ext}} = \frac{\mathrm{Pe}}{a}\hat{\mathbf{z}} \tag{7.5}$$

where $a = \sigma/2$ is the tracer radius, and Pe is the Péclet number which gives the ratio of advection to thermal forces. The displacement of the HBPs' centres of mass, $\delta \mathbf{r}_i$, is decoupled into three terms: $\delta \mathbf{r}_{c,i} = X_W \hat{\mathbf{u}} + X_T \hat{\mathbf{v}} + X_L \hat{\mathbf{w}}$, where X_α, with $\alpha = W, T, L$, is the maximum displacement allowed to a generic HBP. These displacements are set by the following Einstein relations:

$$|X_\alpha| \leq \sqrt{2D^{\mathrm{tra}}_{\alpha,i}\delta t_{\mathrm{MC,c}}}, \tag{7.6}$$

where $D_{\alpha,i}^{\mathrm{tra}}$ are the translational diffusion coefficients at infinite dilution along the three particle direction. Similarly, the rotation of the HBPs are performed *via* three consecutive rotations with maximum rotation Y_W, Y_T and Y_L around $\hat{\mathbf{u}}$, $\hat{\mathbf{v}}$ and $\hat{\mathbf{w}}$, respectively. These maximum rotations read

$$|Y_\alpha| \leq \sqrt{2D_{\alpha,i}^{\mathrm{rot}}\delta t_{\mathrm{MC,c}}}, \tag{7.7}$$

where $D_{\alpha,i}^{\mathrm{rot}}$ are the rotational diffusion coefficients at infinite dilution. Both translational and rotational diffusion coefficients have been calculated with the open-source software HYDRO++ [52, 53]. For the specific values of $D_{\alpha,i}^{\mathrm{tra}}$ and $D_{\alpha,i}^{\mathrm{rot}}$, readers are referred to our previous work on the equilibrium dynamics of HBPs [35], where values are reported in units of $D_0 \equiv T^2\tau^{-1}$ (translational) and $D_r \equiv \mathrm{rad}^2\tau^{-1}$ (rotational).

As far as the spherical tracer is concerned, we disregard rotations and only consider translational moves. In particular, the displacement of the tracer's centre of mass reads $\delta\mathbf{r}_s = Z_\parallel\hat{\mathbf{i}} + Z_\perp\hat{\mathbf{j}} + Z_\perp\hat{\mathbf{k}}$, where $\hat{\mathbf{i}}$ is the displacement vector parallel to the external force $\mathbf{F}_{\mathrm{ext}}$ while $\hat{\mathbf{j}}$ and $\hat{\mathbf{k}}$ are vectors orthogonal to $\hat{\mathbf{i}}$ and to each other. Due to the presence of the force, the resulting maximum displacement of the spherical tracers incorporates the inertial contribution and reads

$$\left|Z_\parallel\right| \leq \sqrt{2D_s\delta t_{\mathrm{MC,s}} + (D_s\beta F_{\mathrm{ext}}\delta t_{\mathrm{MC,s}})^2} \tag{7.8}$$

while the maximum displacement in planes perpendicular to $\mathbf{F}_{\mathrm{ext}}$ is similar to that of HBPs:

$$|Z_\perp| \leq \sqrt{2D_s\delta t_{\mathrm{MC,s}}} \tag{7.9}$$

The tracer diffusion coefficient at infinite dilution, D_s, is obtained from the Stokes-Einstein relation:

$$\frac{D_s}{D_0} = \frac{1}{3\pi} \tag{7.10}$$

In this paper, we are interested in the rheology of HBPs in the I phase. To evaluate this, we computed the effective friction coefficient derived from the Stokes-drag expression:

$$\frac{\gamma_{\text{eff}}}{\gamma_0} = \frac{F_{\text{ext}}}{6\pi\eta a\langle v_s\rangle} \tag{7.11}$$

where $\gamma_0 = 6\pi\eta a$ is the friction coefficient of the medium and $\langle v_s\rangle$ is the mean velocity of the tracer at long times. The initial I phases were equilibrated in a way to ensure that all configurations were mutually uncorrelated. Following equilibration, in the DMC production run, we applied an external force of magnitude $(0, 0, F_{\text{ext}}) = (0, 0, \text{Pe}\ k_B T_b/a)$ to the tracer and allowed it to displace a distance of at least $L_z/2$ (half of the longest box length). We set between 2×10^5 to 4×10^6 MC cycles for our simulations, depending on the values of ϕ and Pe. All data points are averaged from 750 independent trajectories.

7.3 Results

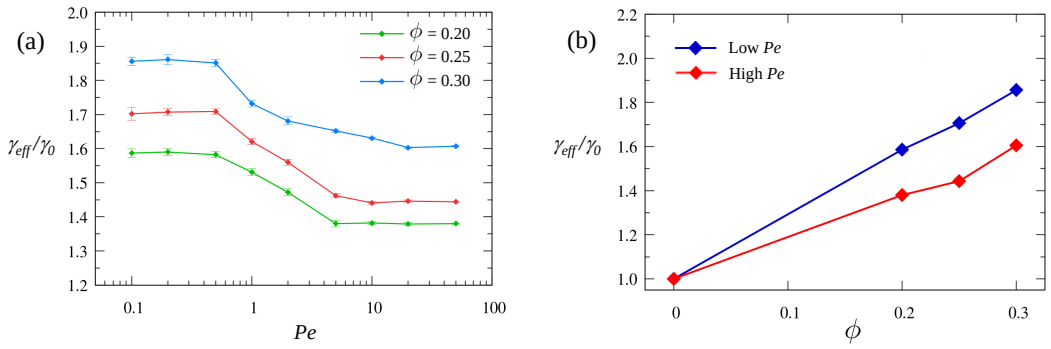

Figure 7.2: (a) Dependence of the friction coefficient with Pe in I phases of HBPs with $L^* = 12$ and $W^* = 3.46$ at $\phi = 0.20$, 0.25 and 0.30. (b) Variation of $\gamma_{\text{eff}}/\gamma_0$ at high and low Pe at different ϕ. The lines are guides for the eye.

We first report the effect of increasing the system packing fraction on the effective friction coefficient in I phases of self-dual-shaped HBPs. At this particular geometry, where $W = \sqrt{LT} \approx 3.46T$, the I phase is stable up to $\phi = 0.30$. At any other particle width, within the range $1 \leq W^* \leq 12$ and $\phi = 0.30$, oblate or prolate nematic LCs are observed [29]. The dependence of the friction coefficient on the Pe number for this family of HBPs is reported in Fig. 7.2(a) for $\phi = 0.20$, 0.25 and 0.30. While the friction experienced by the probe particle increases with the system density, its qualitative behaviour is very similar and characterised by the presence of three separate regimes.

At Pe < 0.5, corresponding to relatively weak external forces, a plateau is observed, with $\gamma_{\text{eff}}/\gamma_0 \approx 1.6$, 1.7 at 1.85 and $\phi = 0.20$, 0.25, and 0.30, respectively. At such small

Pe numbers, the advection force exerted by the tracer is too weak to significantly perturb the local particle distribution of the host HBPs, merely leading to weakly distorted microstructures in the bath [54]. Basically, the thermal fluctuations of the surrounding fluid dominate on the external force applied, leading to an essentially symmetric distribution of HBPs around the tracer. This can be clearly observed by calculating the local changes in density ρ of bath particles within volumes v around the tracer. Since the external force induces an axially symmetrical distribution of host particles near the tracer, the volumes v are defined by virtually dividing the space into an arbitrary set of concentric rings centered on the tracer axis. We have calculated the local densities as $\rho(v) = \langle N(t)/v \rangle$ where $N(t)$ refers to the number of particles in volume v at time t, and $\langle ... \rangle$ indicates time average. As shown in Fig. 7.3, at Pe $= 0.1$ the density distribution of HBPs around the tracer is uniform at both $\phi = 0.20$ (left column) and $\phi = 0.30$ (right column). When the advection force is increased slightly to Pe $= 0.5$, the density of HBPs surrounding the tracer is still relatively uniform, and we expect the effective friction coefficient to be similar to Pe $= 0.1$. This low-Pe linear regime approaches the passive microrheology limit [55, 54]. We also note that the presence of the probe particle does not have a tangible effect on the orientation of the cuboids around it, which maintain their random orientation, similarly to the rest of the bath particles. This does not exclude that some of them change orientation while the tracer is close enough, but the global effect does not indicate substantial alignment. We have recently investigated this scenario in I phases of hard spherocylinders by calculating a local orientational correlation function and found a very weak, negligible ordering at low Pe numbers, which fades out as soon as the applied force increases and the non-linear regime is approached [42]. We indeed see an increase in density around the tracer as revealed by the density maps shown in Fig. 7.3, that agree well with our findings in the I phase of hard spherocylinders. However, this increase in local density is not accompanied by an increase in ordering: the cuboids around the tracer basically remain randomly oriented.

At Pe ≥ 1, advection forces begin to dominate over thermal forces and a force-thinning regime, with the friction coefficient decreasing with increasing the intensity of the force applied, develops. This non-linear regime closely reminds the shear-thinning observed in non-Newtonian fluids, whose viscosity decreases as the shear rate increases. It spans over $1 \leq$ Pe ≤ 5 for $\phi = 0.20$ and 0.25, and over $1 \leq$ Pe ≤ 20 for $\phi = 0.30$.

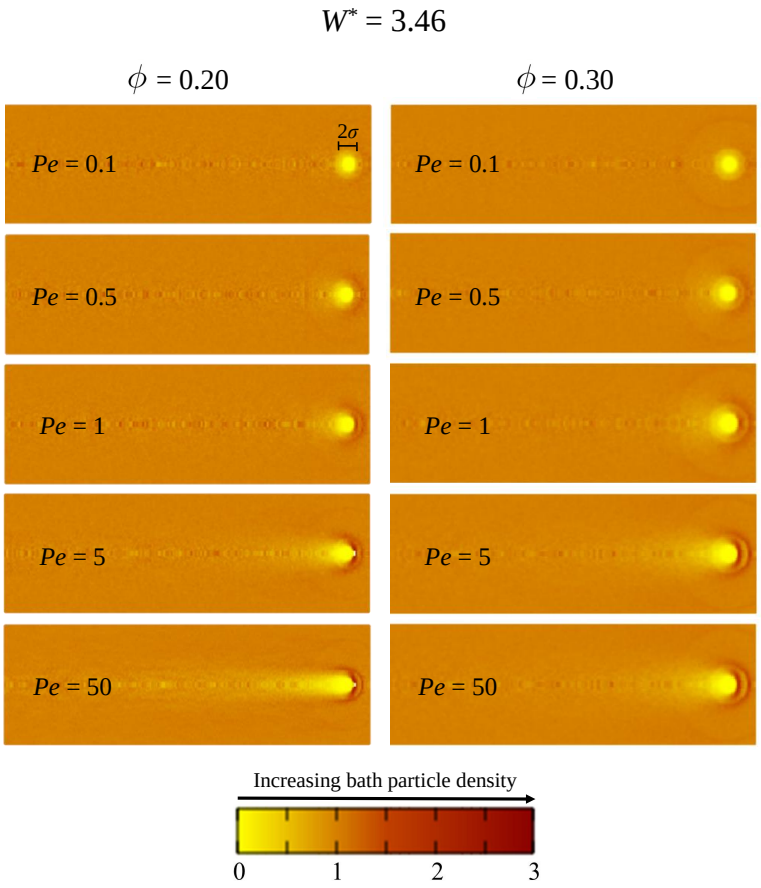

Figure 7.3: Density maps of self-dual shaped HBPs at $\phi = 0.20$ (left) and $\phi = 0.30$ (right) and at the Pe numbers indicated in each frame. The colour palette is shown at the bottom of the figure and refers to the ratio between the local density and the bath density. Yellow regions indicate low bath particle density, while the dark red regions indicate high bath particle density.

Our results can be compared with what has been reported by theoretical predictions [54, 55, 56, 57], simulations [58, 11, 50] and experiments [59, 60] on suspensions of spherical particles. To the best of our knowledge, our investigation proves for the first time that similar force-thinning behaviour at increasing Pe can be observed also in suspensions of particles with cuboidal shape. In this regime, the tracer has sufficient driving force to induce stronger microstructural distortions and cause a symmetry breaking of the HBPs surrounding the tracer. In the density maps shown in Fig. 7.3, at both $\phi = 0.20$ and 0.30, we can see the onset of accumulation of bath particles, represented by a dark blue cap in the upstream face of the tracer. The same density maps reveal the existence of a low-density trail (or wake) that forms behind the tracer, indicating that HBPs need some time to heal the distortions caused by the forced displacement of the tracer. In agreement with past theoretical, simulation and experimental works, this depletion trail increases in length as Pe increases [57, 60, 11]. In this regime, the tracer's mobility increases as the reduction in the effective friction coefficient suggests. It is also noted that the force-thinning regime in I phases of self-dual HBPs spans a much smaller range, especially when compared to systems of (quasi-)hard spheres [58, 11] or hard spherocylinders [42]. For instance, at $\phi = 0.30$, the force-thinning regime for hard spherocylinders spans $2 \leq \mathrm{Pe} \leq 50$ while for (quasi-)hard spheres, it is $2 \leq \mathrm{Pe} \leq 100$. This trend seems to indicate that as the host particles become more anisotropic, the force-thinning regime tends to span a smaller range with the effective friction coefficients also generally becoming smaller. This can be expected as host particles that are more anisotropic are larger and harder to distort; therefore, the tracer's mobility becomes more hindered.

Finally, at larger Pe numbers, the effective friction coefficient exhibits a second plateau. This plateau corresponds to the high-Pe regime, where the advection force dominates thermal forces [55, 54]. When analysing the density distribution in Fig. 7.3, at $\mathrm{Pe} = 50$ (bottom row), the trail of depleted particles is longer for a system that is less packed. More specifically, at $\phi = 0.20$, the trail's length is approximately 5σ, whereas at $\phi = 0.30$, it is about 3σ. This phenomenon is most likely due to the concentration gradient of the bath that forms around the tracer. At $\phi = 0.30$, this concentration gradient is larger than that at $\phi = 0.20$ and hence drives particles back into the depleted trail faster than the concentration gradient forming at $\phi = 0.20$. [56]. We stress, however, that we have neglected hydrodynamic interactions (HI). The theoretical formalism developed by

Khair and Brady suggested that if HI effects are significant, force-thickening may occur at high Pe, and the effective friction coefficient may experience an increase [55, 2].

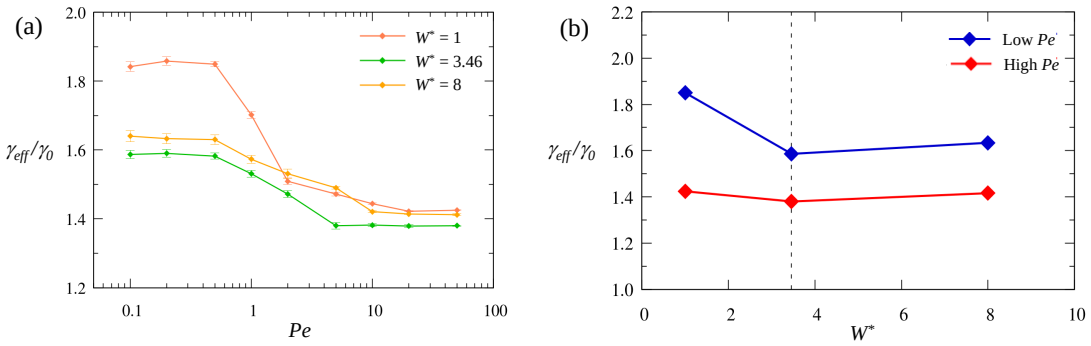

Figure 7.4: (a) Plot of $\gamma_{\text{eff}}/\gamma_0$ *vs.* Pe for I phases at $\phi = 0.20$ at $W^* = 1$, 3.46 and $W^* = 8$ (b) Variation of $\gamma_{\text{eff}}/\gamma_0$ at high and low Pe at different W^* with $\phi = 0.20$. The dotted vertical line indicates the self-dual shape at $W^* = 3.46$. The lines are guides for the eye.

In Fig. 7.2(b), we show the dependence of the averaged effective friction coefficient, $\gamma_{\text{eff}}/\gamma_0$, on the packing fraction. The upper curve has been obtained by averaging the friction coefficients calculated at Pe ≤ 0.5, whereas the lower curve results from the average of friction coefficients measured in the high-Pe regime. In agreement with past works [58, 50], $\gamma_{\text{eff}}/\gamma_0$ tends to be larger in denser systems at both high and low Pe. This is somehow expected as the structure of denser systems is less prone to be distorted, hampering the tracer's mobility and resulting in larger effective frictions. Since HI are disregarded, the effect of ϕ on the effective friction coefficient of dual-shaped HBPs agrees well with the tendencies observed in past works that made similar assumptions [11].

In light of these considerations, we now examine the effect of altering the shape anisotropy of HBPs on the effective friction induced by a tracer with diameter $\sigma = T$ at $\phi = 0.20$. In particular, we investigate the impact of particle anisotropy in baths of prolate ($W^* = 1$), self-dual-shaped ($W^* = 3.46$) and oblate ($W^* = 8$) HBPs. In Fig. 7.4(a), we report the $\gamma_{\text{eff}}/\gamma_0$ *vs* Pe profile of different geometries. In all geometries studied, we once again observe three regimes associated with the effective friction: two plateau regimes corresponding to low and high Pe numbers, and a force-thinning regime at intermediate Pe numbers. In the low Pe range ($0.1 \leq$ Pe ≤ 0.5), the effective friction coefficients for all W^* are substantially constant, within statistical uncertainty. In this regime, the force applied to the tracer is too weak to perturb the microstructure of the HBP bath, so a symmetrical distribution of HBPs is found around the tracer. This tendency can be

appreciated by looking at the density maps in Fig. 7.5, particularly at Pe = 0.1 for both $W^* = 1$ and 8. At Pe = 1, all three systems enter a force-thinning regime, which is characterised by a reduction in the effective friction coefficient. The nonlinear regime of prolate HBPs ($W^* = 1$) spans in the range of $1 \leq \text{Pe} \leq 20$, while that of self-dual-shaped and oblate HBPs spans $1 \leq \text{Pe} \leq 5$ and $1 \leq \text{Pe} \leq 10$, respectively. Force-thinning occurs because inertial forces are strong enough to induce a microstructural distortion of the bath of HBPs, increasing its mobility. In the density maps of Fig. 7.5, we can see an asymmetry of the HBPs' density around the tracer with a region of high-density of HBPs in front of the tracer and low-density trail behind it for $\text{Pe} \geq 1$. At large Pe, the effective friction coefficients achieve a second plateau, which is due to a balance between the advection force from the tracer and a retarding force from the thin layer of very dense HBPs in front of the tracer that tends to scale proportionally with increasing Pe. As we can see clearly in Fig. 7.4(a), at large values of Pe, the effective friction coefficients of all geometries have very similar values.

Fig. 7.4(b) reports how the average effective friction coefficients vary with particle geometry. The low-Pe effective friction coefficients are averaged across $0.1 \leq \text{Pe} \leq 0.5$ for all geometries. For high Pe, it is averaged from $\text{Pe} \geq 20$ for prolate HBPs, $\text{Pe} \geq 5$ for self-dual HBPs and $\text{Pe} \geq 10$ for oblate HBPs. From both Fig. 7.4(a) and Fig. 7.4(b), it is clear that the effective friction coefficient has a dependence on the geometry of the bath HBPs. At low Pe, we observe that $\gamma_{\text{eff}}/\gamma_{0,\text{W}^*=1} > \gamma_{\text{eff}}/\gamma_{0,\text{W}^*=8} > \gamma_{\text{eff}}/\gamma_{0,\text{W}^*=3.46}$. At intermediate Pe numbers, we observe crossovers between the effective friction coefficients at $W^* = 1$ and 8. Finally, in the high-Pe regime, the effective friction coefficients have relatively similar values for the three particle geometries. We believe that these variations are due to an interplay between two factors: (*i*) the relative size of the tracer with respect to that of HBPs and (*ii*) the presence of nematic-like clusters at $\phi = 0.20$. The relative HBP/tracer size sets to what extent the tracer can perturb the microstructure of the bath. Due to the smaller surface area of prolate HBPs, one can assume that it is easier for the tracer to push away prolate HBPs and gain more mobility as compared to oblate HBPs. We note that our model particles do not possess an explicit mass. However, a measure of their inertia to move can still be inferred from their diffusion coefficients at infinite dilution, whose magnitude goes with the inverse of a relevant characteristic length of the particle, which is related to its volume and thus to its mass. Oblate particles diffuse gen-

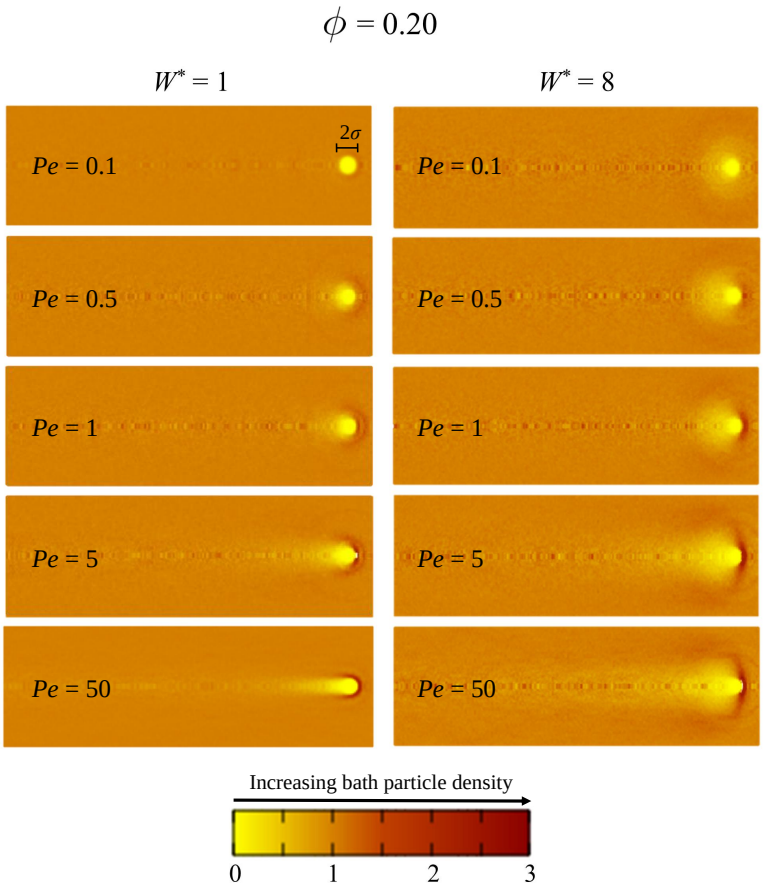

Figure 7.5: Density maps of HBPs with $\phi = 0.20$ at $W^* = 1$ (left) and $W^* = 8$ (right) and at the Pe numbers indicated in each frame. The colour palette is shown at the bottom of the figure and refers to the ratio between the local density and the bath density. Yellow regions indicate low bath particle density, while the dark red regions indicate high bath particle density.

erally slower than prolate particles, except along the vector $\hat{\mathbf{x}}$, as in this case the relevant surface area is LT, being the same for both oblate and prolate HBPs. The resistance to flow offered by larger surface areas can explain why the force-thinning of prolate HBPs is much more drastic in Fig. 7.4(a). When the HBPs have an oblate anisotropy ($W^* = 8$), it is harder for the tracer to push them away, so the tracer's mobility is only mildly enhanced with increasing Pe and a relatively soft force-thinning is detected. In the density map of Fig. 7.5, one can observe that the low-density wake of $W^* = 1$ at Pe $= 50$ is approximately as large as the tracer diameter. This might be due to the rod-like shape of the bath particles, which can better accommodate around the tracer when perturbed, in contrast to suspensions of plate-like bath particles, whose low-density wake appears to be much larger than the tracer diameter. Since the cross-sectional area of the oblate particles is larger, there is a high likelihood for the tracer to be pushing the broader surface of the HBP, and this creates a larger low-density wake. The aforementioned considerations on the effect of tracer/HBPs size ratio can give an interpretation exclusively on the values of γ_{eff}/γ_0 at high Pe numbers, where the external force acting on the probe particle is strong enough to distort the microstructure of the bath. The same arguments can not explain the results obtained at low Pe: in these conditions, we do not observe any relevant differences in the structure of HBPs in the proximity of the tracer and in bulk, because the forces that determine the motion of the tracer (in this case thermal fluctuations of the medium) are too weak to cause any distortion.

In addition to relative tracer/HBP size, also the phase behaviour of each system at $\phi = 0.20$ plays a role in determining the effective friction coefficient of the bath. Although all systems at this packing fraction are in the I phase, the features of their phase behaviour are different due to how far they are from their respective I-N phase boundary. In particular, at $\phi = 0.20$, the systems with prolate ($W^* = 1$) and oblate ($W^* = 8$) HBPs are closer to their respective I-N phase boundary than those made of self-dual-shaped HBPs ($W^* = 3.46$) [29]. The packing fraction at which the I phase first transforms into a N phase is reported in Table 7.1 for each value of the particle width [29]. We also report the difference, $\Delta\phi_{\mathrm{I-N}} \equiv \phi_{\mathrm{I-N}} - \phi$, between this transition point and the actual system packing, which is $\phi = 0.20$ for the three geometries. We stress that the I-N transition in systems of hard cuboids has a strong first-order signature and what we are reporting in Table 7.1 is the packing fraction at which the I phase must be compressed to transform

into a N phase.

W^*	$\phi_{\text{I–N}}$	$\Delta\phi_{\text{I–N}}$
1.00	0.235	0.035
3.46	0.319	0.119
8.00	0.222	0.022

Table 7.1: Difference in packing fraction of HBPs ($\Delta\phi_{\text{I–N}}$) with $W^* = 1, 3.46$ and 8 at $\phi = 0.20$ with their packing at their respective I-N phase boundary ($\phi_{\text{I–N}}$). Here, $\Delta\phi_{\text{I–N}} \equiv \phi_{\text{I–N}} - \phi$ where the values of $\phi_{\text{I–N}}$ are selected at the point where the I phase transitions into the N phase for each geometry.

We also notice that recent simulations in our group reported the formation of nematic-like clusters in systems of HBPs with $W^* = 1$ and 8 at $\phi = 0.20$, that is sufficiently close to the I-N phase transition [43]. The presence of clusters of oriented cuboids, whose local packing can be larger than that of the surrounding I fluid, can slow down the tracer mobility and ultimately determine the MR of the whole system. In support of these arguments, the MR experiments by Paladugu and co-workers showed that N phases of bent-core mesogens exhibit unusual properties due to the presence of cybotactic (smectic) clusters [61]. These authors found that the viscosity anisotropy, defined as the difference between the viscosity measured along the nematic director and that perpendicular to it, is negative in cluster-free N phases and positive in the presence of cybotactic clusters. The increase of viscosity in the direction of the director, and the consequent reduction in particle self-diffusion, is most likely due to the compactness and packing of the oriented clusters.

7.4 Conclusions

In summary, we performed fixed-force active microrheology DMC simulations [50] to study the rheology of I fluids of colloidal cuboids. To gain an insight into their microrheological response, we computed the effective friction coefficient at increasing values of the Pe number, a dimensionless quantity that sets the advection-to-thermal force ratio. In particular, at very small Pe, thermal forces dominate and the tracer's motion is essentially Brownian, whereas at very large Pe, inertial forces dominate and the tracer's motion is basically unaffected by the thermal fluctuations of the surrounding bath. Tuning the system packing fraction, from $\phi = 0.20$ to 0.30, and the particle width, from $W^* = 1$

to $W^* = 8$, dramatically influences the morphology, phase behaviour and dynamics of these fluids and, ultimately, their microrheological response. To clarify the effect of varying the packing fraction, we studied self-dual shaped HBPs, whose width, thickness and length are such that $W = \sqrt{LT}$. These systems have been selected as they exhibit stable I phases up to $\phi = 0.30$ [29]. We found that the effective friction coefficients exhibit two linear regimes at low and high Pe numbers and a force-thinning regime at intermediate Pe, a characteristic observed in colloidal systems when HI are neglected [11, 54]. We found that increasing system density causes an enhanced friction experienced by the tracer since denser systems tend to have stronger local rigidity that is harder to disrupt. When varying the particle geometry from prolate ($W^* = 1$) to oblate ($W^* = 8$) at a fixed ϕ, we found that the effective friction coefficients tend to show non-monotonic trends in all detected regimes. We believe that this behaviour could result from an interplay between the relative tracer/HBP size, and the presence of nematic-like clusters. At the moment, how these effects come into play is not fully clear, and more work is currently under consideration to fully understand these preliminary observations.

Acknowledgments

E.M.R. thanks the Malaysian Government Agency Majlis Amanah Rakyat for funding his Ph.D. at the University of Manchester. A.P., L.T. and F.A.G.D. acknowledge financial support from the Leverhulme Trust Research Project Grant No. RPG-2018-415. A.P. is supported by a Maria Zambrano Senior distinguished researcher fellowship, financed by the European Union within the NextGenerationEU program. All authors acknowledge the assistance given by IT Services and the use of the Computational Shared Facility at the University of Manchester.

Supporting information

We present the details of the systems studied in this paper, consisting of $N_c = 1000$ hard board-like particles (HBPs) with thickness T, length L and width W, and $N_s = 1$ spherical tracer with diameter T. For comparison, we report the Péclet number Pe, reduced width $W^* \equiv W/T$, the bath volume fraction $\phi \approx N_c v_0/V$ with $v_0 = TWL$ the single cuboid

volume, elementary time steps $\delta t_{\mathrm{MC},s}$ and $\delta t_{\mathrm{MC},c}$ in units of τ, and acceptance rates $\mathcal{A}_c$ and $\mathcal{A}_s$.

Pe	$\delta t_{\mathrm{MC,s}}/\tau$	$\delta t_{\mathrm{MC,c}}/\tau$	$\mathcal{A}_c$	$\mathcal{A}_s$
0.1	1.00×10^{-1}	1.25×10^{-1}	0.6802	0.8965
0.2	1.00×10^{-1}	1.20×10^{-1}	0.6855	0.8889
0.5	1.00×10^{-1}	1.24×10^{-1}	0.6812	0.8649
1	1.00×10^{-2}	1.04×10^{-2}	0.8940	0.9386
2	1.00×10^{-3}	9.95×10^{-4}	0.9659	0.9694
5	1.00×10^{-3}	9.72×10^{-4}	0.9662	0.9401
10	1.00×10^{-4}	9.63×10^{-5}	0.9892	0.9647
20	1.00×10^{-4}	9.45×10^{-5}	0.9893	0.9347
50	1.50×10^{-5}	1.42×10^{-5}	0.9958	0.9390

Table 7.2: Details of system with HBPs with $W^* = 1$ at $\phi = 0.20$.

Pe	$\delta t_{\mathrm{MC,s}}/\tau$	$\delta t_{\mathrm{MC,c}}/\tau$	$\mathcal{A}_c$	$\mathcal{A}_s$
0.1	1.00×10^{-1}	1.11×10^{-1}	0.8513	0.9465
0.2	1.00×10^{-1}	1.09×10^{-1}	0.8525	0.9387
0.5	1.00×10^{-1}	1.06×10^{-1}	0.8544	0.9140
1	1.00×10^{-2}	1.00×10^{-2}	0.9527	0.9564
2	1.00×10^{-3}	9.90×10^{-4}	0.9848	0.9761
5	1.00×10^{-3}	9.68×10^{-4}	0.9850	0.9482
10	1.00×10^{-4}	9.75×10^{-5}	0.9952	0.9684
20	1.00×10^{-4}	9.48×10^{-5}	0.9951	0.9400
50	1.50×10^{-5}	1.43×10^{-5}	0.9981	0.9427

Table 7.3: Details of system with HBPs with $W^* = 3.46$ at $\phi = 0.20$.

Pe	$\delta t_{\mathrm{MC,s}}/\tau$	$\delta t_{\mathrm{MC,c}}/\tau$	$\mathcal{A}_c$	$\mathcal{A}_s$
0.1	1.00×10^{-1}	1.19×10^{-1}	0.7810	0.9265
0.2	1.00×10^{-1}	1.11×10^{-1}	0.7832	0.9124
0.5	1.00×10^{-1}	1.14×10^{-1}	0.7853	0.8975
1	1.00×10^{-2}	1.01×10^{-2}	0.9303	0.9492
2	1.00×10^{-3}	9.87×10^{-4}	0.9776	0.9733
5	1.00×10^{-3}	9.65×10^{-4}	0.9778	0.9437
10	1.00×10^{-4}	9.67×10^{-5}	0.9929	0.9663
20	1.00×10^{-4}	9.35×10^{-5}	0.9930	0.9366
50	1.50×10^{-5}	1.40×10^{-5}	0.9973	0.9398

Table 7.4: Details of system with HBPs with $W^* = 3.46$ at $\phi = 0.25$.

Pe	$\delta t_{\mathrm{MC,s}}/\tau$	$\delta t_{\mathrm{MC,c}}/\tau$	$\mathcal{A}_c$	$\mathcal{A}_s$
0.1	1.00×10^{-1}	1.29×10^{-1}	0.7065	0.9105
0.2	1.00×10^{-1}	1.20×10^{-1}	0.7084	0.9026
0.5	1.00×10^{-1}	1.24×10^{-1}	0.7142	0.8760
1	1.00×10^{-2}	1.04×10^{-2}	0.9055	0.9410
2	1.00×10^{-3}	1.00×10^{-3}	0.9696	0.9692
5	1.00×10^{-3}	9.62×10^{-4}	0.9703	0.9375
10	1.00×10^{-4}	9.81×10^{-5}	0.9903	0.9628
20	1.00×10^{-4}	9.55×10^{-5}	0.9904	0.9305
50	1.50×10^{-5}	1.42×10^{-5}	0.9963	0.9345

Table 7.5: Details of system with HBPs with $W^* = 3.46$ at $\phi = 0.30$.

Pe	$\delta t_{\mathrm{MC,s}}/\tau$	$\delta t_{\mathrm{MC,c}}/\tau$	$\mathcal{A}_c$	$\mathcal{A}_s$
0.1	1.00×10^{-1}	1.07×10^{-1}	0.8968	0.9583
0.2	1.00×10^{-1}	1.05×10^{-1}	0.8978	0.9500
0.5	1.00×10^{-1}	1.02×10^{-1}	0.8991	0.9249
1	1.00×10^{-2}	9.95×10^{-3}	0.9672	0.9596
2	1.00×10^{-3}	9.90×10^{-4}	0.9895	0.9770
5	1.00×10^{-3}	9.48×10^{-4}	0.9897	0.9485
10	1.00×10^{-4}	9.71×10^{-5}	0.9966	0.9680
20	1.00×10^{-4}	9.38×10^{-5}	0.9975	0.9381
50	1.50×10^{-5}	1.41×10^{-5}	0.9987	0.9409

Table 7.6: Details of system with HBPs with $W^* = 8$ at $\phi = 0.20$.

Bibliography

[1] Cicuta, P. & Donald, A. M. Microrheology: a review of the method and applications. *Soft matter* **3**, 1449–1455 (2007).

[2] Zia, R. N. Active and passive microrheology: theory and simulation. *Annual Review of Fluid Mechanics* **50**, 371–405 (2018).

[3] Habibi, A., Blanc, C., Mbarek, N. B. & Soltani, T. Passive and active microrheology of a lyotropic chromonic nematic liquid crystal disodium cromoglycate. *Journal of Molecular Liquids* **288**, 111027 (2019).

[4] Chapman, C. D. & Robertson-Anderson, R. M. Nonlinear microrheology reveals entanglement-driven molecular-level viscoelasticity of concentrated dna. *Physical review letters* **113**, 098303 (2014).

[5] Fernandez-Castanon, J., Bianchi, S., Saglimbeni, F., Di Leonardo, R. & Sciortino, F. Microrheology of dna hydrogel gelling and melting on cooling. *Soft Matter* **14**, 6431–6438 (2018).

[6] Levin, M. *et al.* Kinetics of actin networks formation measured by time resolved particle-tracking microrheology. *Soft matter* **16**, 7869–7876 (2020).

[7] Weigand, W. *et al.* Active microrheology determines scale-dependent material properties of chaetopterus mucus. *PloS one* **12**, e0176732 (2017).

[8] Watts, F. *et al.* Investigating the micro-rheology of the vitreous humor using an optically trapped local probe. *Journal of Optics* **16**, 015301 (2013).

[9] Wilson, L., Harrison, A., Schofield, A. B., Arlt, J. & Poon, W. Passive and active microrheology of hard-sphere colloids. *The Journal of Physical Chemistry B* **113**, 3806–3812 (2009).

[10] Nazockdast, E. & Morris, J. F. Active microrheology of colloidal suspensions: Simulation and microstructural theory. *Journal of Rheology* **60**, 733–753 (2016).

[11] Carpen, I. C. & Brady, J. F. Microrheology of colloidal dispersions by brownian dynamics simulations. *Journal of Rheology* **49**, 1483–1502 (2005).

[12] Dussi, S., Tasios, N., Drwenski, T., van Roij, R. & Dijkstra, M. Hard competition: stabilizing the elusive biaxial nematic phase in suspensions of colloidal particles with extreme lengths. *Phys. Rev. Lett.* **120**, 177801 (2018).

[13] Tasios, N. & Dijkstra, M. A simulation study on the phase behavior of hard rhombic platelets. *J. Chem. Phys.* **146**, 144901 (2017).

[14] Chiappini, M., Drwenski, T., van Roij, R. & Dijkstra, M. Biaxial, twist-bend, and splay-bend nematic phases of banana-shaped particles revealed by lifting the "smectic blanket". *Phys. Rev. Lett.* **123**, 068001 (2019).

[15] Fernández-Rico, C. *et al.* Shaping colloidal bananas to reveal biaxial, splay-bend nematic, and smectic phases. *Science* **369**, 950–955 (2020).

[16] Berardi, R. & Zannoni, C. Do thermotropic biaxial nematics exist? a monte carlo study of biaxial gay–berne particles. *The Journal of Chemical Physics* **113**, 5971–5979 (2000).

[17] Lehmann, M. *et al.* From molecular biaxiality of real board-shaped mesogens to phase biaxiality? on the hunt for the holy grail of liquid crystal science. *Soft matter* **15**, 8496–8511 (2019).

[18] van den Pol, E., Petukhov, A. V., Thies-Weesie, D. M. E., Byelov, D. V. & Vroege, G. J. Experimental realization of biaxial liquid crystal phases in colloidal dispersions of boardlike particles. *Phys. Rev. Lett.* **103**, 258301 (2009).

[19] van den Pol, E. *et al.* Onsager revisited: Magnetic field induced nematic- nematic phase separation in dispersions of goethite nanorods. *Chem. Phys. Lett.* **1**, 2174–2178 (2010).

[20] van den Pol, E., Lupascu, A., Davidson, P. & Vroege, G. The isotropic-nematic interface of colloidal goethite in an external magnetic field. *J. Chem. Phys.* **133**, 164504 (2010).

[21] Martínez-Ratón, Y., Varga, S. & Velasco, E. Biaxial nematic phases in fluids of hard board-like particles. *Phys. Chem. Chem. Phys.* **13**, 13247–13254 (2011).

[22] Belli, S., Patti, A., Dijkstra, M. & van Roij, R. Polydispersity stabilizes biaxial nematic liquid crystals. *Phys. Rev. Lett.* **107**, 148303 (2011).

[23] Belli, S., Dijkstra, M. & van Roij, R. Depletion-induced biaxial nematic states of boardlike particles. *J. Phys.: Condens. Matter* **24**, 284128 (2012).

[24] Peroukidis, S. D. & Vanakaras, A. G. Phase diagram of hard board-like colloids from computer simulations. *Soft Matter* **9**, 7419–7423 (2013).

[25] Peroukidis, S. D., Vanakaras, A. G. & Photinos, D. J. Supramolecular nature of the nematic-nematic phase transitions of hard boardlike molecules. *Phys. Rev. E* **88**, 062508 (2013).

[26] Peroukidis, S. D. Biaxial mesophase behavior of amphiphilic anisometric colloids: a simulation study. *Soft Matter* **10**, 4199–4207 (2014).

[27] Mederos, L., Velasco, E. & Martínez-Ratón, Y. Hard-body models of bulk liquid crystals. *J. Phys.: Condens. Matter* **26**, 463101 (2014).

[28] González-Pinto, M., Martínez-Ratón, Y., Velasco, E. & Varga, S. Effect of shape biaxiality on the phase behavior of colloidal liquid-crystal monolayers. *Phys. Chem. Chem. Phys.* **17**, 6389–6400 (2015).

[29] Cuetos, A., Dennison, M., Masters, A. & Patti, A. Phase behaviour of hard board-like particles. *Soft Matter* **13**, 4720–4732 (2017).

[30] Yang, Y. *et al.* Synthesis and assembly of colloidal cuboids with tunable shape biaxiality. *Nat. Commun.* **9**, 4513 (2018).

[31] Patti, A. & Cuetos, A. Monte carlo simulation of binary mixtures of hard colloidal cuboids. *Mol. Simul.* **44**, 516–522 (2018).

[32] Cuetos, A., Mirzad Rafael, E., Corbett, D. & Patti, A. Biaxial nematics of hard cuboids in an external field. *Soft Matter* **15**, 1922–1926 (2019).

[33] Mirzad Rafael, E., Cuetos, A., Corbett, D. & Patti, A. Self-assembly of freely rotating polydisperse cuboids: unveiling the boundaries of the biaxial nematic phase. *Soft Matter* **16**, 5565–5570 (2020).

[34] Skutnik, R. A., Geier, I. S. & Schoen, M. A biaxial nematic liquid crystal composed of matchbox-symmetric molecules. *Mol. Phys.* 1–21 (2020).

[35] Cuetos, A. & Patti, A. Dynamics of hard colloidal cuboids in nematic liquid crystals. *Phys. Rev. E* **101**, 052702 (2020).

[36] Mirzad Rafael, E., Tonti, L., Corbett, D., Cuetos, A. & Patti, A. Dynamics of uniaxial-to-biaxial nematics switching in suspensions of hard cuboids. *Physics of Fluids* **33**, 067115 (2021).

[37] Patti, A. & Cuetos, A. Dynamics of colloidal cubes and cuboids in cylindrical nanopores. *Physics of Fluids* **33**, 097103 (2021).

[38] Gabriel, J.-C. P. & Davidson, P. New trends in colloidal liquid crystals based on mineral moieties. *Advanced Materials* **12**, 9–20 (2000).

[39] Tschierske, C. & Photinos, D. J. Biaxial nematic phases. *Journal of Materials Chemistry* **20**, 4263–4294 (2010).

[40] Lekkerkerker, H. N. W. & Vroege, G. J. Liquid crystal phase transitions in suspensions of mineral colloids: new life from old roots. *Philosophical Transactions of the Royal Society A: Mathematical, Physical and Engineering Sciences* **371**, 20120263 (2013).

[41] Leferink op Reinink, A. B. G. M. *et al.* Tuning biaxiality of nematic phases of board-like colloids by an external magnetic field. *Soft Matter* **10**, 446–456 (2014).

[42] García Daza, F. A., Puertas, A. M., Cuetos, A. & Patti, A. Microrheology of colloidal suspensions via dynamic monte carlo simulations. *Journal of Colloid and Interface Science* (2021).

[43] Tonti, L., García Daza, F. A. & Patti, A. Diffusion of globular macromolecules in liquid crystals of colloidal cuboids. *Journal of Molecular Liquids* **338**, 116640 (2021).

[44] Gottschalk, S., Lin, M. C. & Manocha, D. Obbtree: A hierarchical structure for rapid interference detection. *Comp. Graph.* **30**, 171–180 (1996).

[45] John, B. S. & Escobedo, F. A. Phase behavior of colloidal hard tetragonal parallelepipeds (cuboids): A monte carlo simulation study. *J. Phys. Chem. B* **109**, 23008–23015 (2005).

[46] Tonti, L. & Patti, A. Fast overlap detection between hard-core colloidal cuboids and spheres. the ocsi algorithm. *Algorithms* **14**, 72 (2021).

[47] Patti, A. & Cuetos, A. Brownian dynamics and dynamic monte carlo simulations of isotropic and liquid crystal phases of anisotropic colloidal particles: A comparative study. *Phys. Rev. E* **86**, 011403 (2012).

[48] Cuetos, A. & Patti, A. Equivalence of brownian dynamics and dynamic monte carlo simulations in multicomponent colloidal suspensions. *Phys. Rev. E* **92**, 022302 (2015).

[49] Corbett, D., Cuetos, A., Dennison, M. & Patti, A. Dynamic monte carlo algorithm for out-of-equilibrium processes in colloidal dispersions. *Phys. Chem. Chem. Phys.* **20**, 15118–15127 (2018).

[50] García Daza, F. A., Cuetos, A. & Patti, A. Dynamic monte carlo simulations of inhomogeneous colloidal suspensions. *Phys. Rev. E* **102**, 013302 (2020).

[51] Chiappini, M., Patti, A. & Dijkstra, M. Helicoidal dynamics of biaxial curved rods in twist-bend nematic phases unveiled by unsupervised machine learning techniques. *Phys. Rev. E* **102**, 040601(R) (2020).

[52] Carrasco, B. & García de la Torre, J. Hydrodynamic properties of rigid particles: comparison of different modeling and computational procedures. *Biophys. J.* **76**, 3044–3057 (1999).

[53] García de la Torre, J., del Rio Echenique, G. & Ortega, A. Improved calculation of rotational diffusion and intrinsic viscosity of bead models for macromolecules and nanoparticles. *J. Phys. Chem. B* **111**, 955–961 (2007).

[54] Squires, T. M. & Brady, J. F. A simple paradigm for active and nonlinear microrheology. *Physics of Fluids* **17**, 073101 (2005).

[55] Khair, A. S. & Brady, J. F. Single particle motion in colloidal dispersions: a simple model for active and nonlinear microrheology. *Journal of Fluid Mechanics* **557**, 73–117 (2006).

[56] Gazuz, I., Puertas, A. M., Voigtmann, T. & Fuchs, M. Active and nonlinear microrheology in dense colloidal suspensions. *Physical review letters* **102**, 248302 (2009).

[57] Swan, J. W. & Zia, R. N. Active microrheology: Fixed-velocity versus fixed-force. *Physics of Fluids* **25**, 083303 (2013).

[58] Puertas, A. M. & Voigtmann, T. Microrheology of colloidal systems. *Journal of Physics: Condensed Matter* **26**, 243101 (2014).

[59] Meyer, A., Marshall, A., Bush, B. G. & Furst, E. M. Laser tweezer microrheology of a colloidal suspension. *Journal of rheology* **50**, 77–92 (2006).

[60] Sriram, I., Meyer, A. & Furst, E. M. Active microrheology of a colloidal suspension in the direct collision limit. *Physics of Fluids* **22**, 062003 (2010).

[61] Paladugu, S. *et al.* Microrheology to probe smectic clusters in bent-core nematic liquid crystals. *Soft Matter* **16**, 7556–7561 (2020).

blank page

Chapter 8

Conclusion and Future Work

This thesis focused on the dynamical properties of colloidal particles. In the context of Brownian motion, we aimed to deepen our understanding of colloidal particles diffusion in systems that show a degree of long-range ordering. Instead of studying different phenomena separately, we focused on the intertwined correlations between thermodynamical, dynamical and mechanical properties of suspensions. Despite we know from decades that entropy is sufficient to spark self-assembly of particles, and we enlightened the nature of the peculiar non-deterministic motion of colloids, we still need to better comprehend what happens when both mechanisms come into play, and if and how they relate to each other. In this thesis we wanted to explore how particles self-organisation in ordered systems determines their dynamics, and how particles dynamics itself determines the formation of organised structures, all of this by examining such phenomena in different soft matter systems, consequently showing their sometimes counter-intuitive consequences on particle and suspension properties. These complex mechanisms stem from one simple characteristic of the particles: their topology. Nanoparticles tend to naturally organise in different structures solely because of their shape. Molecules of a fluid interact with the available surface of a colloidal particle, hence, the random motion of the colloid depends on both its surface and its volume, i.e., its shape. When particles tend to diffuse along specific directions, they will naturally organise depending on how they display; their mutual interaction further influences their motion. While every different system requires a focused investigation on different length and time scales to properly understand them, in this thesis we instead chose to fix our attention on particle shape, dynamics and naturally occurring ordering, by modelling our systems as compositions

of hard board-like and spherical particles, and by simulating their diffusive motion with dynamic Monte Carlo methods.

In order to perform Monte Carlo simulations of our model systems, we first needed a collision detection algorithm between cuboids and spheres. To this end, in Chapter 3 we investigated the computational efficiency of different collision detection algorithms available in literature, and we proposed a few improvements that concluded with the Oriented Cuboid Sphere Intersection (OCSI) algorithm that we proposed in our scientific publication. We showed that, aiming to the application of collision detection algorithms in particle simulations, the run-time of some of the algorithms tested is strongly dependent on the size of the colliding particles. The best performance and stability was observed when applying Single Instruction Multiple Data parallelism. Our algorithm OCSI is easy to implement both in C/C++ and FORTRAN existing codes, while being geometry-independent and time efficient, thanks to the use of specific OpenMP directives to generate automatic SIMD vectorization of the code during compilation time.

After we implemented OCSI in the software for DMC simulations, we studied how structural organisation affects the diffusion of globular macromolecules, modelling the system with small hard spheres in a bath of hard board-like particles. The analysis of the dynamics of all the particles, whose results are reported in Chapter 4, showed strong anisotropic diffusion of both cuboidal and spherical particles when the system is assembled in a uniaxial nematic phase. More specifically, the modelled globular macromolecules diffuse preferentially parallel to the nematic phase in prolate nematic systems, and perpendicular to the nematic director in oblate nematics, with deviation from expected Gaussian distribution of particle positions at intermediate times. Variation of the non-Gaussian parameter has been observed also for prolate cuboids in isotropic phases, with increasing deviation from zero at increasing density. We expect this behaviour to be correlated to the formation of nematic-like cluster of cuboids at these densities; a more detailed analysis of the lifetime of these clusters is needed to further clarify this point.

In Chapter 5 we implemented Ewald summation for dipolar interaction into the software to model suspensions of polarisable cubic particles. We first investigated the transition of the electrorheological fluid at low packing fraction 0.02, and we studied the kinetics of formation of chain-like structures commonly observed in these kind of flu-

ids. We used machine learning analysis to optimise the parameters needed for the cluster analysis; we then followed the formation of cluster and the particle relative orientation over time, with a uniaxial order parameter specifically renormalised for particles with cubic symmetry. For a specific strength of the external field, the diluted system of polarised cubes manages to reach the same steady state with an equilibrium chain length distribution, regardless of the initial conditions, with kinetic rates of aggregation and disruption dependent on the size of the clusters involved. Then, we added one spherical tracer to the suspension of cubes and used passive microrheology techniques to investigate the linear viscoelastic response of the fluid at equilibrium with the field on and off. While at low dilution we did not observe any difference in microrheology upon the application of the field, at higher packing fraction 0.20 the system showed anisotropic frequency-dependent viscoelasticity, when splitting the analysis of tracer diffusion in the direction parallel and perpendicular to the field.

In Chapter 6 we studied systems of hard-board like particles in out-of-equilibrium conditions, transitioning from a uniaxial to a biaxial nematic phase induced by an external field, spanning the analysis to particles from prolate to oblate geometries. Self-dual shaped cuboids give the slowest response times, especially for the on-to-off transition, in link with their capability to retain biaxial orientation. In this work, we highlight the non-trivial characteristics of this system when we move from an analysis at equilibrium to out-of-equilibrium conditions: the pros and cons of promoting biaxiality with specific particle shape must be carefully considered in the design of possible future applications in optical instruments. All these results have been observed with a simple model external field; more detailed description of particle polarisation due to an external field is required for a clearer analysis of these systems.

In Chapter 7 we investigated mechanical properties of suspensions of cuboids in the isotropic phase by means of active microrheology DMC simulations. While observing a decay of friction coefficient when changing the magnitude of the force on the tracer from low to high Pe numbers, with a force-thinning behaviour in all cases, the microviscosity of the suspensions resulted dependent on the shape of the cuboids. From the results obtained, such dependency seems to be influenced by the size of the tracer with respect to the size of the cuboids, and the possible formation of nematic-like cluster, which have been previously observed in these systems at the same concentration in Chapter 4. To

further corroborate these observations, more simulations with different tracer size, and the implementation of hydrodynamic interactions between particles are necessary.

Finally, in the last period of the PhD, we started to investigate the effect of confinement in isotropic suspensions of cuboids. More specifically, we are performing MC and DMC simulations of hard board-like particles in the same conditions of particle shape and packing fraction previously investigated and presented in Chapter 7, but now confined between two parallel impenetrable walls, at three selected distances between the walls, namely $z = \{25T, 37T, 49T\}$, for T the thickness of the cuboids and the unit length of the system. Snapshots of these systems for the case with $z = 49T$ are shown in Figure 8.1.

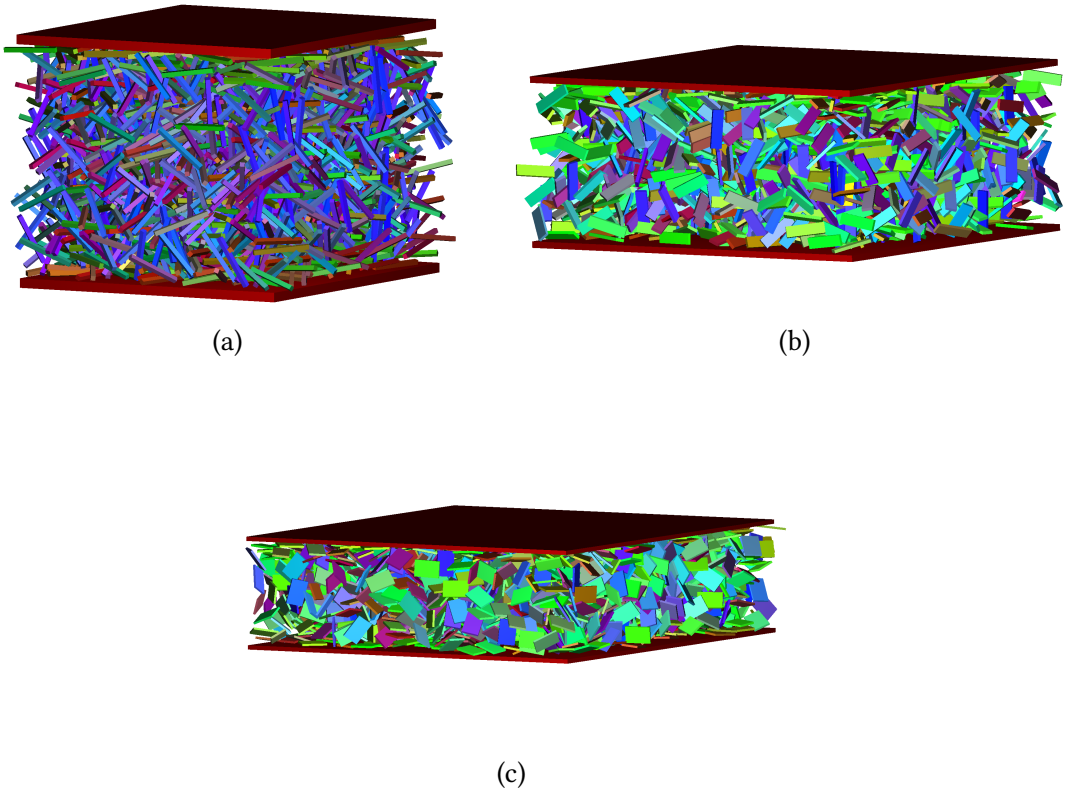

Figure 8.1: Snapshots of $N = 2400$ HBPs in I phase with packing fraction $\eta = 0.150$, confined between parallel walls (in red) at distance $z = 49T$. (a) HBPs with geometry $\{1, 1, 12\}$, (b) HBPs with geometry $\{1, 3.46, 12\}$ (c) HBPs with geometry $\{1, 8, 12\}$.

At the moment we investigated the relative particle orientation and their space distribution as a function of the distance between the walls. We observed that prolate HBPs tend to concentrate in contact with the walls, with their longest extent parallel to them, while dual-shaped and oblate particles showed lower local densities in proximity of the walls, with respect to the bulk density. In all cases, except oblate HBPs at smallest con-

finement $z = 25T$, all the systems manage to reach the average bulk density halfway between the upper and lower walls. At the same time, also uniaxial and biaxial order parameters, computed for particles in slabs parallel to the confinement, show an increase for particles close to the wall, suggesting the local reorientation of the HBPs due to the confinement and neighbouring particles. We are performing DMC simulations of these systems with one added hard spherical tracer of diameter equal to T, the thickness of the cuboids. We are interested in analysing the dynamical properties of the cuboids, and we are planning to apply passive microrheology techniques to investigate the viscoelastic response of the fluid of HBPs in these conditions, letting the spherical tracer diffuse from the center of the simulation box. The analysis of the tracer trajectory should give us an insight of the different local distribution of the cuboids, from the center (in bulk-like conditions) to close to the walls (where strong deviation from I phase has been observed so far).